MAGNETIC EFFECT IN THE BIOLOGICAL FUNCTIONING OF HEMOGLOBIN: DFT+QMC APPROACH WITHIN AN EFFECTIVE MULTI-ORBITAL ANDERSON IMPURITY MODEL

A Thesis Submitted to
the Graduate School of Engineering and Sciences of
İzmir Institute of Technology
in Partial Fulfillment of the Requirements for the Degree of

DOCTOR OF PHILOSOPHY

in Materials Science and Engineering

by
Selma MAYDA BACAKSIZ

July 2019
İZMİR

We approve the thesis of **Selma MAYDA BACAKSIZ**

Examining Committee Members:

Prof. Dr. Nejat BULUT
Department of Physics, İzmir Institute of Technology

Asst. Prof. Dr. Umut ADEM
Department of Materials Science and Engineering, İzmir Institute of Technology

---

Assoc. Prof. Dr. A. Devrim GÜÇLÜ
Department of Physics, İzmir Institute of Technology

Prof. Dr. Sadamichi MAEKAWA
Center for Emergent Matter Science, RIKEN

Prof. Dr. Oğuz GÜLSEREN
Department of Physics, Bilkent University

9 July 2019

Prof. Dr. Nejat BULUT
Supervisor, Department of Physics
İzmir Institute of Technology

Prof. Dr. Mustafa M. DEMİR
Co-Supervisor, Department of
Materials Science and Engineering
İzmir Institute of Technology

Assoc. Prof. Dr. Hâldun SEVİNÇLİ
Head of the Department of
Materials Science and Engineering

Prof. Dr. Aysun SOFUOĞLU
Dean of the Graduate School of
Engineering and Sciences

ACKNOWLEDGMENTS

Foremost, I would like to express my sincere gratitute to my advisor Prof. Dr. Nejat Bulut for his support during my Ph.D., for his patience and motivation. I consider myself fortunate to have the opportunity to work with him.

I would also thank to Prof. Sadamichi Maekawa for his insightful comments about my Ph.D. study.

In addition, I would thank to Assoc. Prof. Dr. A. Devrim Güçlü and Asst. Prof. Dr. Umut Adem for their suggestions about my thesis.

My thanks also go to my group mate Zafer Kandemir for his friendship and discussions on physics.

I express my thanks to Fadıl İyikanat, Zebih Çetin and Mehmet Yağmurcukardeş for their friendship and for their helps. I will never forget the good memories with them.

In addition, I am very grateful to Gökhan Öztarhan, Mustafa Polat, Elif Özçeri İyikanat, Beyhan Puliçe and Nesli Yağmurcukardeş for their helps in the technical issues.

I wish to express my thanks to Assoc. Prof. Dr. Hasan Şahin, Dr. Şeyda Horzum Şahin and especially Emre Turan Şahin for being my second family.

My best friends, Merve Kuzucu Şahin, Emrah Şahin, Derya Akbaş, Burak Akbaş, Şule Kuzucu and Aykut Çetin, have encouraged during the challanges of my whole life for 20 years. Their friendships make my life a wonderful experience.

A great thanks to my husband Cihan Bacaksız for his loving, patience, for the discussions on physics and for the encouragement in all times.

Last but not the least, I would like to thank my family: my parents Ayşe Mayda and Mehmet Mayda, my sisters Fatma Mayda and Safiye Şükran Ayten, my brother-in-law Serdar Ayten and my nephews Mehmet Fatih, Cem and Murat Ayten. Without their love, patience and limitless support in all I undertook, none of what I have achieved would have been possible.

Support by the Turkish Scientific and Technical Research Council (TUBITAK grant number 113F242) is gratefully acknowledged.

The numerical calculations reported here were performed at the TUBITAK ULAKBIM High Performance and Grid Computing Center (TRUBA resources).

ABSTRACT

MAGNETIC EFFECT IN THE BIOLOGICAL FUNCTIONING OF HEMOGLOBIN: DFT+QMC APPROACH WITHIN AN EFFECTIVE MULTI-ORBITAL ANDERSON IMPURITY MODEL

Hemoglobin corresponds to O_2 transportation from lungs to the tissues and exhibits high-spin to low-spin transition by binding of O_2 to Fe. In this thesis, we study the electronic and magnetic properties of the deoxy and the oxy forms of the human adult hemoglobin (HbA) to investigate the mechanism of the spin transition. We use an effective multi-orbital Anderson model and the parameters of this model are determined by the density functional theory (DFT) calculations. Then, this model is solved by using a quantum Monte Carlo (QMC) algorithm. The DFT+QMC results show that new electronic states named as the impurity bound states (IBS) exist in both deoxy-HbA and oxy-HbA. We also observe that as the temperature decreases, a magnetic gap is opened at the Fermi level for oxy-HbA. This gap arises from the Fe-O_2 charge transfer. We find that both the IBS and the opening of the magnetic gap are responsible for the spin transition in hemoglobin. In addition, the DFT+QMC calculations show that antiferromagnetic (AF) correlations between the Fe(3d) and the surrounding orbitals exist in both deoxy-HbA and oxy-HbA. For deoxy-HbA, the anomalous magnetic circular dichrosim signal in the UV region is experimental evidence for these AF correlations. In the light of these magnetic measurements, we propose some explanations for the Bohr effect and the cooperativity which are the fundemental functional properties of the hemoglobin. The results presented in this thesis show that the magnetic effects play a crucial role in the funtioning of the hemoglobin.

ÖZET

HEMOGLOBİNİN BİYOLOJİK İŞLEVİNDEKİ MANYETİK ETKİ:ETKİN ÇOK ORBİTALLİ ANDERSON SAFSIZLIK MODELİ ÇERÇEVESİNDE DFT+QMC YAKLAŞIMI

Hemoglobin molekülü, akciğerlerden hücrelere O_2 taşınımından sorumludur ve O_2'nin demire (Fe) bağlanmasıyla spin durumu yüksek-spinden düşük-spine geçmektedir. Bu tezde, deoksi ve oksi formdaki yetişkin insan hemoglobininin (HbA) elektronik ve manyetik özellikleri etkin çok-orbitalli Anderson modeli ile çalışılmıştır. Bu modelin parametreleri yoğunluk fonksiyoneli teoremi (DFT) ile elde edilmiştir. Daha sonra, kuantum Monte Carlo (QMC) algoritması ile bu model çözülmüştür. DFT+QMC sonuçları deoksi-HbA ve oksi-HbA moleküllerinde safsızlık bağıl durumu (IBS) olarak adlandırılan yeni elektronik hallerin var olduğunu göstermiştir. Ayrıca, sonuçlar, sıcaklık düştükçe, oxy-HbA için Fermi seviyesinde bir manyetik aralığın oluştuğunu göstermektedir. Bu manyetik alınganlık Fe-O_2 yük geçişinden kaynaklanmaktadır. Bu tezde sunulan spin geçiş mekanizması hem IBS'lerin varlığının hem de manyetik aralığın açılmasının yüksek-spinden düşük-spine geçişe neden olduğunu göstermektedir. Buna ek olarak, deoksi-HbA ve oksi-HbA moleküllerinde Fe(3d) ile çevre orbitaller arasında antiferromanyetik (AF) korelasyonların var olduğunu bulduk. Deoksi-HbA için, UV bölgesindeki anomal manyetik dikroizm sinyallerinin bu AF korelasyonlar için deneysel bir kanıt olduğunu gösterdik. Bu manyetik ölçümler ışığında, hemoglobinin önemli fonksiyonel özellikleri olan Bohr etkisi ve kooperativite için açıklamalar önerdik. Bu tezde sunulan sonuçlar manyetik etkilerin hemoglobinin işleyişinde önemli rol oynadığını göstermektedir.

TABLE OF CONTENTS

LIST OF FIGURES xi

LIST OF TABLES xxiii

CHAPTER 1. INTRODUCTION 1
1.1. Molecular structure of the hemoglobin 3
1.2. Magnetic properties of hemoglobin 5
1.2.1. Experimental picture for the spin transition of hemoglobin 5
1.2.2. Mössbauer spectroscopy 7
1.2.3. Magnetic circular dichroism spectroscopy 8
1.2.4. Resonant inelastic X-ray scattering 8
1.3. Bohr effect 10
1.4. Cooperativity 12
1.5. Our results for the magnetic properties and the functioning of hemoglobin 14
1.5.1. Extended multi-orbital Anderson impurity model 14
1.5.2. DFT+QMC approach for the Anderson impurity model 15
1.5.3. Why do we study the hemoglobin molecule? 16
1.5.4. Our proposal of a magnetic mechanism for the functioning of hemoglobin 16
1.6. Outline 17

CHAPTER 2. QUANTUM MONTE CARLO RESULTS FOR THE HEME CLUSTERS 21
2.1. Magnetic moment density for the heme clusters 23
2.2. Magnetic susceptibility measurements for the heme clusters 26
2.3. Impurity bound states 29
2.3.1. Impurity bound states for the deoxy-heme cluster 31
2.3.2. Impurity bound states for the oxy-heme cluster 35
2.3.3. Inter-orbital charge transfer at IBS for oxy-heme cluster 42
2.3.4. Electron and magnetization density distributions of IBS in the host 46
2.4. Opening of a magnetic gap at the Fermi level for oxy-heme cluster 47

CHAPTER 3. MCD SPECTRUM OF THE DEOXY-HEME CLUSTER 57
3.1. Our proposal for the MCD spectrum of the deoxy-heme cluster ... 57
3.2. Calculation of the MCD spectrum in UV region for deoxy-heme cluster 63
3.3. Comparison of the MCD and the optical absorption data in the UV region for deoxy heme cluster 66

CHAPTER 4. RIXS SPECTRUM OF THE HEME CLUSTERS 71
4.1. RIXS spectrum of the deoxy-heme cluster 71
4.2. RIXS spectrum of the oxy-heme cluster 76

CHAPTER 5. XAS OF THE HEME CLUSTERS 84
5.1. XAS of the deoxy-heme cluster 84
5.2. XAS of the oxy-heme cluster 88

CHAPTER 6. IMPLICATION OF THE DFT+QMC FOR THE FUNCTIONING OF HEMOGLOBIN 94
6.1. Magnetic mechanism for Fe-O_2 binding 94
6.2. Bohr effect 95
6.3. Cooperativity 95

CHAPTER 7. FUTURE STUDIES 97

CHAPTER 8. CONCLUSIONS 99

REFERENCES 103

APPENDICES

APPENDIX A. PARAMETERS OF THE ANDERSON HAMILTONIAN 109
A.1. Double-counting term 109
A.2. Density of states 111
A.3. Hybridization matrix elements 112
A.4. Natural atomic orbital weight of the host eigenstates 112

APPENDIX B. QUANTUM MONTE CARLO ALGORITHM FOR THE MULTI-ORBITAL ANDERSON MODEL WITH THE INTER-ORBITAL COULOMB INTERACTION 120
B.1. Schematic derivation 121
B.2. Multi-orbital Anderson Hamiltonian with the inter-orbital Coulomb interaction 125
B.3. Derivation of G^0 126
B.3.1. Derivation of G^0 from G^{00} 127
B.3.2. Derivation of $G^{00}_{\nu\nu'}(i\omega_n)$ from H_{00} and T 130
B.3.3. Derivation of T 131
B.3.3.1. Calculation of T^U 131
B.3.3.2. Calculation of $T^{U'}$ 132
B.3.3.3. Calculation of $T^{U'-J}$ 134
B.4. Hubbard-Stratonovich transformation 137
B.4.1. Hubbard-Stratonovich transformation for U term 140
B.4.2. Hubbard-Stratonovich transformation for U' term 141
B.4.3. Hubbard-Stratonovich transformation for $U' - J$ term 144
B.5. Writing the Hubbard-Stratonovich transformation terms by using W terms 146
B.5.1. Calculation of $W^U_{\nu\sigma}(l)$ 147
B.5.2. Calculation of $W^{U'}_{\nu\sigma}(l)$ 147
B.5.3. Calculation of $W^{U'-J}_{\nu\sigma}(l)$ 150
B.6. Initial calculation of G^σ Green's function from G^0 and W 154
B.7. Calculation of the ratio of the determinants R_σ for the single spin flip 156
B.7.1. Proof of R_σ 156
B.7.1.1. R_σ for U term 158
B.7.1.2. R_σ for U' term 160
B.7.1.3. R_σ for $U' - J$ term 163
B.7.3. Calculation of $(W_{\nu\sigma}(l))' - (W_{\nu\sigma}(l))$ terms 165
B.7.3.1. Calculation of $(W^U_{\nu\sigma}(l))' - (W^U_{\nu\sigma}(l))$ 165
B.7.3.2. Calculation of $(W^{U'}_{\nu\sigma}(l))' - (W^{U'}_{\nu\sigma}(l))$ 166
B.7.3.3. Calculation of $(W^{U'-J}_{\nu\sigma}(l))' - (W^{U'-J}_{\nu\sigma}(l))$ 168
B.7.4. Calculation of A_σ terms 170
B.7.4.1. Calculation of A^U_σ 170

B.7.4.2. Calculation of $A_\sigma^{U'}$ 173
B.7.4.3. Calculation of $A_\sigma^{U'-J}$ 177
B.8. Updated Green's functions 183
B.8.1. New impurity Green's function for U term 183
B.8.1.1. Calculation of $(A_\sigma^U)^{-1}$ 185
B.8.1.2. Last form of the new impurity Green's function for U term 186
B.8.2. New impurity Green's function for U' term 187
B.8.2.1. Calculation of $(A_\sigma^{U'})^{-1}$ 189
B.8.2.2. Last form of the new impurity Green's function for U' term 191
B.8.3. New impurity Green's function for $U' - J$ term 193
B.8.3.1. General $(A_\sigma^{U'-J})_{5L\times 5L}$ matrix and its inverse 195
B.8.3.2. Calculation of $[(A_\sigma^{U'-J})^{-1}]_{2L\times 2L}$ matrix 196
B.8.3.3. Last form of the new impurity Green's function for $U'-J$ term 199

APPENDIX C. DETERMINATION OF THE FERMI LEVELS FOR THE HEME CLUSTERS 202

APPENDIX D. COMPETITION OF THE HUND'S COUPLING WITH THE FE(3D)-HOST ANTIFERROMAGNETIC CORRELATIONS 206

APPENDIX E. EFFECT OF THE U' AND J TERMS ON THE IMPURITY BOUND STATES 209

APPENDIX F. POTENTIAL SOURCES FOR THE COMPUTATIONAL ERRORS IN DFT+QMC APPROACH 211
F.1. Double-counting term 211
F.2. $\Delta\tau$ error 212
F.3. Spin-flip and the pair-hopping terms 213

APPENDIX G. DEPENDENCE ON THE FE-PORPHYRIN DISTANCE FOR DEOXY-HEME CLUSTER 219

LIST OF FIGURES

Figure **Page**

Figure 1.1. (a) Molecular structure of deoxy-HbA, which was obtained by X-ray diffraction at room temperature (Park *et al.* (2006)) (Protein Data Bank, Keyword: 2DN2). HbA molecule contains four inequivalent heme groups, $\alpha_1 - \alpha_2 - \beta_1 - \beta_2$. (b) Molecular structure of the truncated α_1 heme group of deoxy-HbA (the Protein Data Bank keyword: 2DN2). This deoxy-heme cluster ($C_{32}H_{30}FeN_{10}O_2$) contains 75 atoms and 334 electrons. (c) Molecular structure of the truncated α_1 heme group of oxy-HbA (the Protein Data Bank keyword: 2DN1). This oxy-heme cluster ($C_{32}H_{30}FeN_{10}O_4$) has 77 atoms and 350 electrons. 4

Figure 1.2. Results on the oxy-hemoglobin molecule from the various experimental and theoretical methods. Source:(Chen *et al.* (2008)). 6

Figure 1.3. Schematic representation of the experimental explanation for the high-spin to low-spin transition in hemoglobin molecule. 6

Figure 1.4. Schematic presentation of the resonant inelastic X-ray scattering method. Source: (Ament *et al.* (2011)) 9

Figure 1.5. RIXS spectrum of the deoxyMb and MbCO molecules. Source: (Harada *et al.* (2009)) 10

Figure 1.6. Schematic representation of the transportation of O_2 and CO_2 in red blood cells (RBC). Source:(Kaneko *et al.* (2008)) 11

Figure 1.7. The oxygen dissociation curve. Source:(Ferrell (2009)) 12

Figure 1.8. The structural changes of hemoglobin by binding of O_2. Source: (Ferrell (2009)). 13

Figure 1.9. In the left picture, the intra-orbital Coulomb interaction U is shown. The inter-orbital Coulomb interaction U' for antiparallel spins is shown in the middle picture, whereas U'' is for parallel spins as seen in the right picture. In the atomic limit $U' = U - 2J$ and $U'' = U - 3J$, where J is the ferromagnetic Hund's coupling. 15

Figure 2.1. QMC results on the local magnetic-moment density $M(\mathbf{r})$ are sketched for the (a) deoxy and (b) oxy-heme clusters at $T = 150$ K. Here, the red color shows the atomic orbitals which have magnetic moments pointing up, while the blue color shows the down magnetic moments. 25

Figure 2.2. (a) The temperature dependence of the total and of the Fe spin susceptibilities χ_t for the deoxy and oxy-heme clusters. Here, the dotted blue line denotes the Curie-type $1/T$ temperature dependence. (b) The total magnetic susceptibility as a function of chemical potential μ for oxy-heme for different temperatures. Here, the vertical black solid line represents the Fermi level $\mu_{\rm F}$ at T=150 K. 27

Figure 2.3. QMC results for deoxy on the Fe(3d) electron occupation number and Fe(3d) magnetic moments. (a) Electron occupation number $\langle n_\nu \rangle$ of the Fe($3d_\nu$) orbitals versus the chemical potential μ. (b) Square of magnetic moment $\langle (M_\nu^z)^2 \rangle$ for Fe($3d_\nu$) orbitals versus the chemical potential μ. Here, the vertical solid line denotes the Fermi level of molecule. The Fermi level of molecule is obtained by QMC. In addition, these results are for $U = 4$ eV, $J = 0.9$ eV and $T = 300$ K. 33

Figure 2.4. QMC results for deoxy on the host electron occupation number and magnetic moments of host states. (a) Electron occupation number of the m'th host state $\langle n_m \rangle$ versus the chemical potential μ. (b) Square of the magnetic moment of the m'th host state $\langle (M_m^z)^2 \rangle$ versus the chemical potential μ. Here, the vertical solid line denotes the Fermi level of molecule. The Fermi level of molecule is obtained by QMC. In addition, these results are for $U = 4$ eV, $J = 0.9$ eV and $T = 300$ K. 34

Figure 2.5. QMC results for deoxy on the host electron occupation number and magnetic moments of host orbitals. (a) Electron occupation number of the m'th host state $\langle n_m \rangle$ versus the chemical potential μ. (b) Square of the magnetic moment of the m'th host state $\langle (M_m^z)^2 \rangle$ versus the chemical potential μ. Here, the vertical solid line denotes the Fermi level of molecule. The Fermi level of molecule is obtained by QMC. In addition, these results are for $U = 4$ eV, $J = 0.9$ eV and $T = 300$ K. 36

Figure 2.6. QMC results for deoxy on the magnetic correlation function $\langle M_\nu^z M_m^z \rangle$ between the m'th host state and the Fe($3d_\nu$) orbitals. (a) $\langle M_\nu^z M_m^z \rangle$ versus the chemical potential μ for the 144'th host state, (b) for 145'th host state, (c) for 146'th host state, (d) for 152'nd host state, (e) for 153'rd host state and (f) for 163'rd host state The vertical solid line denotes the Fermi level of molecule. The Fermi level of molecule is obtained by QMC. In addition, these results are for $U = 4$ eV, $J = 0.9$ eV and $T = 300$ K. 37

Figure 2.7. QMC results for deoxy on the magnetic correlation function $\langle M_\nu^z M_m^z \rangle$ between the m'th host state and the Fe($3d_\nu$) orbitals. $\langle M_\nu^z M_m^z \rangle$ versus the chemical potential μ (a) for 166'th host state and (b) 167'th host state. The vertical solid line denotes the Fermi level of molecule. The Fermi level of molecule is obtained by QMC. In addition, these results are for $U = 4$ eV, $J = 0.9$ eV and $T = 300$ K. 38

Figure 2.8. QMC results for oxy on the Fe(3d) electron occupation number and Fe(3d) magnetic moments. (a) Electron occupation number $\langle n_\nu \rangle$ of the Fe($3d_\nu$) natural atomic orbitals versus the chemical potential μ. (b) Square of magnetic moment $\langle (M_\nu^z)^2 \rangle$ for Fe($3d_\nu$) natural atomic orbitals versus the chemical potential μ. Here, the vertical solid blue line shows the Fermi level for oxy. The Fermi level of molecules is obtained by QMC. In addition, these results are for $U = 4$ eV, $J = 0.9$ eV and T = 300 K. 40

Figure 2.9. QMC results for oxy on the host electron occupation number and magnetic moments of host orbitals. (a) Electron occupation number of the m'th host state $\langle n_m \rangle$ versus the chemical potential μ. (b) Square of the magnetic moment of the m'th host state $\langle (M_m^z)^2 \rangle$ versus the chemical potential μ. Here, the vertical solid denotes the Fermi level for oxy. The Fermi level of molecules is obtained by QMC. In addition, these results are for $U = 4$ eV, $J = 0.9$ eV and $T = 300$ K. 41

Figure 2.10. QMC results for oxy on the host electron occupation number and magnetic moments of host orbitals. (a) Electron occupation number of the m'th host state $\langle n_m \rangle$ versus the chemical potential μ. (b) Square of the magnetic moment of the m'th host state $\langle (M_m^z)^2 \rangle$ versus the chemical potential μ. Here, the vertical solid denotes the Fermi level for oxy. The Fermi level of molecules is obtained by QMC. In addition, these results are for $U = 4$ eV, $J = 0.9$ eV and $T = 300$ K. 43

Figure 2.11. QMC results for oxy on the magnetic correlation function $\langle M_\nu^z M_m^z \rangle$ between the m'th host state and the Fe($3d_\nu$) orbitals. (a) $\langle M_\nu^z M_m^z \rangle$ versus the chemical potential μ for $m = 153$rd host state, (b) 154'th host state, (c) 158'th host state, (d) 159'th host state and (e) 173rd host state. The vertical solid denotes the Fermi level for oxy. The Fermi level of molecules is obtained by QMC. In addition, these results are for $U = 4$ eV, $J = 0.9$ eV and $T = 300$ K. 44

Figure 2.12. QMC results for oxy on the magnetic correlation function $\langle M_\nu^z M_m^z \rangle$ between the m'th host state and the Fe($3d_\nu$) orbitals. (a) $\langle M_\nu^z M_m^z \rangle$ versus the chemical potential μ for $m = 174$'th host state, (b) 175'th host state and (c) 176'th host state. The vertical solid denotes the Fermi level for oxy. The Fermi level of molecules is obtained by QMC. In addition, these results are for $U = 4$ eV, $J = 0.9$ eV and $T = 300$ K. ... 45

Figure 2.13. (a) Total Fe(3d) magnetic moment $M_{\rm 3d}$ versus chemical potential μ. (b) Total host magnetic moment $M_{\rm h}$ versus μ. (c) Total Fe(3d)-host effective magnetic correlation function $\langle M_{\rm 3d}^{\rm z} M_{\rm h}^z \rangle$ versus μ. (d) Total effective magnetic moment $M_{\rm t}$ versus μ. The black circular represents the deoxy and the blue square represents the oxy. Here, vertical solid blue line shows the Fermi level of oxy-heme and the vertical solid black line shows the Fermi level of deoxy-heme. These Fermi level values are obtained by QMC calculations. In addition, these results are for $U = 4$ eV, $J = 0.9$ eV and $T = 300$ K. 47

Figure 2.14. Electron occupation number $\langle n_\nu \rangle$ for the Fe(3d) orbitals $\nu = x^2 - y^2$ and $\nu = yz$ versus the chemical potential μ. Here, the blue vertical solid line represents the Fermi level of oxy-heme. 48

Figure 2.15. For deoxy-heme, (Left) Electron density distribution for the host IBS. (Right) Magnetization density distribution for the host IBS. 49

Figure 2.16. For oxy-heme, (Left) Electron density distribution for the host IBS. (Right) Magnetization density distribution for the host IBS. These figures are for the IBS located at -1.5 eV. 50

Figure 2.17. For oxy-heme, (Left) Electron density distribution for the host IBS. (Right) Magnetization density distribution for the host IBS. These figures are for the IBS located at -5.5 eV. 51

Figure 2.18. (a) Total magnetic susceptibility versus temperature T. Here, the dotted blue line denotes the Curie-type $1/T$ temperature dependence. (b)The total magnetic moment M_t of the oxy-heme cluster is shown as function of μ near the Fermi level. Here, the vertical black solid line represents the Fermi level $\mu_{\rm F}$ at T=150 K. 53

Figure 2.19. The total electron number of the oxy-heme cluster $\langle n_t \rangle$ versus μ at various temperatures. Here, the black vertical line represents the Fermi level μ_F at 150 K and the blue vertical line represents the μ_F at 300 K. .. 54

Figure 2.20. For oxy-heme, (a) The total number of electrons in the Fe($3d$) orbitals $\langle n_d \rangle$ plotted as a function of the chemical potential μ at various temperatures. (b) The electron number of the five Fe($3d_\nu$) orbitals $\langle n_\nu \rangle$ versus μ at $T = 200$ K. (c) Total magnetic moment of the Fe($3d$) orbitals M_{3d} versus μ. (d) Illustration of the wave function of the $m = 171$'st host state. Here, the magenta and green colors denote the positive and the negative regions. The vertical black solid line represents the Fermi level $\mu_{\rm F}$ at T=150 K. 55

Figure 2.21. For oxy-heme, (a) Electron number of the $m = 171$'st host state $\langle n_m \rangle$ versus μ. (b) Magnetic moment of the $m = 171$'st host state M_m versus μ. Here, the vertical black solid line represents the Fermi level $\mu_{\rm F}$ at T=150 K. 56

Figure 2.22. For deoxy, (a) The number of electrons in the Fe($3d_\nu$) orbitals $\langle n_\nu \rangle$ plotted as a function of the chemical potential μ at $T = 250\,K$. (b) The total number of the electrons $\langle n_t \rangle$ versus μ for the deoxy-heme cluster at various temperatures. The deoxy-heme cluster with 75 atoms has 334 electrons. This figure shows that the Fermi level located at -2.8 eV is T independent. (c) The total magnetic moment of the deoxy-heme cluster $\langle M_t \rangle$ versus μ at various temperatures. The vertical black solid line denotes the Fermi level at $T = 250$ K. 57

Figure 3.1. (a) The magnetic polarizations of various states are sketched. (b) Feynman diagram represents the absorption of left-circularly polarized (LCP) light. (c) Feynman diagram represents the absorption of right-circularly polarized (RCP) light. 61

Figure 3.2. Host wave functions are shown in terms of the atomic orbitals. (a) Wavefunction of the π_1 host state, which is a bonding $2p_z$ orbitals of the C atoms in the porphyrin layer. (b) and (c) Wavefunctions of the antibonding π_1^* and π_2^* host states, respectively. 63

Figure 3.3. (Top) This Feynman diagram illustrates that an electron in a bonding π state can gain an effective spin-orbit coupling through the hybridization. Here, and up-spin electron in the π state can become an up-spin $3d$ electron through hybridization. Here, V is the hybridization matrix element between the π state and the Fe(3d) orbitals, and λ is the spin-orbit coupling constant for the Fe(3d) orbitals. (Bottom) This Feynman diagram shows that an electron in the π state can gain an effective spin-orbit coupling λ'. 64

Figure 3.4. These figures illustrate the left-circularly polarized (LCP) light absorption process in MCD for an applied magnetic field pointing in the up direction, which is in the direction of light propagation. The left panel shows the initial state, the middle panel is the intermediate state and the last one is the final state. 65

Figure 3.5. (a) Electron occupation $\langle n \rangle$ of the π_1^* and π_2^* host states plotted as a function of the chemical potential μ. Here, the Fermi level is located at μ_F. (b) Single-particle spectral weight $A(\omega)$ versus ω obtained from the $\langle n \rangle$ versus μ plot shown in (a). Here, the vertical black line represents the Fermi level, $\mu_{\rm F}$. 67

Figure 3.6. (a) Square of the magnetic moment $\langle (M^z)^2 \rangle$ of the π_1^* and π_2^* states plotted as a function of the chemical potential μ. (b) Equal-time correlations function of the Fe(3d) magnetic moment $\langle M_{3d}^z M_m \rangle$ with the moment of the π_1^* and π_2^* states plotted as a function of μ. Here, the vertical black line represents the Fermi level, $\mu_{\rm F}$. 68

Figure 3.7. (a) Experimental magnetic circular dichroism (MCD) spectra in UV region of deoxy HbA obtained by Treu and Hopfield (Treu and Hopfield (1975)) at 8 C in a 16 Tesla applied magnetic field. The inset figure shows normally expected line shape for the temperature-dependent MCD spectrum (Mason (2007)). In (b), results from the calculation of the MCD spectra for the deoxy-heme cluster are shown. 70

Figure 3.8. (a) Experimental data on the frequency dependence of the optical absorption normalized by energy, $\epsilon(E)/E$, for deoxy-HbA obtained by Treu and Hopfield (Treu and Hopfield (1975)). (b) Calculated optical absorption $I(E)/E$ (normalized by energy) for deoxy-heme. The blue bars denote the weights of the various $\pi \rightarrow \pi^*$ transitions. 71

Figure 3.9. Here, the black line denotes the contribution to the MCD spectra from the $\pi_1 \rightarrow \pi_1^*$ and $\pi_1 \rightarrow \pi_2^*$ transitions. The red-dashed line denotes the same contribution in the case where the π_2^* state is artificially shifted by 0.2 eV to higher energies so that there is no overlap between the π_1^* and π_2^* states. 72

Figure 4.1. (Top) For deoxy-heme, the electron occupation number of the Fe(3d) orbitals $\langle n_\nu \rangle$ as a function of chemical potential μ. Here, the black solid line shows the Fermi level of the deoxy-heme cluster. This Fermi level is obtained by the DFT+QMC. (Bottom) Schematic plot of the single-particle spectrum for the deoxy-heme. The blue line shows the Fermi level of the molecule. This picture is obtained from the $\langle n_\nu \rangle$ versus μ graph and the peak locations correspond the electron increasing points. The height of the peaks is proportional to the increase in the occupation number of the orbitals. The peak located at ≈ -4 eV corresponds to the impurity bound state. Here, $U = 4$ eV and $J = 0.9$ eV and temperature is T=300 K. 75

Figure 4.2. For deoxy-heme cluster, (Top) total electron number of the Fe(3d) orbitals $\langle n_d \rangle$ as a function of the chemical potential μ. (Bottom) The Fe(3d) single-particle spectral weight $A_d(\omega)$ versus frequency ω. $A_d(\omega)$ is obtained by taking the derivative of the $\langle n_d \rangle$ with respect to μ. The peak located at ≈ -4 eV corresponds to the impurity bound state. The black vertical line represents the Fermi level obtained by the QMC for the deoxy-heme molecule. Here, $U = 4$ eV and $J = 0.9$ eV and temperature is T=300 K. 76

Figure 4.3. For deoxy-heme cluster, (Top) DFT+QMC results for the RIXS spectrum I_{dd}. I_{dd} is calculated from Eq.4.2. Here, these results are obtained for the $\mu = -2.8$ eV because it is the Fermi level for the deoxy-heme cluster. In addition, $U = 4$ eV and $J = 0.9$ eV and temperature is T=300 K. (Bottom) RIXS data on deoxyMb from the Harada et.al. (Harada *et al.* (2009)). 77

Figure 4.4. For deoxy-heme molecule, (Top) the single-particle spectral weight $A_d(\omega)$ versus frequency ω. $A(\omega)$ is obtained by taking the derivative of the $\langle n_d \rangle$ with respect to μ. (Bottom) In this figure, we set the $A_d(\omega)$ to 0 for the impurity bound state located ≈ -4 eV, which is shown by the dashed red circle. Here, the black line represent the Fermi level obtained by the QMC for the deoxy-heme molecule. Here, $U = 4$ eV and $J = 0.9$ eV and temperature is T=300 K. 78

Figure 4.5. For deoxy-heme cluster, (Top) the black line shows the DFT+QMC results for the RIXS spectrum I_{dd}. The red dashed line shows the I_{dd} for the case in which the spectral weight of the impurity bound state equals 0. Here, $U = 4$ eV, $J = 0.9$ eV, $\mu = -2.8$ eV and temperature is T=300 K. (Bottom) RIXS data on deoxyMb from the Harada et.al.(Harada *et al.* (2009)). 79

Figure 4.6. For oxy-heme, (Top) the electron occupation number of the Fe(3d) orbitals $\langle n_\nu \rangle$ as a function of chemical potential μ. Here, the black solid line shows the Fermi level of the deoxy-heme cluster. This Fermi level is calculated by the DFT+QMC. (Bottom) Schematic plot of the single-particle spectrum for the oxy-heme. The blue line shows the Fermi level of the molecule. This picture is obtained from the $\langle n_\nu \rangle$ versus μ graph and the peak locations correspond the electron increasing points. The height of the peaks is proportional to the increase in the occupation number of the orbitals. The peaks located at ≈ -1.5 eV, ≈ 2.4 eV and ≈ 2.5 eV correspond to the impurity bound state. Here, $U = 4$ eV and $J = 0.9$ eV and temperature is T=300 K. 81

Figure 4.7. For oxy-heme cluster, (Top) total electron number of the Fe(3d) orbitals $\langle n_d \rangle$ as a function of the chemical potential μ. (Bottom) The Fe(3d) single-particle spectral weight $A_d(\omega)$ versus frequency ω. $A_d(\omega)$ is obtained by taking the derivative of the $\langle n_d \rangle$ with respect to μ. The peaks located at ≈ -1.5 eV, ≈ 2.4 eV and ≈ 2.5 eV correspond to the impurity bound state The black vertical line represents the Fermi level obtained by the QMC for the oxy-heme molecule. Here, $U = 4$ eV and $J = 0.9$ eV and temperature is T=300 K. 82

Figure 4.8. For oxy-heme cluster, (Top) DFT+QMC results for the RIXS spectrum I_{dd}. I_{dd} is calculated from Eq.4.2. Here, the chemical potential is -3.8 eV which is the Fermi level for the oxy-heme molecule. In addition, $U = 4$ eV and $J = 0.9$ eV and temperature is T=300 K. (Bottom) RIXS data on MbCO from the Harada et.al.(Harada *et al.* (2009)). 83

Figure 4.9. For oxy-heme molecule, (Top) the single-particle spectral weight $A_d(\omega)$ versus frequency ω. $A(\omega)$ is obtained by taking the derivative of the $\langle n_d \rangle$ with respect to μ. (Bottom) In this figure, we set the $A_d(\omega)$ to 0 for the impurity bound states located at ≈ -1.5 eV, ≈ 2.4 eV and ≈ 2.5 , which are shown by the dashed red circle. Here, the black line represent the Fermi level obtained by the QMC for the oxy-heme molecule. Here, $U = 4$ eV and $J = 0.9$ eV and temperature is T=300 K. 84

Figure 4.10. For oxy-heme cluster, (Top) the black line shows the DFT+QMC results for the RIXS spectrum I_{dd}. The red dashed line shows the I_{dd} for the case in which the spectral weight of the impurity bound state equals 0. Here, $U = 4$ eV, $J = 0.9$ eV, $\mu = -3.8$ eV and temperature is T=300 K. (Bottom) RIXS data on MbCO from the Harada et.al.(Harada *et al.* (2009)). 85

Figure 5.1. The single-particle spectral weight $A_d(\omega)$ for the high-spin heme molecule. These data are obtained from (Aziz *et al.* (2009)) 87

Figure 5.2. The single-particle spectral weight $A_d(\omega)$ for the high-spin heme molecule. These data are obtained from (Hocking *et al.* (2007)). 87

Figure 5.3. (Top) The single-particle spectral weight $A_d(\omega)$ for the high-spin heme molecule (Aziz *et al.* (2009)). Here, ε_F is the Fermi level for the experimental data. (Bottom) $A_d(\omega)$ obtained from the DFT+QMC results for the deoxy-heme.In DFT+QMC, $U = 4$ eV, $J = 0.9$ eV and $T = 300$ K. . 88

Figure 5.4. For deoxy-heme, total Fe(3d) electron numbers as a function of chemical potential μ. The black, blue and green lines are obtained from (Aziz *et al.* (2009)). Here, ε_F shows the Fermi level for the experimental data for the high-spin heme. The red line shows the DFT+QMC results for the total electron number of Fe(3d) orbitals for deoxy-heme. Here, the black vertical line represents the Fermi level for deoxy-heme. In this calculations, $U = 4$ eV, $J = 0.9$ eV and $T = 300$ K. 89

Figure 5.5. For deoxy-heme, total Fe(3d) electron numbers as a function of chemical potential μ. The black, blue and green lines are obtained from (Aziz *et al.* (2009)). Here, ε_F shows the Fermi level for the experimental data for the high-spin heme. The red line shows the DFT+QMC results for the total electron number of Fe(3d) orbitals for deoxy-heme. Here, the black vertical line represents the Fermi level for deoxy-heme. In this calculations, $U = 3$ eV, $J = 0.9$ eV and $T = 1500$ K. 90

Figure 5.6. For deoxy-heme, total Fe(3d) electron numbers as a function of chemical potential μ. The black, blue and green lines are obtained from the (Aziz *et al.* (2009)). Here, ε_F shows the Fermi level for the experimental data for the high-spin heme. The red line shows the DFT+QMC results for the total electron number of Fe(3d) orbitals for deoxy-heme. Here, the black vertical line represents the Fermi level for deoxy-heme. In this calculations, $U = 3$ eV, $J = 0.6$ eV and $T = 1500$ K. 91

Figure 5.7. The single-particle spectral weight $A_d(\omega)$ for the low-spin heme molecule (Hocking *et al.* (2007)). (Bottom) $A_d(\omega)$ obtained from the DFT+QMC results for the oxy-heme. In DFT+QMC, $U = 4$ eV, $J = 0.9$ eV and $T = 300$ K. 92

Figure 5.8. For oxy-heme, total Fe(3d) electron numbers as a function of chemical potential μ. The black, blue and green lines are obtained from (Hocking *et al.* (2007)). Here, ε_F shows the Fermi level for the experimental data for the low-spin heme. The red line shows the DFT+QMC results for the total electron number of Fe(3d) orbitals for oxy-heme. Here, the black vertical line represents the Fermi level for oxy-heme. In this calculations, $U = 4$ eV, $J = 0.9$ eV and $T = 300$ K. 93

Figure 5.9. For oxy-heme, total Fe(3d) electron numbers as a function of chemical potential μ. The black, blue and green lines are obtained from (Hocking *et al.* (2007)). Here, ε_F shows the Fermi level for the experimental data for the low-spin heme. The red line shows the DFT+QMC results for the total electron number of Fe(3d) orbitals for oxy-heme. Here, the black vertical line represents the Fermi level for oxy-heme. In this calculations, $U = 3$ eV, $J = 0.9$ eV and $T = 1500$ K. 94

Figure 5.10. For oxy-heme, total Fe(3d) electron numbers as a function of chemical potential μ. The black, blue and green lines are obtained from (Hocking *et al.* (2007)). Here, ε_F shows the Fermi level for the experimental data for the low-spin heme. The red line shows the DFT+QMC results for the total electron number of Fe(3d) orbitals for oxy-heme. Here, the black vertical line represents the Fermi level for oxy-heme. In this calculations, $U = 3$ eV, $J = 0.6$ eV and $T = 1500$ K. 95

Figure 6.1. Illustration of the change of the location of Fermi level with respect to pH values of the environment. Here, the vertical black line represents the Fermi level, $\mu_{\rm F}$. In the left picture, the Fermi level is located in the magnetic gap which is about 0.1 eV. In the right picture, the Fermi level moves the out of the magnetic gap due to change in the pH of the environment. 97

Figure 6.2. Illustration of the magnetic mechanism for cooperativity. Here, the dashed lines represent the ferromagnetic correlations between the heme groups. The red balls represent the Fe atoms located at the centers of hemes. 99

Figure 7.1. The left figure shows the molecular structure of hemoglobin molecule. The right figure shows the molecular structure of chlorophyll molecule. Chlorophyll contains Mg atom at the center of porphyrin layer. Hemoglobin contains Fe atom at the center of porphyrin layer. 102

LIST OF TABLES

Table **Page**

Table 2.1. Electron occupation number $\langle n_\nu \rangle$ of Fe($3d_\nu$) orbitals for deoxy-heme and oxy-heme. For deoxy, the chemical potential $\mu = -2.8$ eV. For oxy molecules, μ equals -3.8 eV. Here, $U = 4$ eV, $J = 0.9$ eV and $T = 300$ K. 29

Table 2.2. For deoxy, magnetic correlation function $\langle M_\nu M_{\nu'} \rangle$ between the Fe($3d_\nu$) orbitals, ν and ν', at chemical potential $\mu = -2.8$ eV. Here, $U = 4$ eV, $J = 0.9$ eV and $T = 300$ K. 29

Table 2.3. For oxy, magnetic correlation function $\langle M_\nu M_{\nu'} \rangle$ between the Fe($3d_\nu$) orbitals, ν and ν', at chemical potential $\mu = -3.8$ eV. Here, $U = 4$ eV, $J = 0.9$ eV and $T = 300$ K. 30

Table 2.4. For oxy, magnetic correlation function $\langle M_\nu M_{\nu'} \rangle$ between the Fe($3d_\nu$) orbitals, ν and ν', at chemical potential $\mu = -3.8$ eV. Here, $U = 4$ eV, $J = 0.9$ eV and $T = 150$ K. 30

Table 2.5. QMC results on the total intra-orbital magnetic correlation $\langle (M_\nu^z)^2 \rangle$ of Fe($3d$) orbitals ,square of the total inter-orbital magnetic correlation $\langle M_\nu^z M_{\nu'}^z \rangle$ of Fe($3d$) orbitals and square of the total effective magnetic moment $\langle (M_{\rm 3d}^z)^2 \rangle$ of Fe($3d$) orbitals for deoxy and oxy. Here, $\langle (M_{\rm 3d}^z)^2 \rangle = \sum_\nu \langle (M_\nu^z)^2 \rangle + \sum_{\nu \neq \nu'} \langle M_\nu^z M_{\nu'}^z \rangle$. For these results, $U = 4$ eV, $J = 0.9$ eV and $T = 300$ K. 31

Table 2.6. Electron occupation numbers $\langle n_\nu \rangle$ of the Fe($3d_\nu$) orbitals for deoxy-heme and oxy-heme cluster. Here, the last column shows the total electron number $\langle n_{3d} \rangle$ of the Fe(3d) orbitals. In this table, the occupation numbers for the oxy-heme cluster are shown for 300 K, 200 K and 150 K. For the deoxy case, the results are only shown for 300 K. Here, $U = 4$ eV and $J = 0.9$ eV. 58

Table 2.7. Effective magnetic moments $M_\nu^{\rm eff}$ of the Fe($3d_\nu$) orbitals for the deoxy-heme and oxy-heme cluster.In this table, the occupation numbers for the oxy-heme cluster are shown for 300 K and 150 K. For the deoxy case, the results are only shown for 300 K. Here, $U = 4$ eV and $J = 0.9$ eV. .. 58

Table 2.8. DFT+QMC results on the total Fe(3d) magnetic moment M_{3d} in μ_B, total effective spin of Fe(3d) electrons S_{3d}^{eff}, total host magnetic moment M_h in μ_B, total effective spin of host electrons S_h^{eff}, total Fe(3d)-host effective magnetic correlation function $\langle M_{3d}^z M_h^z \rangle$, total effective magnetic moment M_t in μ_B and total effective spin of molecule S_t^{eff} for deoxy and oxy. In addition, total effective spin S^{eff} is calculated by $M = 2\sqrt{S^{eff}(S^{eff}+1)}$. For the deoxy-case, the results are shown only for 300 K. For the oxy-case, 300 K and 150 K results are presented. Here, $U = 4$ eV and $J = 0.9$ eV. 59

CHAPTER 1

INTRODUCTION

Proteins that contain transition metal atoms at their active site are called as metalloproteins. In metalloproteins, the metal atom is usually coordinated with nitrogen, oxygen and sulfur atoms. These molecules play an essential role in many chemical reactions such as transportation of O_2 and CO_2 through the cells, normal functioning of brain and nervous systems, transportation and storage of the proteins. Metalloproteins have been studied for many years (Kepp (2017), Wang *et al.* (2019), Schuth *et al.* (2017), Bren *et al.* (2015)). The researches show that the metal-binding site are responsible for catalyzing functions of metalloproteins (Degtyarenko (2000), Reif (1992),). On the other hand, there are many questions that remain to be answered about the mechanism of metalloproteins and the role of the transition metal atom in their functioning (Schuth *et al.* (2017), Bren *et al.* (2015)).

Hemoglobin molecule is one of the widely studied metalloprotein because of its interesting electronic and magnetic properties (Pauling and Coryell (1936), Poulos (2014)). This molecule is composed of 4 heme groups. Each heme group contains iron (Fe) atom at its center and a surrounding porphyrin ring. Hemoglobin molecule is responsible for the transportation of O_2 from lungs to the tissues. During this biological process, two types of hemoglobin, which are deoxyhemoglobin and oxyhemoglobin, are formed. Deoxyhemoglobin is the form of hemoglobin without bound oxygen while the oxyhemoglobin is the oxygenated form of the hemoglobin. Along with having different molecular structures, deoxy- and oxyhemoglobin have also completely different electronic and magnetic properties. It is well known that the spin state changes with respect to structure of the hemoglobin molecule(Phillips (1980),Vojtěchovskỳ *et al.* (1999), Ellison *et al.* (2002)). For deoxy case, Fe atom is five-coordinated and the displacement of Fe from the porphyrin layer is about 0.4 Å. In this form, hemoglobin has the high-spin state. On the other hand, Fe atom is six-coordinated and it prefers in-plane position for the oxyhemoglobin molecule. For this form, the molecule has the low-spin state (Pauling and Coryell (1936)). Many experimental and theoretical studies have been done to reveal the changing in the magnetic properties of the hemoglobin by binding the O_2 molecule (Pauling and Coryell (1936), Perutz *et al.* (1960), Lang and Marshali (1966), Treu and Hopfield (1975), Weiss (1964), McCLURE (1960), Goddard and Olafson (1975), Scheidt

and Reed (1981), Chen *et al.* (2008), Bren *et al.* (2015), Monod *et al.* (1965)).

Pauling and Coryell (Pauling and Coryell (1936)) showed that the deoxy form of human adult hemoglobin (HbA) has a paramagnetic response with a Curie-type (1/T) temperature dependence. On the other hand, for the oxy-HbA, the total spin of molecule is S=0. Mössbauer experiment shows that the Fe atom in the deoxy-HbA is in a S=2 state (Lang and Marshali (1966)). For the oxy-case, the Mössbauer experiment shows that the magnetic moment of Fe is about 1 μ_B. In addition to these data, the magnetic circular dichroism (MCD) measurements (Treu and Hopfield (1975)) for deoxy-HbA finds an anomalous line shape for the temperature-dependent MCD spectra in UV region.

In addition to having these magnetic behaviours, hemoglobin molecules exhibit remarkable functional properties such as Bohr effect and cooperativity. The Bohr effect is known as the dependency of the oxygen affinity of hemoglobin on the pH of the medium (Adair*et al.* (1925), Ferry and Green (1929)). On the other side, the cooperativity states that when an O_2 molecule binds to one of the heme group, the affinity to oxygen of the remaining heme groups increases (Monod *et al.* (1965), Perutz *et al.* (1998), Yuan *et al.* (2015)). The importance of these structural changes is that they increase the oxygen-transporting efficiency of hemoglobin molecule. In other words, Bohr effect and cooperativity change the molecular structure to regulate the action of hemoglobin. Although Bohr effect and cooperativity are very crucial for the functioning of hemoglobin, there are many questions about their microscopic origin (Swietach *et al.* (2010), Josephy (1992)).

In this thesis, we study the electronic and magnetic properties of HbA by using an effective multi-orbital Haldane-Anderson impurity model (Haldane and Anderson (1976)). In this model, the five Fe(3d) orbitals are taken as impurity states and the remaining orbitals are treated as host states. For both deoxy-HbA and oxy-HbA molecules, we concentrate on one heme group with a Fe site. The effective Anderson Hamiltonian includes the bare energy level of the impurity and host states, the hybridization between them, and the electron interactions at the Fe site. In this model, both the intra- and inter-orbital interactions are taken into account along with the ferromagnetic Hund's coupling. We obtain the energy levels of host and impurity states, and the hybridization matrix elements by performing density functional theory (DFT) (Kohn and Sham (1965)) calculations for the deoxy-heme and oxy-heme clusters. In order to perform DFT calculations, we have used the molecular coordinates of the deoxy and oxy-HbA obtained by the X-ray measurements (Park *et al.* (2006)), and we did not any DFT optimizations for the coordinates. Then, we perform QMC simulations using Hirsch-Fye algorithm (Hirsch and Fye (1986)) for this constructed model. In the QMC simulations, we took the intra-orbital

Coulomb interaction parameter U as 4 eV and the Hund's coupling J as 0.9 eV. Within DFT+QMC technique, we calculate the magnetic moments in the clusters, the correlations among these moments, the magnetic susceptibilities and the charge distributions through the clusters.

In the rest of this chapter, the molecular structure of heme clusters and their functional properties, the experimental studies on them, the Haldane-Anderson model, and the DFT+QMC technique will be explained in more detail.

1.1. Molecular structure of the hemoglobin

Figure 1.1(a) shows X-ray molecular structure of deoxy-HbA molecule obtained from the Protein Data Bank with the keyword 2DN2. This structure was determined with 1.25 Å resolution on a crystal of deoxy-HbA at room temperature (Park *et al.* (2006)). Deoxy-HbA has the four heme groups which are $\alpha_1 - \alpha_2 - \beta_1 - \beta_2$. For this molecular structure, the nearest-neighbor Fe-Fe distance are between the 34 Å and 39.5 Å. The HbA molecule contains approximately 9700 atoms and performing calculations for this molecule is very difficult. Hence, we reduced heme cluster obtained from the α_1 group which is shown in Fig. 1.1(b). In order to obtain this cluster, the four methyl (-CH_3), two vinly (-CH=CH_2) and two propionate groups (-CH_2-CH_2-COO^-) are truncated and the sides of these groups are replaced by hydrogen atoms. The deoxy-heme cluster contains porphyrin ring and a Fe atom located at the center. The histal histidine (HisE7) is attached to imidazole part and the proximal histidine (HisF8) part is located at top of the porphyrin ring. It is thought that the attachment of the proximal histidine is necessary for the stability of O_2 binding. The obtained deoxy-heme has 75 atoms and 334 electrons ($C_{32}H_{30}FeN_{10}O_2$). For the oxy-heme cluster, we again use the X-ray molecular structure of oxy-HbA obtained from the Protein Data Bank with the keyword 2DN1. We obtain the truncated oxy-heme cluster from the α_1 group of the oxy-HbA in the same way described for the deoxy-heme. Figure 1.1 (c) shows the molecular structure of the oxy-heme. This molecule has 77 atoms and 350 electrons ($C_{32}H_{30}FeN_{10}O_4$).

In deoxy-heme cluster, the displacement of Fe atom from the porphyrin layer is about 0.4 Å. On the other hand, for the oxy-heme cluster, Fe moves to porphyrin ring by binding O_2 molecule and the electronic state of the heme changes from high-spin to low-spin. It is shown that this stereochemical effects play a role in the understanding of the functioning of HbA (Phillips (1980),Vojtěchovskỳ *et al.* (1999), Ellison *et al.* (2002)). We use X-ray coordinates for the deoxy and oxy cases. Hence, this stereochemical effect

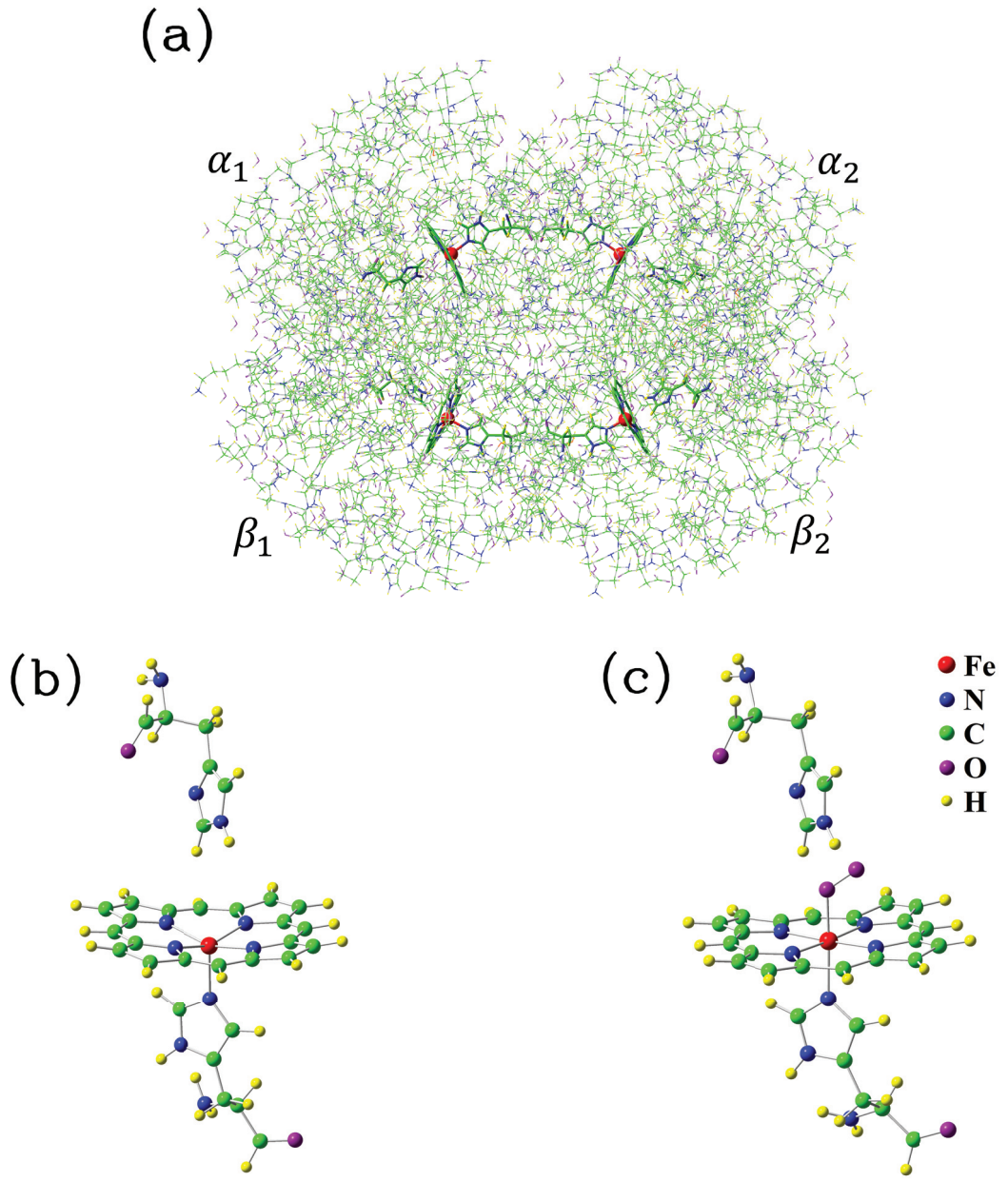

Figure 1.1. (a) Molecular structure of deoxy-HbA, which was obtained by X-ray diffraction at room temperature (Park *et al.* (2006)) (Protein Data Bank, Keyword: 2DN2). HbA molecule contains four inequivalent heme groups, $\alpha_1 - \alpha_2 - \beta_1 - \beta_2$. (b) Molecular structure of the truncated α_1 heme group of deoxy-HbA (the Protein Data Bank keyword: 2DN2). This deoxy-heme cluster ($C_{32}H_{30}FeN_{10}O_2$) contains 75 atoms and 334 electrons. (c) Molecular structure of the truncated α_1 heme group of oxy-HbA (the Protein Data Bank keyword: 2DN1). This oxy-heme cluster ($C_{32}H_{30}FeN_{10}O_4$) has 77 atoms and 350 electrons.

of O_2 are already included in our model.

1.2. Magnetic properties of hemoglobin

In this section, first, we will show the experimental picture for the high-spin to low-spin transition in the hemoglobin molecule. Here, we will also mention our mechanism for the spin transition which will be discussed in Chapter 2.

Then, the important three experimental methods used to find the electronic and magnetic properties of hemoglobin molecules will be explained. These methods are Mössbauer spectroscopy, magnetic circular dichroism (MCD) and resonant inelastic X-ray scattering (RIXS). The results obtained by using these techniques for hemoglobin molecules are also given in this section.

1.2.1. Experimental picture for the spin transition of hemoglobin

As mentioned in the previous sections, the hemoglobin molecule shows different magnetic behaviours by binding of O_2 molecule to the Fe atom. While deoxyhemoglobin has high-spin state, the spin state is 0 for the oxyhemoglobin. The mechanism of high-spin to low-spin transition in hemoglobin has been studied for many years. However, the debate on the mechanism is ongoing and there are many conclusions on it.

Figure 1.2 shows some experimental and theoretical results for the spin state of Fe atom and O_2 molecule in the oxyhemoglobin. Three corners of the square represent the three models which are Pauling, Weiss and McClure-Goddard (Pauling and Coryell (1936), Weiss (1964), McCLURE (1960)), and the fourth corner represents a model which involves the transfer of an electron from O_2 to Fe atom. Inside the square, the circulus, squares and triangles correspond to various computational methods performed for the oxyhemoglobin. In 1936, Pauling and Coryell (Pauling and Coryell (1936)) said that Fe atom and O_2 molecule have the singlet state. In 1964, Weiss (Weiss (1964)) suggested that the Fe gives an electron to O_2 and all have the S=$1/2$ spin state. According to the McClue model (McCLURE (1960)), the Fe goes to S=1 spin state and two electrons in Fe are shared with the O_2 which has the S=1 spin state. As shown in Fig. 1.2, the conclusions of the theoretical studies vary with respect to used computational methods.

The general experimental picture for the spin transition in hemoglobin is shown in Fig.1.3. As seen in the left part of this figure, Fe atom is located out of plane in the

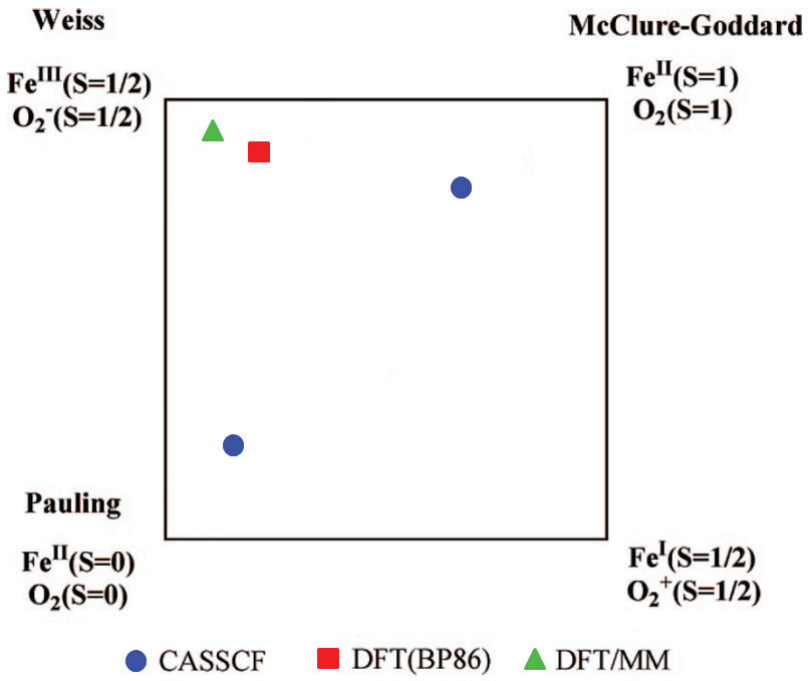

Figure 1.2. Results on the oxy-hemoglobin molecule from the various experimental and theoretical methods. Source:(Chen *et al.* (2008)).

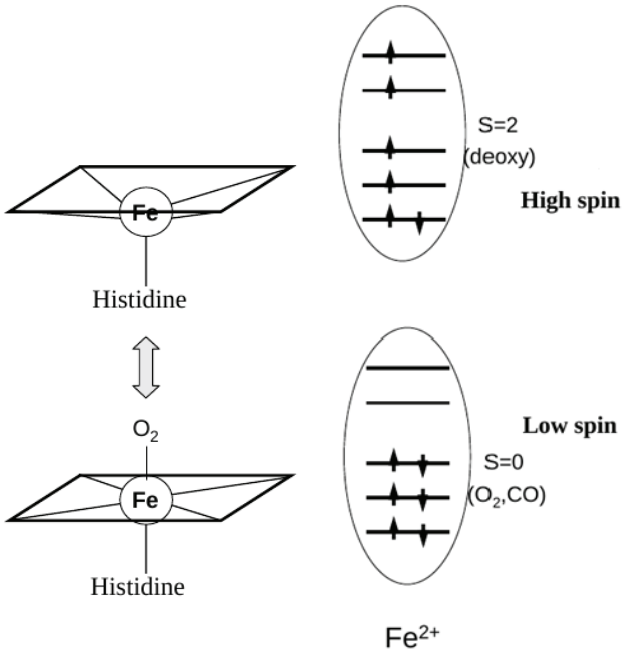

Figure 1.3. Schematic representation of the experimental explanation for the high-spin to low-spin transition in hemoglobin molecule.

deoxy form. By binding of O_2 molecule, the Fe atom goes into the porphyrin ring. The right side of the Fig. 1.3 shows that the spin transition in the hemoglobin molecule. For deoxyhemoglobin, one Fe(3d) orbital is double-occupied and the other orbitals have 1 electron. Hence, molecule has the S=2 spin state. On the other hand, for oxyhemoglobin, the situation is very different. According to this explanation, the three Fe(3d) orbitals are double-occupied and the remaining two orbitals are empty. Hence, the molecule has S=0 spin state. In this picture, the spin transition is explained by the occupancy of the Fe(3d) orbitals.

The mechanism suggested in this thesis is different from the experimental picture. In our explanation, all Fe(3d) orbitals are single-occupied for the deoxy case. On the other hand, for the oxy case, there is one double-occupied Fe(3d) orbital and the electron numbers of the remaining orbitals vary between 1.2 electrons and 1.5 electrons. In contrast to the experimental picture, we do not explain the spin transition in hemoglobin by the occupancy of the Fe(3d) orbitals. We observe that the magnetic correlations between the Fe(3d) electrons and the host electrons play an essential role in the high-spin to low-spin transition. For the deoxyhemoglobin, the effective spin equals 1.60 due to ferromagnetic Hund's coupling between the Fe(3d)-Fe(3d) electrons. By binding O_2, the spin state goes from high-spin to low-spin due to both impurity bound states (IBS) and the opening of magnetic gap as the temperature decreases. The IBS are magnetically correlated electronic states arising from the impurity-host hybridization and the Coulomb interaction between the Fe(3d) orbitals. The occupancy of the IBS determines the spin state of the molecule. For deoxy, IBS are located above the chemical potential and molecule has the high-spin state. On the other side, IBS are located above the chemical potential for the oxy case and the effective spin equals 0.68. In addition, for oxy case, we observe that the effective spin decreases with temperature (T). The charge transfer occurs between the Fe(3d) and O_2 orbitals as the T decreases and antiferromagnetic (AF) correlations occur between these orbitals. The total magnetic moment of oxy is decreased due to these AF correlations and the effective spin of the oxy case equals 0.10 at $T = 150$ K. This mechanism will be explained in Chapter 2.

1.2.2. Mössbauer spectroscopy

The Mössbauer spectroscopy technique is a widely used to examine the valance state of Fe, Fe^{2+} and Fe^{3+}. It is also used to determine the coordination number and the magnetic properties of the iron atom in the molecules. The Mössbauer spectroscopy

detects the small changes in the energy levels of an atomic nucleus in response to its environment.

Mössbauer spectroscopy for hemoglobin molecule show that the spin state of Fe in deoxy-HbA is S=2 (Lang and Marshali (1966)). The results for the oxy-HbA shows that the magnetic moment of Fe is about 1 μ_B. The DFT+QMC results on the magnetic moments and the effective spin of deoxy and oxy hemoglobins will be compared with the Mössbauer spectroscopy results in Chapter 2.

1.2.3. Magnetic circular dichroism spectroscopy

Magnetic circular dichroism (MCD) spectroscopy uses circularly polarized light to study the transitions between the molecular orbitals. In the MCD spectroscopy, the left circularly polarized (LCP) light and the right circularly polarized (RCP) light are induced by a strong magnetic field which is oriented parallel to the direction of propagation the measuring light beam. By measuring the differences between the LCP and RCP lights, the number of molecular transitions in a wide range can be observed. MCD spectroscopy is used to study the transitions which are weak to be seen in an optical absorption spectra, paramagnetic properties of the systems and electronic structure of the materials.

In recent years, the MCD spectroscopy has been widely used for the metalloprophyrins . Because of the presence of the metal atom, the MCD signals are very strong for these molecules. In the heme proteins, both the oxidation and spin states can be determined by MCD (Kirk and Peariso (2003), Mack *et al.* (2007), McMaster and Oganesyan (2010), Lehnert *et al.* (2001)).

The MCD spectra on deoxy-HbA has a peak near 3 eV which is an anomalous line shape and it has 1/T temperature dependency (Treu and Hopfield (1975)). The origin of this anomalous line shape has been debated since its discovery. In this thesis, we propose that the anomalous line shape originates from the antiferromagnetic correlations between the Fe(3d) orbitals and the partially occupied π^* states of the porphyrin layer. The detail of MCD spectrum calculations and the $\pi \rightarrow \pi^*$ transitions will be explained in Chapter 3.

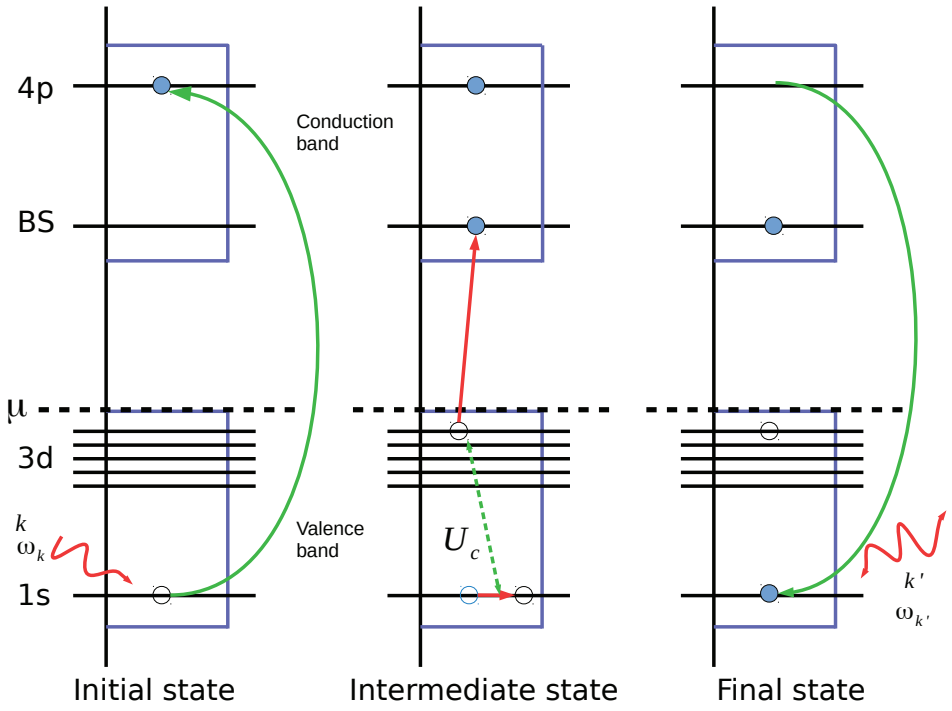

Figure 1.4. Schematic presentation of the resonant inelastic X-ray scattering method. Source: (Ament *et al.* (2011))

1.2.4. Resonant inelastic X-ray scattering

Resonant inelastic X-ray scattering (RIXS) is a "phonon in-phonon out" X-ray spectroscopy technique. In RIXS, a sample is irradiated by X-rays and the scattered X-ray photons are observed. This technique is inelastic because the photons give energy to the sample and leave it in an excited state. Figure 1.4 shows the schematic representation of the RIXS process. In the initial state, a core electron is excited into the valence band. Then, in the intermediate state, the interaction U_c between the valence hole and valence electrons leads to excitation of a valence electron. In the final state, the core hole decays and the system is left in an excited state. By using RIXS, intra-atomic d-d transitions, the charge transfer excitations, orbital excitations and magnetic excitations can be examined.

Figure 2.6(a-b) shows the RIXS results on the d-d transitions for the deoxymyoglobin (deoxyMb) and carboxymyoglobin (MbCO) (Harada *et al.* (2009)). Hemoglobin and myoglobin molecules have the similar structure. Hence, the RIXS measurements for these molecules are compatible with each other. For deoxyMb, Fig.2.6(a) shows that

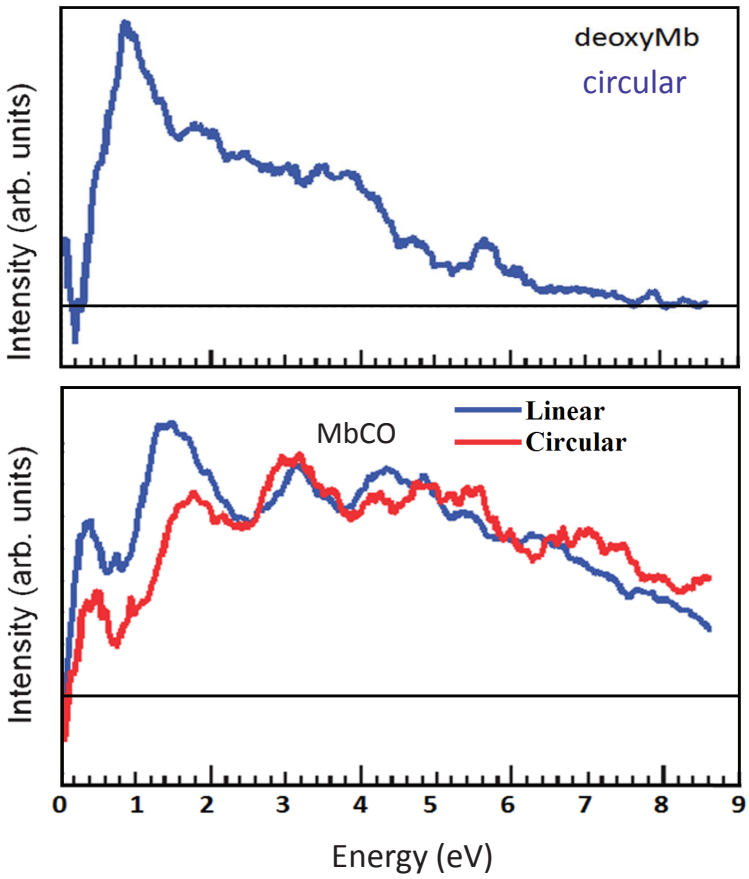

Figure 1.5. RIXS spectrum of the deoxyMb and MbCO molecules. Source: (Harada *et al.* (2009))

dominant d-d transitions are located at approximately 1 eV. On the other hand, the d-d transitions are located at 0.4 eV, 1.8 eV and 3 eV for the MbCO as seen in Fig. 2.6(b).

1.3. Bohr effect

The effect of pH on the dissociation of oxygen is known as the Bohr effect. It was shown that the oxygen affinity of hemoglobin decreases by the increasing acidity and the concentration of carbondioxide (Adair*et al.* (1925), Ferry and Green (1929)). As seen in Fig. 1.6, when the CO_2 diffuses in to the blood and then into the red blood cells, most CO_2 reacts with the water to form carbonic acid, H_2CO_3:

$$H_2O + CO_2 \rightleftharpoons H_2CO_3 \tag{1.1}$$

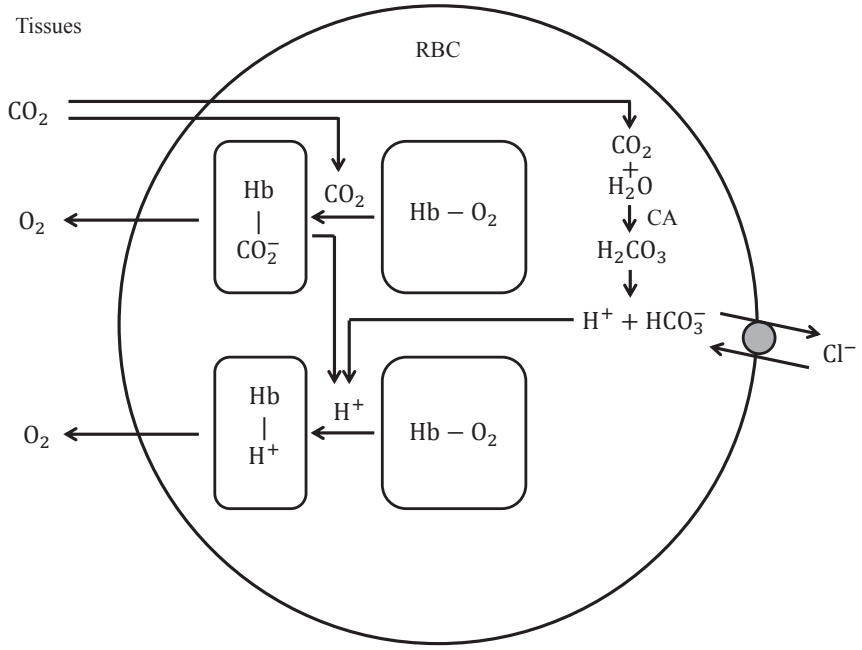

Figure 1.6. Schematic representation of the transportation of O_2 and CO_2 in red blood cells (RBC). Source:(Kaneko *et al.* (2008))

This reaction occurs in the presence of the catalysts carbonic anhydrase. H_2CO_3 dissociates to form H^+ and hydrogencarbonate, $HCO_3{}^-$;

$$H_2CO_3 \rightleftharpoons H^+ + HCO_3^- \tag{1.2}$$

The dissociation of H_2CO_3 increases H^+ and decreases the pH in blood. Then, H^+ associates with the aminoacids of oxyhemoglobin. Oxyhemoglobin releases bound oxygen and the acidity of the blood is decreased. By this reaction, CO_2 molecules bind the hemoglobin and it is transported to the lungs. This process is continues because O_2 content ratio is always higher than the O_2 concentration in the lungs.

The amount of the oxygen binds to hemoglobin at a time to form oxyhemoglobin is named as percentage saturation. The percentage saturation of the hemoglobin versus the partial pressure of oxygen (P_{O_2}) is called oxygen dissociation curve shown in Fig. 1.7. The oxygen dissociation curve is sigmodial shape. This graph shows that there is little or no any oxyhemoglobin at low oxygen concentration (in the body tissues). On the other hand, there is little or no any deoxyhemoglobin at relatively high oxygen concentration (in the lungs).

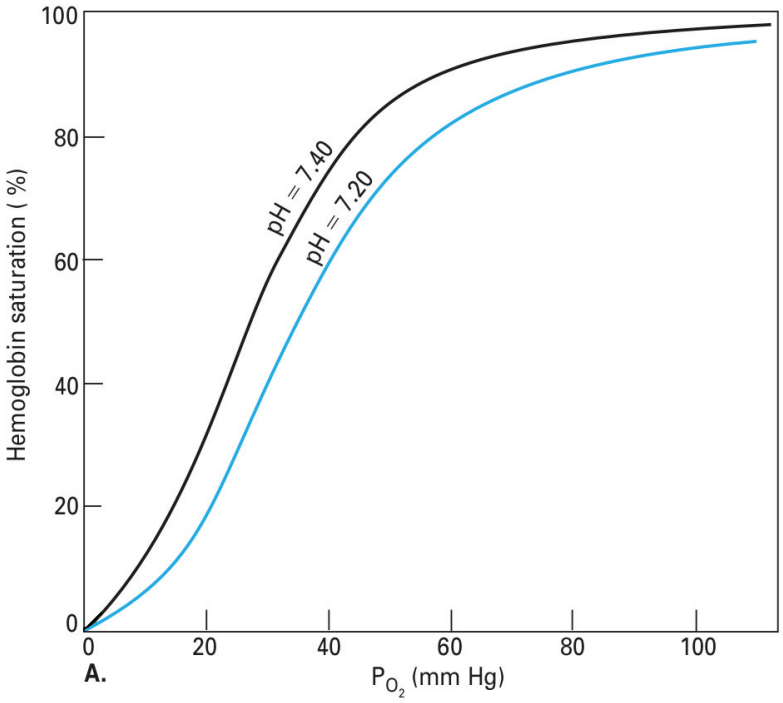

Figure 1.7. The oxygen dissociation curve. Source:(Ferrell (2009))

pH in healthy lungs is between 7.38 and 7.42 and the pH values of the tissues is about 7.2. Figure 1.7 shows the percentage saturation of the hemoglobin for the different pH values. As seen in this figure, the oxygen affinity of hemoglobin decreases with decreasing in pH. Hence, when hemoglobin moves into a region of low pH, its tendency to release oxygen increases. For example, transportation from the lungs with pH 7.4 and the oxygen partial pressure of 100 torr to an muscle with pH 7.2 and oxygen partial pressure 20 torr results in a releasing of oxygen as 77% of the total carrying capacity. Figure 1.7 says that the regulation of the hemoglobin by the hydrogen ions and also by CO_2 further increases the oxygen-transporting efficiency of hemoglobin.

1.4. Cooperativity

The oxygen affinity of the hemoglobin molecule is regulated by many factors. One of the most important regulator is the presence of oxygen.

Deoxyhemoglobin has low affinity for oxygen. When one oxygen is attached to molecule, the second one binds more easily. This means that the affinity of the hemoglobin

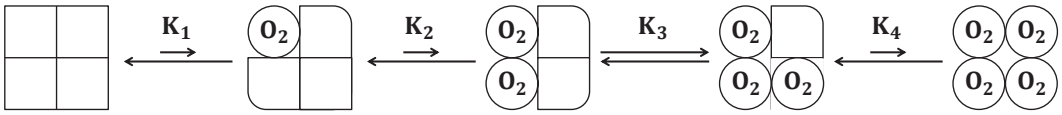

Figure 1.8. The structural changes of hemoglobin by binding of O_2. Source: (Ferrell (2009)).

molecule increases by the increase in the quantity of the oxygen bound at a given time. In the same manner, the loss of one oxygen molecule from the oxyhemoglobin leads to unbind the other oxygen molecule more easily, and so forth. This phenomenon is named as cooperativity.

Cooperativity is very important for the functioning of hemoglobin. It allows carrying the maximum amount of oxygen from lungs to the tissues, and also it allows to release the maximum amount of oxygen into the tissues.

Hemoglobin is an allosteric molecule. It has two different states which are named as T-state (tense) and the R-state (relaxed). The deoxyhemoglobin is the T-state and the oxyhemoglobin is the R-state. As the oxygen molecule binds the hemoglobin molecule, the transition from T-state to R-state occurs.

Figure 1.8 shows the sequential model for the cooperativity. This model says that conformational changes are seen in hemoglobin by binding the one O_2 molecule. When the next O_2 molecule is bound, another conformational changes occurs for more bindings.

The experimental data shows the conformational changes in hemoglobin by binding O_2 as the following:

- In deoxyhemoglobin, the Fe is bound the nitrogen atom which is in HisE8. Due to this bond, Fe is located out of plane.
- When oxygen binds the Fe, the new bond pulls the iron into the nitrogen plane.
- The histidine residue and the alpha-helix of the hemoglobin start to move by moving of Fe.
- Hence, resides between the alpha and beta dimers also move.
- The position of the carboxyl terminal end changes and so the favorable conditions for the transition between the T-state and the R-state of hemoglobin created. The new configuration is more favorable for bindig of O_2.

1.5. Our results for the magnetic properties and the functioning of hemoglobin

In this section, our study on the electronic and magnetic properties of hemoglobin molecule will be summarized.

We use extended multi-orbital Haldane-Anderson impurity model to study the electronic properties of hemoglobin molecule. The parameters of this model are obtained by using density functional theory (DFT) calculations. Then, we solve this effective Anderson Hamiltonian by using a quantum Monte Carlo (QMC) technique. In this technique, we use Hirsch-Fye QMC algorithm. In my master thesis (Mayda (2013)), I changed single-orbital Haldane-Anderson model to the multi-orbital single impurity Haldane-Anderson model. In this model, only the intra-orbital Coulomb interactions were taken into account.

In this thesis, both the intra- and inter-orbital Coulomb interactions are taken into account. The details of the Hirsch-Fye QMC algorithm for this Anderson model are given in Appendix B.

In the following of this section, the Anderson model and the combined DFT+QMC method will be described. In addition, our proposal for the mechanism for the functioning of hemoglobin will summarized.

1.5.1. Extended multi-orbital Anderson impurity model

We use an effective multi-orbital Anderson model to describe the magnetic properties of HbA. In this model, the Fe(3d) orbitals of the HbA are described by the impurity and the remaining orbitals are named as host part.

The multi-orbital single-impurity Anderson Hamiltonian (Anderson (1961), Haldane and Anderson (1976)) with the intra and inter-orbital Coulomb interactions is given by

$$\begin{aligned} H = \sum_{m,\sigma}(\varepsilon_m - \mu)c^{\dagger}_{m\sigma}c_{m\sigma} \quad &+ \quad \sum_{\nu,\sigma}(\varepsilon_{d\nu} - \mu)d^{\dagger}_{\nu\sigma}d_{\nu\sigma} + \sum_{m,\nu,\sigma}\left(V_{m\nu}c^{\dagger}_{m\sigma}d_{\nu\sigma} + V^{*}_{m\nu}d^{\dagger}_{\nu\sigma}c_{m\sigma}\right) \\ &+ \quad \sum_{\nu} U_{\nu}n_{\nu\uparrow}n_{\nu\downarrow} + \sum_{\nu>\nu',\sigma}\left(U'n_{\nu\sigma}n_{\nu'-\sigma} + (U'-J)n_{\nu\sigma}n_{\nu'\sigma}\right) \end{aligned} \tag{1.3}$$

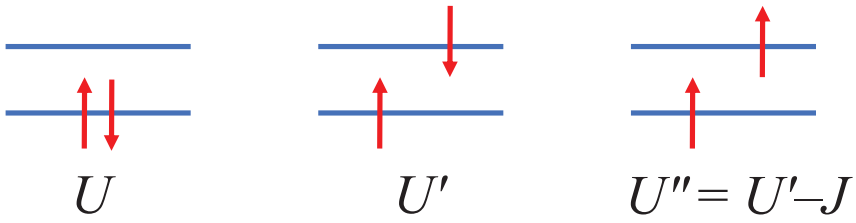

Figure 1.9. In the left picture, the intra-orbital Coulomb interaction U is shown. The inter-orbital Coulomb interaction U' for antiparallel spins is shown in the middle picture, whereas U'' is for parallel spins as seen in the right picture. In the atomic limit $U' = U - 2J$ and $U'' = U - 3J$, where J is the ferromagnetic Hund's coupling.

where $c^{\dagger}_{m\sigma}$ ($c_{m\sigma}$) operator creates (annihilates) an electron in the m'th host state with spin σ, $d^{\dagger}_{\nu\sigma}$ ($d_{\nu\sigma}$) is the creation (annihilation) operator for a localized electron with spin σ at the Fe($3d_{\nu}$) orbital, and the electron occupation operator for the Fe($3d_{\nu}$) orbitals is $n_{\nu\sigma} = d^{\dagger}_{\nu\sigma} d_{\nu\sigma}$. Here, ε_m and $\varepsilon_{d\nu}$ are the energies of the host and the Fe($3d_{\nu}$) impurity states, respectively. The hybridization matrix element between the m'th host and the Fe($3d_{\nu}$) state is $V_{m\nu}$. The intra-orbital Coulomb repulsion is U, while U' and $U'' = U' - J$ are the Coulomb interactions between two $3d$ electrons in different orbitals with opposite and parallel spins, respectively. Here J is the ferromagnetic Hund's coupling constant. In the case of a free atom, the relation $U' = U - 2J$ holds. Finally, the chemical potential μ is introduced since the QMC calculations are performed at finite temperatures in the grand canonical ensemble.

We use Anderson impurity model to obtain the electronic and magnetic properties of hemoglobin molecule. This model treats the host part and impurity part, separately. Hence, the electronic correlations in Fe(3d) orbitals are taken into account independently from the host part. This enables to obtain the magnetic properties of hemoglobin molecule with a realistic model.

1.5.2. DFT+QMC approach for the Anderson impurity model

The electronic correlations in the molecules containing transition metal atoms play an essential role to determine the electronic and magnetic properties. Since these correlations are not a pertubative effect, they have to be solved exactly.

In this thesis, the electronic structure of the hemoglobin molecule is described by

the extended multi-orbital Haldane-Anderson model explained in the Subsection 1.5.1. The parameters of this model are obtained by the density functional theory (DFT) (Kohn and Sham (1965)) calculations. Then, the Anderson Hamiltonian is solved by the Hirsch-Fye (Hirsch and Fye (1986)) quantum Monte Carlo algorithm (HF-QMC). This algorithm takes into account intra- and inter-orbital Coulomb interactions without using any approximation. Hence, the combined DFT+QMC method provides to obtain electronic and magnetic properties of hemoglobin molecule, accurately.

1.5.3. Why do we study the hemoglobin molecule?

Hemoglobin molecules exhibit energy gaps in their spectrum and contain transition-metal atoms. In this respect, they are similar to an entirely different class of materials which are named as diluted magnetic semiconductors (DMS) (Ohno *et al.* (1992), Ohno *et al.* (1996)). The DMS materials are obtained by substituting transition-metal impurities into a semiconductor host. For example, (Ga,Mn)As is obtained by substituting Mn impurities for Ga in the GaAs semiconductor.

DMS materials have attracted much attention because of their magnetic and semiconducting properties. They display high Curie temperatures. In addition, an impurity bound state, which is a sharp resonant state in the single-particle spectrum, exists 110 meV above the top of the valence band in the semiconducting gap ((Jungwirth *et al.*, 2007)). The impurity bound state consists of spectral weight from both the Mn impurity and the host. Calculations performed by using the Haldane-Anderson model show that this new electronic state is important in determining the electronic and magnetic properties of (Ga,Mn)As ((Ichimura *et al.*, 2006), (Bulut *et al.*, 2007), (Tomoda *et al.*, 2009)). In particular, long-range ferromagnetic correlations exist among Mn impurities when the chemical potential is located between the top of the valence band and IBS. These ferromagnetic correlations disappear rapidly as the IBS becomes occupied by electrons. Due to these electronic and magnetic properties, the DMS materials have potential for new device applications (Ohno *et al.* (1992)) for example in spintronics ((Maekawa *et al.*, 2013)).

When studied within the framework of the Haldane-Anderson model (Anderson (1961)), hemoglobin molecule and the DMS materials have similar electronic structures; they have semiconducting energy gaps, they contain transition-metal impurities. In addition, we observe that all these different classes of materials have impurity bound states in the electronic spectrum which control the magnetic properties.

1.5.4. Our proposal of a magnetic mechanism for the functioning of hemoglobin

Our proposal for the functioning of hemoglobin molecule is very different than the experimental picture described in Section 1.2.

DFT+QMC results show that the new electronic states are names as impurity bound states (IBS) are formed in hemoglobin molecule. The occupancy of IBS determines the magnetic properties of the molecule. For the deoxy-heme cluster, IBS are located below the Fermi level and the molecule has the low-spin states. On the other hand, IBS are located above the Fermi level for the oxy-heme cluster and the molecule has the lower spin state than the deoxy-heme.

Our results show that IBS are not sufficient to obtain the low-spin state for the oxy-heme. We see that the magnetic gap is formed by decreasing the temperature for the oxy-heme. Fe(3d)-O_2 charge transfer is seen at the low temperatures ($T < 300$ K) and the antiferromagnetic correlations occur between the Fe(3d) and O_2 electrons. These AF correlations lower the total magnetic moment of the molecule and so low-spin state is obtained for the oxy-heme cluster. The details of this mechanism will be explained in Chapter 2.

DFT+QMC results show that both the IBS and the opening of magnetic gap are necessary for obtaining the high-spin to low-spin transition in hemoglobin. The results presented in this thesis show that the magnetic effects play an important role in the functioning of hemoglobin molecule.

1.6. Outline

The outline of this thesis as the following; in Chapter 2, the DFT+QMC results will be shown. In this chapter, we will show that Fe(3d) and host electrons have magnetic moment in both deoxy-heme and oxy-heme clusters. In addition, the susceptibility measurements and the magnetic formations for the deoxy and oxy-heme clusters will be presented. These results show that the deoxy-heme cluster has the Curie-type magnetic susceptibility. In addition, we will see that the spin state of deoxy-heme is S=1.6 at 300 K. On the other hand, the spin state of oxy-heme cluster equals to S=0.68 at 300 K. For the deoxy-heme, we see strong ferromagnetic correlations between the Fe(3d) electrons. These ferromagnetic correlations are suppressed by the antiferromagnetic correlations be-

tween the Fe(3d) and host electrons for the oxy-heme. Hence, the oxy-heme has lower spin state than the deoxy-heme. In additon, magnetic measurements show that the new electronic states named as impurity bound states (IBS) are formed both in the deoxy-heme and oxy-heme. The location of the IBS is very important in determining the magnetic properties of the hemoglobin molecule. On the contrary, the IBS are not sufficient to obtain the spin 0 state for the oxy-heme. In this section, we will show that the charge transfer from O_2 to Fe(3d) orbitals occurs by decreasing the temperature and the magnetic gap is formed. The antiferromagnetic correlations between the O_2 and Fe(3d) electrons lead to obtain S=0 state for the oxy-heme. The DFT+QMC results presented in Chapter 2 show that both the IBS and the opening of magnetic gap are necessary for obtaining the high-spin to low-spin transition in hemoglobin.

In Chapter 3, we will present the magnetic circular dichroism (MCD) spectra for the deoxy-heme and we will compare it with the experimental results. The DFT+QMC results show that the antiferromagnetic (AF) correlations occur between the Fe(3d) and host electrons. In the MCD spectra, an anomalous line shape is seen. Our results show that Fe(3d)-host AF correlations correspond to this line shape in MCD spectrum.

In Chapter 4, the calculated RIXS spectrum for the deoxy-heme and oxy-heme clusters will be shown. In addition, we will compare our DFT+QMC results with the experimental RIXS spectrum. Here, the d-d transitions are obtained with these calculations.

In Chapter 5, we compare the DFT+QMC results with the X-ray absorption spectrum results. Here, we see that our DFT+QMC results are not good agreement with the XAS results. We find that the spectrum obtained by DFT+QMC calculations are more broaden than the XAS. The reason may be the U and J parameters used in the DFT+QMC calculations.

The implications of DFT+QMC results for the functioning of hemoglobin will be explained in Chapter 6. In this chapter, the magnetic mechanism for the Fe-O_2 bindig, the Bohr effect and the cooperativity will be explained. The DFT+QMC results find that S=0 spin state develops in a narrow energy gap. If the chemical potential is slightly changed, the molecule has different magnetic properties. Hence, the binding of the O_2 to Fe is affected. This mechanism may be the explanation of the origin of the Boh effect. In addition, in this chapter, we will present two proposals for the mechanism of cooperativity. The first one is the simple ferromagnetic bound breaking. The second one is based on the spin non-conservancy in the binding of O_2 to heme. The details of these mechanism will be given in this chapter.

In Chapter 7, the future applications of DFT+QMC approach to the different

molecules will be mentioned. There are many bio-inorganic molecules which have similar electronic structures with the hemoglobin such as chlorophyll and organic light emitting diodes (OLED's). In the future, the DFT+QMC approach will be used to obtain the electronic and magnetic properties of these molecules.

Chapter 8 gives the conclusion of the thesis.

We have appendix chapters for explanations of the details of our results. In Appendix A, the DFT results will be presented. In this chapter, the density of states and matrix elements of the hybridizations between the Fe(3d) and host states will be shown.

The detail of the Hirsch-Fye algorithm for the multi-orbital Anderson impurity model will be explained in Appendix B.

In Appendix C, the determinations for the Fermi levels for the deoxy-heme and oxy-heme clusters will be shown. In this part, we will present the calculations of the electron numbers of Fe(3d) orbitals, host orbitals and total electron number of the molecules as a function of the chemical potentials.

In Appendix D, the competition of the Hund's coupling with the Fe(3d)-host AF correlations will be explained. We see that deoxy-heme has the high-spin state due to strong Hund's coupling between the Fe(3d) electrons. On the other hand, for the oxy-heme, we see the AF correlations between the Fe(3d)-host electrons and these AF correlations compress the Hund's coupling. Hence, the oxy-heme has lower spin state than the deoxy-heme. Its details will be explained in this chapter.

We observe the effect of the inter-orbital interactions on the IBS. These results will be shown in Appendix E. Our results show that inter-orbital Coulomb interactions are very important for the location of the IBS for the deoxy-heme. On the other hand, the location of the IBS are not affected by the interactions for the oxy-heme.

In Appendix F, we will present the potential sources for the computational errors in DFT+QMC approach. In this approach, we use the double-counting term. The Coulomb interactions are taken into account both the DFT and QMC. In order to prevent this double-counting, we substract the double-counting term from the energy levels of the Fe(3d) orbitals. On the other hand, we make approximation in this substraction. Hence, this will lead to some errors in our calculations. In addition, we will show the effect of $\Delta\tau$ in our DFT+QMC calculations. We use Trotter approximation in the Hirsch-Fye algorithm. We separate the non-interaction part and the interaction part to calculate the partition function (the details are given in Appendix B) with the ($\Delta\tau$) error. In this chapter, we will show results for the susceptibility, total Fe(3d) electron number, total electron number and the total magnetic moment for different $\Delta\tau$ at different temperatures. In

Haldane-Anderson model, we neglect the spin flip and pair hopping term. In order to see the effect of these terms on the DFT+QMC results, we solve the Anderson Hamiltonian with the exact diagonalization. We see that these terms may be important for the oxy-heme and we may see the spin 0 state for oxy-heme at 300 K when we add them in the Anderson Hamiltonian.

In Appendix G, we will present the effect of the Fe-porphyrin distance on the magnetic properties of the deoxy-heme.

CHAPTER 2

QUANTUM MONTE CARLO RESULTS FOR THE HEME CLUSTERS

In this section, the QMC data on the effective Haldane-Anderson model for deoxy-heme and oxy-heme clusters are presented. The parameters for this model is shown in Appendix A. The QMC calculations are performed by using the Hirsch-Fye QMC algorithm (Hirsch and Fye (1986)). The details of this algorithm is explained in the Appendix B. In my master thesis, Hirsch-Fye algorithm was developed for the multi-obital case and it includes the intra-orbital Coulomb interactions (Mayda (2013)). In this thesis, the inter-orbital Coulomb interactions are added along with the Hund's coupling.

Here, we find that Fe(3d) and host orbitals have magnetic moments in deoxy-heme and oxy-heme. In addition, we see that the antiferromagnetic correlations occur between the Fe(3d) and host states in both deoxy-heme and oxy-heme. We will show in Chapter 3 that these AF correlations in deoxy-heme is responsible for the anomalous line shape in MCD spectrum.

In this section, we show that the impurity bound states (IBS) which are the correlated electronic states are formed both in deoxy-heme and oxy-heme. The IBS are occupied for deoxy-heme and they are unoccupied for the oxy-heme. The magnetic moment of the hemoglobin is lowered by binding the O_2 because the antiferromagnetic correlations between the Fe(3d) and host states compete with the Hund's coupling. These AF correlations lower the total magnetic moment of oxy-heme. On the other hand, the effective spin of oxy-heme equals 0.68. DFT+QMC results show that as the temperature decreases, a magnetic gap opens at the Fermi level for oxy-heme and Fe(3d)-O_2 charge transfer is seen. In addition, AF correlations occur between the Fe(3d) and O_2 states, and these AF correlations lower the total magnetic moment and we obtain effective spin state as S=0.1. Hence, our DFT+QMC results show that both the IBS and the opening of magnetic gap are responsible for the high-spin to low-spin transition in hemoglobin.

Here, in particular, we have calculated the single-particle Green's functions for the Fe($3d_\nu$) NAO's defined by

$$G_{\nu\sigma}(\tau) = -\langle T_\tau d_{\nu\sigma}(\tau) d^\dagger_{\nu\sigma}(0)\rangle. \tag{2.1}$$

Similarly, the host Green's function is defined by

$$G_{m\sigma}(\tau) = -\langle T_\tau c_{m\sigma}(\tau) c^\dagger_{m\sigma}(0)\rangle. \tag{2.2}$$

Here, T_τ is the usual Matsubara τ-ordering operator and $d_{\nu\sigma}(\tau) = e^{H\tau} d_{\nu\sigma} e^{-H\tau}$. We calculate the electron occupation number of Fe(3d) orbitals by using

$$\langle n_d \rangle = \sum_{\nu=1}^{5} \sum_{\sigma} \langle d^\dagger_{\nu\sigma} d_{\nu\sigma} \rangle. \tag{2.3}$$

We also calculate the electron occupation number of host orbital which is defined by

$$\langle n_h \rangle = \sum_{m=1}^{N-5} \sum_{\sigma} \langle c^\dagger_{m\sigma} c_{m\sigma} \rangle. \tag{2.4}$$

The total electron number of molecule is defined by

$$\langle n_T \rangle = \sum_{\nu=1}^{5} \sum_{\sigma} \langle d^\dagger_{\nu\sigma} d_{\nu\sigma} \rangle + \sum_{m=1}^{N-5} \sum_{\sigma} \langle c^\dagger_{m\sigma} c_{m\sigma} \rangle. \tag{2.5}$$

In addition, we calculate the effective magnetic moments $M^{\rm eff}_\nu$ defined as $M^{\rm eff}_\nu = \sqrt{\langle (M^z_\nu)^2 \rangle}$ and magnetic correlations $\langle M^z_\nu M^z_{\nu'} \rangle$ of Fe($3d_\nu$) orbitals, where

$$M^z_\nu = d^\dagger_{\nu\uparrow} d_{\nu\uparrow} - d^\dagger_{\nu\downarrow} d_{\nu\downarrow}. \tag{2.6}$$

In order to understand the correlations around the Fe atom, we calculate the equal-time magnetic correlations between the Fe($3d_\nu$) and host states $\langle M^z_\nu M^z_m \rangle$, where

$$M^z_m = c^\dagger_{m\uparrow} c_{m\uparrow} - c^\dagger_{m\downarrow} c_{m\downarrow}. \tag{2.7}$$

Moreover, we calculate the total Fe($3d$) magnetic susceptibility χ_{3d} and the total molecu-

lar magnetic susceptibility χ_T. χ_{3d} is defined by

$$\chi_{\mathrm{3d}}(\tau) = \langle T_\tau M^{\mathrm{z}}_{\mathrm{3d}}(\tau) M^{\mathrm{z}}_{\mathrm{3d}}(0)\rangle. \tag{2.8}$$

Here, $M^{\mathrm{z}}_{\mathrm{3d}}$ is as $M^{\mathrm{z}}_{\mathrm{3d}} = \sum_\nu (d^\dagger_{\nu\uparrow} d_{\nu\uparrow} - d^\dagger_{\nu\downarrow} d_{\nu\downarrow})$ Similarly, χ_T is defined by

$$\chi_{\mathrm{t}}(\tau) = \langle T_\tau M^{\mathrm{z}}_{\mathrm{T}}(\tau) M^{\mathrm{z}}_{\mathrm{T}}(0)\rangle. \tag{2.9}$$

Here, $M^{\mathrm{z}}_{\mathrm{t}}$ equals

$$M^{\mathrm{z}}_{\mathrm{t}} = \sum_m (c^\dagger_{m\uparrow} c_{m\uparrow} - c^\dagger_{m\downarrow} c_{m\downarrow}) + \sum_\nu (d^\dagger_{\nu\uparrow} d_{\nu\uparrow} - d^\dagger_{\nu\downarrow} d_{\nu\downarrow}). \tag{2.10}$$

Total 3d magnetic susceptibility and total molecular magnetic susceptibility is calculated by the Fourier transformation,

$$\chi_{\mathrm{3d}}(i\omega_m) = \int_0^\beta d\tau\, e^{i\omega_m \tau} \chi_{\mathrm{3d}}(\tau) \tag{2.11}$$

and

$$\chi_{\mathrm{t}}(i\omega_m) = \int_0^\beta d\tau\, e^{i\omega_m \tau} \chi_{\mathrm{t}}(\tau). \tag{2.12}$$

We present the zero-frequency magnetic susceptibilities in this thesis.

In obtaining QMC data, discrete Matsubara time step of $\Delta\tau = 0.13\,\mathrm{eV}^{-1}$ was used for 400 K and 300 K. On the other hand, for 200 K, $\Delta\tau = 0.16\,\mathrm{eV}^{-1}$ was used and for 150 K, $\Delta\tau = 0.19\ \mathrm{eV}^{-1}$ was used. We used different $\Delta\tau$ values for different temperatures values due to computation time problem. Hence, we made the measurements as a function of $\Delta\tau$ for various temperatures and we extrapolated them to see the values at $\Delta\tau \to 0$ limit. These results will be shown in Appendix F.

The results are presented for temperature $T = 150$ K, $T = 200$ K, $T = 300$ K and $T = 400$ K in the grand canonical ensemble.

2.1. Magnetic moment density for the heme clusters

In this section, we show the magnetic moment density for the deoxy and oxy-heme clusters. We obtain the effective magnetic moments of the m'th host states from

$$(M_m^{\rm eff})^2 = \langle (M_m^z)^2 \rangle, \tag{2.13}$$

where

$$M_m^z = c_{m\uparrow}^\dagger c_{m\uparrow} - c_{m\downarrow}^\dagger c_{m\downarrow}, \tag{2.14}$$

and $\langle (M_m^z)^2 \rangle$ is calculated with QMC simulations. While we were constructing the effective Anderson model, we obtained the following expression for the host states in terms of natural atomic orbitals (NAO's) and atomic orbitals;

$$c_{m\sigma} = \sum_i D_{m,i}\, \tilde{c}_{i\sigma}, \tag{2.15}$$

which leads to the operator definition

$$M_m^z = \sum_{i,j} D_{m,i}^* D_{m,j} \sum_{\sigma=\pm 1} \sigma\, \tilde{c}_{i\sigma}^\dagger \tilde{c}_{j\sigma}. \tag{2.16}$$

For $i \neq j$, we obtain the following approximate expression for the effective moment of the m'th host state $M_m^{\rm eff}$ and that of the i'th atomic orbital $\tilde{M}_i^{\rm eff}$

$$M_m^{\rm eff} \approx \sum_i |D_{m,i}|^2\, \tilde{M}_i^{\rm eff}, \tag{2.17}$$

where $\tilde{M}_i^{\rm eff}$ is the effective moment of the i'th atomic orbital.

Figure 2.1 shows the total host magnetization density in the basis of the atomic orbitals with blue colored bubbles. In this figure, the volume of the bubbles are proportional to the magnitute of $\tilde{M}_i^{\rm eff}$.

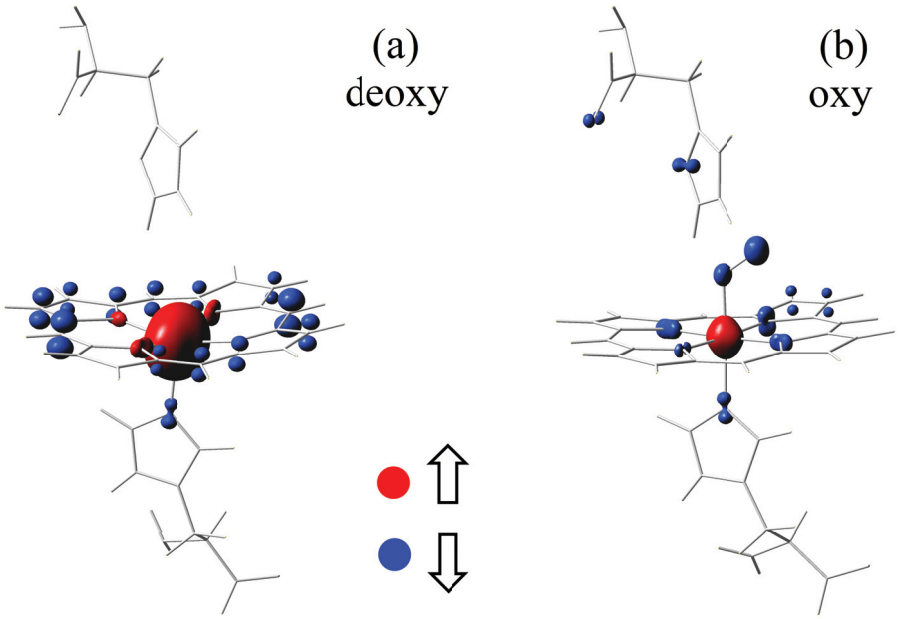

Figure 2.1. QMC results on the local magnetic-moment density $M(\mathbf{r})$ are sketched for the (a) deoxy and (b) oxy-heme clusters at $T = 150$ K. Here, the red color shows the atomic orbitals which have magnetic moments pointing up, while the blue color shows the down magnetic moments.

Figure 2.1(a) shows the magnetization density for the deoxy-heme cluster. Here, we observe that the Fe site has up magnetic moment and it equals 4.5 μ_B. For deoxy, the neighboring N sites have small magnetic moments which are also in up direction. On the other hand, the ferromagnetic correlations between the N and Fe sites are very weak. The C sites which are located away from the Fe site has down magnetic moment density. Hence, Fe-C sites have the antiferromagnetic (AF) correlations. These AF correlations originate from the partially filled π^* host states (166'th and 167'th host states) which consist of C($2p_z$) as shown in Fig. A.6. Hence, we see that the AF correlations occur between the Fe magnetic moment and the host magnetic moment which are spread out in the porphyrin layer in deoxy-heme.

Figure 2.1(b) shows the magnetic moment density for the oxy-heme cluster. The magnetic moment of the Fe site is reduced with respect to the deoxy but it remains finite. In addition, we see the strong Fe-O_2 and Fe-N antiferromagnetic correlations. In the following section, we will see that Fe-O_2 antiferromagnetic correlations are the temperature dependent, and the magnetic moment of Fe goes to 0 as decreasing of temperature.

2.2. Magnetic susceptibility measurements for the heme clusters

We begin this section by presenting Fig. 2.2(a-b). Here, in Figure 2.2(a), we show the total spin susceptibility χ_t and total the Fe susceptibility χ_{Fe}. In Figure 2.2(b), the total susceptibility is shown as a function of chemical potential μ for different temperatures for oxy-heme. In Figure 2.2(a), for the deoxy-heme cluster, we see that $\chi_{\rm t}$ increases rapidly as T decreases. Here, the dotted blue line represents the $1/T$ Curie dependence. Hence, $\chi_{\rm t}$ displays a T dependence which is close to that of a free moment. We find that the effective magnetic moment of the whole deoxy cluster is $4.07\,\mu_B$ at $T = 300$ K, which is reduced from that of the Fe moment which is 4.56 μ_B because of the Fe-porphyrin antiferromagnetic correlations. The Fe moment exhibits a perfect Curie T dependence however its value of 4.56 μ_B is smaller than 4.9 μ_B of an $S = 2$ spin.

In Figure 2.2(a) we observe that for oxy-heme $\chi_{\rm t}$ is reduced significantly with respect to that of the deoxy case. We also observe that there are two different temperature regimes for $\chi_{\rm t}$ of the oxy-heme cluster: above 300 K, $\chi_{\rm t}$ has a Curie-type T dependence with an effective moment of $2.1\,\mu_B$, while below 300 K we see that $\chi_{\rm t}$ gets suppressed as T decreases. We find that these two temperature regimes are both due to strong electron correlations but have different microscopic origins, which we discuss below.

In the high-temperature regime for $T > 300$ K, we observe that $\chi_{\rm t}$ of the oxy-heme cluster is reduced with respect to χ_t of the deoxy-heme cluster. This is mainly due to the collapse of the Fe magnetic moment and this is because the existence of impurity bound states in the multi-orbital Anderson model. In the deoxy case, the impurity bound states are occupied by electrons, while for the oxy case the impurity bound states become unoccupied. When the impurity bound states are unoccupied by electrons, there exist antiferromagnetic correlations between the Fe and the host magnetic moments, which compete with the Hund's coupling responsible for the large magnetic moment of Fe. Hence, when the impurity bound state is unoccupied, the Fe-host antiferromagnetic correlations cause the total magnetic moment of the cluster to decrease. This is responsible for the drop in $\chi_{\rm t}$ in the high-temperature regime as we go from the deoxy to the oxy case.

In the low-temperature regime for $T < 300$ K, $\chi_{\rm t}$ of oxy-heme decreases as T decreases. This decrease is shown in Fig. 2.2 (b). As shown here, as the temperature decreases, the total magnetic susceptibility decreases and a narrow gap is opened at the Fermi level at 150 K.

Our DFT+QMC results show that deoxy-heme cluster has the Curie type magnetic susceptibility. We also see that the deoxy-heme has high-spin state. On the other hand,

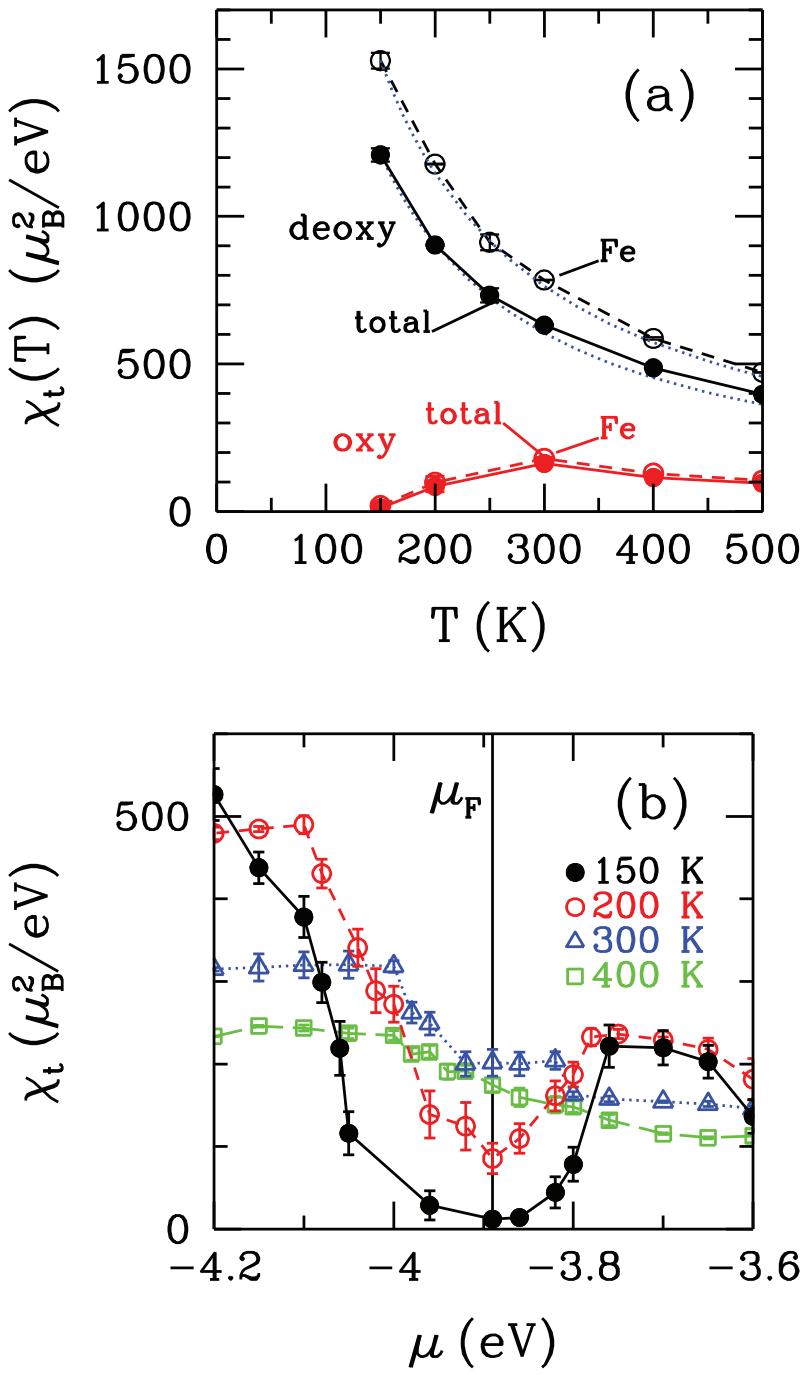

Figure 2.2. (a) The temperature dependence of the total and of the Fe spin susceptibilities χ_t for the deoxy and oxy-heme clusters. Here, the dotted blue line denotes the Curie-type $1/T$ temperature dependence. (b) The total magnetic susceptibility as a function of chemical potential μ for oxy-heme for different temperatures. Here, the vertical black solid line represents the Fermi level μ_F at T=150 K.

the magnetic susceptibility of the oxy-heme has the different behaviours for $T > 300$ K and $T < 300$ K. The results show that for $T > 300$ K, the oxy-heme has lower magnetic moment than deoxy-heme but its spin state is not equal 0. At $T < 300$ K, the spin state of oxy-heme goes to spin 0 state as seen in Fig. 2.2 (b).

We explain the high-spin to low-spin transition in hemoglobin by both the impurity bound states and the opening of the magnetic gap at the Fermi level. We see that the new electronic states which are impurity bound states (IBS) are formed both in the deoxy-heme and oxy-heme. The IBS are located below the Fermi level for the deoxy, and IBS are located above the Fermi level for oxy-heme. For the deoxy-heme, we see strong ferromagnetic correlations between the Fe(3d) electrons due to Hund's coupling. On the other hand, when the IBS are located above the Fermi level as oxy-heme, the antiferromagnetic (AF) correlations between the Fe(3d) and host states occur. These AF correlations suppress the ferromagnetic correlations at Fe(3d)'s. Hence, the magnetic moment for oxy-heme is lowered.

When we decrease the temperature, we see that a magnetic gap is formed and the charge transfer from O_2 to Fe(3d) orbitals occurs. This charge transfer leads to Fe(3d)-O_2 AF correlations. The total magnetic moment for oxy-heme decreases due to these AF correlations. Hence, the spin state of oxy-heme goes to 0.

Our DFT+QMC results show that both the IBS and Fe(3d)-O_2 charge transfer are necessary for obtaining the high-spin to low-spin transition in hemoglobin.

In the following sections, we will present the results on the formation of the IBS for the deoxy-heme and oxy-heme. In addition, the results on the opening of magnetic gap will be shown for the oxy-heme.

2.3. Impurity bound states

In this section, we discuss the electron occupation number $\langle n_\nu \rangle$ for Fe($3d_\nu$) orbitals as a function of chemical potential μ for deoxy. Similarly, we show the square of the magnetic moments $\langle (M_\nu^z)^2 \rangle$ at the Fe($3d_\nu$) orbitals as a function of μ. It is possible to obtain information on the single-particle spectral weight distribution and the local moment formation from μ dependence results. In addition, we study the magnetic moments for host states and their magnetic correlations with the Fe($3d_\nu$) orbitals. These results show that the new electronic states named as impurity bound states (IBS) are formed in deoxy molecule. These electronic states are located below the Fermi level of deoxy molecule. In addition, the antiferromagnetic (AF) correlations occur between the Fe(3d)

Table 2.1. Electron occupation number $\langle n_\nu \rangle$ of Fe($3d_\nu$) orbitals for deoxy-heme and oxy-heme. For deoxy, the chemical potential $\mu = -2.8$ eV. For oxy molecules, μ equals -3.8 eV. Here, $U = 4$ eV, $J = 0.9$ eV and $T = 300$ K.

$\langle n_\nu \rangle$	xy	xz	yz	$3z^2 - r^2$	$x^2 - y^2$	total ($\langle n_d \rangle$)
deoxy	1.00	1.12	1.06	1.07	1.13	5.38
oxy	1.84	1.17	1.15	0.92	0.75	5.83

Table 2.2. For deoxy, magnetic correlation function $\langle M_\nu M_{\nu'} \rangle$ between the Fe($3d_\nu$) orbitals, ν and ν', at chemical potential $\mu = -2.8$ eV. Here, $U = 4$ eV, $J = 0.9$ eV and $T = 300$ K.

$\langle M^z_\nu M^z_{\nu'} \rangle$	xy	xz	yz	$3z^2 - r^2$	$x^2 - y^2$
xy	0.98	0.84	0.90	0.88	0.84
xz		0.86	0.79	0.77	0.73
yz			0.92	0.83	0.78
$3z^2 - r^2$				0.90	0.77
$x^2 - y^2$					0.86

states and host states. These correlations are disappeared by the electron fillings of IBS. QMC results for deoxy molecule show that when IBS are located below the Fermi level and they are occupied, the molecule has high-spin state.

In Table 2.1, we show the QMC results on the electron occupations $\langle n_\nu \rangle$ for deoxy and oxy-heme clusters at their chemical potentials. These results are for $U = 4$ eV, $J = 0.9$ eV and temperature $T = 300$ K. Here, we observe that Fe($3d_\nu$) orbitals have approximately 1.1 electrons in deoxy molecule. The second row of the Table 2.1 shows the $\langle n_\nu \rangle$ for oxy. Here, we see that the occupation of $x^2 - y^2$ is 0.75 and $3z^2 - r^2$, xz and yz orbitals are singly occupied. On the other hand, xy orbital has 1.84 electrons. For oxy-heme, the occupation number of xy, xz and yz orbitals increase and the occupation number of the remaining orbitals decrease. The last column of the Table 2.1 shows the total electron number of the Fe(3d) orbitals, $\langle n_d \rangle$. For deoxy-heme, $\langle n_d \rangle = 5.38$ which means that Fe is in between the ferric (+3) and the ferrous (+2) states. For oxy-heme, the total electron number of the Fe(3d) orbitals equal 5.83 at $T = 300$ K.

Table 2.2 shows the magnetic correlation function $\langle M_\nu M_{\nu'} \rangle$ between the Fe($3d_\nu$) orbitals in deoxy for $U = 4$ eV and $J = 0.9$ eV. We find that ferromagnetic correlations

Table 2.3. For oxy, magnetic correlation function $\langle M_\nu M_{\nu'} \rangle$ between the Fe($3d_\nu$) orbitals, ν and ν', at chemical potential $\mu = -3.8$ eV. Here, $U = 4$ eV, $J = 0.9$ eV and $T = 300$ K.

$\langle M^z_\nu M^z_{\nu'} \rangle$	xy	xz	yz	$3z^2 - r^2$	$x^2 - y^2$
xy	0.16	0.06	0.06	0.04	0.01
xz		0.79	0.60	0.25	0.14
yz			0.81	0.25	0.14
$3z^2 - r^2$				0.62	0.08
$x^2 - y^2$					0.55

Table 2.4. For oxy, magnetic correlation function $\langle M_\nu M_{\nu'} \rangle$ between the Fe($3d_\nu$) orbitals, ν and ν', at chemical potential $\mu = -3.8$ eV. Here, $U = 4$ eV, $J = 0.9$ eV and $T = 150$ K.

$\langle M^z_\nu M^z_{\nu'} \rangle$	xy	xz	yz	$3z^2 - r^2$	$x^2 - y^2$
xy	0.12	0.02	0.02	0.02	0.00
xz		0.59	-0.09	0.05	0.04
yz			0.58	0.04	0.04
$3z^2 - r^2$				0.59	0.04
$x^2 - y^2$					0.52

occur between the Fe($3d_\nu$) orbitals due to Hund's coupling.

Table 2.3 shows the $\langle M_\nu M_{\nu'} \rangle$ at 300 K for oxy molecule. The weak ferromagnetic correlations occur in oxy with respect to deoxy and there are no any antiferromagnetic correlations between the Fe(3d) orbitals.

In Table 2.4, $\langle M_\nu M_{\nu'} \rangle$ at 150 K for the oxy case is represented. The comparison of these results with the results in Table 2.3 shows that the inter-orbital correlations between the Fe(3d) electrons decrease with the changing of temperature from 300 K to 150 K.

In Table 2.5, we compare the the total intra-orbital magnetic correlation $\sum_\nu \langle (M^z_\nu)^2 \rangle$ of Fe($3d$) orbitals, total inter-orbital magnetic correlation $\sum_{\nu,\nu'} \langle M^z_\nu M^z_{\nu'} \rangle$ of Fe($3d$) orbitals and square of the total effective magnetic moment $\langle (M^z_{3d})^2 \rangle$ of Fe($3d$) orbitals for deoxy and oxy clusters.

The first column of Table 2.5 denotes the total intra-orbital magnetic correlations of Fe(3d) orbitals in deoxy and oxy. Here, we observe that $\sum_\nu \langle (M^z_\nu)^2 \rangle$ equals 4.50 for deoxy and 2.90 for oxy.

The second column shows the Fe(3d) inter-orbital correlations. There are too

Table 2.5. QMC results on the total intra-orbital magnetic correlation $\langle (M_\nu^z)^2 \rangle$ of Fe($3d$) orbitals ,square of the total inter-orbital magnetic correlation $\langle M_\nu^z M_{\nu'}^z \rangle$ of Fe($3d$) orbitals and square of the total effective magnetic moment $\langle (M_{\rm 3d}^{\rm z})^2 \rangle$ of Fe($3d$) orbitals for deoxy and oxy. Here, $\langle (M_{\rm 3d}^{\rm z})^2 \rangle = \sum_\nu \langle (M_\nu^z)^2 \rangle + \sum_{\nu \neq \nu'} \langle M_\nu^z M_{\nu'}^z \rangle$. For these results, $U = 4$ eV, $J = 0.9$ eV and $T = 300$ K.

	$\sum_\nu \langle (M_\nu^z)^2 \rangle$	$\sum_{\nu \neq \nu'} \langle M_\nu^z M_{\nu'}^z \rangle$	$\langle (M_{\rm 3d}^{\rm z})^2 \rangle$
deoxy	4.50	16.20	20.70
oxy	2.90	3.30	6.20

much differences between the total $\langle M_\nu^z M_{\nu'}^z \rangle$ values for these molecules. The reason of this difference is that while only ferromagnetic correlations occur between the Fe(3d) orbitals of deoxy, only small ferromagnetic correlations occur in oxy molecule so the correlations between the Fe(3d) orbitals equal 3.30.

In the third column of Table 2.5, the square of the total effective Fe(3d) magnetic moment $\langle (M_{\rm 3d}^{\rm z})^2 \rangle$ are shown for deoxy and oxy clusters. Here, we see that Fe(3d) orbitals in deoxy have high effective magnetic moment due to strong ferromagnetic correlations between them. On the other hand, $\langle (M_{\rm 3d}^{\rm z})^2 \rangle$ value for oxy is smaller than for deoxy due to weak ferromagnetic correlations.

The high-spin to low-spin transition by binding the O_2 molecule to Fe in hemoglobin is explained by the occupation numbers of Fe(3d) orbitals. It is said that deoxy-hemoglobin has high-spin state because all Fe(3d) orbitals are single occupied. In this picture, t_{2g} and e_g orbitals are not separated. On the other hand, oxy-hemoglobin molecule has low-spin state because three e_g orbitals Fe(3d) are double occupied and the t_{2g} orbitals are empty. This causes that Fe atom has not magnetic moments. Hence, molecule goes to low-spin state by binding the O_2 molecule.

Our explanation for high-spin to low-spin transition in hemoglobin is very different from this picture. As shown in Table 2.1, the Fe(3d) orbitals are not doubly occupied for deoxy and oxy. In addition, Table 2.2 and 2.3 show that all 3d orbitals have magnetic moments in two heme clusters. The key point of our mechanism is the magnetic correlations between the Fe(3d) orbitals. Table 2.5 shows that strong ferromagnetic correlations occur in deoxy molecule due to Hund's coupling. On the other hand, we see small ferromagnetic correlations between the Fe(3d) orbitals for oxy-heme. Hence, Fe in oxy has the lowered-spin state.

2.3.1. Impurity bound states for the deoxy-heme cluster

We begin the section by presenting the data with Figure 2.3 (a) which shows the the occupation number $\langle n_\nu \rangle$ for Fe($3d_\nu$) orbitals as a function of chemical potential μ. Similarly, Figure 2.3(b) shows the square of the magnetic moments $\langle (M_\nu^z)^2 \rangle$ at the Fe($3d_\nu$) orbitals as a function of μ.

In Figure 2.3(a), we observe that the $\langle n_\nu \rangle$ for all 3d orbitals increases gradually up to $\mu \approx -7$ eV. For $3z^2 - r^2$, xy, yz and xz orbitals, $\langle n_\nu \rangle$ exhibits a small jump at $\mu \approx -6.5$ eV. These orbitals are singly occupied at $\mu \approx -4.5$ eV. Above $\mu \approx -4.5$ eV, the occupations of $3z^2 - r^2$, xy, yz and xz orbitals continue to increase and they are doubly occupied at $\mu = 3$ eV. $\langle n_\nu \rangle$ for $x^2 - y^2$ orbital increase slightly until μ reaches ≈ -4 eV, where $\langle n_{x^2-y^2} \rangle$ exhibits a sudden increase. This orbital has approximately 1.1 electrons in the inteval -4 eV $\lesssim \mu \lesssim 2.5$ eV. Above $\mu = 2.5$ eV, the occupation of $x^2 - y^2$ orbital increases and it equals 1.5 electrons at $\mu = 3$ eV.

Figure 2.3(b) shows that $\langle (M_\nu^z)^2 \rangle$ for $3z^2 - r^2$, xy, yz and xz orbitals increases slightly up to $\mu \approx -7$ eV. For these orbitals, $\langle (M_\nu^z)^2 \rangle$ increases suddenly at $\mu \approx -6.5$ eV. The magnetic moments are nearly constant for $3z^2 - r^2$, xy, $x^2 - y^2$ and xz orbitals in the interval -6 eV $\lesssim \mu \lesssim -3$ eV. Above $\mu = -3$ eV, these four orbitals become doubly occupied and so $\langle (M_\nu^z)^2 \rangle$ decrease rapidly. In a similar manner, $\langle \left(M_{x^2-y^2}^z \right)^2 \rangle$ slightly changes up to $\mu \approx -4$ eV. At $\mu \approx -4$ eV, the magnetic moment of $x^2 - y^2$ orbital increase suddenly. In the interval -4 eV $\lesssim \mu \lesssim 2.5$ eV, it is nearly constant and above the $\mu = 2.5$ eV, $\langle \left(M_{x^2-y^2}^z \right)^2 \rangle$ decreases due to electron filling of orbital.

We note that the sudden increases are seen in both $\langle n_\nu \rangle$ and $\langle (M_\nu^z)^2 \rangle$ for $3z^2 - r^2$, xy, yz and xz orbitals at $\mu \approx -6.5$ eV and for $x^2 - y^2$ orbital at $\mu \approx -4$ eV. We think that the new electronic states named as impurity bound states (IBS) are formed at these μ points.

IBS arises from the strong hybridizations between the Fe($3d_\nu$) orbitals and some host orbitals. These host states develop magnetic moments and the size of their magnetic moments depend on the electron filling of IBS. In addition, the host states, which are strongly hybridized with Fe(3d) orbitals, are coupled antiferromagnetically to Fe(3d) magnetic moments. These correlations vanish with the filling of the IBS. Hence, we study the electron occupations of host states and their magnetic correlations with Fe(3d) orbitals to define IBS.

Figure 2.4 shows occupation number $\langle n_m \rangle$ and magnetic moments $\langle (M_m^z)^2 \rangle$ of some host states. We discuss the results for these host states because they are strongly

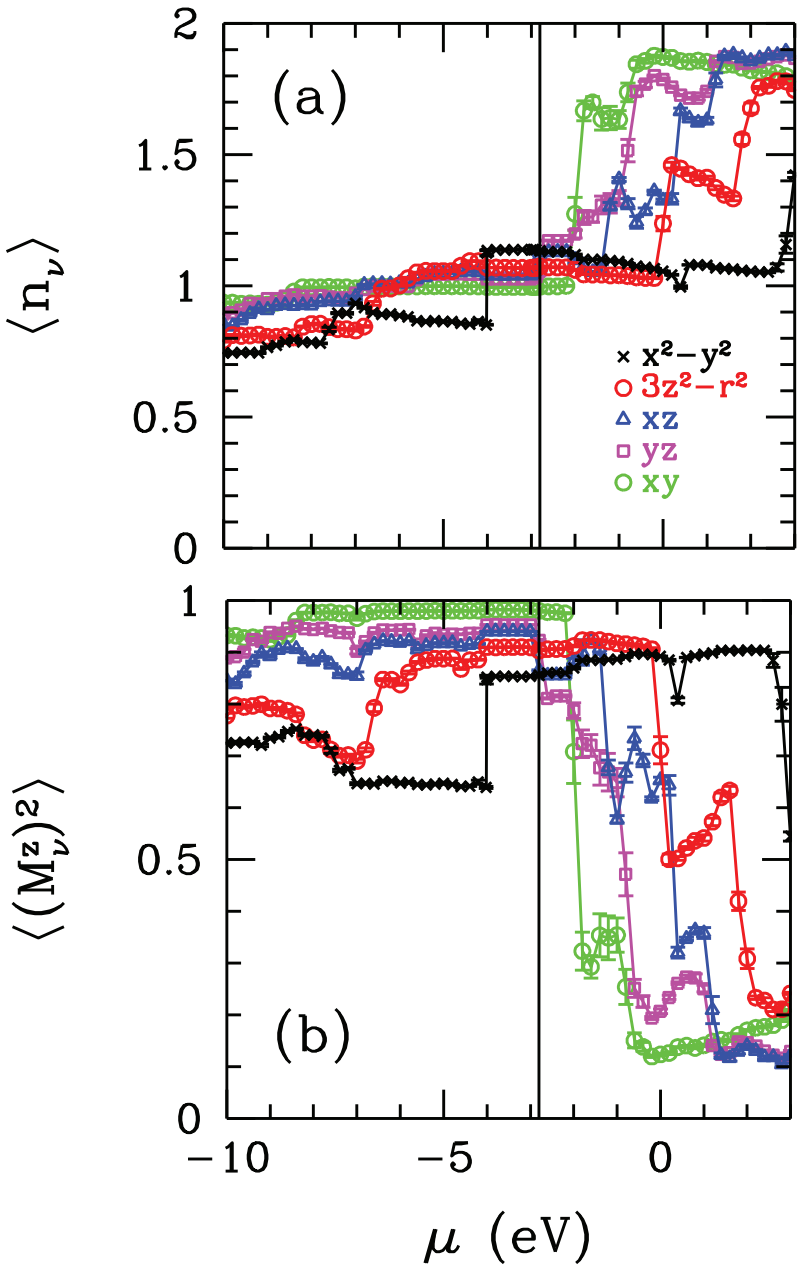

Figure 2.3. QMC results for deoxy on the Fe(3d) electron occupation number and Fe(3d) magnetic moments. (a) Electron occupation number $\langle n_\nu \rangle$ of the Fe($3d_\nu$) orbitals versus the chemical potential μ. (b) Square of magnetic moment $\langle (M_\nu^z)^2 \rangle$ for Fe($3d_\nu$) orbitals versus the chemical potential μ. Here, the vertical solid line denotes the Fermi level of molecule. The Fermi level of molecule is obtained by QMC. In addition, these results are for $U = 4$ eV, $J = 0.9$ eV and $T = 300$ K.

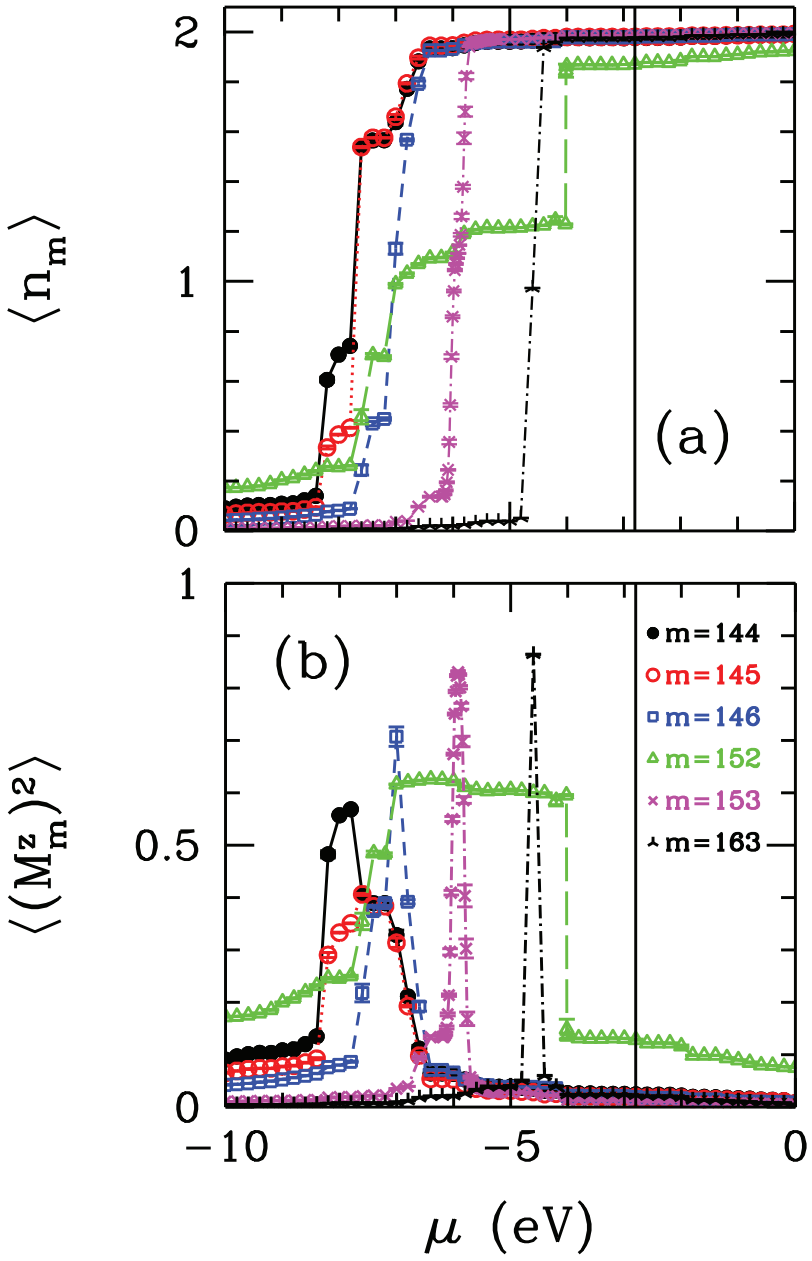

Figure 2.4. QMC results for deoxy on the host electron occupation number and magnetic moments of host states. (a) Electron occupation number of the m'th host state $\langle n_m \rangle$ versus the chemical potential μ. (b) Square of the magnetic moment of the m'th host state $\langle (M_m^z)^2 \rangle$ versus the chemical potential μ. Here, the vertical solid line denotes the Fermi level of molecule. The Fermi level of molecule is obtained by QMC. In addition, these results are for $U = 4$ eV, $J = 0.9$ eV and $T = 300$ K.

hybridized with Fe(3d) orbitals as shown in Fig. A.4. The changes in $\langle n_m \rangle$ as a function of μ is shown in Fig. 2.4(a). The bare energy ε_m for $m = 144$, 145, 146, 152, 153 and 163 are -7.76 eV, -7.65 eV, -7.06 eV, -5.98 eV, -5.95 eV and -4.59 eV, respectively. When the μ equals to ε_m, the sharp increases are seen in $\langle n_m \rangle$. In addition, these host states have magnetic moments at their energy values as seen in Fig. 2.4(b). At $\mu = -4$ eV, there is a sharp increase in occupation of $m = 152$'nd host state. We show in Fig. 2.3 that there is also a sharp increase in the occupation and magnetic moment of $x^2 - y^2$ orbital at $\mu = -4$ eV. When $\mu = -3$ eV, host states have small magnetic moments. Above this chemical potential, their magnetic moments vanish due to electron filling. Figure 2.3 shows that the IBS are filled at $\mu \approx -6.5$ eV and $\mu \approx -4$ eV. It is the important to note that host states are nearly doubly occupied at these μ values and their magnetic moments decrease rapidly by the filling of IBS.

In addition to these six host states, we present $\langle n_m \rangle$ versus μ and $\langle (M_m^z)^2 \rangle$ versus μ for $m = 166$ and 167 in Fig. 2.5. These host states are located near the Fermi level of deoxy molecule. Hence, they have contribution to the total magnetic moments of molecule. Figure 2.5 shows that $\langle n_m \rangle$ values for $m = 166$ and 167 are 0.21 and 0.1 at $\mu = -3$ eV. They have magnetic moments at this chemical potential as seen in Fig. 2.5(b). When μ passes through their energy values, $\langle n_m \rangle$ values equal 2 and their magnetic moments are 0.

Next, we discuss the magnetic correlations between the Fe($3d_\nu$) states and host states. Figure 2.6 shows the magnetic correlation function $\langle M_\nu^z M_m^z \rangle$ as a function of μ for host states $m = 144$, 145, 146, 152, 153 and 163. These results are for $U = 4$ eV and $J = 0.9$ eV. In Figure 2.6(a-c), we observe that 144'th, 145'th and 146'th host states have antiferromagnetic correlations with Fe($3d_\nu$) states. These antiferromagnetic correlations diminish rapidly at $\mu \approx -6.5$ eV. Similarly, we see in Fig. 2.6 (d) that $\langle M_\nu^z M_{152}^z \rangle$ goes to 0 at $\mu \approx -4$ eV. Figure 2.6 (e) and (f) show that AF correlations between the $m = 153$ and 163'rd states go to 0 at $\mu \approx -6.5$ eV. As seen in Fig. 2.3(a), IBS are filled by electrons at these energy values. Hence, our results show that the antiferromagnetic correlations between the host states and Fe(3d) states diminish rapidly when the IBS are occupied.

It is the important point to note that we identify the new states located at $\mu \approx -6.5$ eV and $\mu \approx -4$ eV as IBS because of μ dependency results in Fig. 2.3, 2.4 and 2.6.

We have also studied the $\langle M_\nu^z M_m^z \rangle$ as a function of μ for host states $m = 166$ and $m = 167$. As seen in Fig. 2.7 (a-c), these host states have antiferromagnetic correlations at Fermi level of deoxy molecule $\mu = -2.8$ eV. These antiferromagnetic correlations diminish rapidly when μ equals to bare energy values of these host states.

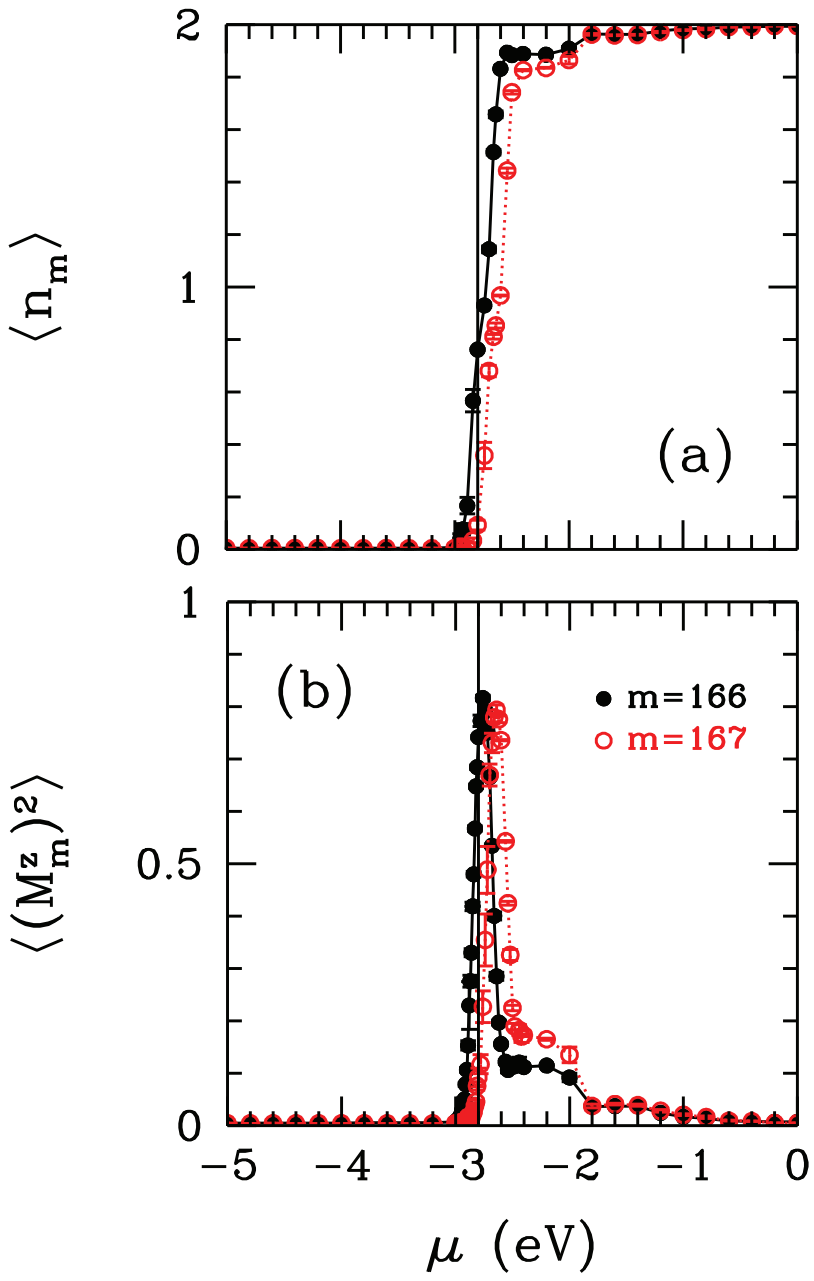

Figure 2.5. QMC results for deoxy on the host electron occupation number and magnetic moments of host orbitals. (a) Electron occupation number of the m'th host state $\langle n_m \rangle$ versus the chemical potential μ. (b) Square of the magnetic moment of the m'th host state $\langle (M_m^z)^2 \rangle$ versus the chemical potential μ. Here, the vertical solid line denotes the Fermi level of molecule. The Fermi level of molecule is obtained by QMC. In addition, these results are for $U = 4$ eV, $J = 0.9$ eV and $T = 300$ K.

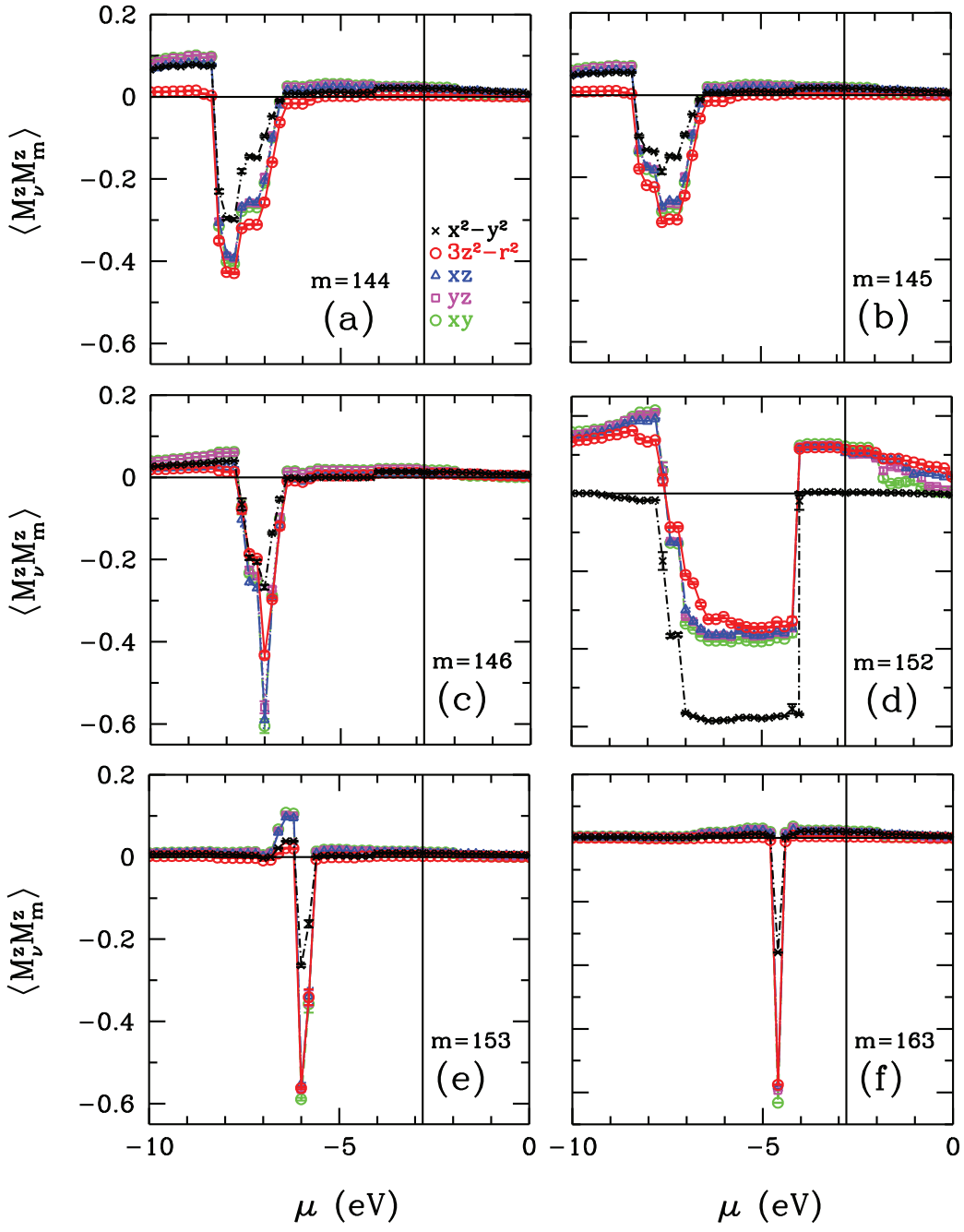

Figure 2.6. QMC results for deoxy on the magnetic correlation function $\langle M_\nu^z M_m^z \rangle$ between the m'th host state and the Fe($3d_\nu$) orbitals. (a) $\langle M_\nu^z M_m^z \rangle$ versus the chemical potential μ for the 144'th host state, (b) for 145'th host state, (c) for 146'th host state, (d) for 152'nd host state, (e) for 153'rd host state and (f) for 163'rd host state The vertical solid line denotes the Fermi level of molecule. The Fermi level of molecule is obtained by QMC. In addition, these results are for $U = 4$ eV, $J = 0.9$ eV and $T = 300$ K.

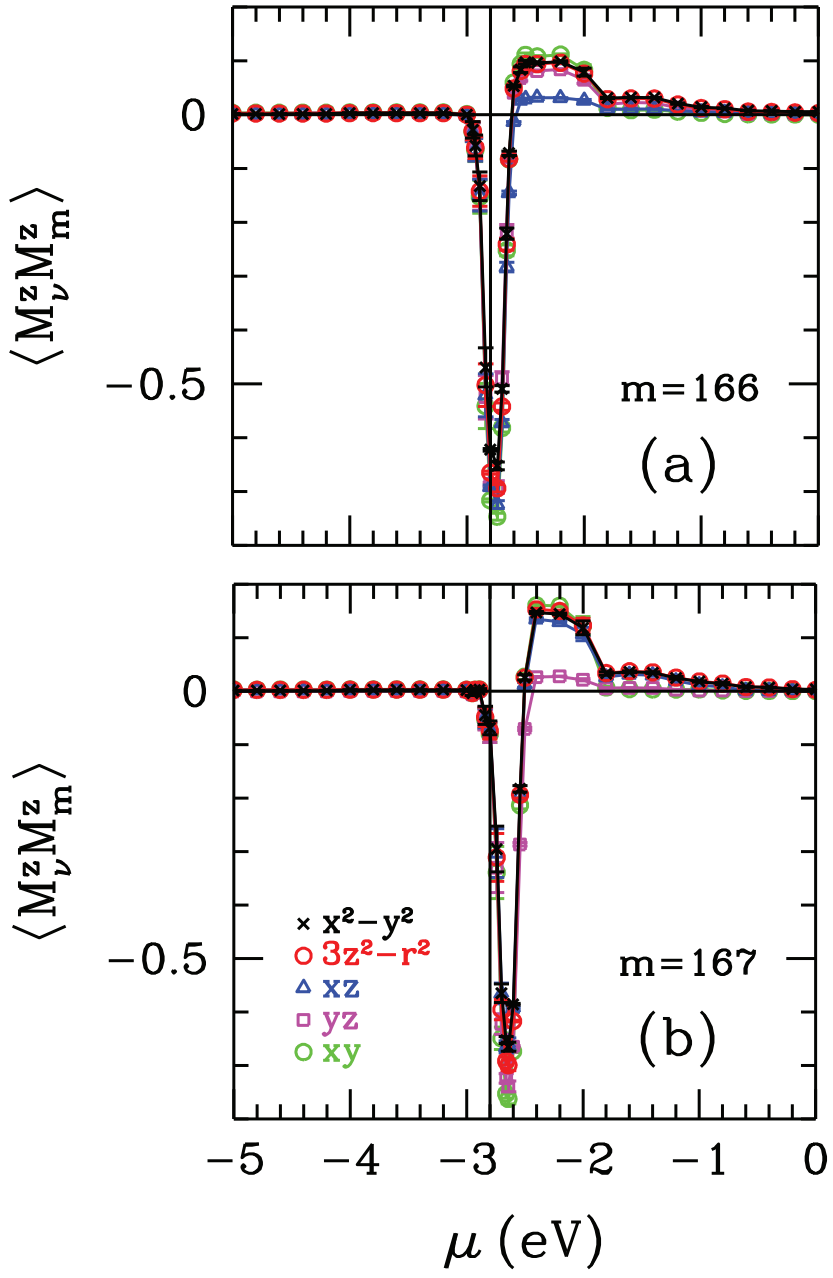

Figure 2.7. QMC results for deoxy on the magnetic correlation function $\langle M_\nu^z M_m^z \rangle$ between the m'th host state and the Fe($3d_\nu$) orbitals. $\langle M_\nu^z M_m^z \rangle$ versus the chemical potential μ (a) for 166'th host state and (b) 167'th host state. The vertical solid line denotes the Fermi level of molecule. The Fermi level of molecule is obtained by QMC. In addition, these results are for $U = 4$ eV, $J = 0.9$ eV and $T = 300$ K.

2.3.2. Impurity bound states for the oxy-heme cluster

In this section, we present the QMC results on $\langle n_\nu \rangle$ as a function of chemical potential μ and $\langle (M_\nu^z)^2 \rangle$ as a function of μ. In addition, we show the magnetic moments of host states and their magnetic correlations with Fe(3d) orbitals. The QMC results for oxy molecule show that the IBS are located above the Fermi level, and so they are unoccupied. This causes that the oxy molecule has low-spin state. AF correlations occur between the Fe(3d) and host states. Different from the results for deoxy molecule, these AF correlations disappear above the Fermi level by the fillings of the IBS.

Figure 2.8 (a) and (b) show the electron occupation number $\langle n_\nu \rangle$ of the Fe($3d_\nu$) and square of magnetic moment $\langle (M_\nu^z)^2 \rangle$ for Fe($3d_\nu$) as a function of μ, respectively. The occupations of xy, xz and yz orbitals change slightly up to $\mu \approx -6$ eV in Fig. 2.8 (a). At $\mu \approx -6$ eV, these orbitals become single occupied. Above this chemical potential, electron number of these Fe(3d) orbitals increase continuously and xy orbital becomes doubly occupied at $\mu \approx -3.8$ eV and, xz and yz orbitals have 2 electrons at $\mu \approx 1$ eV. Similarly, we see that $\langle n_\nu \rangle$ change slightly up to $\mu \approx -5.2$ eV for $3z^2 - r^2$ and $x^2 - y^2$ orbitals. At $\mu \approx -5$ eV and ≈ -1.5 eV, we see sharp increases in the occupation numbers of these three orbitals. We think that these are the energy levels at which impurity bound states are located. Here, the other important point is that at $\mu \approx -1.5$ eV, we see d-d charge transfer. At this chemical potential, while the occupation of yz decreases, the occupations of $3z^2 - r^2$ and $x^2 - y^2$ orbitals increase. The IBS is located $\mu \approx -1.5$ eV and the inter-orbital charge transfer exists at the location of the IBS. This will be very important in explanation of the electronic properties of oxy molecule.

In Fig. 2.8 (b), we observe that $\langle (M_\nu^z)^2 \rangle$ change continuously for Fe(3d) NAO's except $x^2 - y^2$. When the occupations of these orbitals are higher than 1 electron, their magnetic moments start to decrease. On the other hand, in Fig. 2.8 (b), we see the sudden increase in the magnetic moments of $3z^2 - r^2$ and $x^2 - y^2$ orbitals at $\mu \approx -5$ eV and ≈ -1.5 eV as seen in their occupations. Above $\mu = -1$ eV, the magnetic moment of these three orbitals change slightly and $\mu = 3$ eV, it goes to 0 due to double occupancy.

The QMC data on the host electron number $\langle n_m \rangle$ versus μ are presented for the $m = 153$, 154, 158, 159 and 173 host eigenstates in Fig. 2.9 (a). In this figure, we observe that at the chemical potential $\mu = -3.8$ eV, calculated by the QMC, these host states are not doubly occupied. Consequently, these host states have magnetic moments when $\mu = -3.8$ eV and $\mu = -3$ eV as seen in Fig. 2.9(b) for oxy.

This is the important point to note that the host states in deoxy molecule are doubly

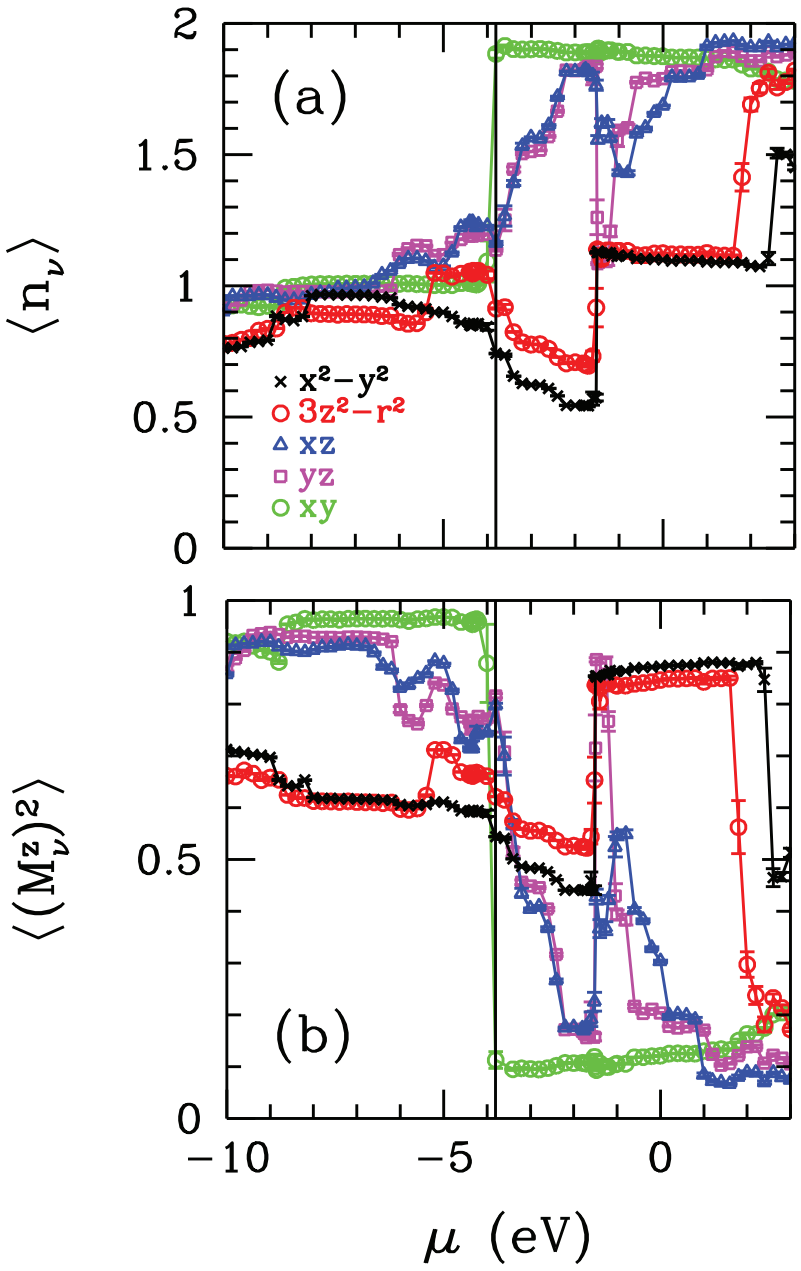

Figure 2.8. QMC results for oxy on the Fe(3d) electron occupation number and Fe(3d) magnetic moments. (a) Electron occupation number $\langle n_\nu \rangle$ of the Fe($3d_\nu$) natural atomic orbitals versus the chemical potential μ. (b) Square of magnetic moment $\langle (M_\nu^z)^2 \rangle$ for Fe($3d_\nu$) natural atomic orbitals versus the chemical potential μ. Here, the vertical solid blue line shows the Fermi level for oxy. The Fermi level of molecules is obtained by QMC. In addition, these results are for $U = 4$ eV, $J = 0.9$ eV and T = 300 K.

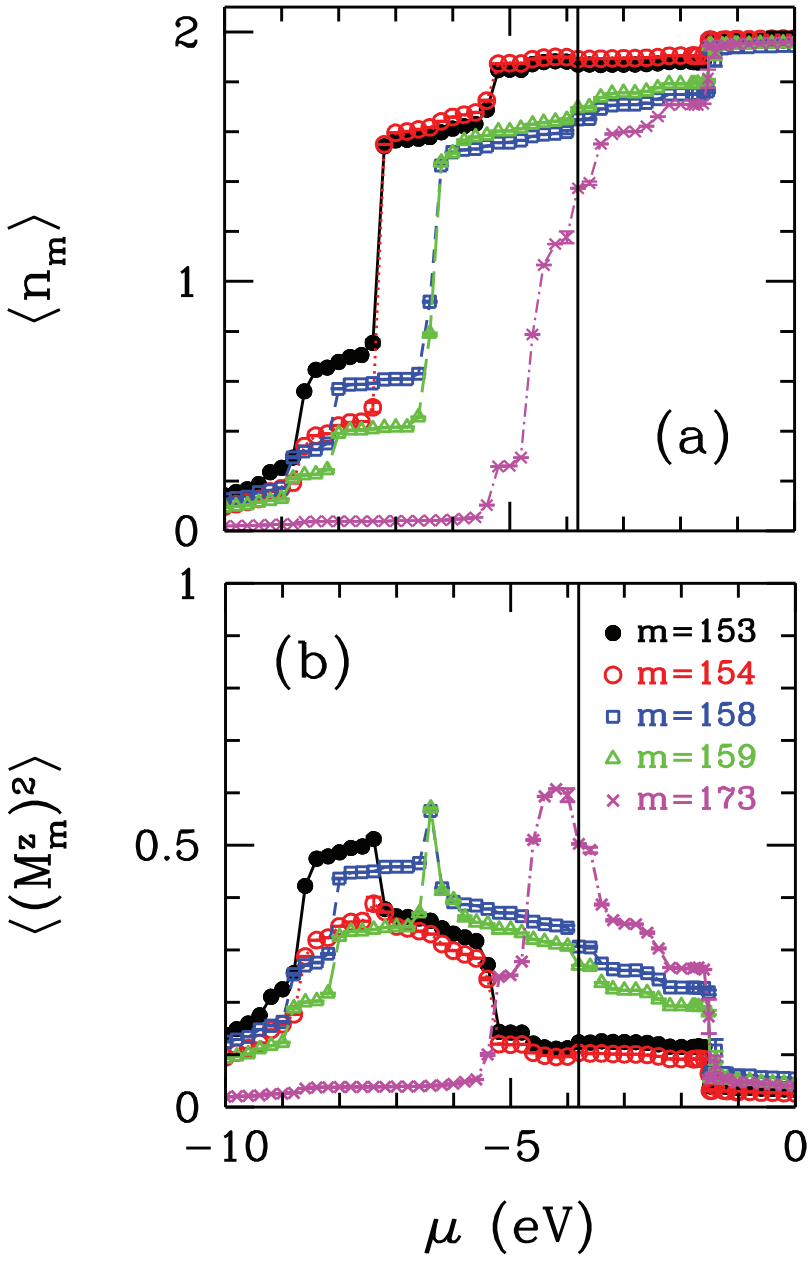

Figure 2.9. QMC results for oxy on the host electron occupation number and magnetic moments of host orbitals. (a) Electron occupation number of the m'th host state $\langle n_m \rangle$ versus the chemical potential μ. (b) Square of the magnetic moment of the m'th host state $\langle (M_m^z)^2 \rangle$ versus the chemical potential μ. Here, the vertical solid denotes the Fermi level for oxy. The Fermi level of molecules is obtained by QMC. In addition, these results are for $U = 4$ eV, $J = 0.9$ eV and $T = 300$ K.

occupied and they do not have magnetic moment as seen in Fig. 2.4 (a) and (b). On the other hand, host states in oxy are not doubly occupied at the chemical potential $\mu = -3.8$ eV, and they have magnetic moments as shown in Fig. 2.9 (a) and (b). This difference between the deoxy and oxy molecules will be crucial point to explaine the high-spin to low-spin mechanism in hemoglobin.

Figure 2.10 (a) and (b) show $\langle n_m \rangle$ and $\langle (M_m^z)^2 \rangle$ as a function of μ for host states $m = 174, 175$ and 176. When μ equals -3.8 eV, they have no any electrons and their magnetic moments are 0. On the other hand, they have magnetic moments at $\mu = -3$ eV. As seen in Fig. 2.10(a), the occupation numbers of these host states are 2 when the μ passes through their energy values. In addition, Figure 2.10(b) shows that $\langle (M_m^z)^2 \rangle$ values goes to 0 at their energy values due to double occupancy.

We also calculate the magnetic correlation function $\langle M_\nu^z M_m^z \rangle$ between the Fe($3d$) NAO's and host states which have the strongest hybridization with the $3d$ orbitals. In Fig. 2.11 (a-e), we discuss $\langle M_\nu^z M_m^z \rangle$ as a function of chemical potential μ for $m = 153$, 154, 158, 159 and 173.

In Fig.2.11(a-e), we observe that antiferromagnetic correlations occur between the Fe($3d$) NAO's and host states $m = 153$, 154, 158, 159 and 173 at the chemical potential of oxy $\mu = -3.8$ eV.

It is the important point that the IBS locate at $\mu \approx -5$ eV and $\mu \approx -1.5$ eV. Different from the deoxy, the IBS are located above the Fermi level in oxy. Moreover, we see from the Fig.2.11 that IBS states are not occupied by electrons and antiferromagnetic correlations occur between the Fe($3d$) NAO's and host states. This situation in oxy differs from deoxy. We know from Fig. 2.6 that IBS locate $\mu \approx -6.5$ eV and -4 eV for deoxy. This means that IBS are below the Fermi level of deoxy molecule, and IBS are occupied. The different situation of occupancy of IBS in deoxy and oxy affects the magnetic properties of hemoglobin molecule, and while deoxy has the high-spin state, oxy has the low-spin state.

We also study the magnetic correlations between the Fe(3d) and $m = 174, 175$ and 176'th host states. Figure 2.12(a-c) shows that when μ equals -3.8 eV, we do not observe any Fe(3d)-host correlations.

In addition to all results for the existence of the IBS, in Fig.2.13, we discuss the total effective magnetic moment of the Fe($3d_\nu$) orbitals $M_{\rm 3d}$, total effective magnetic moment of the host states $M_{\rm h}$, total Fe(3d)-host correlation function $\langle M_{\rm 3d}^{\rm z} M_{\rm h}^{\rm z} \rangle$ and total effective magnetic moment of the molecule $M_{\rm t}^{\rm eff}$ for deoxy-heme and oxy-heme. In these figures, the vertical solid blue line shows the chemical potential for oxy-heme and the

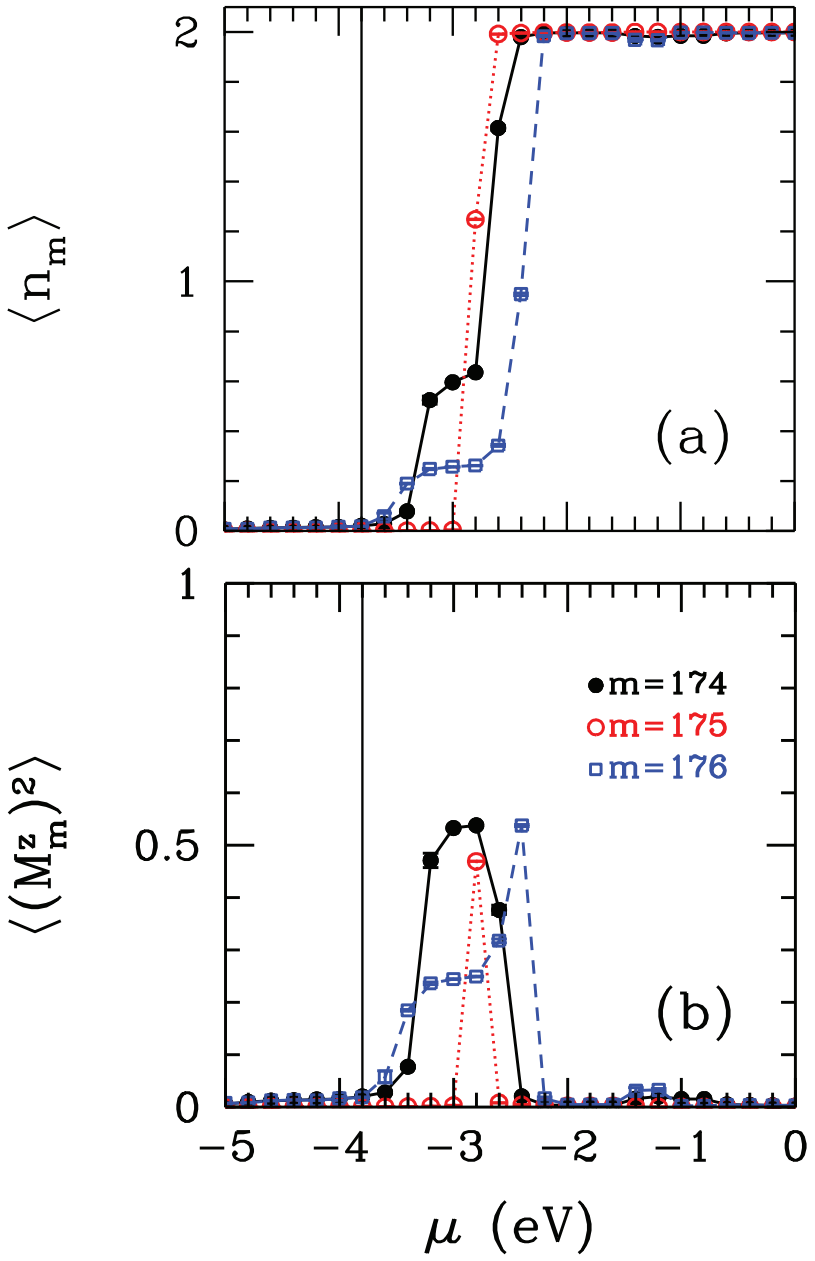

Figure 2.10. QMC results for oxy on the host electron occupation number and magnetic moments of host orbitals. (a) Electron occupation number of the m'th host state $\langle n_m \rangle$ versus the chemical potential μ. (b) Square of the magnetic moment of the m'th host state $\langle (M_m^z)^2 \rangle$ versus the chemical potential μ. Here, the vertical solid denotes the Fermi level for oxy. The Fermi level of molecules is obtained by QMC. In addition, these results are for $U = 4$ eV, $J = 0.9$ eV and $T = 300$ K.

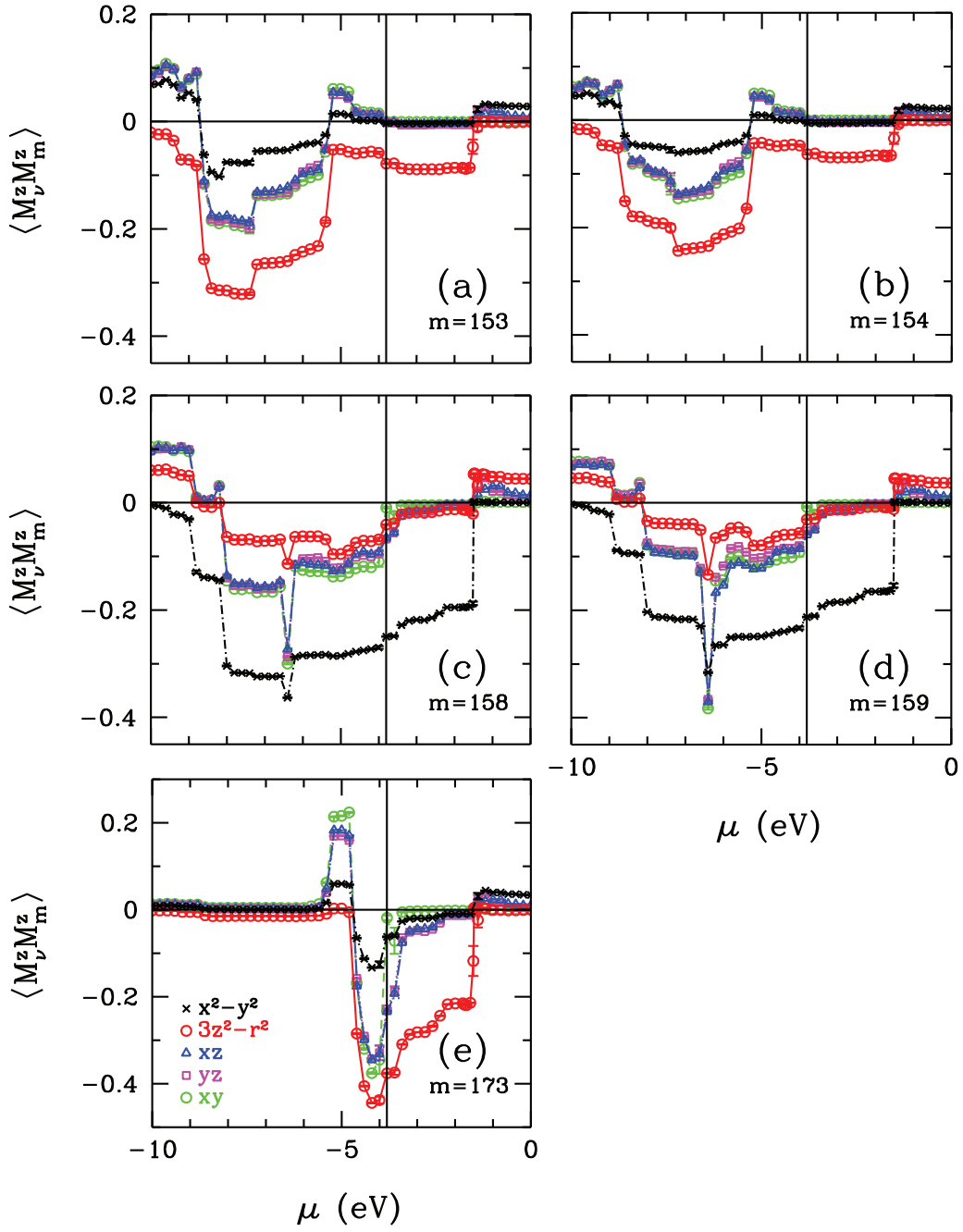

Figure 2.11. QMC results for oxy on the magnetic correlation function $\langle M_\nu^z M_m^z \rangle$ between the m'th host state and the Fe($3d_\nu$) orbitals. (a) $\langle M_\nu^z M_m^z \rangle$ versus the chemical potential μ for $m = 153$rd host state, (b) 154'th host state, (c) 158'th host state, (d) 159'th host state and (e) 173rd host state. The vertical solid denotes the Fermi level for oxy. The Fermi level of molecules is obtained by QMC. In addition, these results are for $U = 4$ eV, $J = 0.9$ eV and $T = 300$ K.

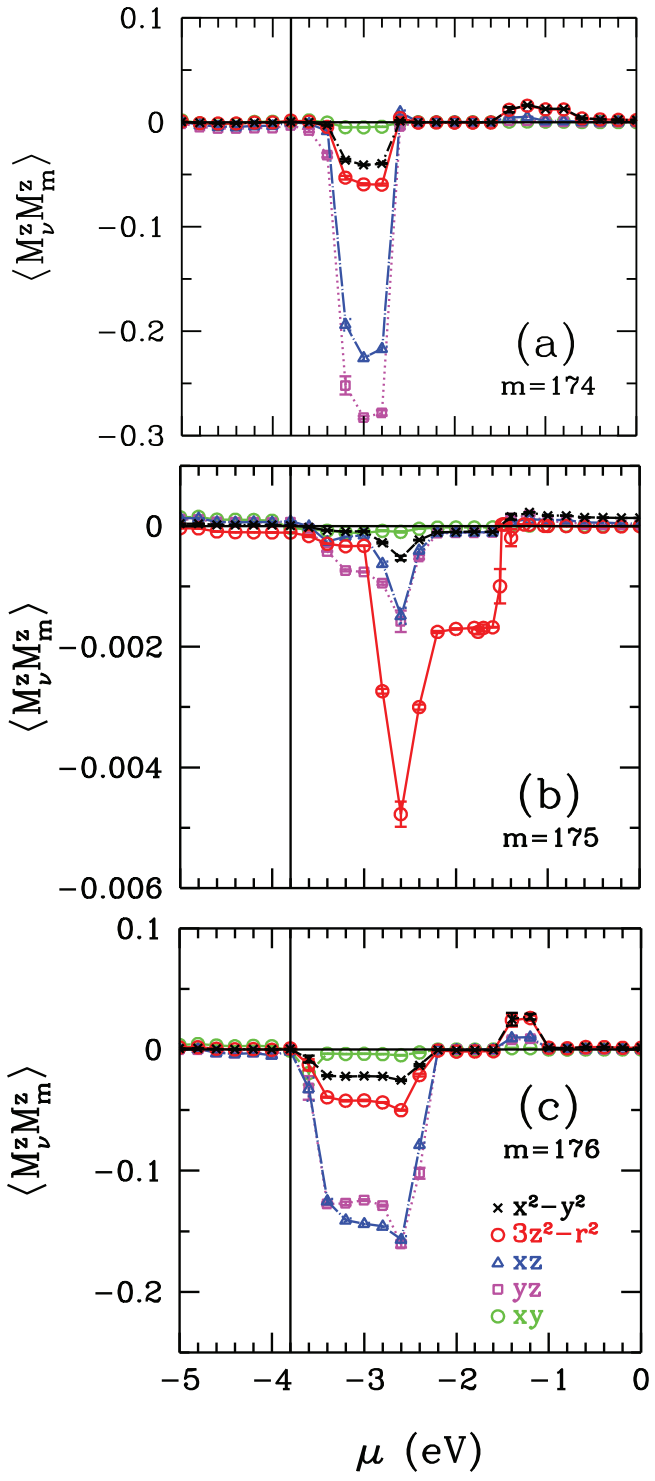

Figure 2.12. QMC results for oxy on the magnetic correlation function $\langle M_\nu^z M_m^z \rangle$ between the m'th host state and the Fe($3d_\nu$) orbitals. (a) $\langle M_\nu^z M_m^z \rangle$ versus the chemical potential μ for $m = 174$'th host state, (b) 175'th host state and (c) 176'th host state. The vertical solid denotes the Fermi level for oxy. The Fermi level of molecules is obtained by QMC. In addition, these results are for $U = 4$ eV, $J = 0.9$ eV and $T = 300$ K.

solid black line shows the Fermi level for deoxy-heme.

Figure 2.13(a) shows the total effective magnetic moments of Fe(3d) orbitals as a function of μ. Here, we see that the M_{3d} does not change up to $\mu = -4$ eV for deoxy. At $\mu = -4$ eV, we see a small jump due to IBS. M_{3d} decreases between the -4 eV $\lesssim \mu \lesssim -3$ eV. For oxy molecule, we see similar jump at $\mu = 1.5$ eV where the IBS are located.

In Figure 2.13(b), the total magnetic moment M_h of host states are shown as a function of μ. Here, we see that host states have magnetic moments in both deoxy and oxy molecules. In addition, we observe in this figure that the total magnetic moments of host states in deoxy is smaller than in and oxy.

We also study the total Fe(3d)-host magnetic correlation function $\langle M^z_{3d} M^z_h \rangle$ for different μ values in Fig. 2.13(c). This figure shows that deoxy has ferromagnetic correlations up to $\mu = -3$ eV. Above this chemical potential, AF correlations occur between the Fe(3d) states due to host states located at near the chemical potential of deoxy. At $\mu \gtrsim -2.2$ eV, ferromagnetic correlations are seen between the Fe(3d) and host states for deoxy. On the other hand, the AF correlations are developed in oxy.

Figure 2.13(d) shows the total magnetic moments M_t as a function of μ for deoxy and oxy. This figure shows that total magnetic moment of deoxy does not change up to $\mu = -3$ eV. Due to AF correlations between the Fe(3d) and host states, M_T decreases in -2.8 eV $\lesssim \mu \lesssim -2.3$ eV. Above $\mu \approx -2.2$ eV, M_T increases. The total magnetic moments of oxy molecule decreases up to $\mu \approx -3$ eV. At $\mu = -3$ eV, it has the minumum value. For deoxy molecule, a jump exist at $\mu = -4$ eV. Similarly, a discontinuity is seen at $\mu = -1.5$ eV for oxy molecule. These are the location of the IBS.

2.3.3. Inter-orbital charge transfer at IBS for oxy-heme cluster

Figure 2.14 shows the electron number of $\langle n_\nu \rangle$ Fe(3d) $\nu = x^2 - y^2$ and $\nu = yz$ states as a function of chemical potential μ. We know from the previous section that IBS is located above the chemical in oxy-heme. As seen in Fig. 2.14, the sudden jump at $\mu \approx -1.5$ in the occupation number of $x^2 - y^2$ orbital corresponds to the IBS. At this energy level, we also see the drop in the occupation number of yz Fe(3d) orbital.

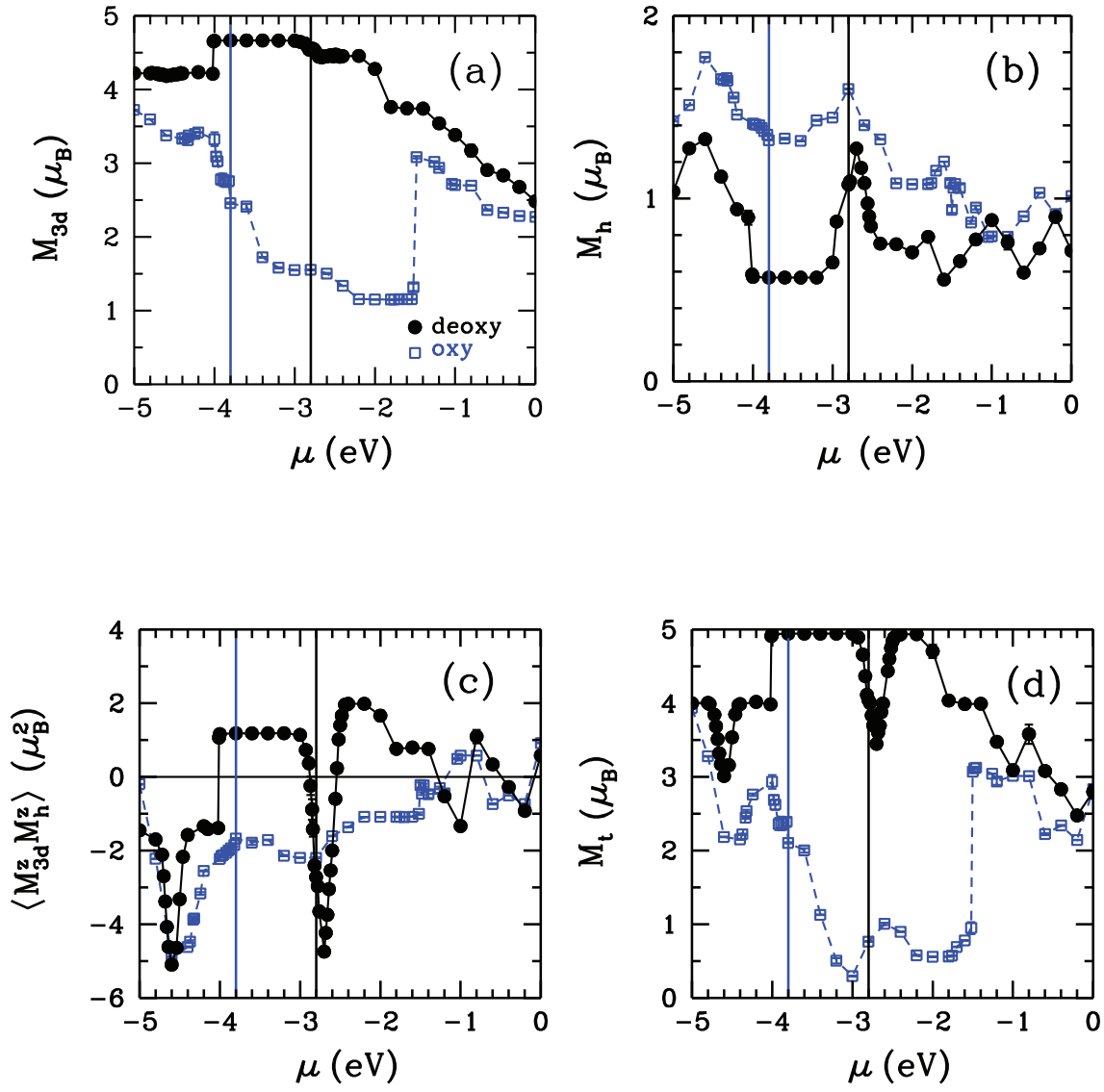

Figure 2.13. (a) Total Fe(3d) magnetic moment M_{3d} versus chemical potential μ. (b) Total host magnetic moment M_h versus μ. (c) Total Fe(3d)-host effective magnetic correlation function $\langle M^z_{3d} M^z_h \rangle$ versus μ. (d) Total effective magnetic moment M_t versus μ. The black circular represents the deoxy and the blue square represents the oxy. Here, vertical solid blue line shows the Fermi level of oxy-heme and the vertical solid black line shows the Fermi level of deoxy-heme. These Fermi level values are obtained by QMC calculations. In addition, these results are for $U = 4$ eV, $J = 0.9$ eV and $T = 300$ K.

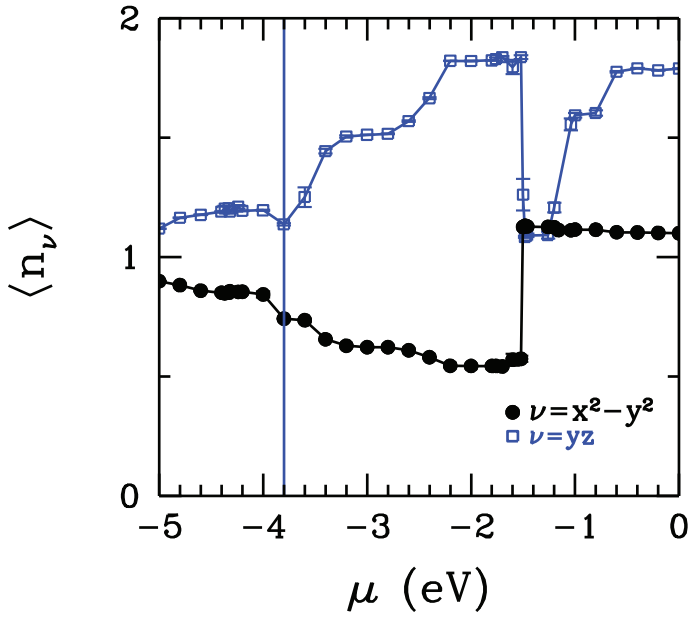

Figure 2.14. Electron occupation number $\langle n_\nu \rangle$ for the Fe(3d) orbitals $\nu = x^2 - y^2$ and $\nu = yz$ versus the chemical potential μ. Here, the blue vertical solid line represents the Fermi level of oxy-heme.

2.3.4. Electron and magnetization density distributions of IBS in the host

In this section, we show the electron density and magnetization density of IBS in the host states for deoxy-heme and oxy-heme. We know from the DFT+QMC results, the IBS is located at -4 eV for the deoxy. On the other hand, the IBS are located at -1.5 eV and -5.5 eV for oxy-heme.

From QMC calculations, we obtain the electron density and magnetization density of the IBS in the host eigenstates. We convert them to obtain the electron and magnetization density distributions in terms of NAO's.

The electron density is calculated from the

$$n_i = \sum_m |u_{mi}|^2 \Delta_m^{\mathrm{IBS}} \tag{2.18}$$

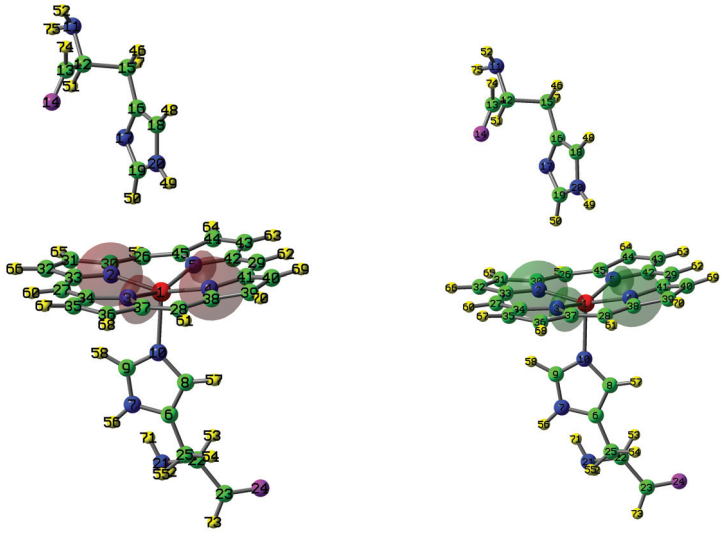

Figure 2.15. For deoxy-heme, (Left) Electron density distribution for the host IBS. (Right) Magnetization density distribution for the host IBS.

where

$$\Delta_m^{\mathrm{IBS}} \equiv \Delta n_m|_{\mu=\omega_{\mathrm{IBS}}} \tag{2.19}$$

The magnetization density is calculated by

$$M_i = \sum_m |u_{mi}|^2 \Delta_m^{\mathrm{IBS}} \tag{2.20}$$

where

$$\Delta_m^{\mathrm{IBS}} \equiv \Delta M_m|_{\mu=\omega_{\mathrm{IBS}}} \tag{2.21}$$

Figure 2.15 shows the electron density distribution and the magnetization density distribution of the IBS at host states for deoxy-heme, respectively. We see from this figure that the host states contribute the IBS are surrounding C and N orbitals. Here, the magnetization densities of these orbitals are shown with the green color. This shows that these states have negative magnetic moments.

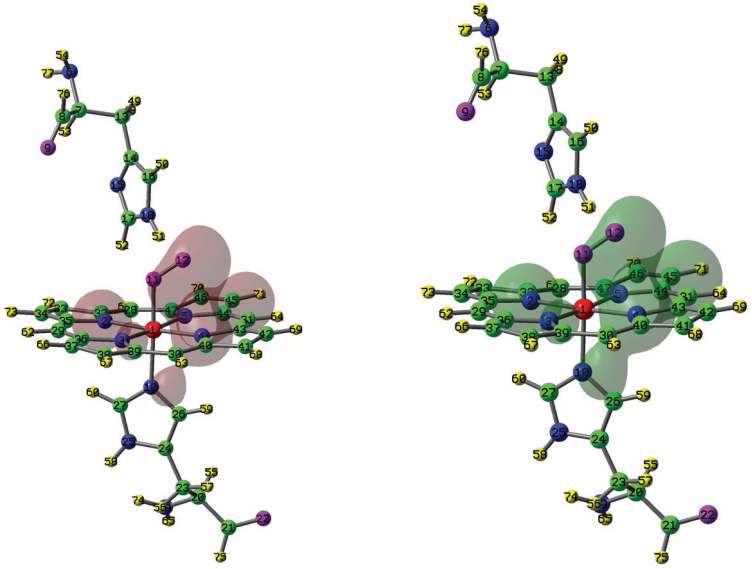

Figure 2.16. For oxy-heme, (Left) Electron density distribution for the host IBS. (Right) Magnetization density distribution for the host IBS. These figures are for the IBS located at -1.5 eV.

Figure 2.16 shows the the electron density distribution and the magnetization density distribution of the IBS at host states for oxy-heme, respectively. We see that the O_2 states contribute the IBS which is located at -1.5 eV. Here, the magnetization density also shows that these host states have the negative magnetic moments.

Figure 2.17 shows the the electron density distribution and the magnetization density distribution of the IBS at host states for oxy-heme, respectively. These figure shows that O_2 do not have any contribution to IBS which is located at -5.5 eV. The magnetization density also shows that these host states have the negative magnetic moments.

2.4. Opening of a magnetic gap at the Fermi level for oxy-heme cluster

Figure 2.18(a-b) shows the total magnetic susceptibility χ_t as a function of temperature T and magnetic moment $M_{\rm t}$ of the oxy-heme cluster as a function of the chemical potential μ around the Fermi level, respectively. We see that $M_{\rm t}$ gets suppressed within $\sim$ 0.1 eV of the Fermi level, as T is reduced. The opening of this gap as T decreases below the crossover temperature $T^* \approx 300$ K arises from the transfer of electrons from

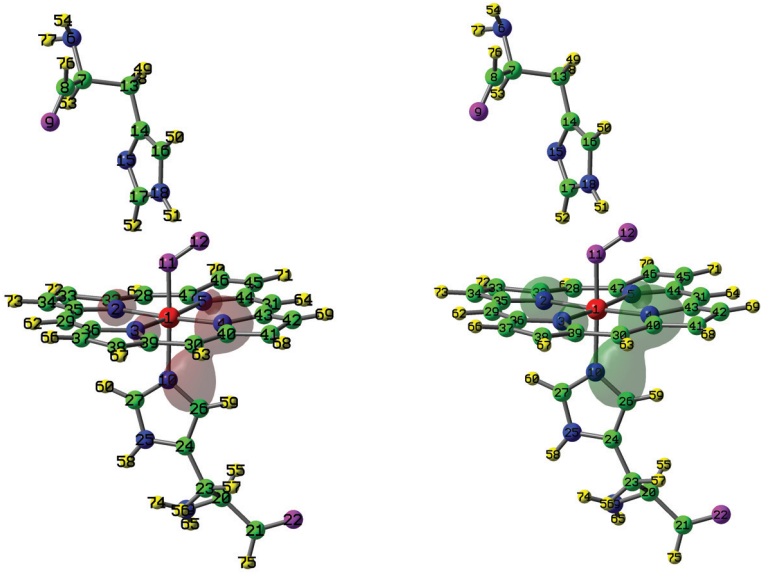

Figure 2.17. For oxy-heme, (Left) Electron density distribution for the host IBS. (Right) Magnetization density distribution for the host IBS. These figures are for the IBS located at -5.5 eV.

mainly the O_2 to the Fe($3d$) orbitals, in particular the Fe($3d_{xy}$) orbital. This is reminiscent of the Kondo effect where a localized magnetic moment in a metallic host gets completely screened by the formation of an antiferromagnetic screening cloud in the host around the impurity. In that case, the metallic host develops a magnetic moment by bringing in an electron from the boundary of the system at infinity. In the case of the oxy-heme cluster, however, we observe that the host develops the screening moment by transfering electrons from mainly the O_2 to the Fe($3d$) orbitals. In particular, a peak with half-width of ~ 0.1 eV develops in the total Fe(3d) electron number at the Fermi level as T decreases below 300 K. We find that as $T \to 0$, the Fe($3d$) magnetic moment $M_{\rm Fe}$ decreases towards ~ 1.7 μ_B, which is the value of a spin $S = 1/2$, while the total effective moment of the host $M_{\rm h}$ increases towards this value. As $T \to 0$, the total spin $S = 0$ state develops because of the antiferromagnetic correlations between $M_{\rm Fe}$ and $M_{\rm h}$.

In Figure 2.19, we observe that the total electron number has strong dependence on temperature. The total electron number of oxy-heme is 350. As seen in this figure, the Fermi level is shifted from -3.8 eV to -3.89 eV when the temperature goes from 300 K to 150 K. Hence, the Fermi level exhibits strong dependence on T.

Figure 2.20(a) shows the total number of electrons in the Fe($3d$) orbitals $\langle n_{3d} \rangle$ plotted as a function of the chemical potential μ at various temperatures. Here, we observe

that a peak of width ~ 0.2 eV develops at the Fermi level as T is lowered.

In Figure 2.20(b), the electron number of the five Fe($3d_\nu$) orbitals $\langle n_\nu \rangle$ versus μ is shown for $T = 200$ K. In addition, the dotted lines represent the electron number of Fe(3d) orbitals at $T = 400$ K. Here, we see that the upper-Hubbard band of the xy orbital is located near the Fermi level at 200 K. On the other hand, it removes from the Fermi level as the temperature increases. The electron numbers of the xz and yz orbitals decrease and the electron numbers of the $3z^2 - r^2$ and $x^2 - y^2$ orbitals increase as T increases.

Figure 2.20(c) shows total magnetic moment of Fe(3d) orbitals, M_{3d} as a function of chemical potential μ. At low T, M_{3d} approaches 1.65 $\mu_{\rm B}$.

Figure 2.20(d) shows the illustration of the wavefunctions for the $m = 171$'st host state. Here, we see that this host state consists of orbitals of O_2 molecules.

Figure 2.21(a-b) shows the electron number of the $m = 171$'st host state $\langle n_m \rangle$ and the magnetic moment of the $m = 171$'st host state M_m as a function of chemical potential μ. Here, we see that as the temperature decreases, the electron number of the 171'st state decreases and its magnetic moment increases. While the electron number of the Fe(3d) orbitals increases, the electron number of the 171'th host orbital decreases as the temperature decreses. Hence, the results show that a charge transfer occurs between the Fe(3d) and O_2 orbitals.

It is the important point that the upper-Hubbard level of the Fe($3d_{xy}$) orbital is located near the Fermi level as seen in Fig. 2.20(b) at low temperature. When the upper-Hubbard level of the $3d_{xy}$ orbital remove from the Fermi level, we do not observe charge transfer from O_2 to Fe(3d) orbitals. Hence, we say that the $S = 0$ state is possible when the upper-Hubbard level of the $3d_{xy}$ orbital is located near the Fermi level.

Additional DFT+QMC results on the electronic and magnetic state of the deoxy-heme cluster are shown in Fig. 2.22(a-c). As seen in Fig. 2.22(a), the electron numbers of the Fe(3d) orbitals equal approximately 1. In Fig. 2.22(b), the total electron number $\langle n_t \rangle$ of the deoxy-heme cluster is shown as a function of μ. Here, we observe that the $\langle n_t \rangle$ does not change as the T decrease. The total magnetic moment of the deoxy-heme cluster $\langle M_t \rangle$ is represented as function of μ for different temperatures. Here, it is seen that $\langle M_t \rangle$ values are the same for various T values at Fermi level. Hence, these results show that as the temperature changes, there are no any significant changes in the measurements for deoxy case.

Table 2.6 shows the number of electrons in the Fe($3d_\nu$) orbitals $\langle n_\nu \rangle$ for the deoxy and oxy cases. In Table 2.6, for the deoxy case, we see that the electron number $\langle n_\nu \rangle$ is close to unity for all five of the 3d orbitals. The total number of the Fe(3d) electrons in

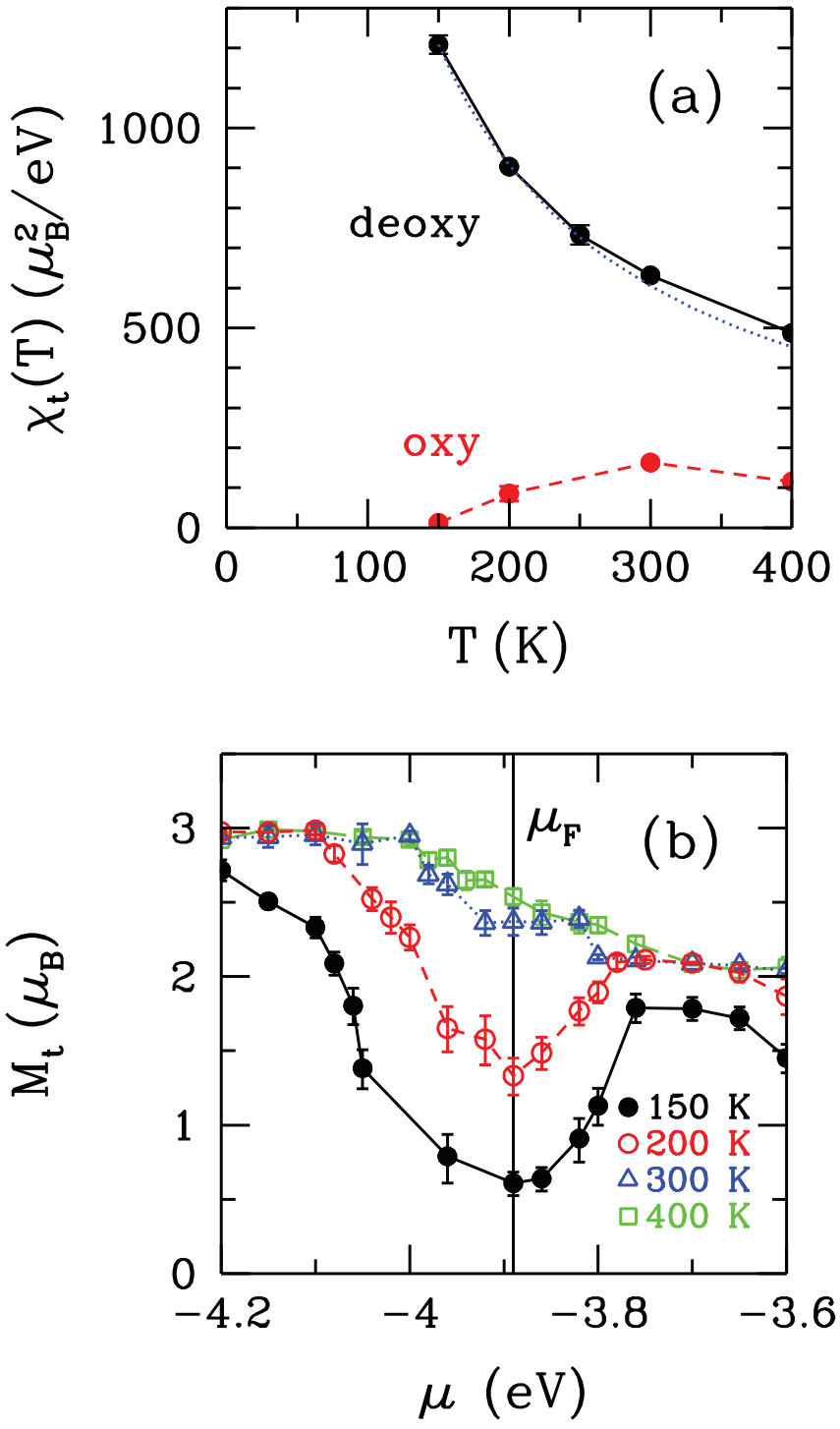

Figure 2.18. (a) Total magnetic susceptibility versus temperature T. Here, the dotted blue line denotes the Curie-type $1/T$ temperature dependence. (b)The total magnetic moment M_t of the oxy-heme cluster is shown as function of μ near the Fermi level. Here, the vertical black solid line represents the Fermi level $\mu_{\rm F}$ at T=150 K.

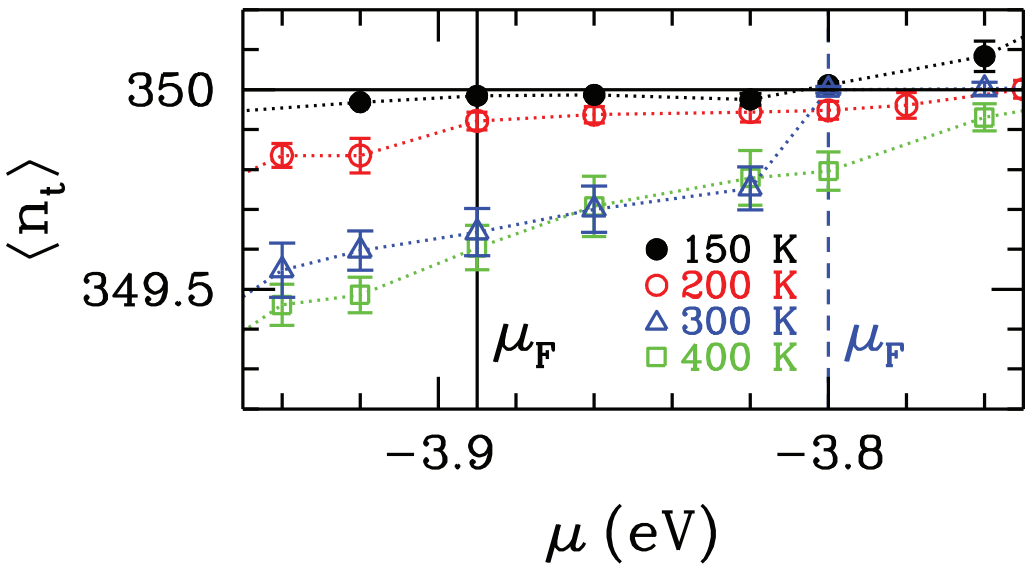

Figure 2.19. The total electron number of the oxy-heme cluster $\langle n_t \rangle$ versus μ at various temperatures. Here, the black vertical line represents the Fermi level μ_F at 150 K and the blue vertical line represents the μ_F at 300 K.

the deoxy case is 5.38, hence Fe is closer to being in the ferric state (+3) than the ferrous state (+2). The corresponding M_ν^{eff} for the Fe(3d) orbitals are slightly less than 1 μ_B as seen in Table 2.7.

For the oxy case, Table 2.6 shows that the electron occupation of the Fe($3d_{xy}$) orbital increases to 1.84 at 300 K, which is close to double occupancy, however the remaining electron numbers remain close to unity. The QMC results show that the total electron number is 5.83 in which case the molecule is close to being in a ferrous state. The magnetic moment of the Fe($3d_{xy}$) orbital drops to 0.40 μ_B in the oxy case as seen in Table 2.7. The remaining orbitals have moments varying between 0.7 μ_B and 0.9 μ_B.

In Table 2.6, the electron numbers of Fe(3d) orbitals are shown for 150 K. Here, we see that as temperature decreases from 300 K to 150 K, the electron number of the xz and yz orbitals increase about 0.2 electrons and the electron number of the xy orbital goes from 1.84 to 1.88. On the other hand, the electron number of $3z^2 - r^2$ and $x^2 - y^2$ orbitals decrease about 0.1 electrons. The total electron number $\langle n_{3d} \rangle$ of the Fe(3d) orbitals goes from 5.83 to 6.07 for the oxy-heme as the T decreases.

Table 2.8 represents the magnetic moments of $3d$ and host states, and total magnetic moments of deoxy and oxy molecules. In addition, we show the Fe(3d)-host magnetic correlations in Table 2.8. We also discuss the total effective spin of 3d orbitals, host orbitals and total spin of molecules. We know that strong ferromagnetic correlations oc-

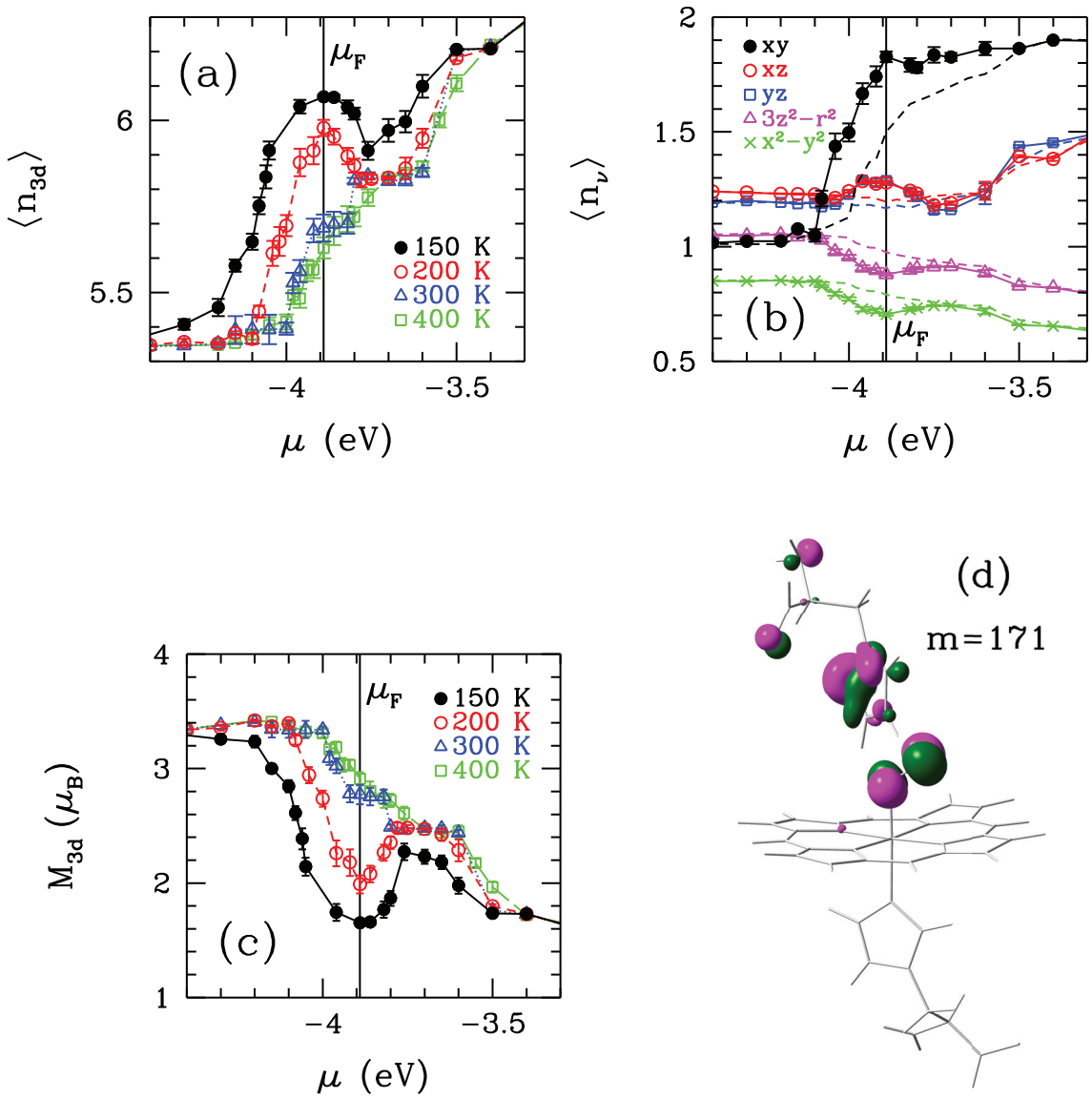

Figure 2.20. For oxy-heme, (a) The total number of electrons in the Fe($3d$) orbitals $\langle n_d \rangle$ plotted as a function of the chemical potential μ at various temperatures. (b) The electron number of the five Fe($3d_\nu$) orbitals $\langle n_\nu \rangle$ versus μ at $T = 200$ K. (c) Total magnetic moment of the Fe($3d$) orbitals M_{3d} versus μ. (d) Illustration of the wave function of the $m = 171$'st host state. Here, the magenta and green colors denote the positive and the negative regions. The vertical black solid line represents the Fermi level μ_F at T=150 K.

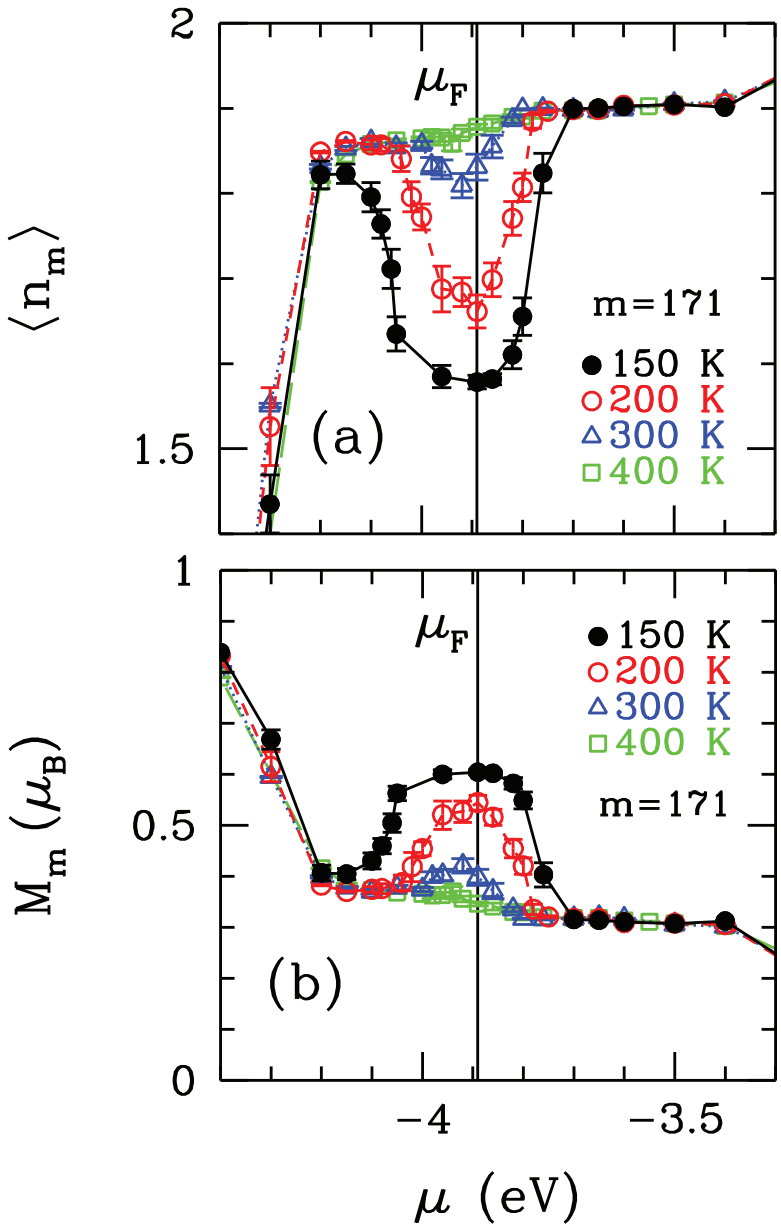

Figure 2.21. For oxy-heme, (a) Electron number of the $m = 171$'st host state $\langle n_m \rangle$ versus μ. (b) Magnetic moment of the $m = 171$'st host state M_m versus μ. Here, the vertical black solid line represents the Fermi level μ_F at T=150 K.

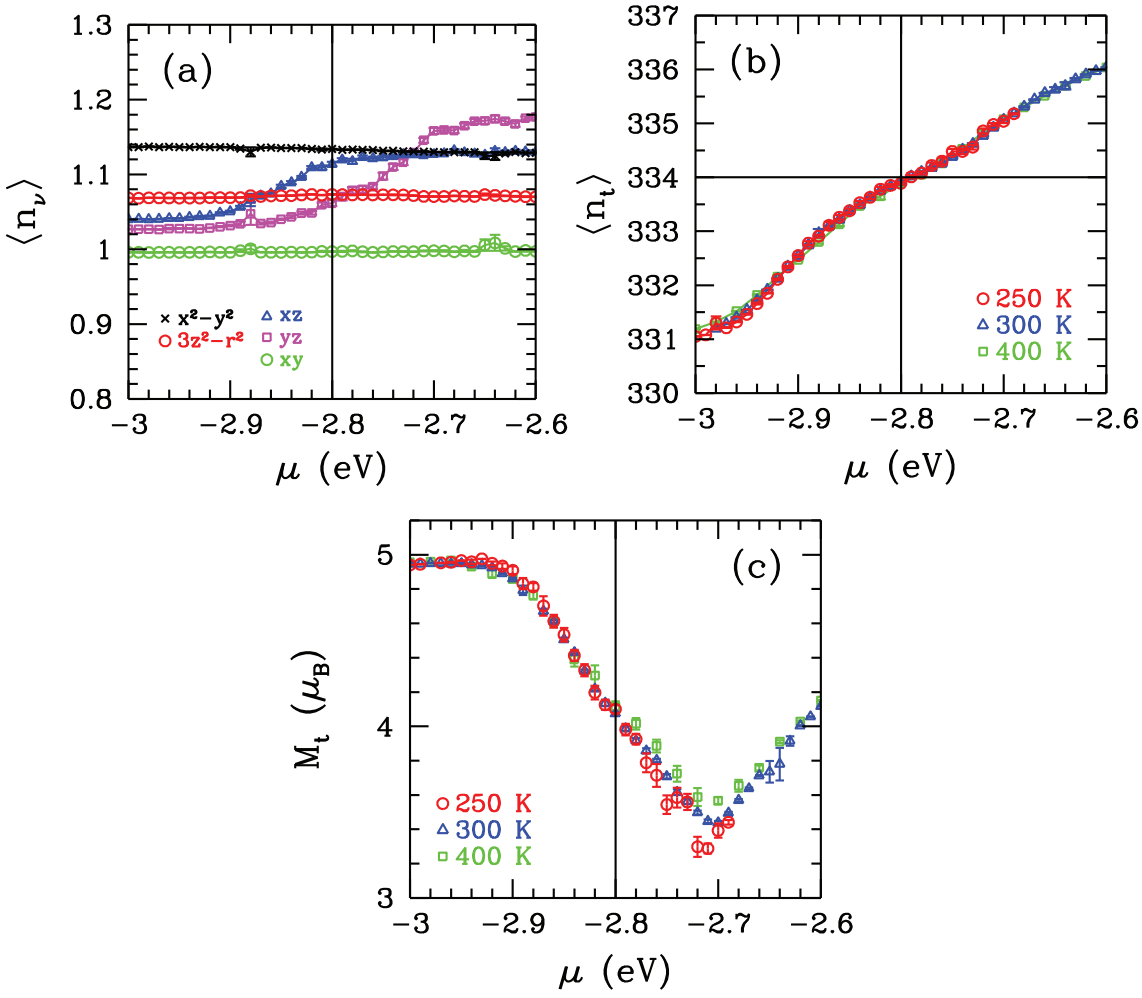

Figure 2.22. For deoxy, (a) The number of electrons in the Fe($3d_\nu$) orbitals $\langle n_\nu \rangle$ plotted as a function of the chemical potential μ at $T = 250\,K$. (b) The total number of the electrons $\langle n_t \rangle$ versus μ for the deoxy-heme cluster at various temperatures. The deoxy-heme cluster with 75 atoms has 334 electrons. This figure shows that the Fermi level located at -2.8 eV is T independent. (c) The total magnetic moment of the deoxy-heme cluster $\langle M_t \rangle$ versus μ at various temperatures. The vertical black solid line denotes the Fermi level at $T = 250$ K.

Table 2.6. Electron occupation numbers $\langle n_\nu \rangle$ of the Fe($3d_\nu$) orbitals for deoxy-heme and oxy-heme cluster. Here, the last column shows the total electron number $\langle n_{3d} \rangle$ of the Fe(3d) orbitals. In this table, the occupation numbers for the oxy-heme cluster are shown for 300 K, 200 K and 150 K. For the deoxy case, the results are only shown for 300 K. Here, $U = 4$ eV and $J = 0.9$ eV.

$\langle n_\nu \rangle$	xy	xz	yz	$3z^2 - r^2$	$x^2 - y^2$	total ($\langle n_{3d} \rangle$)
deoxy (300 K)	1.00	1.12	1.06	1.07	1.13	5.38
oxy (300 K)	1.84	1.17	1.15	0.92	0.75	5.83
oxy (150 K)	1.88	1.32	1.34	0.85	0.68	6.07

Table 2.7. Effective magnetic moments M_ν^{eff} of the Fe($3d_\nu$) orbitals for the deoxy-heme and oxy-heme cluster.In this table, the occupation numbers for the oxy-heme cluster are shown for 300 K and 150 K. For the deoxy case, the results are only shown for 300 K. Here, $U = 4$ eV and $J = 0.9$ eV.

M_ν^{eff} (μ_{B})	xy	xz	yz	$3z^2 - r^2$	$x^2 - y^2$
deoxy (300 K)	0.99	0.93	0.96	0.95	0.93
oxy (300 K)	0.40	0.89	0.89	0.79	0.74
oxy (150 K)	0.35	0.77	0.76	0.77	0.72

cur between the Fe(3d) orbitals due to Hund's coupling in deoxy, and so $S_{\text{3d}}^{\text{eff}}$ equals 1.83 for deoxy. On the other hand, we see weak ferromagnetic correlations between the Fe(3d) in oxy molecule and so its spin state equals 0.85.

As seen in Table 2.8, the host states in three molecules have magnetic moments. M_{h} for oxy is higher than for deoxy. The effective spin of host states are 0.23 and 0.33 for deoxy and oxy, respectively.

We also show the $\langle M_{\text{3d}}^{\text{z}} M_{\text{h}}^{\text{z}} \rangle$ for all molecules. Here, it is seen that Fe-host correlations are ferromagnetic in deoxy and AF in oxy molecules. These AF correlations in oxy suppress the ferromagnetic correlations due to Hund's coupling. Hence, this molecule has lower spin state with respect to deoxy. As shown in Table 2.8, the effective spin of deoxy is 1.60. On the other hand $S_{\text{t}}^{\text{eff}}$ is 0.68 for the oxy.

We see strong ferromagnetic correlations between the Fe($3d_\nu$) orbitals in deoxy. Due to this ferromagnetic correlations, Fe atom in deoxy has the high-spin state. On the other hand, the weak ferromagnetic correlations occur between the Fe(3d) orbitals in oxy. Hence, this molecule has lower spin state than deoxy-heme.

In Table 2.8, we also show the results for different temperatures. As seen in Table

Table 2.8. DFT+QMC results on the total Fe(3d) magnetic moment M_{3d} in μ_B, total effective spin of Fe(3d) electrons S_{3d}^{eff}, total host magnetic moment M_h in μ_B, total effective spin of host electrons S_h^{eff}, total Fe(3d)-host effective magnetic correlation function $\langle M_{3d}^z M_h^z \rangle$, total effective magnetic moment M_t in μ_B and total effective spin of molecule S_t^{eff} for deoxy and oxy. In addition, total effective spin S^{eff} is calculated by $M = 2\sqrt{S^{eff}(S^{eff}+1)}$. For the deoxy-case, the results are shown only for 300 K. For the oxy-case, 300 K and 150 K results are presented. Here, $U = 4$ eV and $J = 0.9$ eV.

	M_{3d}	M_h	$\langle M_{3d}^z M_h^z \rangle$	M_t	S_{3d}^{eff}	S_h^{eff}	S_t^{eff}
deoxy (300 K)	4.56	1.06	-2.65	4.07	1.83	0.23	1.60
oxy (300 K)	2.50	1.32	-1.71	2.13	0.85	0.33	0.68
oxy (150 K)	1.65	1.50	-2.30	0.61	0.47	0.40	0.10

2.8, the total magnetic moment and the total effective spin are decreased by the decreasing of temperature. Also, the results presented in this table show that the magnetic moment of host states increase and the magnetic correlations between the Fe(3d) and host states are more negative. The reason is the opening of the magnetic gap at the Fermi level and the Fe(3d)-O_2 charge transfer. The antiferromagnetic correlations between the Fe(3d) and O_2 states increase and the total magnetic moment is lowered. Hence, the total spin goes to 0 for T<300 K.

CHAPTER 3

MCD SPECTRUM OF THE DEOXY-HEME CLUSTER

The DFT+QMC results show that the antiferromagnetic (AF) correlations occur between the Fe(3d) and porphyrin layer. The magnetic circular dichroism (MCD) data on deoxy-HbA is the experimental evidence for this AF correlations.

The MCD intensity $\Delta\epsilon(E)$ is obtained from the differences between the left-circularly polarized (LCP) and the right-circularly polarized (RCP) light absorption. The light propagates in an external magnetic field and the magnetic field points along the direction of light as shown in Fig. 3.1 (a).

Treu and Hopfield showed that the MCD spectrum of deoxy-HbA has a peak near 3 eV and this peak has $1/T$ temperature dependence (Treu and Hopfield (1975)). The usual temperature dependent MCD spectrum first has a dip and then a peak as the frequency increases. On the other hand, in deoxy-HbA the MCD spectrum first has a peak and then a shallow dip. The origin of this anomalous line shape has been debated since its discovery.

The optical absorption spectrum also has a peak at the same energy called Soret band due to $\pi \rightarrow \pi^*$ transitions. Here, π is the bonding and π^* is the antibonding orbitals of the porphyrin layer.

In this thesis, we propose that the anomalous line shape of deoxy-heme originates from the AF correlations between the Fe(3d) and partially filled π^* states of the porphyrin layer. The MCD signal comes from the optical transitions from the occupied π orbitals to two partially occupied π^* orbitals. The DFT+QMC results show that π_1^* is half-filled and π_2^* is nearly empty. In addition, we see that the coupling between the π^* orbitals and Fe(3d) moment about 0.1 eV. This is greater than any applied magnetic field.

3.1. Our proposal for the MCD spectrum of the deoxy-heme cluster

In this section, we explain our proposal for the MCD spectrum of the deoxy-heme cluster. For this explanation, we add a spin-orbit coupling term to impurity model. This term acts at the Fe(3d) orbitals. While the π and π^* states do not have a significant spin-orbit coupling, they can gain an effective coupling through hybridization with the Fe(3d)

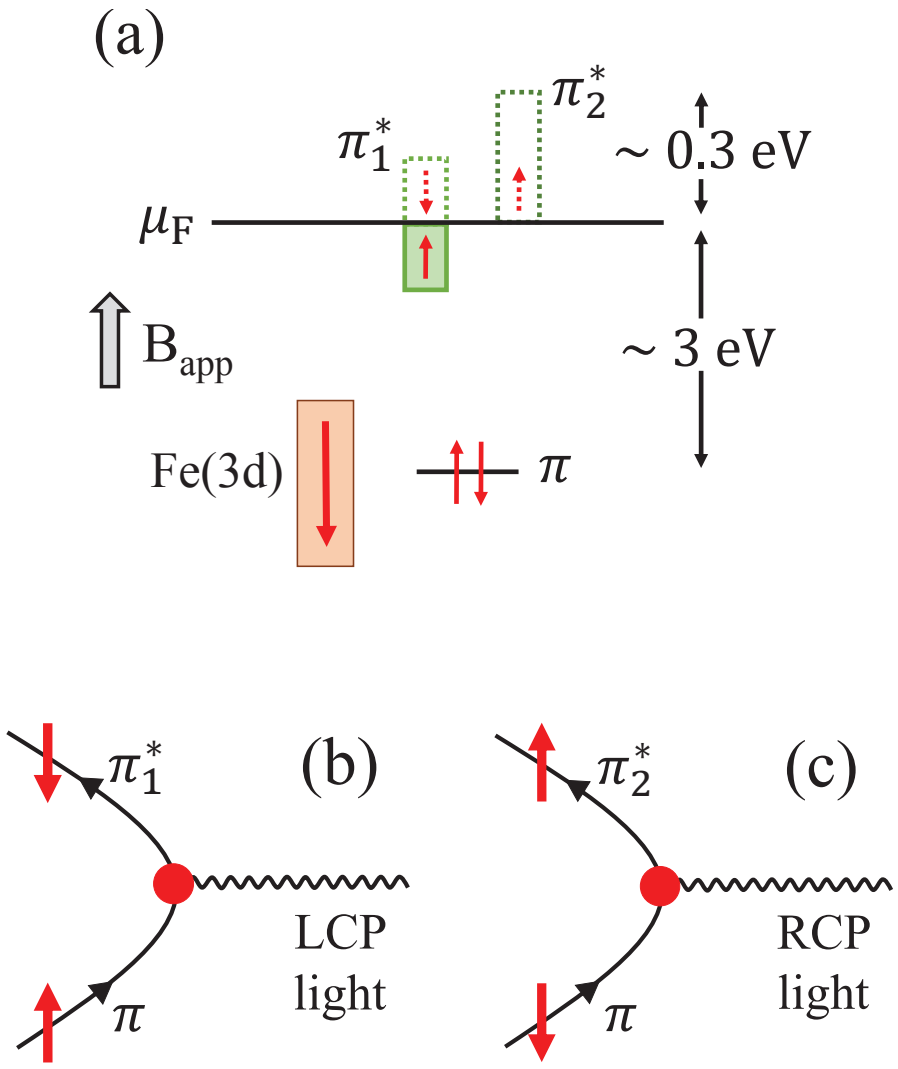

Figure 3.1. (a) The magnetic polarizations of various states are sketched. (b) Feynman diagram represents the absorption of left-circularly polarized (LCP) light. (c) Feynman diagram represents the absorption of right-circularly polarized (RCP) light.

orbitals.

As illustrated in Fig. 3.1(a), in an applied field which is in the up direction, the Fe spin will be polarized in the down direction, while the spin of the π_1^* state will be along the field. Hence, during an optical transition from the π state, it will be energetically more favourable for the π_1^* state to absorb a down electron. On the other hand, for the nearly-empty π_2^* state it will be more favorable to absorb an up electron. We note that even though the π state does not have a spin-orbit coupling (SOC), it can gain an effective spin-orbit coupling because of hybridization and the subsequent magnetic correlations with the Fe($3d$) orbitals which have SOC. Because of the effective SOC of the π state, an up-spin π electron can make a transition to the empty π_1^* state becoming a down-spin electron upon absorbing left-circularly-polarized (LCP) light, as illustrated in Fig. 3.1(b) as a Feynman diagram. It would not be energetically favorable for the up-spin π electron to move to the π_2^* state. However, upon absorbing right-circularly-polarized (RCP) light, it would become favorable for a down-spin π electron to make a transition to the up-spin π_2^* state, which is illustrated in Fig. 3.1(c). Hence, it is energetically more favorable for LCP (RCP) light absorption to cause a $\pi \rightarrow \pi_1^*$ ($\pi \rightarrow \pi_2^*$) transition.

The π and π^* host states consist of the bonding and antibonding C($2p_z$) orbitals and we show the wave functions of these π and π^* states in Fig. 3.2.

While the π states do not have significant spin-orbit coupling, they can gain an effective coupling because of antiferromagnetic correlations and hybridization with the Fe($3d$) orbitals. This process is shown in Fig. 3.3. In the top figure of Fig. 3.3, an up-spin electron in the π state can become an up-spin $3d$ electron through hybridization. Because of the spin-orbit coupling at the Fe site, this up-spin $3d$ electron can now flip its spin down. Through hybridization for a second time, it then becomes a down-spin π electron. Here, V is the hybridization matrix element between the π state and the Fe($3d$) orbitals, and λ is the spin-orbit coupling constant for the Fe($3d$) orbitals. Because of this process, an electron in a π state can gain an effective spin-orbit coupling λ' as shown in the bottom part of the Fig. 3.3.

Figure 3.4 illustrates our proposal for the mechanism for MCD in the Soret region. This figure shows the left-circularly light absorption process in Soret MCD where there is an applied magnetic field in the up direction. The left panel shows the initial state. In this case, the Fe(3d) orbital hybridizing with the bonding π state is occupied by one down electron, while the π state is doubly occupied. The antibonding π_1^* state is occupied by one up electron because of antiferromagnetic exchange coupling to the Fe(3d) spin. In the intermediate state (middle panel), with LCP light absorption one down electron

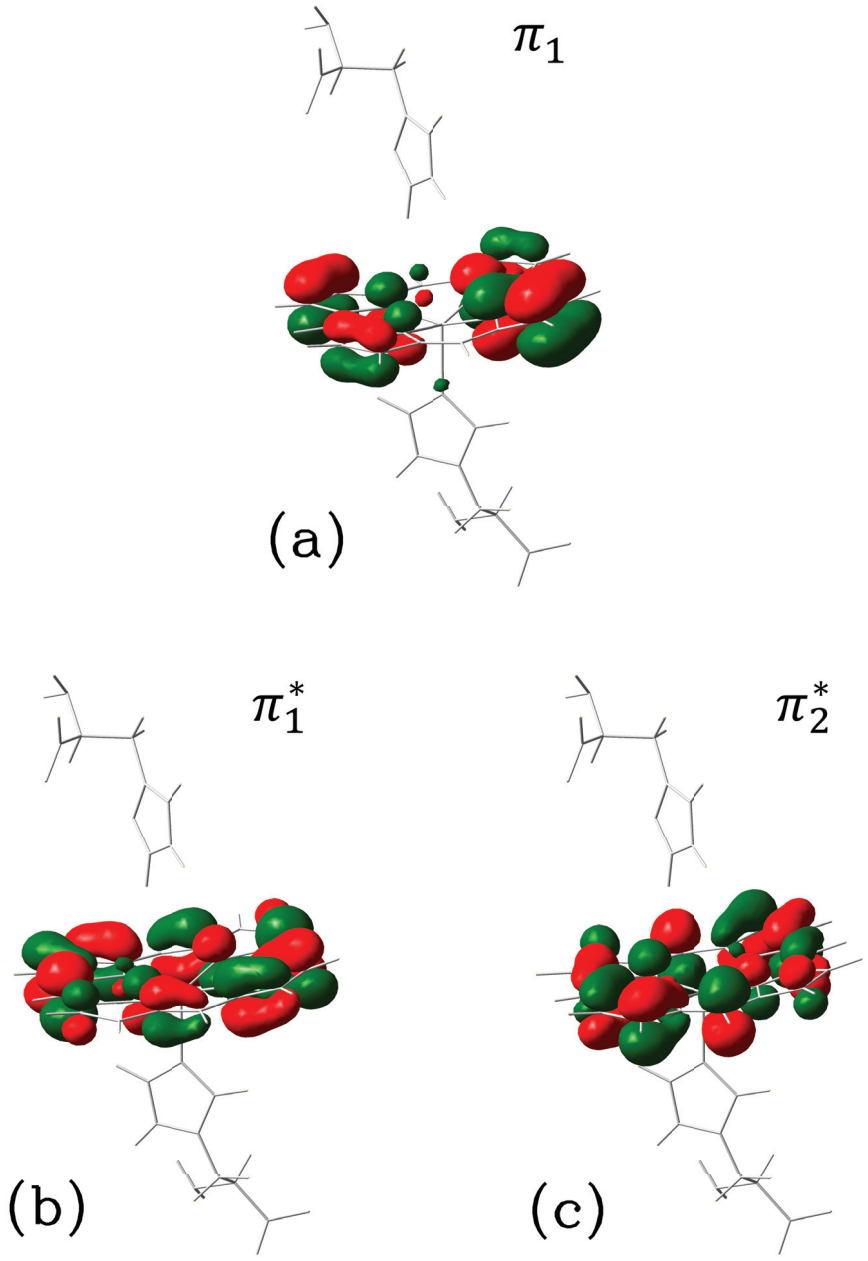

Figure 3.2. Host wave functions are shown in terms of the atomic orbitals. (a) Wavefunction of the π_1 host state, which is a bonding $2p_z$ orbitals of the C atoms in the porphyrin layer. (b) and (c) Wavefunctions of the antibonding π_1^* and π_2^* host states, respectively.

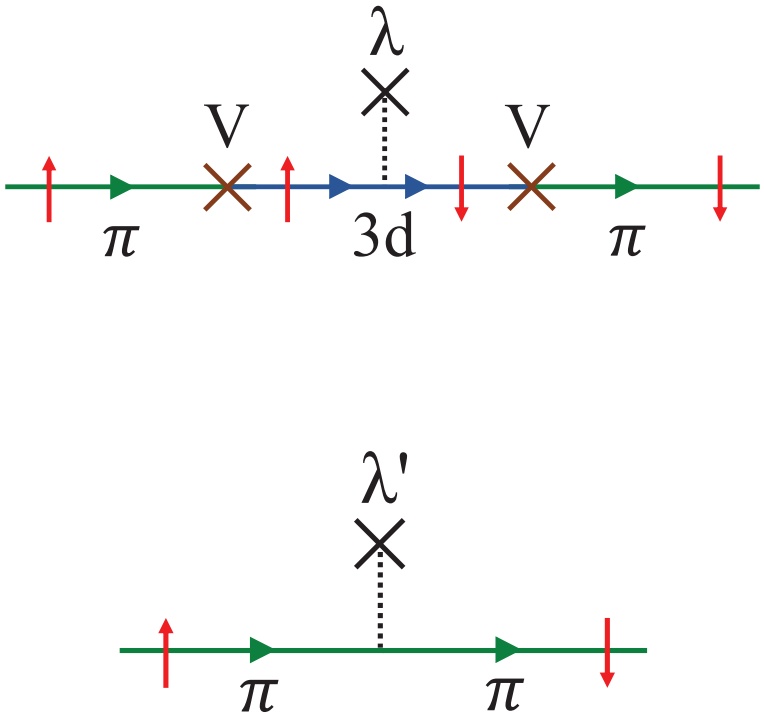

Figure 3.3. (Top) This Feynman diagram illustrates that an electron in a bonding π state can gain an effective spin-orbit coupling through the hybridization. Here, and up-spin electron in the π state can become an up-spin $3d$ electron through hybridization. Here, V is the hybridization matrix element between the π state and the Fe(3d) orbitals, and λ is the spin-orbit coupling constant for the Fe(3d) orbitals. (Bottom) This Feynman diagram shows that an electron in the π state can gain an effective spin-orbit coupling λ'.

located in the π state moves to the π_1^* state, and the up-spin electron in the π state spin-flips with the Fe(3d) down-spin electron through antiferromagnetic exchange. Next, the up-spin electron in the Fe(3d) orbital flips its spin one more time because of the spin-orbit coupling, which leads to the final state shown in the right panel. Here, the π state is located about 3 eV below the Fermi level, and the widths of the π_1^* and π_2^* states are about 0.3 eV. There is a similar process where an RCP light absorption causes a transition of a down-spin π electron in the initial state to make a transition to an up-spin π_2^* electron in the final state. Hence, in this scenario we are suggesting, the Soret MCD transitions are spin and orbital selective.

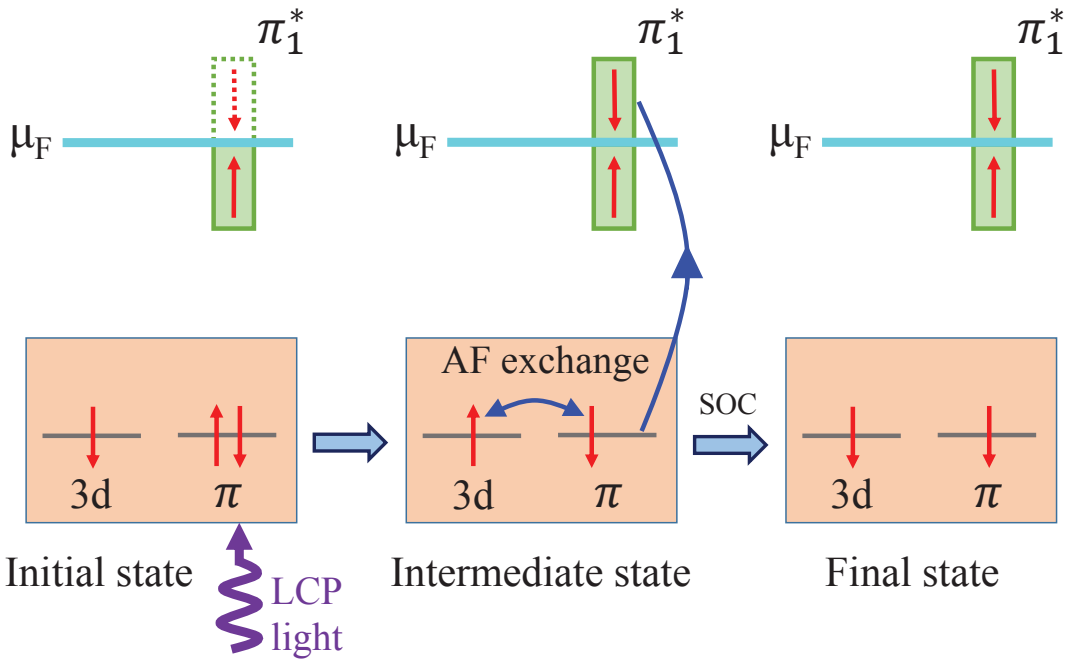

Figure 3.4. These figures illustrate the left-circularly polarized (LCP) light absorption process in MCD for an applied magnetic field pointing in the up direction, which is in the direction of light propagation. The left panel shows the initial state, the middle panel is the intermediate state and the last one is the final state.

3.2. Calculation of the MCD spectrum in UV region for deoxy-heme cluster

According to the MCD mechanism outline above, the temperature-dependent Soret MCD spectra arises from transitions $\pi \rightarrow \pi_1^*$ with LCP light and $\pi \rightarrow \pi_2^*$ with RCP light. We note that while there are a number of bonding π states which can cause transitions near 3 eV, the main transitions arise from one of these which we labelled as the π_1 state. This scenario leads to the following equation for the temperature-dependent MCD spectra in the Soret region,

$$\Delta I(E) = \sum_m \Big(C_1 \quad |\langle \pi_1^* | \mathbf{p} | m \rangle|^2 \, A_{\pi_1^*}(\epsilon_m + E) \qquad (3.1)$$

$$- \quad C_2 \, |\langle \pi_2^* | \mathbf{p} | m \rangle|^2 \, A_{\pi_2^*}(\epsilon_m + E) \Big) f(\epsilon_m)(1 - f(\epsilon_m + E)).$$

Here, m sums over the bonding π states, and ε_m is the energy of the m'th π state. In addition, $f(\epsilon_m)$ is the Fermi-Dirac distribution.

The QMC data on the host states π_1^* and π_2^* are displayed in Fig. 3.5 (a)-(b) and in Fig. 3.6(a-b). The spectral weights $A(\omega)$ for π_1^* and π_2^* have been obtained by taking the derivative of $\langle n \rangle$, shown in Fig. 3.5 (a), with respect to μ. The single-particle spectral weights $A_{\pi_1^*}(\omega)$ and $A_{\pi_2^*}(\omega)$ of the π_1^* and π_2^* states, respectively, are shown in 3.5 (b). Clearly this is an approximate way for obtaining the spectral function since it assumes that there is no spectral weight transfer as μ changes. Figure 3.6 (a) shows the square of the magnetic moment $\langle (M^z)^2 \rangle$ for the π_1^* and π_2^* states. Figure 3.6 (b) shows the magnetization correlation function $\langle M_{3d}^z M_m \rangle$ between the Fe(3d) magnetic moment and the moment of the host state $m = \pi_1^*$ and π_2^*. Here, we clearly see the antiferromagnetic coupling of the π^* orbitals to the Fe(3d) moment.

In the above expression for $\Delta I(E)$ we have used the electric-dipole transition matrix element $|\langle m'|\mathbf{p}|m\rangle|^2$, instead of $|\langle m'|p_-|m\rangle|^2$ or $|\langle m'|p_+|m\rangle|^2$, where $p_\pm = p_x \pm i p_y$. This is because the optical absorption and the MCD measurements (Treu and Hopfield (1975)) were taken using a sample in a solution, where the **z**-axis of the molecule will have a random angle with the direction of the applied magnetic field. In this case, it is necessary to perform an averaging over all directions.

We have taken the ratio C_1/C_2 to be 4. This reflects the strength of the magnetic correlations of the Fe(3d) total spin to the spin of the electron placed into the π_1^* and π_2^* in the final state of the optical absorption illustrated in Fig. 3.4. Since π_1^* is already occupied by one up-spin electron and π_2^* is nearly empty, we expect the C_1 to be larger than C_2. Instead of estimating C_1/C_2 microscopically, we have used this ratio as a fitting parameter. Actually, it is the only fitting parameter we use in obtaining the spectra. We find that the MCD curve passes through zero at 3 eV, while the experimental value for this is 2.94 eV.

3.3. Comparison of the MCD and the optical absorption data in the UV region for deoxy heme cluster

We have calculated the MCD spectrum for the deoxy-heme cluster based on these orbital selective optical transitions. Here, Figures 3.7(a) and 3.7(b) present the experimental and the calculated MCD spectrum for the deoxy case, respectively. In Fig. 3.7(a), the inset figure represents the normally expected line shape of the temperature-dependent

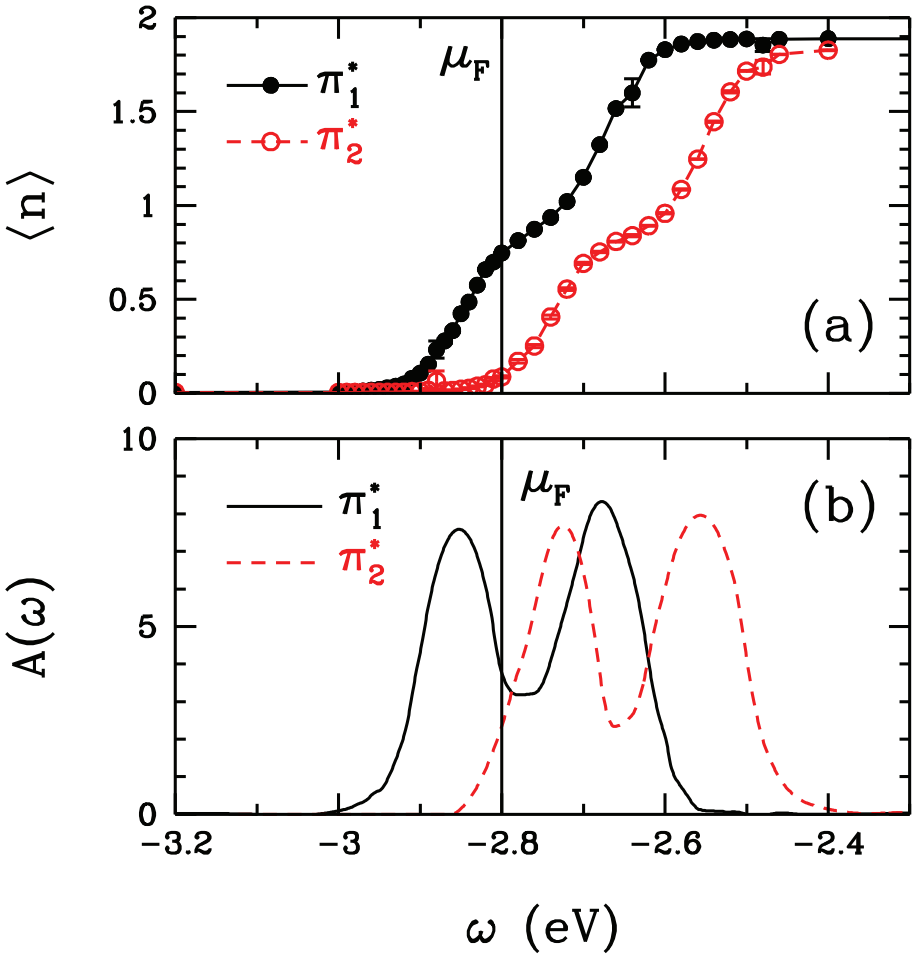

Figure 3.5. (a) Electron occupation $\langle n \rangle$ of the π_1^* and π_2^* host states plotted as a function of the chemical potential μ. Here, the Fermi level is located at μ_F. (b) Single-particle spectral weight $A(\omega)$ versus ω obtained from the $\langle n \rangle$ versus μ plot shown in (a). Here, the vertical black line represents the Fermi level, $\mu_{\rm F}$.

MCD spectrum (Mason (2007)). As seen here, for the expected situation, spectrum first has a dip and then a peak. The anomalous lines shape of the MCD spectrum of the deoxy-HbA shows opposite behaviour with respect to expected spectrum and it has first a peak and then a dip. We are suggesting that the anomalous line shape originates from the antiferromagnetic coupling between the large Fe($3d$) magnetic and the spin of the π^* host states. Figure 3.7(a-b) show that the experimental MCD spectrum and the calculated MCD spectrum is in good agreement.

In order to show the agreement with the experiment, we also calculate absorption spectrum and we compare it with the experimental results. Figure 3.8(a) shows experimental results on the optical absorption of deoxy-heme by Treu and Hopfield (Treu and

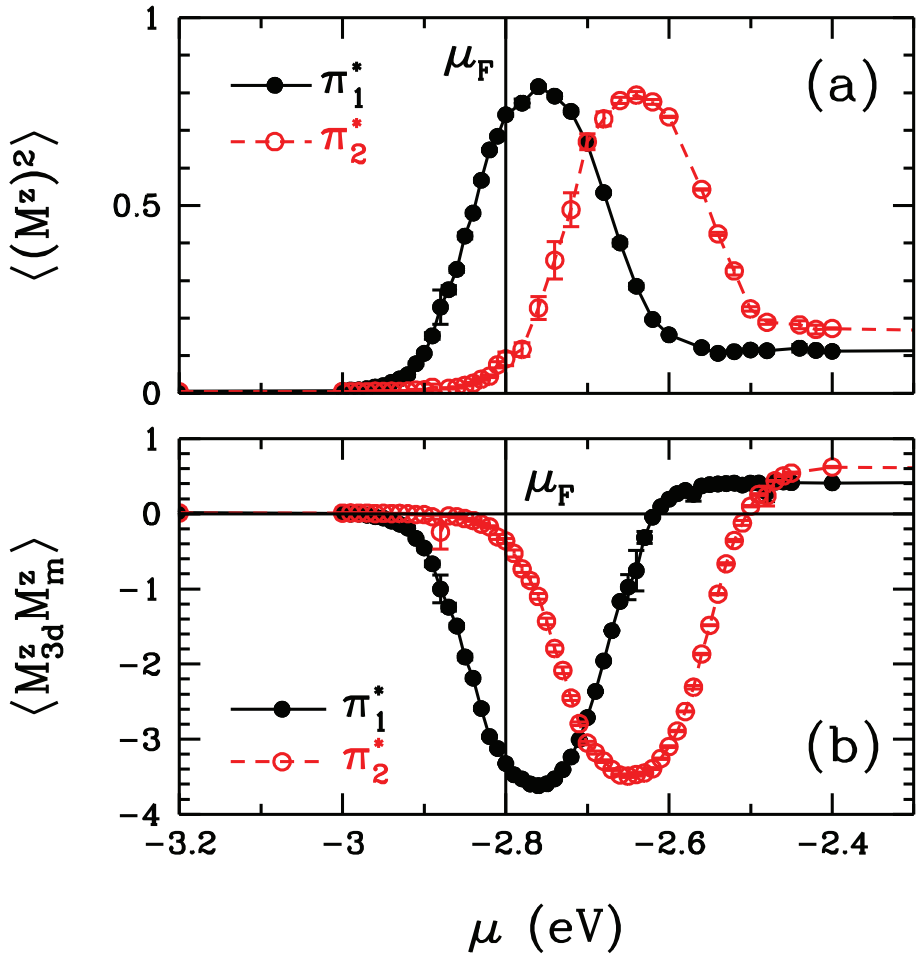

Figure 3.6. (a) Square of the magnetic moment $\langle (M^z)^2 \rangle$ of the π_1^* and π_2^* states plotted as a function of the chemical potential μ. (b) Equal-time correlations function of the Fe(3d) magnetic moment $\langle M^z_{3d} M_m \rangle$ with the moment of the π_1^* and π_2^* states plotted as a function of μ. Here, the vertical black line represents the Fermi level, $\mu_{\rm F}$.

Hopfield (1975)). The peak near 3 eV is named the Soret band, and it is considered to originate from $\pi \rightarrow \pi^*$ transitions.

We obtained an estimate of the optical absorption from the simple form

$$I(E) = \sum_{m',m=1} |\langle m'|\mathbf{p}|m\rangle|^2 f(\epsilon_m)(1 - f(\epsilon_{m'}))\delta(E - (\epsilon_{m'} - \epsilon_m)) \tag{3.2}$$

Here, m and m' sums over the host states, and $\mathbf{p} = \sum_i (-e)\mathbf{r}_i$ is the operator for the electric-dipole moment of the cluster. $f(\epsilon_{m'})$ is the Fermi-Dirac distribution. For the

energies of the host states, ε_m, we have used the DFT results and ignored the Coulomb interaction effects. Since the Coulomb interactions do not drastically broaden or shift the spectral weights for the π and π^* states, this is a reasonable approximation for estimating the UV optical absopriton. The results are shown as the blue bars for each transition in Fig. 3.8(b).

Comparing the experimental data on $\varepsilon(E)$ with this simple estimate, we see that the dominant contribution is arising from the $\pi_1 \rightarrow \pi_1^*$ and $\pi_1 \rightarrow \pi_2^*$ transitions. If we ignore other transitions and calculate the MCD spectra only for this case, then we obtain the results seen in Fig.3.8 (b). Here, the solid black curve has been obtained by assuming that the transitions to π_1^* and π_2^* states originate from only the π_1 state.

As seen in Fig.3.5(b), the spectral weight distributions of the π_1^* and π_2^* states have an overlap in energy which is about 0.2 eV. We artificially reduced the overlap of π_1^* and π_2^* by moving π_2^* higher in energy by 0.2 eV. Its result on $\Delta I(E)/E$ is shown as the dashed red curve in Fig. 3.9, which has better resemblance to the experimental line shape. Hence, we suggest that the anomalous Soret MCD lineshape of deoxy-HbA can be explained based on spin-selective transitions from a bonding π state to a pair of antibonding π^* states where one is half-filled and the other is empty. Spin selectivity is induced by the presence of antiferromagnetic correlations between the Fe(3d) and π^* magnetic moments.

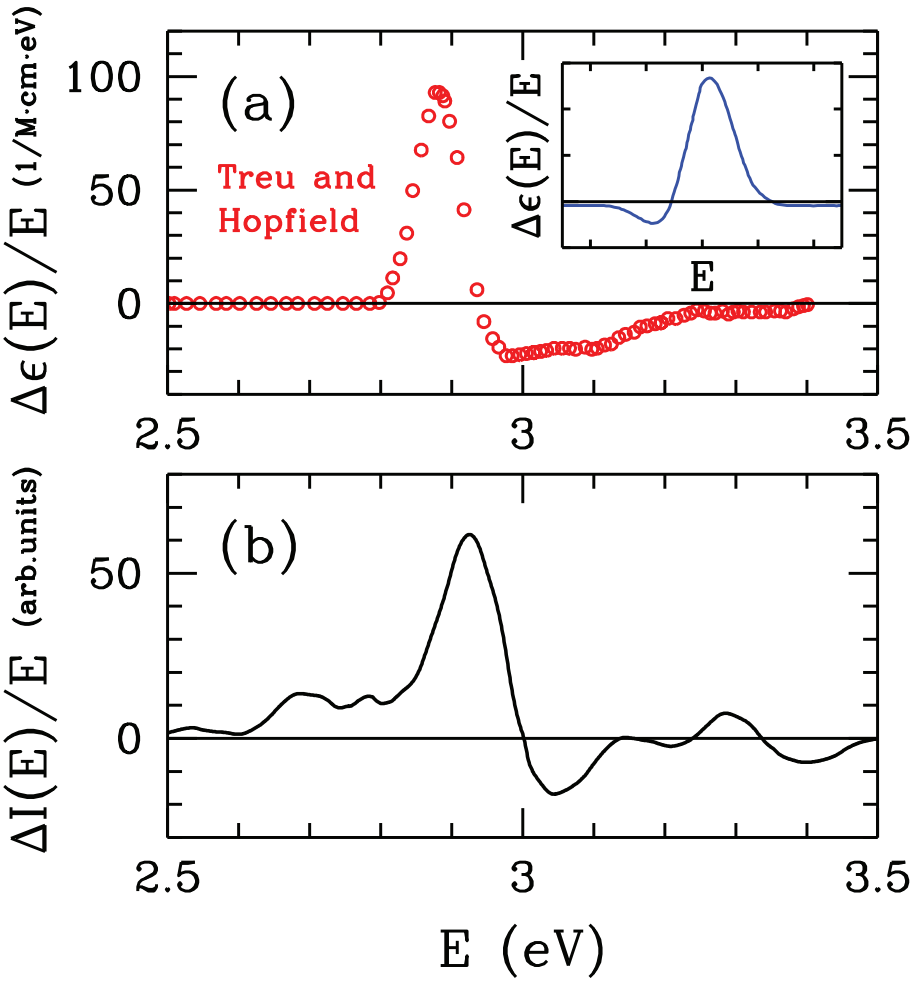

Figure 3.7. (a) Experimental magnetic circular dichroism (MCD) spectra in UV region of deoxy HbA obtained by Treu and Hopfield (Treu and Hopfield (1975)) at 8 C in a 16 Tesla applied magnetic field. The inset figure shows normally expected line shape for the temperature-dependent MCD spectrum (Mason (2007)). In (b), results from the calculation of the MCD spectra for the deoxy-heme cluster are shown.

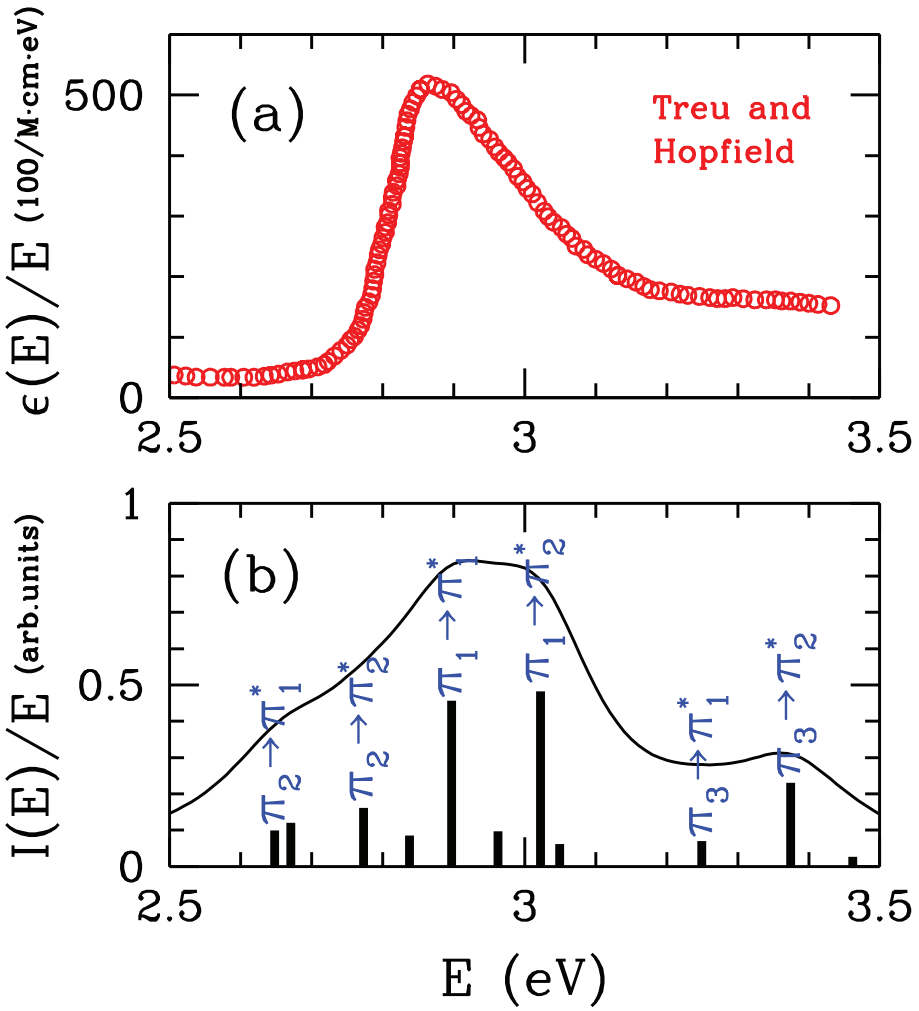

Figure 3.8. (a) Experimental data on the frequency dependence of the optical absorption normalized by energy, $\epsilon(E)/E$, for deoxy-HbA obtained by Treu and Hopfield (Treu and Hopfield (1975)). (b) Calculated optical absorption $I(E)/E$ (normalized by energy) for deoxy-heme. The blue bars denote the weights of the various $\pi \to \pi^*$ transitions.

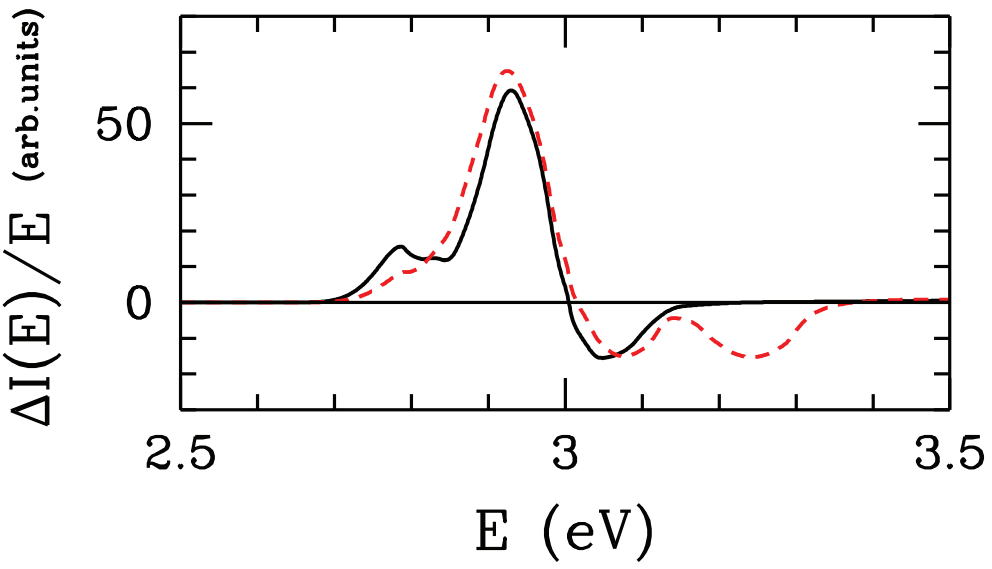

Figure 3.9. Here, the black line denotes the contribution to the MCD spectra from the $\pi_1 \rightarrow \pi_1^*$ and $\pi_1 \rightarrow \pi_2^*$ transitions. The red-dashed line denotes the same contribution in the case where the π_2^* state is artificially shifted by 0.2 eV to higher energies so that there is no overlap between the π_1^* and π_2^* states.

CHAPTER 4

RIXS SPECTRUM OF THE HEME CLUSTERS

In this chapter, we will present the resonant inelastic X-ray scattering (RIXS) spectrum of the deoxy-heme and oxy-heme clusters. In addition, we will compare results for the deoxy-heme with the RIXS spectrum of the deoxymyoglobin (deoxyMb) and results for the oxy-heme with the RIXS spectrum of the carboxymyoglobin (MbCO). We can do this comparison because hemoglobin and myoglobin have the similar molecular structure, and deoxyMb has the high-spin state as deoxy-heme and MbCO has the low-spin as oxy-heme molecule. The RIXS spectrum of myoglobin molecules were obtained by Harada et.al (Harada *et al.* (2009)).

In order to obtain RIXS spectrum, we calculate the single-particle spectral weight of the Fe(3d) orbitals by taking the derivative of the total electron number of 3d orbitals $\langle n_d \rangle$ calculated by using QMC with respect to the chemical potential μ.

$$A_d(\omega) = \frac{d}{d\mu}\langle n_d \rangle \Big|_{\mu=\omega} \tag{4.1}$$

is evaluated at $\mu = \omega$ and then, we calculate the spectrum by using the following equation

$$I_{dd} = \int d\omega' A(\omega') A(\omega' + \omega) f(\omega')(1 - f(\omega' + \omega)) \tag{4.2}$$

where $f(\omega)$ is the Fermi-Dirac distribution:

$$f(\omega) = \frac{1}{e^{\beta(\omega-\mu)} + 1} \tag{4.3}$$

Here, β is the inverse of the temperature and μ is the chemical potential.

4.1. RIXS spectrum of the deoxy-heme cluster

In this section, we show the RIXS spectrum of the deoxy-heme cluster. In addition, we compare our results with the RIXS spectrum of deoxyMb molecule (Harada *et al.* (2009)).

Figure 4.1 shows the changing in the electron number $\langle n_\nu \rangle$ of the Fe(3d) orbitals with respect to chemical potential μ. The black vertical line represents the Fermi level for the deoxy-heme cluster. This figure was discussed in Chapter 3. In this figure, we see sudden increases in the occupations of the Fe(3d) states. The increase located at ≈ -4 eV corresponds to the impurity bound states. Above the Fermi level, the occupation of the xy orbitals goes double occupancy at ≈ -2 eV. Similarly, the electron numbers of the other 3d orbitals goes 2 at -1.5 eV, -1 eV, 4 eV. In Figure 4.1, these increasing point are represented by the peaks. The height of the peaks are proportional to the increasing in the occupation numbers of the orbitals. Here, we put the Fermi level at 0 point.

In Figure 4.1, we see the decreasing in the occupation number of the Fe(3d) orbitals at some μ values due to charge transfer between the 3d orbitals. Hence, we can not obtain the spectral-weight graph from the $\langle n_\nu \rangle$ versus μ graph.

In order to obtain the single-particle weight $A(\omega)$, we calculate the total Fe(3d) electron number $\langle n_d \rangle$ as a function of μ as seen in Fig. 4.2. By taking the derivative of $\langle n_d \rangle$ with respect to μ, we obtain the $A(\omega)$ for the deoxy-heme cluster. We know from the Fig. 4.1 that the peak located at ≈ -4 eV comes from the IBS. In addition, the peaks located above the Fermi level are mainly originated from the double-occupancy of the Fe(3d) orbitals.

In Figure 4.3, we show the RIXS spectrum obtained by the QMC calculations for the deoxy-heme cluster and we compare it with the RIXS spectrum of the deoxyMb (Harada *et al.* (2009)). As seen in this figure, the calculated spectrum has a peak at ≈ 0.9 eV. The experimental spectrum also has a peak at ≈ 1 eV. For deoxy-heme, our calculated RIXS spectrum has similarities with the experimental results on deoxyMb.

In order to see the effect of the IBS on the transition density, we set $A(\omega)$ of IBS to 0. This new single-particle spectral weight is shown in Fig. 4.4 with the red dashed circle. Then, we calculate the I_{dd} from this new $A(\omega)$. In Figure 4.5, we present this transition density with the red dashed lines and also we compare this results with the experimental RIXS spectrum. As seen in this figure that the peak located at ≈ 0.9 eV is not originated from the IBS. On the other hand, the peak located at 2.1 eV in I_{dd} along with some other low-energy weight disappear.

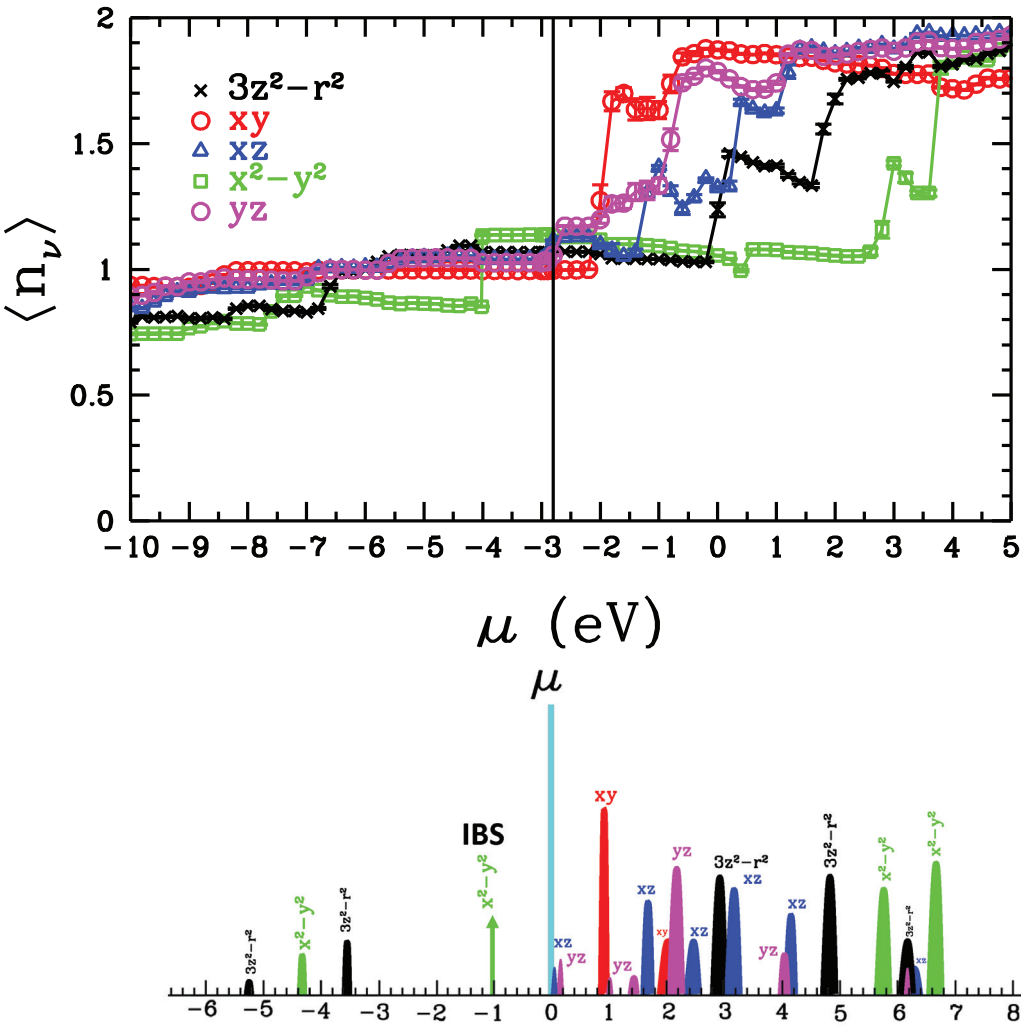

Figure 4.1. (Top) For deoxy-heme, the electron occupation number of the Fe(3d) orbitals $\langle n_\nu \rangle$ as a function of chemical potential μ. Here, the black solid line shows the Fermi level of the deoxy-heme cluster. This Fermi level is obtained by the DFT+QMC. (Bottom) Schematic plot of the single-particle spectrum for the deoxy-heme. The blue line shows the Fermi level of the molecule. This picture is obtained from the $\langle n_\nu \rangle$ versus μ graph and the peak locations correspond the electron increasing points. The height of the peaks is proportional to the increase in the occupation number of the orbitals. The peak located at ≈ -4 eV corresponds to the impurity bound state. Here, $U = 4$ eV and $J = 0.9$ eV and temperature is T=300 K.

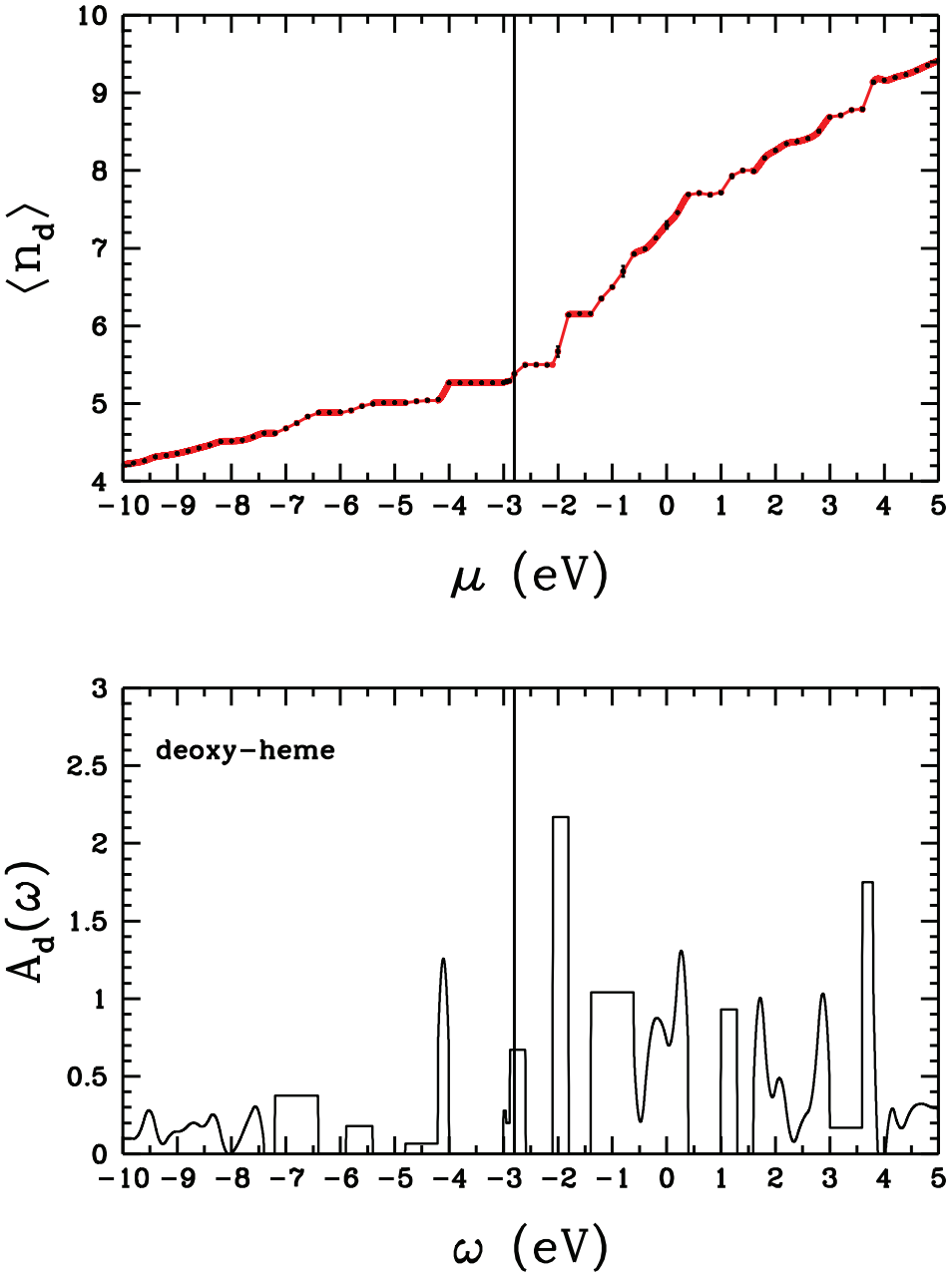

Figure 4.2. For deoxy-heme cluster, (Top) total electron number of the Fe(3d) orbitals $\langle n_d \rangle$ as a function of the chemical potential μ. (Bottom) The Fe(3d) single-particle spectral weight $A_d(\omega)$ versus frequency ω. $A_d(\omega)$ is obtained by taking the derivative of the $\langle n_d \rangle$ with respect to μ. The peak located at ≈ -4 eV corresponds to the impurity bound state. The black vertical line represents the Fermi level obtained by the QMC for the deoxy-heme molecule. Here, $U = 4$ eV and $J = 0.9$ eV and temperature is T=300 K.

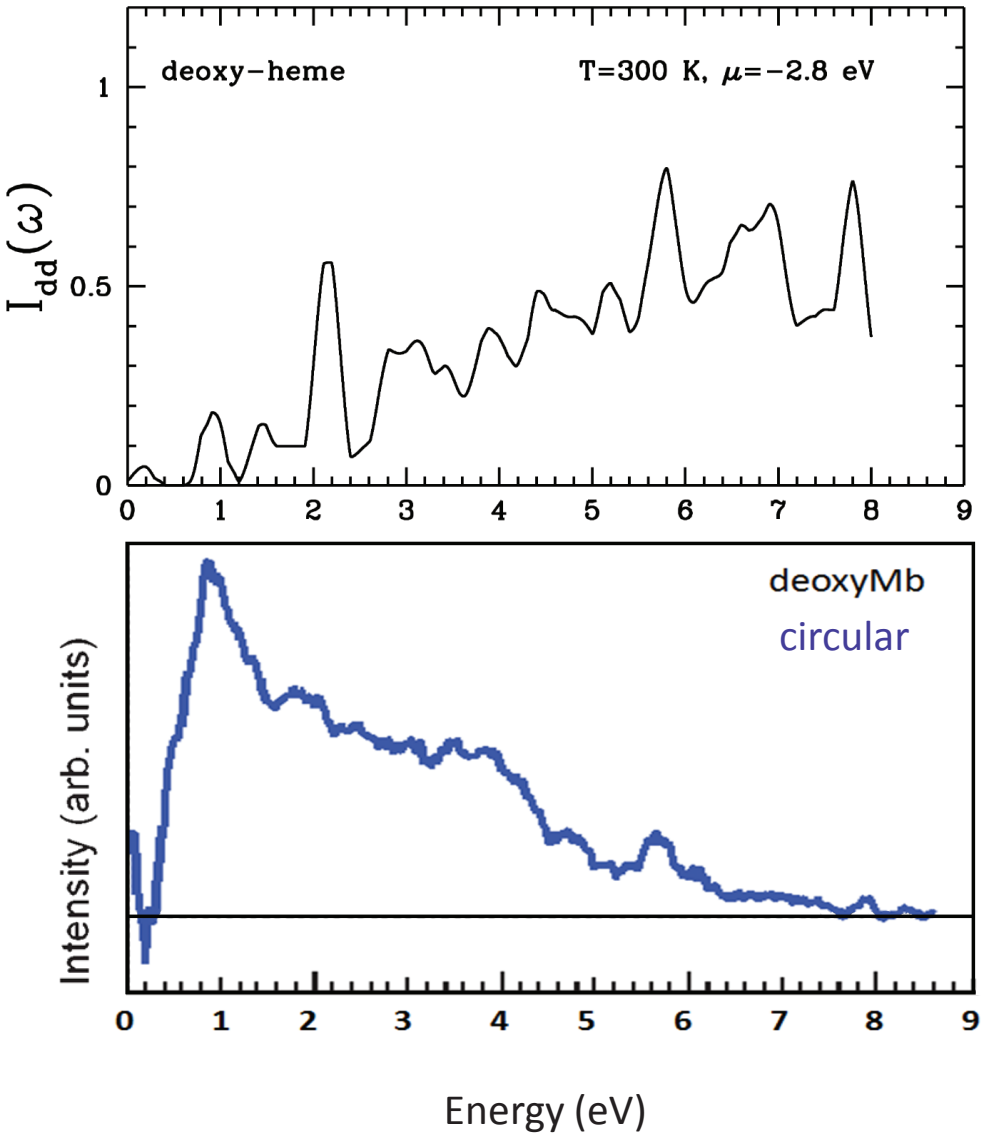

Figure 4.3. For deoxy-heme cluster, (Top) DFT+QMC results for the RIXS spectrum I_{dd}. I_{dd} is calculated from Eq.4.2. Here, these results are obtained for the $\mu = -2.8$ eV because it is the Fermi level for the deoxy-heme cluster. In addition, $U = 4$ eV and $J = 0.9$ eV and temperature is T=300 K. (Bottom) RIXS data on deoxyMb from the Harada et.al. (Harada *et al.* (2009)).

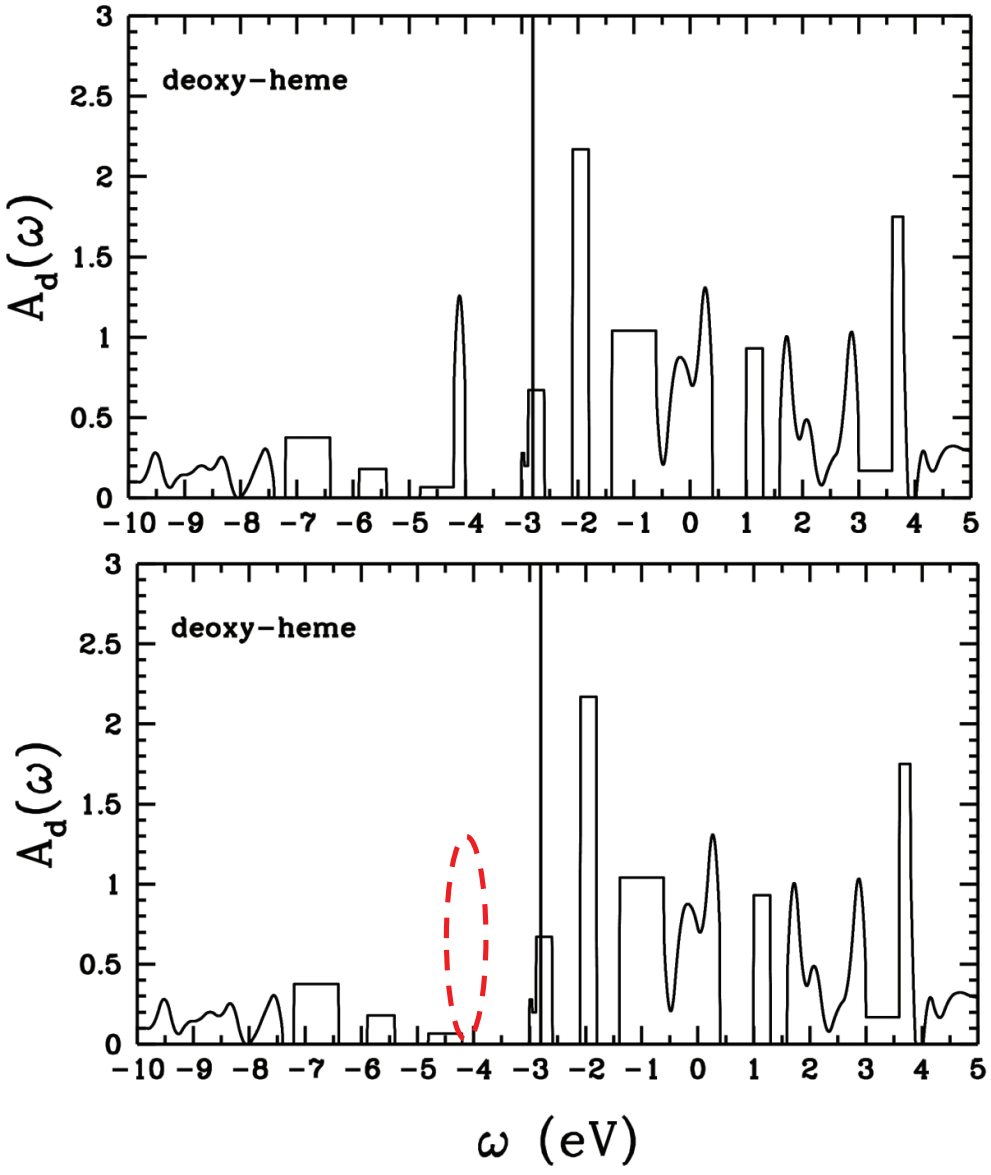

Figure 4.4. For deoxy-heme molecule, (Top) the single-particle spectral weight $A_d(\omega)$ versus frequency ω. $A(\omega)$ is obtained by taking the derivative of the $\langle n_d \rangle$ with respect to μ. (Bottom) In this figure, we set the $A_d(\omega)$ to 0 for the impurity bound state located ≈ -4 eV, which is shown by the dashed red circle. Here, the black line represent the Fermi level obtained by the QMC for the deoxy-heme molecule. Here, $U = 4$ eV and $J = 0.9$ eV and temperature is T=300 K.

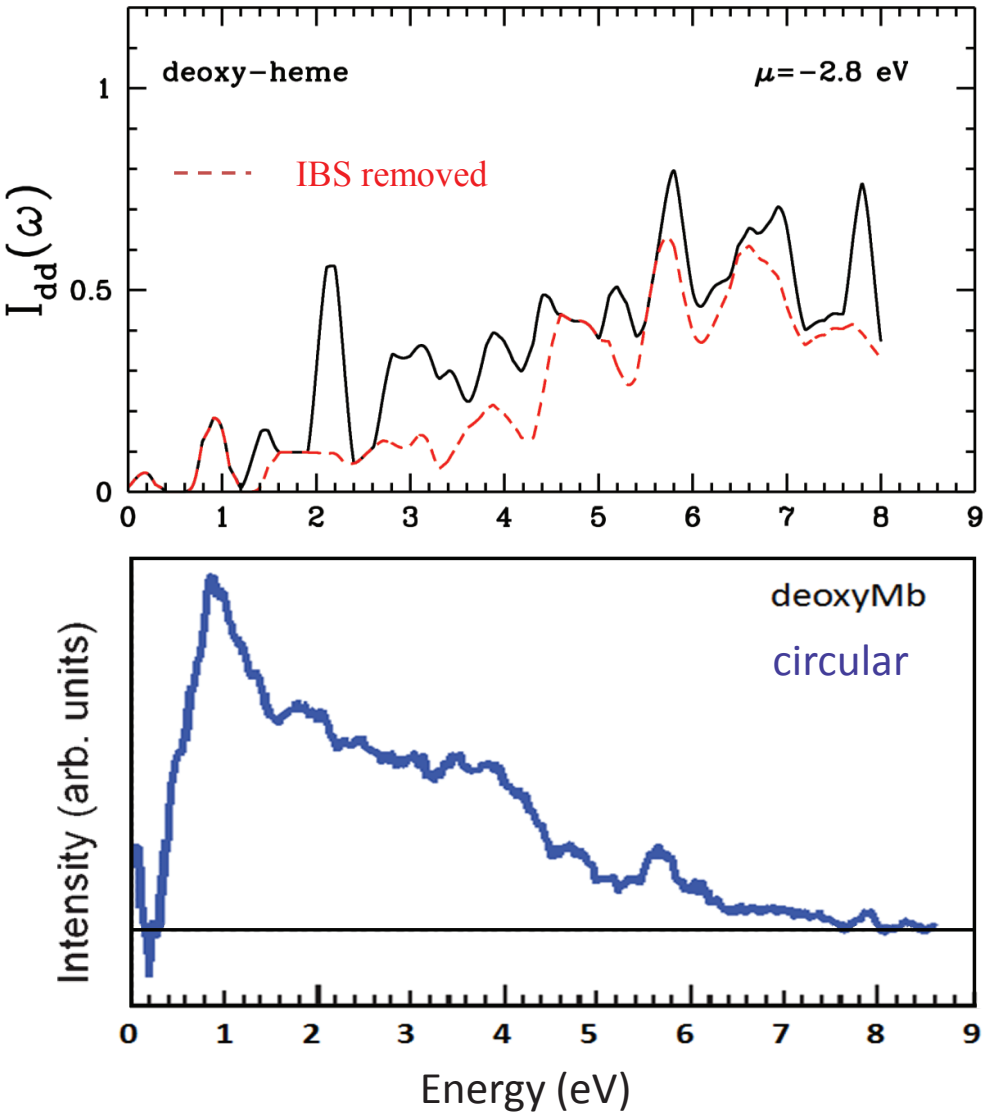

Figure 4.5. For deoxy-heme cluster, (Top) the black line shows the DFT+QMC results for the RIXS spectrum I_{dd}. The red dashed line shows the I_{dd} for the case in which the spectral weight of the impurity bound state equals 0. Here, $U = 4$ eV, $J = 0.9$ eV, $\mu = -2.8$ eV and temperature is T=300 K. (Bottom) RIXS data on deoxyMb from the Harada et.al.(Harada *et al.* (2009)).

4.2. RIXS spectrum of the oxy-heme cluster

In this section, we show the RIXS spectrum of the oxy-heme cluster. In addition, we compare our results with the RIXS spectrum of MbCO molecule (Harada *et al.* (2009)).

Figure 4.6 shows the changing $\langle n_\nu \rangle$ of the Fe(3d) orbitals with respect to chemical potential μ. The black vertical line represents the Fermi level for the deoxy-heme cluster. This figure was discussed in Chapter 3. In this figure, we see sudden increases in the occupations of the Fe(3d) states. The increase located at ≈ -5.5 eV, ≈ -1.5 eV and ≈ 1.5 eV correspond to the impurity bound states. In Figure 4.6, these increasing points are represented by the peaks. The height of the peaks are proportional to the increasing in the occupation numbers of the orbitals. Here, we put the Fermi level at 0 point.

In Figure 4.6, we see the decreasing in the occupation number of the Fe(3d) orbitals at some μ values due to charge transfer between the 3d orbitals. Hence, we can not obtain the spectral-weight graph from the $\langle n_\nu \rangle$ versus μ graph.

In order to obtain the single-particle weight $A(\omega)$, we calculate the total Fe(3d) electron number $\langle n_d \rangle$ as a function of μ as seen in Fig. 4.7. By taking the derivative of $\langle n_d \rangle$ with respect to μ, we obtain the $A(\omega)$ for the oxy-heme cluster. We know from the Fig. 4.6 that the peak located at at ≈ -5.5 eV, ≈ -1.5 eV and ≈ 1.5 eV come from the IBS.

In Figure 4.8, we show the RIXS spectrum obtained by the QMC calculations for the oxy-heme cluster and we compare it with the RIXS spectrum of the MbCO (Harada *et al.* (2009)). As seen in this figure, the calculated spectrum has a peak at ≈ 0.4 eV and ≈ 1.4 eV and at the above points. The experimental spectrum also have also peaks ≈ 0.4 eV and ≈ 1.4 eV This results show that the spectrum obtained from the DFT+QMC results agree well with the RIXS data on MbCO. In particular, the peak positions up to 6 eV are in good agreement with the experimental data.

In order to see the effect of the IBS on the transition density, we set $A(\omega)$ of IBS to 0. This new single-particle spectral weight is shown in Fig. 4.9 with the red dashed circle. Then, we calculate the I_{dd} from this new $A(\omega)$. In Figure 4.10, we presents this transition density with the red dashed lines and also we compare this results with the experimental RIXS spectrum. As seen in this figure that the peak located at ≈ 2.4 eV and ≈ 2.8 eV in I_{dd} along with the some other low-energy spectral weight disappear.

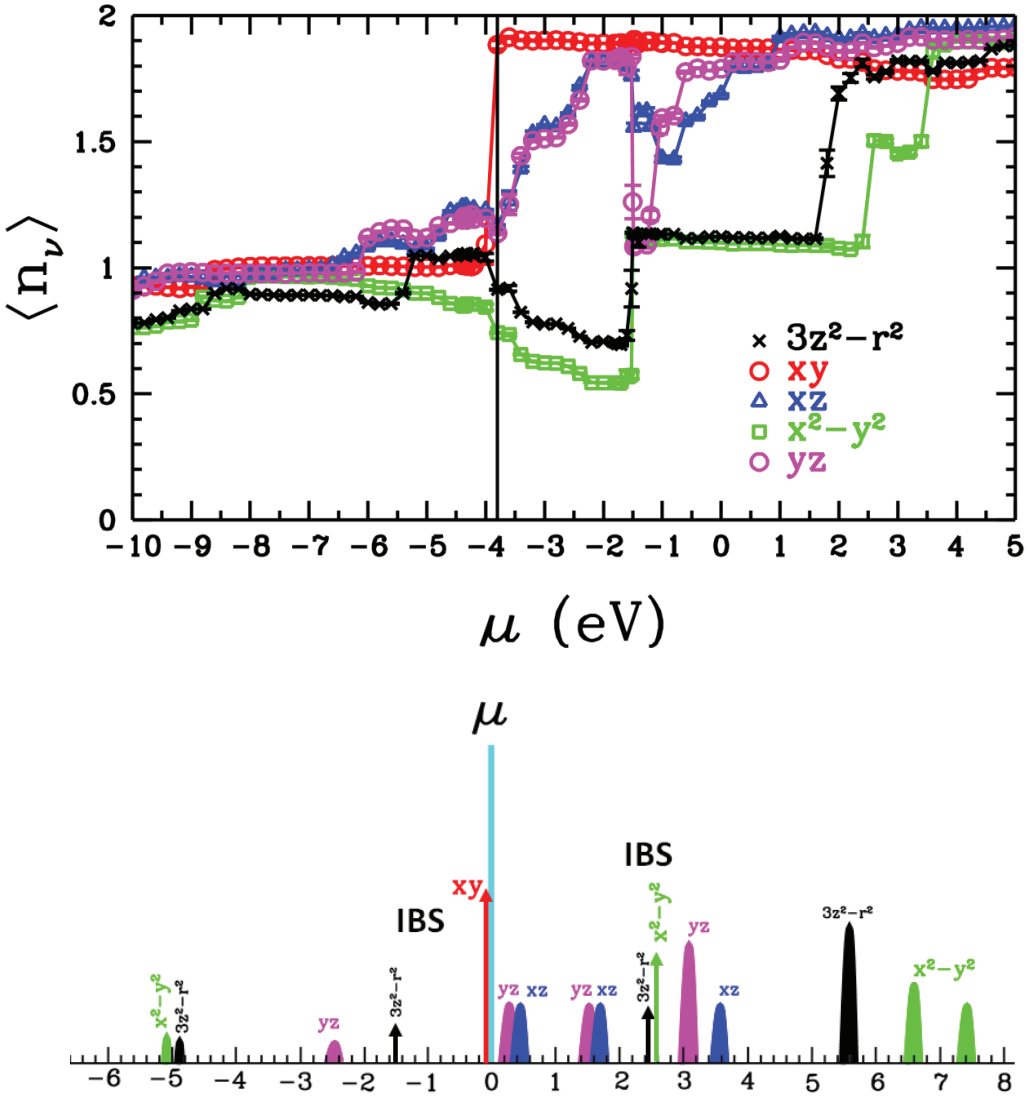

Figure 4.6. For oxy-heme, (Top) the electron occupation number of the Fe(3d) orbitals $\langle n_\nu \rangle$ as a function of chemical potential μ. Here, the black solid line shows the Fermi level of the deoxy-heme cluster. This Fermi level is calculated by the DFT+QMC. (Bottom) Schematic plot of the single-particle spectrum for the oxy-heme. The blue line shows the Fermi level of the molecule. This picture is obtained from the $\langle n_\nu \rangle$ versus μ graph and the peak locations correspond the electron increasing points. The height of the peaks is proportional to the increase in the occupation number of the orbitals. The peaks located at ≈ -1.5 eV, ≈ 2.4 eV and ≈ 2.5 eV correspond to the impurity bound state. Here, $U = 4$ eV and $J = 0.9$ eV and temperature is T=300 K.

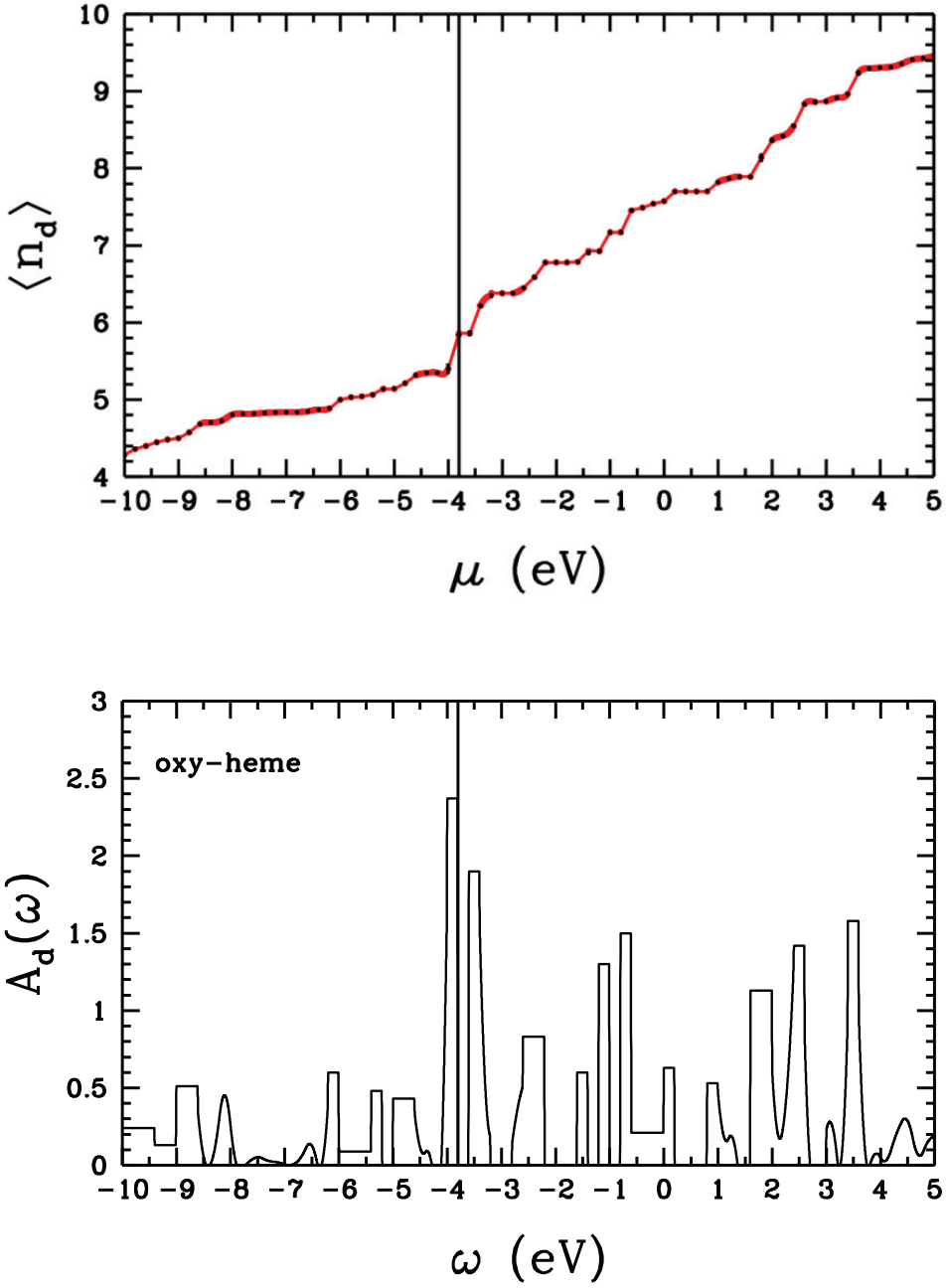

Figure 4.7. For oxy-heme cluster, (Top) total electron number of the Fe(3d) orbitals $\langle n_d \rangle$ as a function of the chemical potential μ. (Bottom) The Fe(3d) single-particle spectral weight $A_d(\omega)$ versus frequency ω. $A_d(\omega)$ is obtained by taking the derivative of the $\langle n_d \rangle$ with respect to μ. The peaks located at ≈ -1.5 eV, ≈ 2.4 eV and ≈ 2.5 eV correspond to the impurity bound state The black vertical line represents the Fermi level obtained by the QMC for the oxy-heme molecule. Here, $U = 4$ eV and $J = 0.9$ eV and temperature is T=300 K.

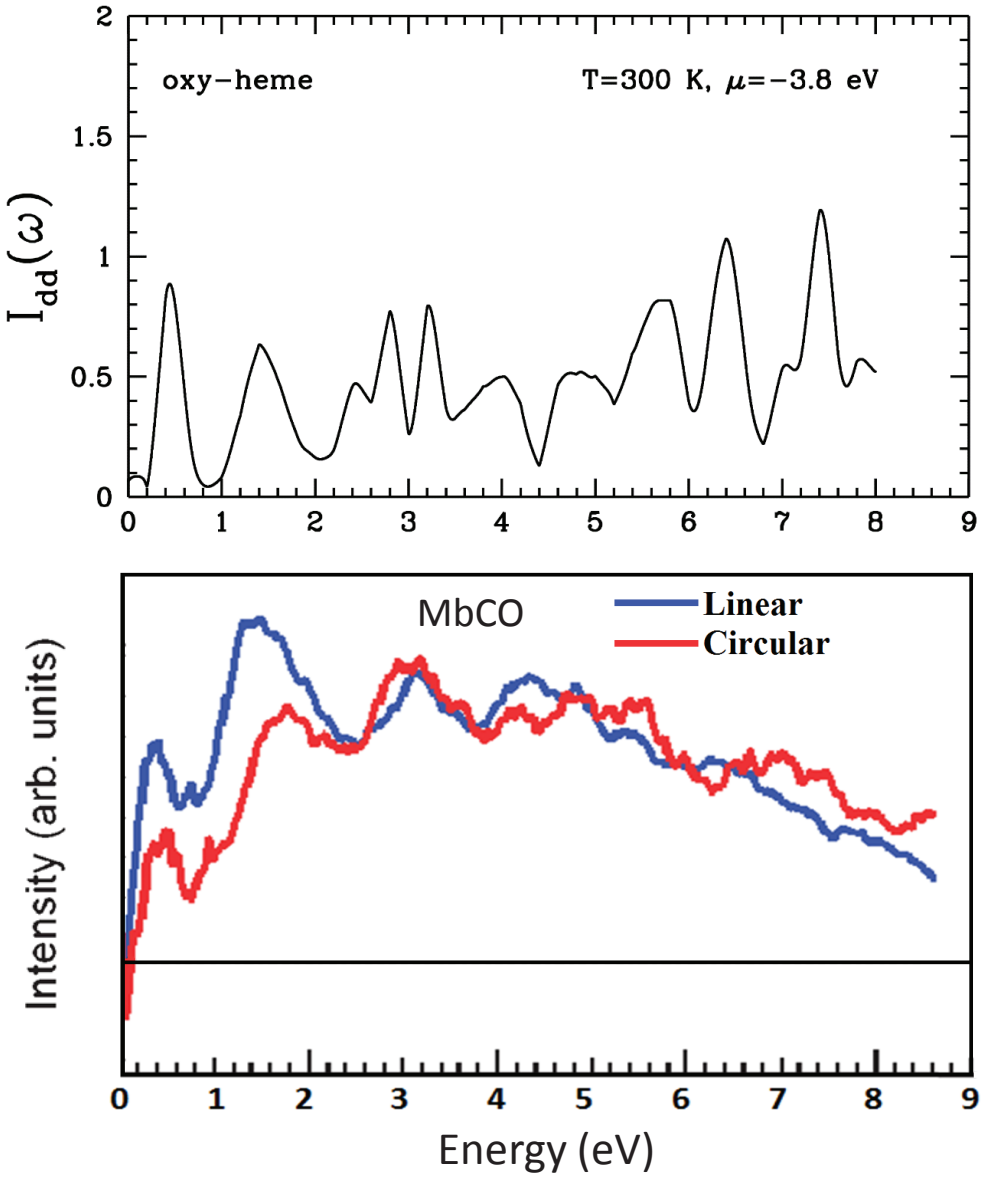

Figure 4.8. For oxy-heme cluster, (Top) DFT+QMC results for the RIXS spectrum I_{dd}. I_{dd} is calculated from Eq.4.2. Here, the chemical potential is -3.8 eV which is the Fermi level for the oxy-heme molecule. In addition, $U = 4$ eV and $J = 0.9$ eV and temperature is T=300 K. (Bottom) RIXS data on MbCO from the Harada et.al.(Harada *et al.* (2009)).

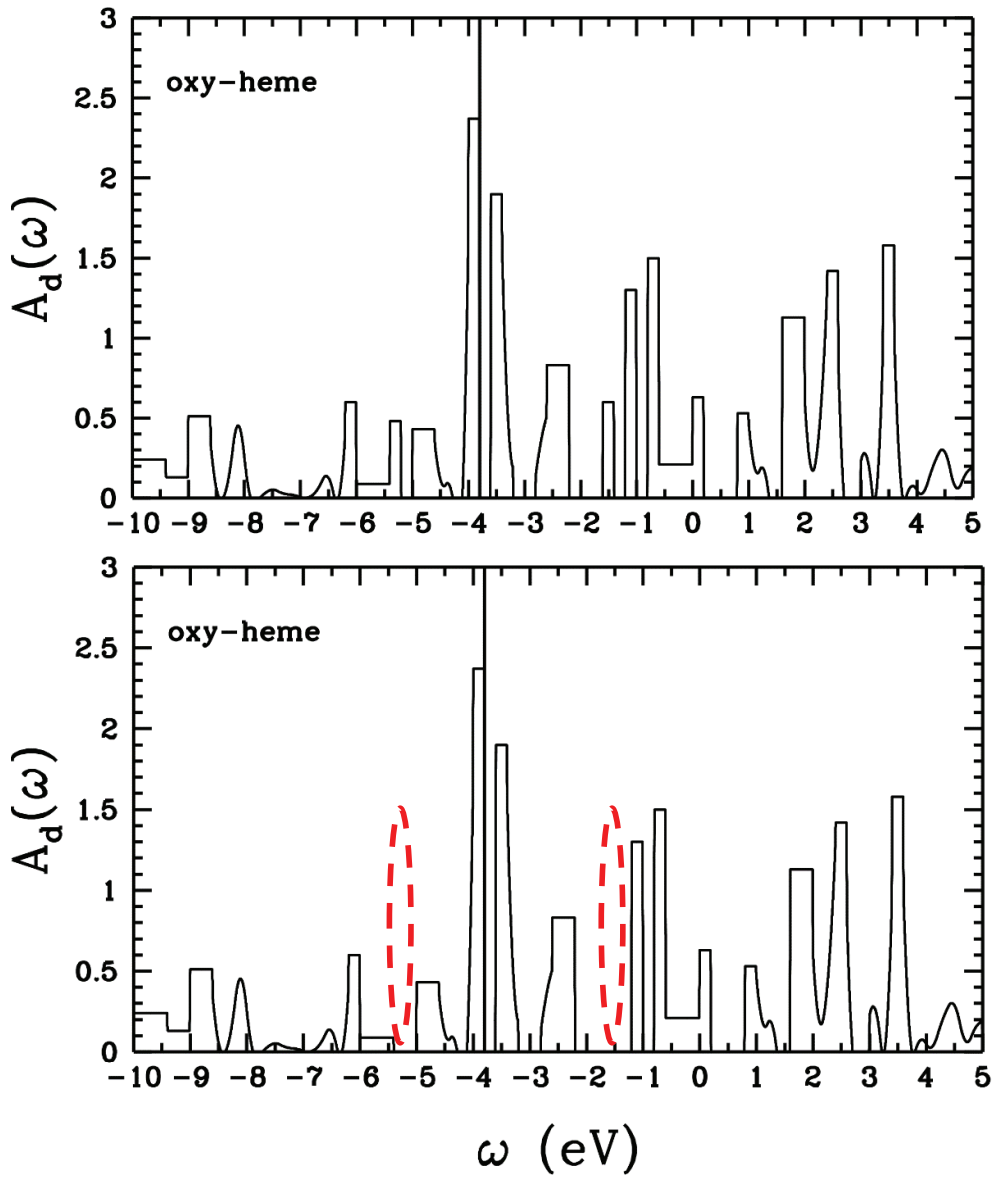

Figure 4.9. For oxy-heme molecule, (Top) the single-particle spectral weight $A_d(\omega)$ versus frequency ω. $A(\omega)$ is obtained by taking the derivative of the $\langle n_d \rangle$ with respect to μ. (Bottom) In this figure, we set the $A_d(\omega)$ to 0 for the impurity bound states located at ≈ -1.5 eV, ≈ 2.4 eV and ≈ 2.5 , which are shown by the dashed red circle. Here, the black line represent the Fermi level obtained by the QMC for the oxy-heme molecule. Here, $U = 4$ eV and $J = 0.9$ eV and temperature is T=300 K.

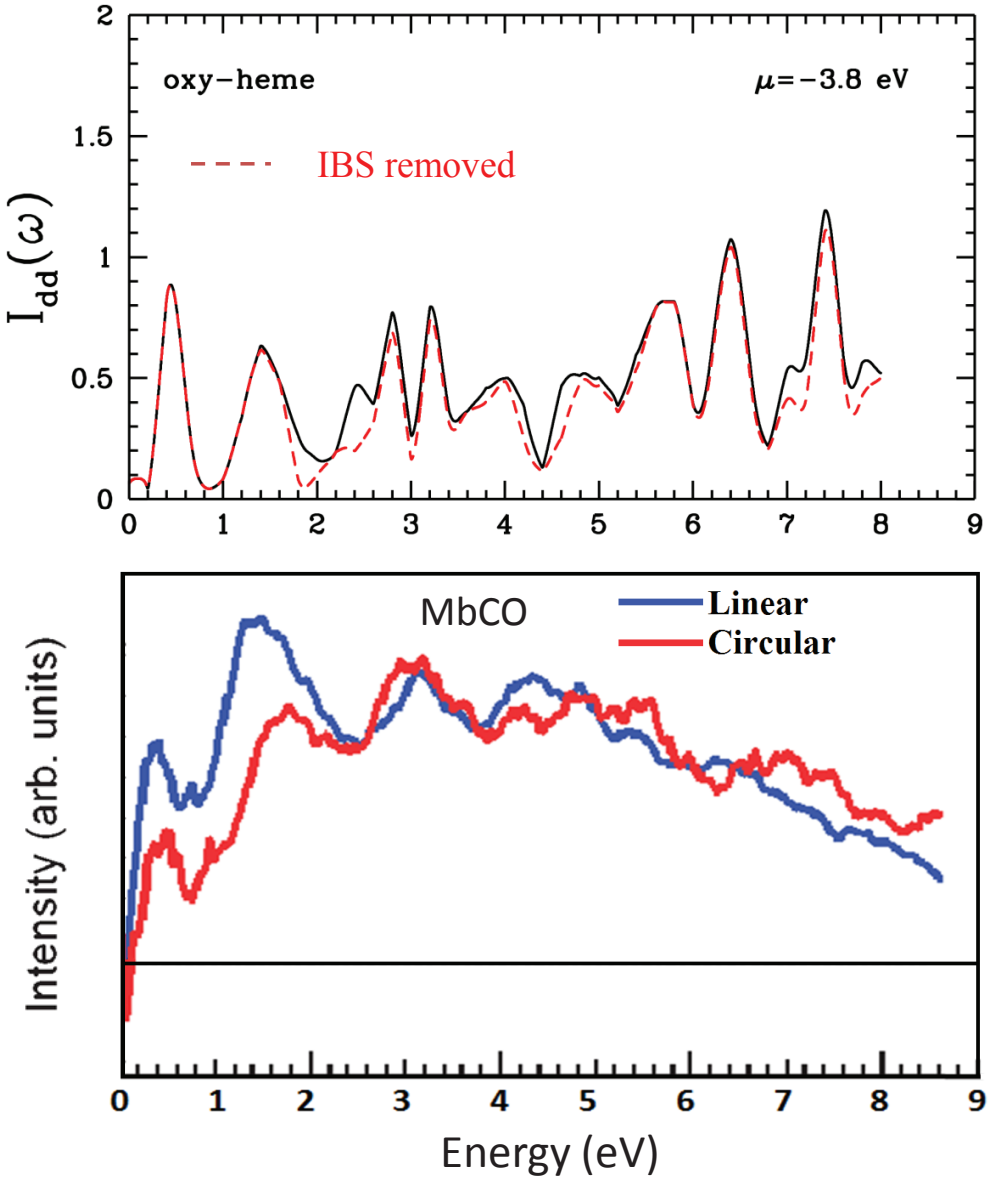

Figure 4.10. For oxy-heme cluster, (Top) the black line shows the DFT+QMC results for the RIXS spectrum I_{dd}. The red dashed line shows the I_{dd} for the case in which the spectral weight of the impurity bound state equals 0. Here, $U = 4$ eV, $J = 0.9$ eV, $\mu = -3.8$ eV and temperature is T=300 K. (Bottom) RIXS data on MbCO from the Harada et.al.(Harada *et al.* (2009)).

CHAPTER 5

XAS OF THE HEME CLUSTERS

In this section, we compare the DFT+QMC results with the X-ray absorption spectroscopy (XAS) data on the high-spin and low-spin hemes. XAS probes the single-particle spectral weight $A_d(\omega)$ above the Fermi level.

For the high-spin case, we compare DFT+QMC results with the XAS measurements by Aziz et al (Aziz *et al.* (2009)) on the deoxy-heme in solution. The $A_d(\omega)$ of this molecule is shown in Fig. 5.1.

For the low-spin heme molecule, we make comparison with the XAS data on [Fe(ttp)-(ImH_2)Cl]$_2$ (Hocking *et al.* (2007)). $A_d(\omega)$ for this low-spin molecule is shown in Fig. 5.2. We first compare $A_d(\omega)$ with the DFT+QMC results. Then, we integrate $A_d(\omega)$ above the Fermi level and compare this quantity for XAS and DFT+QMC.

5.1. XAS of the deoxy-heme cluster

Figure 5.3 the comparison of $A_d(\omega)$ for the high-spin heme with the deoxy-HbA. In the experimental data, peaks are located about 1 eV and 3 eV. Here, the Fermi level is located at 708 eV for the experimental data. The DFT+QMC results on $A_d(\omega)$ show that a dominant peak is located about 1 eV and 3 eV. Different from the experimental results, the spectrum of deoxy-heme is more broaden.

In Figure 5.4, 5.5 and 5.6, we compare the total Fe(3d) electron numbers obtained from the experimental results and DFT+QMC results. Here, we calculate the electron number for different Fermi levels because we do not exactly know the location of the chemical potential for the experimental results.

In Fig. 5.4, we use $U = 4$ eV and $J = 0.9$ eV for the DFT+QMC calculations. Here, we see that the change in the Fe(3d) electron numbers as a function of chemical potential μ is similar with the experimental data for the $\varepsilon_F = 709$ eV.

For results represented in Fig. 5.5, we use $U = 3$ eV, $J = 0.9$ eV parameters for the DFT+QMC calculations. This results are obtained at $T = 1500$ K. Here, we see that the total electron number behaviour with respect to μ is very different from the experimental results.

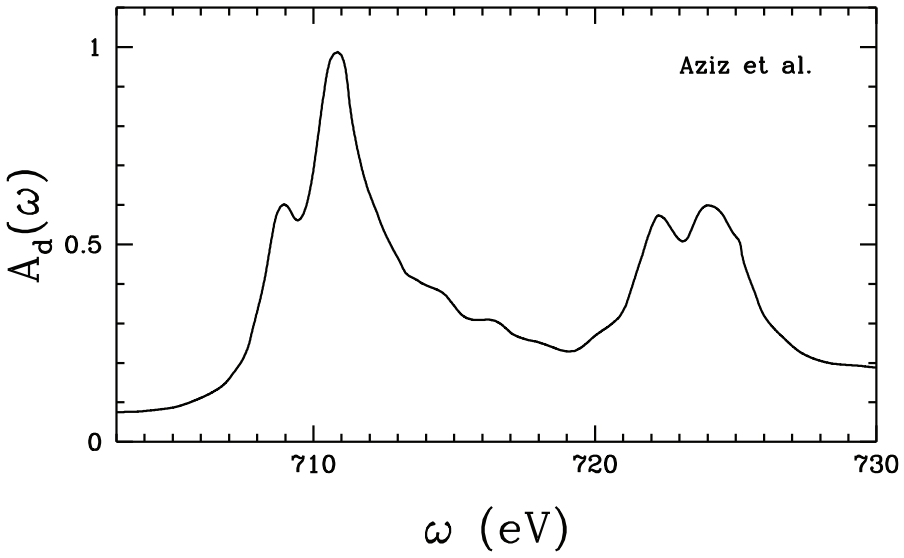

Figure 5.1. The single-particle spectral weight $A_d(\omega)$ for the high-spin heme molecule. These data are obtained from (Aziz *et al.* (2009))

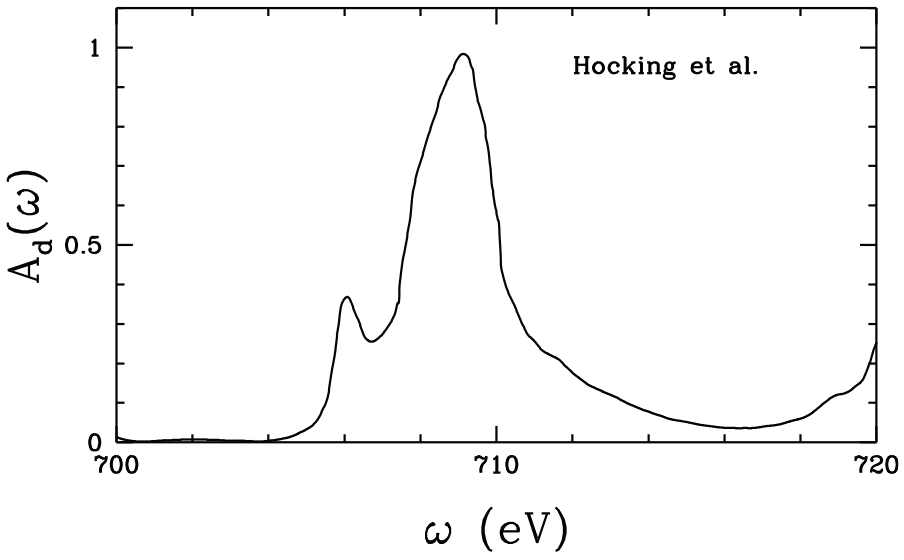

Figure 5.2. The single-particle spectral weight $A_d(\omega)$ for the high-spin heme molecule. These data are obtained from (Hocking *et al.* (2007)).

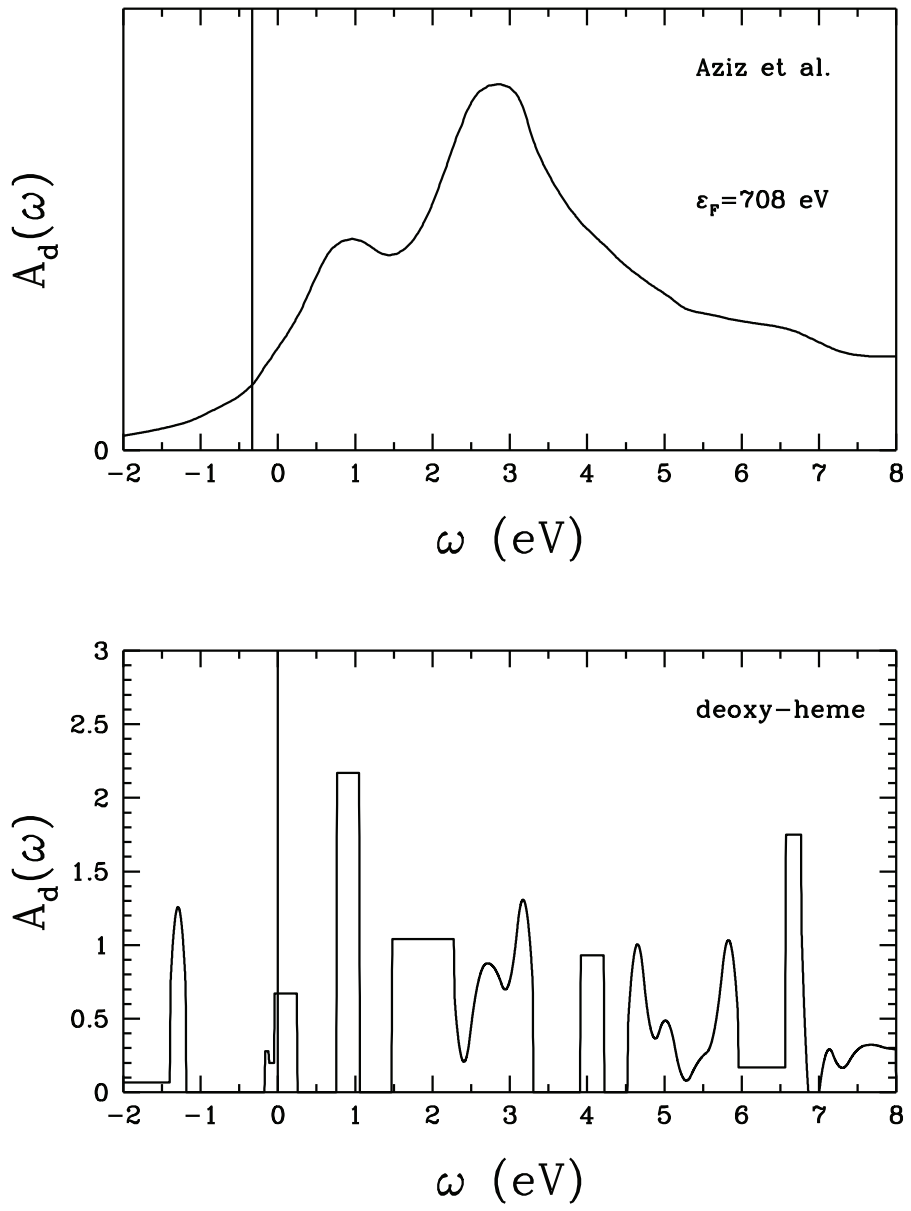

Figure 5.3. (Top) The single-particle spectral weight $A_d(\omega)$ for the high-spin heme molecule (Aziz *et al.* (2009)). Here, ε_F is the Fermi level for the experimental data. (Bottom) $A_d(\omega)$ obtained from the DFT+QMC results for the deoxy-heme.In DFT+QMC, $U = 4$ eV, $J = 0.9$ eV and $T = 300$ K.

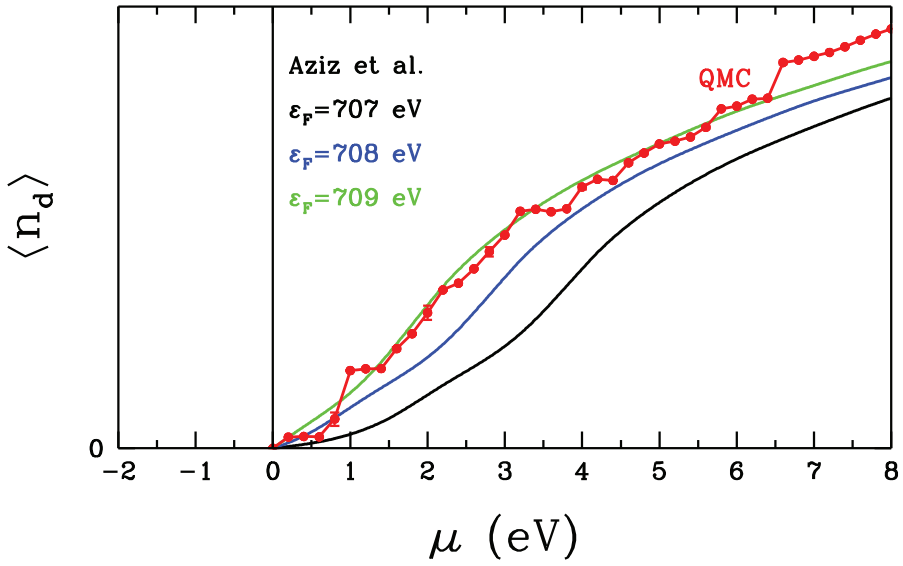

Figure 5.4. For deoxy-heme, total Fe(3d) electron numbers as a function of chemical potential μ. The black, blue and green lines are obtained from (Aziz *et al.* (2009)). Here, ε_F shows the Fermi level for the experimental data for the high-spin heme. The red line shows the DFT+QMC results for the total electron number of Fe(3d) orbitals for deoxy-heme. Here, the black vertical line represents the Fermi level for deoxy-heme. In this calculations, $U = 4$ eV, $J = 0.9$ eV and $T = 300$ K.

In Fig. 5.6, we show the DFT+QMC results for $U = 3$ eV, $J = 0.6$ eV and $T = 1500$ K. Here, we observe that the DFT+QMC results are similar with the experimental results.

5.2. XAS of the oxy-heme cluster

Figure 5.7 the comparison of $A_d(\omega)$ for the low-spin heme with the oxy-HbA. In the experimental data, peaks are located about 0 eV and 3 eV. Here, the Fermi level is located at 706 eV for the experimental data. The DFT+QMC results on $A_d(\omega)$ show that the spectrum is broaden and we see peaks at many energy levels.

In Figure 5.8, 5.9 and 5.10, we compare the total Fe(3d) electron numbers obtained from the experimental results and DFT+QMC results. Here, we calculate the electron number for different Fermi levels because we do not exactly know the location of the chemical potential for the experimental results. These results show that the DFT+QMC results for the oxy-heme are not compatible with the experimental results. We change the

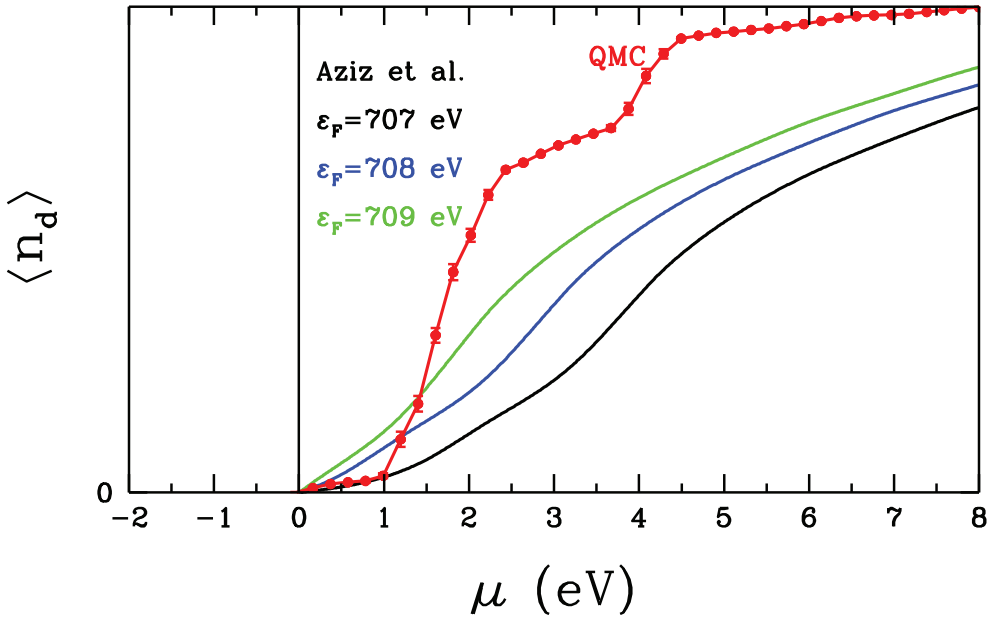

Figure 5.5. For deoxy-heme, total Fe(3d) electron numbers as a function of chemical potential μ. The black, blue and green lines are obtained from (Aziz *et al.* (2009)). Here, ε_F shows the Fermi level for the experimental data for the high-spin heme. The red line shows the DFT+QMC results for the total electron number of Fe(3d) orbitals for deoxy-heme. Here, the black vertical line represents the Fermi level for deoxy-heme. In this calculations, $U = 3$ eV, $J = 0.9$ eV and $T = 1500$ K.

interaction values and the Fermi levels for the experimental results, and we do not obtain the similar results with the experimental data.

For both the deoxy-heme and oxy-heme, XAS data do not agree very well with the DFT+QMC calculations. The reason may be that we do not use correct U and J values for the heme clusters. Hence, the different interaction parameters may be used for the comparison with the XAS data and DFT+QMC results.

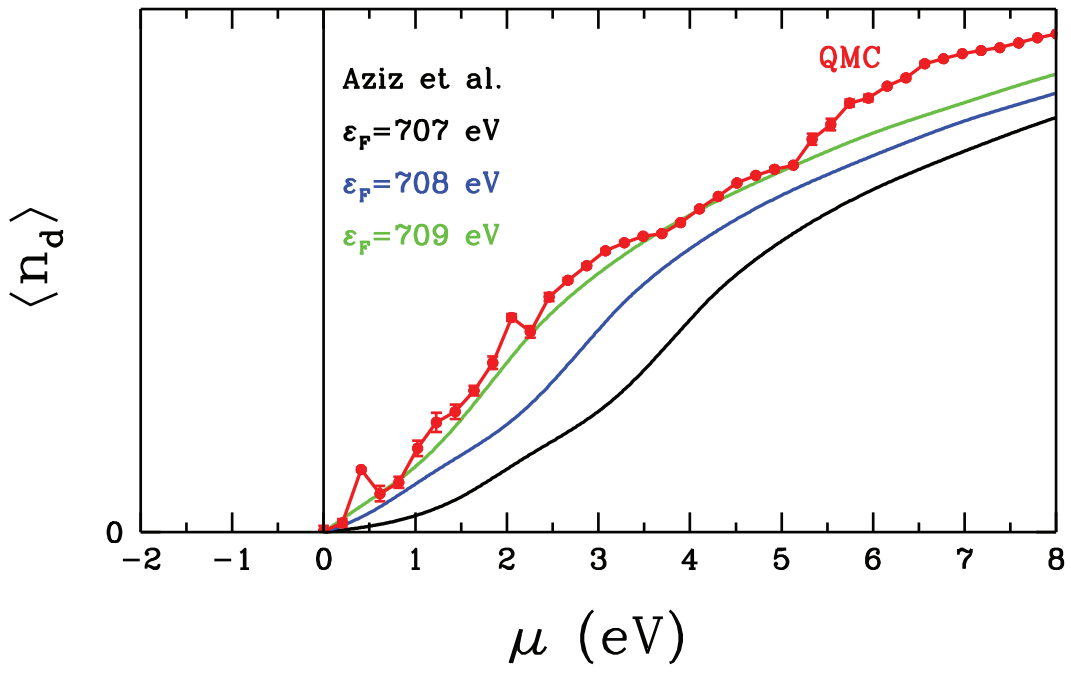

Figure 5.6. For deoxy-heme, total Fe(3d) electron numbers as a function of chemical potential μ. The black, blue and green lines are obtained from the (Aziz *et al.* (2009)). Here, ε_F shows the Fermi level for the experimental data for the high-spin heme. The red line shows the DFT+QMC results for the total electron number of Fe(3d) orbitals for deoxy-heme. Here, the black vertical line represents the Fermi level for deoxy-heme. In this calculations, $U = 3$ eV, $J = 0.6$ eV and $T = 1500$ K.

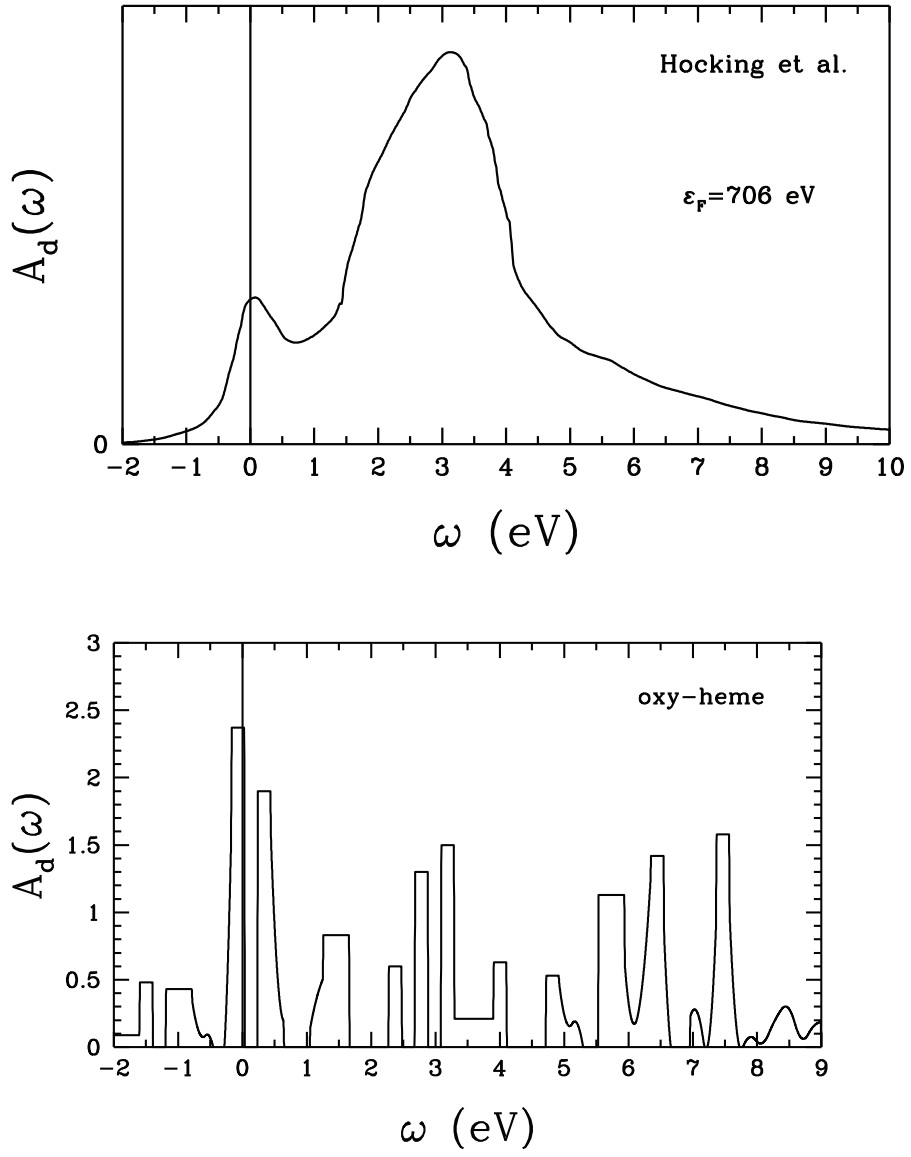

Figure 5.7. The single-particle spectral weight $A_d(\omega)$ for the low-spin heme molecule (Hocking *et al.* (2007)). (Bottom) $A_d(\omega)$ obtained from the DFT+QMC results for the oxy-heme. In DFT+QMC, $U = 4$ eV, $J = 0.9$ eV and $T = 300$ K.

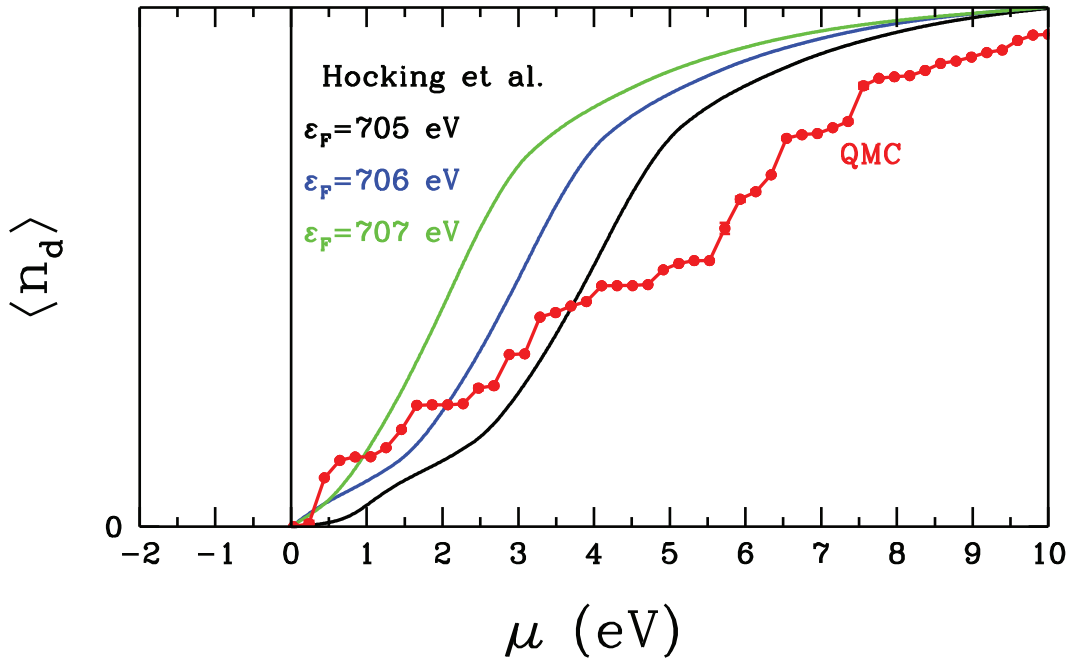

Figure 5.8. For oxy-heme, total Fe(3d) electron numbers as a function of chemical potential μ. The black, blue and green lines are obtained from (Hocking *et al.* (2007)). Here, ε_F shows the Fermi level for the experimental data for the low-spin heme. The red line shows the DFT+QMC results for the total electron number of Fe(3d) orbitals for oxy-heme. Here, the black vertical line represents the Fermi level for oxy-heme. In this calculations, $U = 4$ eV, $J = 0.9$ eV and $T = 300$ K.

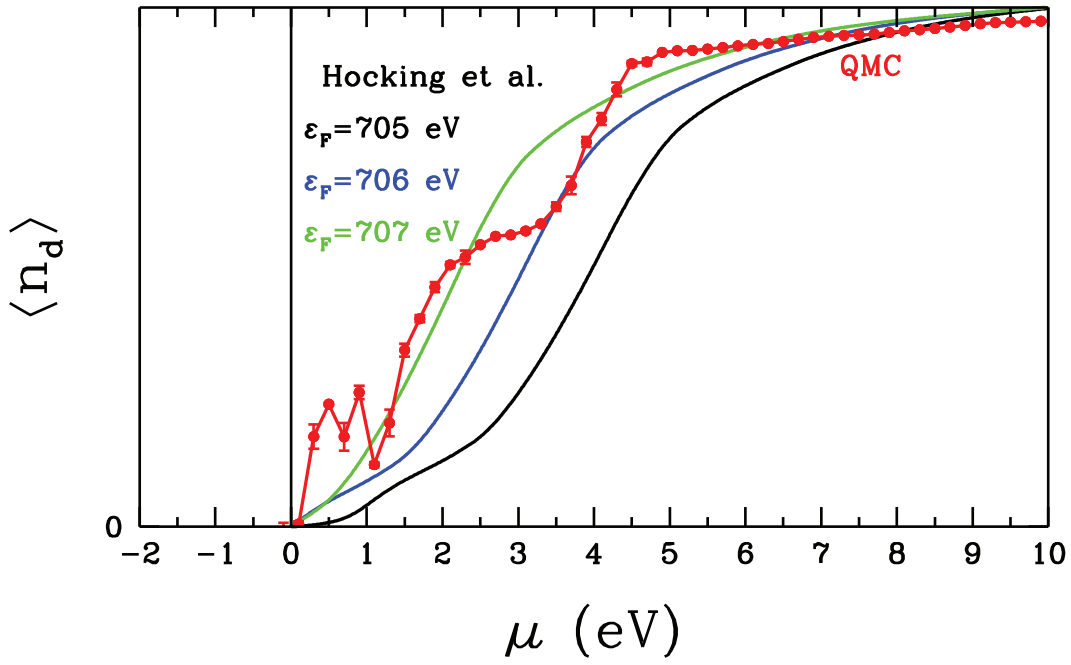

Figure 5.9. For oxy-heme, total Fe(3d) electron numbers as a function of chemical potential μ. The black, blue and green lines are obtained from (Hocking *et al.* (2007)). Here, ε_F shows the Fermi level for the experimental data for the low-spin heme. The red line shows the DFT+QMC results for the total electron number of Fe(3d) orbitals for oxy-heme. Here, the black vertical line represents the Fermi level for oxy-heme. In this calculations, $U = 3$ eV, $J = 0.9$ eV and $T = 1500$ K.

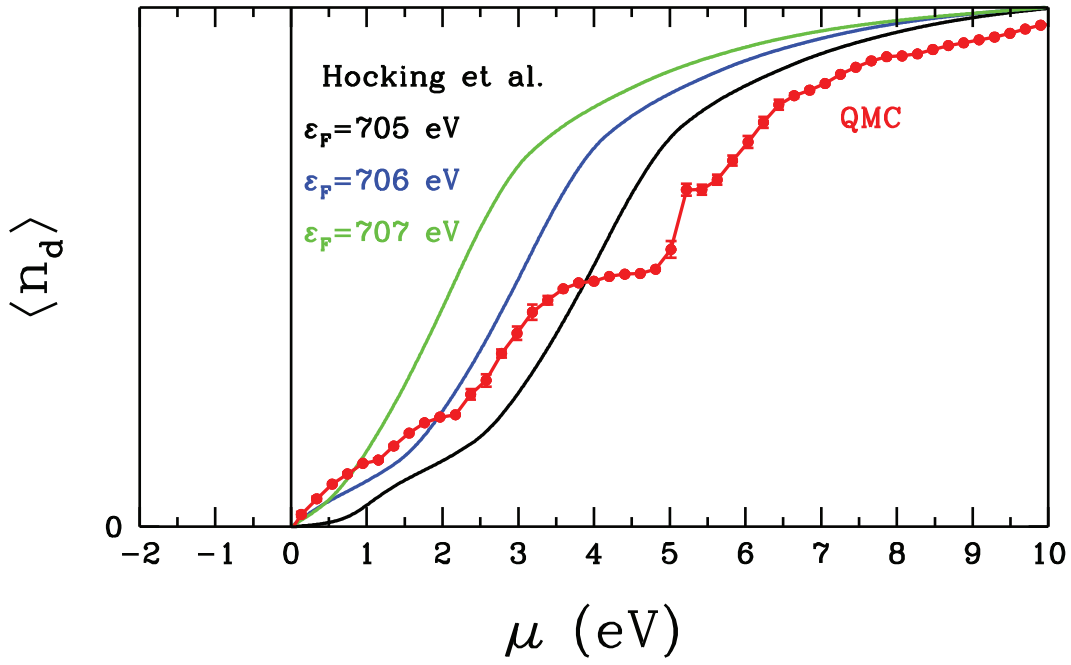

Figure 5.10. For oxy-heme, total Fe(3d) electron numbers as a function of chemical potential μ. The black, blue and green lines are obtained from (Hocking *et al.* (2007)). Here, ε_F shows the Fermi level for the experimental data for the low-spin heme. The red line shows the DFT+QMC results for the total electron number of Fe(3d) orbitals for oxy-heme. Here, the black vertical line represents the Fermi level for oxy-heme. In this calculations, $U = 3$ eV, $J = 0.6$ eV and $T = 1500$ K.

CHAPTER 6

IMPLICATION OF THE DFT+QMC RESULTS FOR THE FUNCTIONING OF HEMOGLOBIN

6.1. Magnetic mechanism for Fe-O_2 binding

DFT+QMC results show that the magnetic moment of hemoglobin molecule is lowered by bindig O_2 molecule to Fe atom.

At temperature $T = 300$ K, we find that oxy-heme has effective spin $S = 0.68$. When the temperature is decreased, the magnetic gap is formed and the effective spin of molecule equals $S = 0.1$ at $T = 150$ K.

As seen in Fig. 2.19, the Fermi level is located at -3.8 eV at 300 K. On the other hand, the Fermi level shifts from -3.8 eV to -3.89 eV as temperature is lowered. The total electron number continuously changes as the chemical potential is changed at $T = 400$ K and $T = 300$ K. The reason is that the new electronic states are formed at these energy levels. On the contrary, we see that total electron number is nearly constant in a narrow energy gap at $T = 200$ K and $T = 150$ K. Figure 2.18 show the total magnetic moment M_t of oxy-heme as a function of chemical potential μ for the different temperatures. We see clearly that the magnetic moment of molecule decreases with formation of the magnetic gap.

In this thesis, we propose a magnetic mechanism for the Fe-O_2 bonding. Combined DFT+QMC results show that the charge transfer occurs between the Fe(3d) and O_2 orbitals. On the other hand, the charge transfer to 3d orbitals is an energetically costly process due to strong Coulomb interactions. This difficulty is overcome by the location of the upper-Hubbard level of the Fe($3d_{xy}$) orbital. Our results show that the upper-Hubbard level of the Fe($3d_{xy}$) orbital is located very close to Fermi level. Hence, the charge transfer occurs easily from the O_2 to Fe(3d) orbitals, in particular Fe($3d_{xy}$) orbital and the spin 0 state is obtained in a narrow energy region. We say that the magnetic moment and the magnetic correlations are developed by the electron transfer, and the energy of the system is minimized in this way.

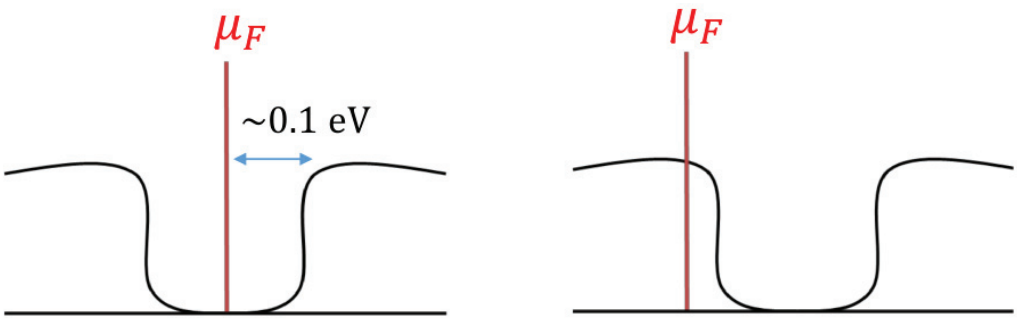

Figure 6.1. Illustration of the change of the location of Fermi level with respect to pH values of the environment. Here, the vertical black line represents the Fermi level, μ_{F}. In the left picture, the Fermi level is located in the magnetic gap which is about 0.1 eV. In the right picture, the Fermi level moves the out of the magnetic gap due to change in the pH of the environment.

6.2. Bohr effect

As explained in the Introduction, the Bohr effect is the effect of pH on the dissociation of oxygen. When the H^+ concentration increases, the pH decreases and the hemoglobin releases O_2 to the tissues. pH in the lungs is about 7.4 and in the tissues about 7.2. The differences between the pH values of lungs and tissues enable the O_2 transportation and the molecule releases O_2 with a small change in the pH. In this thesis, we propose an explanation for the functioning of Bohr effect.

In Chapter 2, we observe the change in the electron number as a function of chemical potential. The change in the electron number is similar to the chnage in H^+ ions in the environment. DFT+QMC results show that the magnetic properties of hemoglobin are easily changed by chemical potential. Hence, the changing of the pH may lead to moving the chemical potential out side of the magnetic gap as seen in Fig. 6.1. We show that the O_2-Fe charge transfer occurs in narrow energy gap and the spin state goes to 0. This may be mechanism for how the pH controls the oxygen affinity in the red blood cells.

6.3. Cooperativity

Cooperativity means that the O_2 affinity of hemoglobin is increased by the quantity of oxygen bounds.

Pauling and Coryell (Pauling and Coryell (1936)) found that the magnetic moment per heme equals 5.49 μ_B. It is known that if the molecule is in the spin 2 state, the magnetic moment equals to 4.9 μ_B. Pauling and Coryell suggested that the ferromagnetic heme-heme correlations may lead to 5.49 μ_B.

The total molecular susceptibility χ_{HbA} is calculated by using the Eq. 6.1. Here, the total magnetic moment M^z_{HbA} of the molecule is the summation of the magnetic moment of the each heme groups as in the Eq. 6.2.

$$\chi_{\mathrm{HbA}} = \int_0^\beta d\tau \langle M^z_{\mathrm{HbA}}(\tau) M^z_{\mathrm{HbA}}(0)\rangle \tag{6.1}$$

$$M^z_{\mathrm{HbA}} = \sum_i^4 M^z_{\mathrm{heme},i} \tag{6.2}$$

If the Eq. 6.2 is placed in Eq. 6.1, the following equations is obtained:

$$\langle M^z_{\mathrm{HbA}}(\tau) M^z_{\mathrm{HbA}}(0)\rangle = \left\langle \left(\sum_i^4 M^z_{\mathrm{heme},i}(\tau)\right)\left(\sum_j^4 M^z_{\mathrm{heme},j}(0)\right)\right\rangle \tag{6.3}$$

and the total molecular susceptibility equals to

$$\chi^{\mathrm{exp}}_{\mathrm{HbA}} = \int_\beta^0 d\tau \left[\sum_{i=1}^4 \langle M^z_{\mathrm{heme},i}(\tau) M^z_{\mathrm{heme},i}(0)\rangle + \sum_{i,j=1}^4 \langle M^z_{\mathrm{heme},i}(\tau) M^z_{\mathrm{heme},j}(0)\rangle\right] \tag{6.4}$$

The DFT+QMC results show that the total heme moments equals to 4.1 μ_B. From

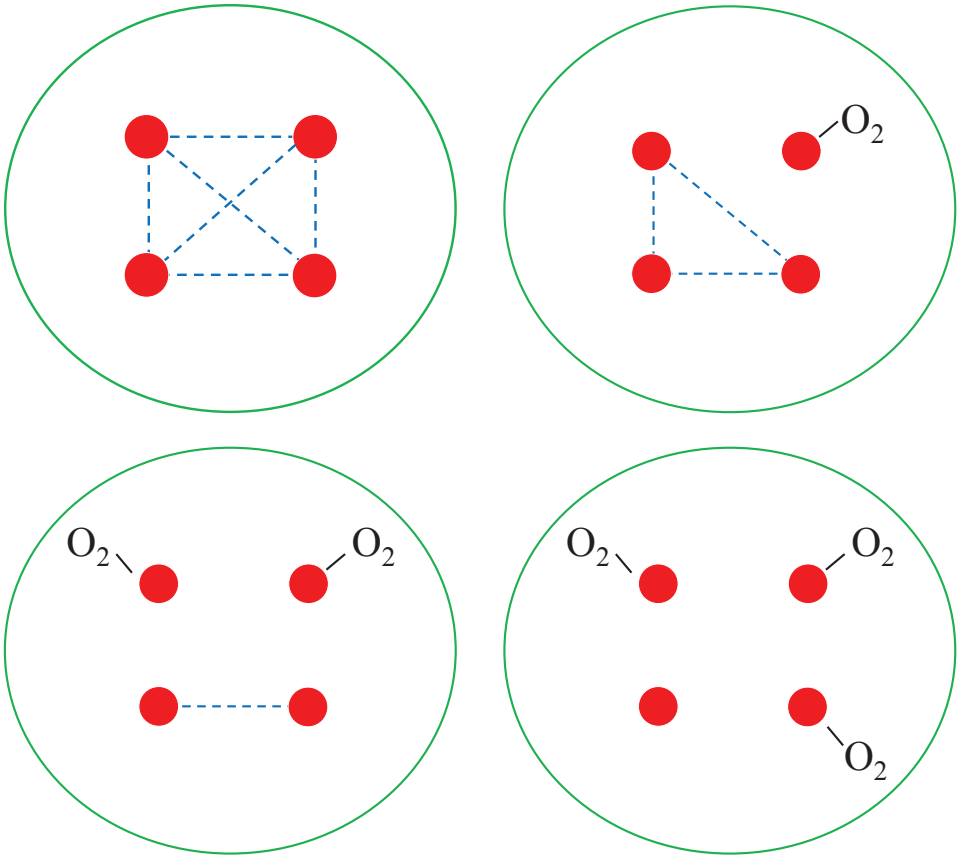

Figure 6.2. Illustration of the magnetic mechanism for cooperativity. Here, the dashed lines represent the ferromagnetic correlations between the heme groups. The red balls represent the Fe atoms located at the centers of hemes.

Eq. 6.4, the difference between the experimental results and our results require an average heme-heme ferromagnetic correlations, 4.3 $(\mu_B)^2$. This ferromagnetic heme-heme correlations may arise indirectly from the Fe-host AF coupling. The large number of host sites in the AF screening cloud of Fe may lead to heme-heme ferromagnetic correlations and this could lead to cooperativity.

In this thesis, we propose two explanations for the mechanism of cooperativity. The first one is the simple ferromagnetic bound breaking. As seen in Fig. 6.2, when the first O_2 binds the hemoglobin, it must break 6 ferromagnetic bonds. When the second O_2 binds the molecule, the 3 ferromagnetic correlations must be broken. On the other hand, when the last O_2 binds, there are no ferromagnetic correlations to be broken.

The other explanation is based on the spin non-conservancy in the binding of O_2 to heme. As known that the spin state of deoxy is 2 and the spin state of O_2 is 1. When O_2 binds the molecule, the resultant oxy-heme is in S=0 spin state. This spin non-

conservancy may limit the reaction rate. If ferromagnetic heme-heme correlations occur, spin transfer can be possible from one heme to other. Hence, the O_2 may easily binds to Fe.

CHAPTER 7

FUTURE STUDIES

There are many bio-inorganic molecules which have the similar electronic structure as hemoglobin molecule. Chlorophyll (Chls) is an example for these kind of molecules.

Chls are green pigments found in some bacterias and the chloroplast of algae and plants. Chls contain a porphyrin with magnesium ion (Mg^{+2}) in the center. They channel energy from absorbed photons to the reaction center with the efficiency 95% through the process of photosynthesis. In addition, they participate charge separation and electron transfer in the reaction center. Many theoretical works have been done to understand the electronic absorption in various Chls. However, their mechanism have not been completely understood.

As shown in Fig. 7.1, Chl contains a Mg atom. We know that hemoglobin molecule consists of Fe atom as metal atom. In these two molecules, the metal atoms are located in a porphyrin layer.

Because of this structural similarity, we will use the Haldane-Anderson model to study the electronic and magnetic properties of Chls molecule, and we will solve this model by using DFT+QMC algorithm to understand the role of metal atom in the functioning of Chl molecule.

Organo-transition metal compounds such as triplet emitters are studied by many research group due to their usage in organic light-emitting diodes (OLEDs). $Ir(ppy)_3$ or $[Ru(bpy)_3]^{+2}$ are examples for triplet emitters. These organo-transition metal compounds offer a great advantage to obtain the high efficient and low power consuming light-emitting systems.

In the future studies, we will study the electronic properties of triplet emitters for OLEDs applications. In particular, we will focus on what is the role of transition metal on efficiency of OLEDs and how the functioning of OLEDs change by changing the magnetic properties of triplet emitters.

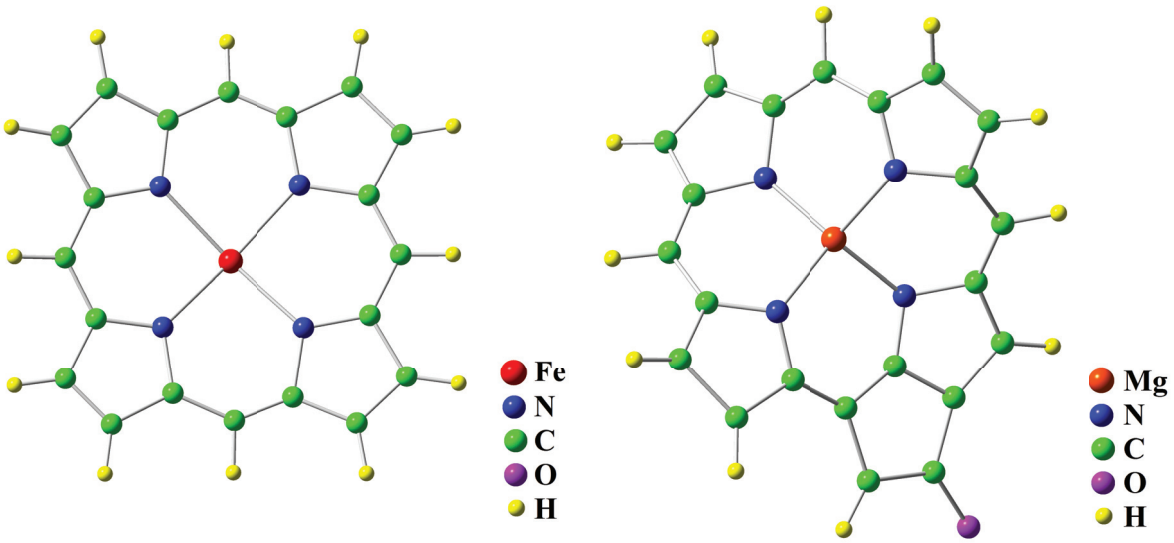

Figure 7.1. The left figure shows the molecular structure of hemoglobin molecule. The right figure shows the molecular structure of chlorophyll molecule. Chlorophyll contains Mg atom at the center of porphyrin layer. Hemoglobin contains Fe atom at the center of porphyrin layer.

CHAPTER 8

CONCLUSIONS

In this thesis, we study the electronic and magnetic properties of the human adult deoxy and oxy hemes by using an extended multi-orbital Haldane-Anderson model. We obtained the molecular structure of the hemoglobin molecules from the Protein Data Bank. These structures were determined by X-ray measurements with the 1.25 Å resolution on a crystal of hemoglobin molecules at room temperature. Since the hemoglobin molecule consists of about 9700 atoms, we perform our calculations for the reduced heme clusters. For the Haldane-Anderson model of these clusters, we include the inter-orbital Coulomb interactions along with the Hund's coupling. We have calculated the model parameters of the Anderson Hamiltonian by the DFT method. Then, we have used the QMC technique to study electronic and magnetic properties of the hemoglobin molecule. By using combined DFT+QMC method, we calculate the magnetic correlations and the susceptibility of the deoxy and oxy-heme molecules.

Firstly, we calculated the magnetic moments at each Fe(3d) orbitals and the magnetic correlations between them. Our results show that Fe(3d) and the host electrons have finite magnetic moments for both the deoxy-heme and oxy-heme clusters. We see ferromagnetic correlations between the Fe(3d) orbitals in the deoxy-heme and the molecule has the effective spin S=1.60 at 300 K. On the other hand, Fe(3d) correlations are very small for the oxy-heme with respect to the deoxy cluster. The reason is that for the oxy-case, the antiferromagnetic (AF) correlations occur between the Fe(3d) electrons and host electrons. These antiferromagnetic correlations suppress the Fe(3d) ferromagnetic correlations. Hence, the effective spin of the oxy-heme decreases to 0.68 at 300 K. We observe that the effective spin is lowered from 1.60 to 0.68 by binding of O_2 due to existence of the impurity bound states (IBS). These new electronic states are formed both in deoxy-heme and oxy-heme clusters. IBS are occupied by electrons in deoxy, while they are unoccupied in oxy. When IBS are occupied as in the deoxy, Fe(3d) orbitals have strong ferromagnetic correlations due to Hund's coupling. Hence, deoxy molecule has the high-spin state. On the other hand, when IBS are unoccupied as being in oxy, AF correlations develop between the Fe(3d) and host orbitals. These AF correlations suppress the Hund's coupling between the Fe(3d) orbitals. Due to competition between the Hund's coupling and Fe(3d)-host AF correlations, oxy-heme cluster has the lower spin state than

the deoxy-heme.

We observe that the existence of the IBS is not sufficient to obtain the low-spin state for the oxy case. We changed the temperature from 400 K to 150 K and we calculated the susceptibility and magnetic moments of Fe(3d) and host electrons.

For the deoxy-heme, the susceptibility shows the 1/T Curie type behaviour and the susceptibility increases rapidly as temperature decreases. On the other hand, the susceptibility of the oxy-heme has the two different temperature regime. Above T=300 K, the susceptibility has a Curie type dependency while below the T=300 K, wee see that the susceptibility of the oxy-heme is suppressed as T decreases. This suppression of the susceptibility is due to the opening of a gap in the magnetic response within a narrow energy range of the Fermi level.

Then, for the oxy-heme cluster, we discuss the temperature dependence of the magnetic correlations. We observe that the total electron number of Fe(3d) orbitals and the O_2 orbitals depend on the temperature. In other words, the Fermi level exhibits strong dependence on the temperature. By decreasing the temperature, we see the electron transfer from mainly O_2 (2p) states to the Fe($3d_{xy}$) states. These electrons transfers lead to negatively increase in the antiferromagnetic correlations between the Fe(3d) and host states. In addition, the ferromagnetic correlations between the Fe(3d) states decrease with the decreasing in the T. Due to these weak Fe(3d) ferromagnetic correlations and the strong Fe(3d)-O_2 (2p) AF correlations, the oxy-heme cluster has the low-spin state at small temperatures.

In this thesis, we propose a magnetic mechanism for the Fe-O_2 bonding. Combined DFT+QMC results show that the charge transfer occurs between the Fe(3d) and O_2 orbitals. On the other hand, the charge transfer to 3d orbitals is an energetically costly process due to strong Coulomb interactions. This difficulty is overcome by the location of the upper-Hubbard level of the Fe($3d_{xy}$) orbital. Our results show that the upper-Hubbard level of the Fe($3d_{xy}$) orbital is located very close to Fermi level. Hence, the charge transfer occurs easily from the O_2 to Fe(3d) orbitals, in particular Fe($3d_{xy}$) orbital and the spin 0 state is obtained in a narrow energy region. We say that the magnetic moment and the magnetic correlations are developed by the electron transfer, and the energy of the system is minimized in this way. This means that Fe-O_2 binding has the magnetic origin for the oxy case.

We observe that the Fe-porphyrin layer AF correlations exist in both deoxy and oxy-cases. The experimental evidence for this is provided by the MCD data on the deoxy-HbA. The MCD spectra of on deoxy-HbA has a peak near 3 eV. This peak has an anoma-

lous line shape and 1/T temperature dependency. In the same energy range, the optical absorption has a temperature-independent peak. Our results show that the anomalous line shape originates from the antiferromagnetic correlations between the Fe(3d) orbitals and the partially filled π^* states of the porphyrin layer. In DFT+QMC calculations, we find the π_1^* which is a nearly-half filled state and π_2^* which is nearly empty state. In addition, the bonding π state is located at about 3 eV. In the light of our DFT+QMC results, our explanation for the anomalous line shape of the MCD spectrum for the deoxy-HbA as the following: in an applied magnetic field which is the up direction, the Fe spin which is polarized in the down direction hybridizes with the one down electron of π. Also, there is an one up electron in the π_1^* states due to antiferromagnetic exchange coupling with the Fe(3d) spin. One down electron located at π state moves to the π_1^* and the the up-spin electron in the π state spin-flips electron through the AF coupling with the left-circularly polarized light. In the next step, the up-spin of Fe flips again its spin because of the spin-orbit coupling. In this case, the electron transition occurs between the $\pi \rightarrow \pi_2^*$ states. According to our explanation on the MCD spectrum of deoxy-HbA, the temperature-dependent MCD spectra arises from the $\pi \rightarrow \pi_1^*$ with the LCP and $\pi \rightarrow \pi_2^*$ with the RCP. In addition, our explanation says that the Soret MCD transitions are spin and orbital selective.

In the light of the magnetic measurements presented in this thesis, we propose some explanations for the Bohr effect and the cooperativity. These are the fundemantal functional properties of the hemoglobin molecule because they increase the oxygen transporting effiency of the molecule. DFT+QMC results find that the magnetic properties of the molecule depend sensitively to the electron fillings. We see S=0 state in a narrow energy gap. The out of this energy gap, the hemoglobin molecule exhibits different magnetic behaviours. The dependency of the magnetic properties of the hemoglobin on the location of the chemical potential may be the mechanism for how the pH of the red blood cells controls the oxygen affinity.

In this thesis, we propose two possible mechanisms for the cooperativity. The first one is the simple ferromagnetic bound breaking. When the first O_2 binds the hemoglobin, it must break 6 ferromagnetic bonds. When the second O_2 binds the molecule, the 3 ferromagnetic correlations must be broken. On the other hand, when the last O_2 binds, there are no ferromagnetic correlations to be broken.

The second one is based on the spin non-conservancy in the binding of O_2 to heme. As known that the spin state of deoxy is 2 and the spin state of O_2 is 1. When O_2 binds the molecule, the resultant oxy-heme is in S=0 spin state. This spin non-conservancy may

limit the reaction rate. If ferromagnetic heme-heme correlations occur, spin transfer can be possible from one heme to other. Hence, the O_2 may easily binds to Fe.

In this thesis, we compare our DFT+QMC results with the RIXS and XAS. The d-d transitions are obtained by the RIXS. For deoxy-heme, we see that the DFT+QMC results and the experimental RIXS are not compatible. On the other hand, the DFT+QMC results for oxy-heme are good agreement with the experimental results. We also compare the DFT+QMC results with the XAS. Here, we see that the spectrum for the deoxy-heme and oxy-heme are broaden with respect to XAS. These results show that the U and J, and also double-counting term may affect the spectrum. In addition, the continuous-time quantum Monte Carlo may be developed to study the RIXS and XAS spectrum of deoxy-heme and oxy-heme molecules.

The DFT+QMC results show that the magnetic properties and the functioning of the HbA molecule is a strongly-correlated electron problem. There are many metalloproteins, metalloenzymes and bioinorganic molecules which contain transition metal atoms and have the similar molecular structure with the hemoglobin. The electronic structures of these molecules may be modeled within the same framework and their magnetic properties and the functions may be studied by using the many-body technique which is described in this thesis.

REFERENCES

Adair, G. S. *et al.* (1925). The hemoglobin system vi. the oxygen dissociation curve of hemoglobin. *Journal of Biological Chemistry 63*(2), 529–545.

Ament, L. J., M. Van Veenendaal, T. P. Devereaux, J. P. Hill, and J. Van Den Brink (2011). Resonant inelastic x-ray scattering studies of elementary excitations. *Reviews of Modern Physics 83*(2), 705.

Anderson, P. W. (1961). Localized magnetic states in metals. *Physical Review 124*(1), 41.

Anisimov, V. I., J. Zaanen, and O. K. Andersen (1991). Band theory and mott insulators: Hubbard U instead of stoner I. *Physical Review B 44*(3), 943.

Aziz, E. F., N. Ottosson, S. Bonhommeau, N. Bergmann, W. Eberhardt, and M. Chergui (2009). Probing the electronic structure of the hemoglobin active center in physiological solutions. *Physical Review Letters 102*(6), 068103.

Bren, K. L., R. Eisenberg, and H. B. Gray (2015). Discovery of the magnetic behavior of hemoglobin: A beginning of bioinorganic chemistry. *Proceedings of the National Academy of Sciences 112*(43), 13123–13127.

Bulut, N., K. Tanikawa, S. Takahashi, and S. Maekawa (2007). Long-range ferromagnetic correlations between anderson impurities in a semiconductor host: Quantum monte carlo simulations. *Physical Review B 76*(4), 045220.

Chen, H., M. Ikeda-Saito, and S. Shaik (2008). Nature of the Fe-O2 bonding in oxy-myoglobin: Effect of the protein. *Journal of the American Chemical Society 130*(44), 14778–14790.

Czyżyk, M. and G. Sawatzky (1994). Local-density functional and on-site correlations: the electronic structure of la 2 cuo 4 and lacuo 3. *Physical Review B 49*(20), 14211.

Degtyarenko, K. (2000). Bioinorganic motifs: towards functional classification of metalloproteins. *Bioinformatics 16*(10), 851–864.

Ellison, M. K., C. E. Schulz, and W. R. Scheidt (2002). Structure of the deoxymyoglobin model [Fe (TPP)(2-MeHIm)] reveals unusual porphyrin core distortions. *Inorganic Chemistry 41*(8), 2173–2181.

Ferrell, J. E. (2009). Q&a: cooperativity. *Journal of Biology 8*(6), 53.

Ferry, R. M. and A. A. Green (1929). Studies in the chemistry of hemoglobin iii. the equilibrium between oxygen and hemoglobin and its relation to changing hydrogen ion activity. *Journal of Biological Chemistry 81*(1), 175–203.

Goddard, W. A. and B. D. Olafson (1975). Ozone model for bonding of an O2 to heme in oxyhemoglobin. *Proceedings of the National Academy of Sciences 72*(6), 2335–2339.

Haldane, F. and P. Anderson (1976). Simple model of multiple charge states of transition-metal impurities in semiconductors. *Physical Review B 13*(6), 2553.

Harada, Y., M. Taguchi, Y. Miyajima, T. Tokushima, Y. Horikawa, A. Chainani, Y. Shiro, Y. Senba, H. Ohashi, H. Fukuyama, *et al.* (2009). Ligand energy controls the heme-fe valence in aqueous myoglobins. *Journal of the Physical Society of Japan 78*(4), 044802–044802.

Hirsch, J. E. and R. M. Fye (1986). Monte carlo method for magnetic impurities in metals. *Physical Review Letters 56*(23), 2521.

Hocking, R. K., E. C. Wasinger, Y.-L. Yan, F. M. deGroot, F. A. Walker, K. O. Hodgson, B. Hedman, and E. I. Solomon (2007). Fe l-edge x-ray absorption spectroscopy of low-spin heme relative to non-heme fe complexes: Delocalization of fe d-electrons into the porphyrin ligand. *Journal of the American Chemical Society 129*(1), 113–125.

Ichimura, M., K. Tanikawa, S. Takahashi, G. Baskaran, and S. Maekawa (2006). Foundations of quantum mechanics in the light of new technology, Edited by S. Ishioka and K. Fujikawa.

Josephy, P. (1992). Haemoglobin and cooperativity. *Biochemical Education 20*(2), 91–93.

Jungwirth, T., J. Sinova, A. MacDonald, B. Gallagher, V. Novák, K. Edmonds, A. Rushforth, R. Campion, C. Foxon, L. Eaves, *et al.* (2007). Character of states near the fermi level in (Ga, Mn) As: Impurity to valence band crossover. *Physical Review B 76*(12), 125206.

Kandemir, Z. (2013). Mapping of the electronic structure of metalloproteins onto multi-orbital Anderson model using the density functional theory. Master's thesis, Izmir Institute of Technology.

Kandemir, Z., S. Mayda, and N. Bulut (2016). Electronic structure and correlations of vitamin B 12 studied within the Haldane-Anderson impurity model. *The European Physical Journal B 89*(5), 113.

Kaneko, J. J., J. W. Harvey, and M. L. Bruss (2008). *Clinical biochemistry of domestic animals*. Academic Press.

Karolak, M. (2013). Electronic correlation effects in transition metalsystems: From bulk crystals to nanostructures.

Karolak, M., G. Ulm, T. Wehling, V. Mazurenko, A. Poteryaev, and A. Lichtenstein (2010). Double counting in LDA+DMFT–The example of nio. *Journal of Electron Spectroscopy and Related Phenomena 181*(1), 11–15.

Kepp, K. P. (2017). Heme: From quantum spin crossover to oxygen manager of life. *Coordination Chemistry Reviews 344*, 363–374.

Kirk, M. L. and K. Peariso (2003). Recent applications of MCD spectroscopy to metalloenzymes. *Current Opinion in Chemical Biology 7*(2), 220–227.

Kohn, W. and L. J. Sham (1965). Self-consistent equations including exchange and correlation effects. *Physical Review 140*(4A), A1133.

Kuneš, J., V. Anisimov, A. Lukoyanov, and D. Vollhardt (2007). Local correlations and hole doping in nio: A dynamical mean-field study. *Physical Review B 75*(16), 165115.

Lang, G. and W. Marshali (1966). Mössbauer effect in some haemoglobin compounds.

Proceedings of the Physical Society 87(1), 3.

Lehnert, N., S. D. George, and E. I. Solomon (2001). Recent advances in bioinorganic spectroscopy. *Current Opinion in Chemical Biology 5*(2), 176–187.

Mack, J., M. J. Stillman, and N. Kobayashi (2007). Application of mcd spectroscopy to porphyrinoids. *Coordination Chemistry Reviews 251*(3-4), 429–453.

Maekawa, S., T. Tohyama, S. E. Barnes, S. Ishihara, W. Koshibae, and G. Khaliullin (2013). *Physics of Transition Metal Oxides*, Volume 144. Springer Science & Business Media.

Mason, W. R. (2007). *Magnetic circular dichroism spectroscopy*. John Wiley & Sons.

Mayda, S. (2013). Electronic correlations in metalloproteins: A quantum Monte Carlo study. Master's thesis, Izmir Institute of Technology.

Mayda, S., Z. Kandemir, and N. Bulut (2017). Electronic structure of cyanocobalamin: DFT+ QMC study. *Journal of Superconductivity and Novel Magnetism 30*(11), 3301–3308.

McCLURE, D. S. (1960). Electronic structure of transition-metal complex ions. *Radiation Research Supplement 2*, 218–242.

McMaster, J. and V. S. Oganesyan (2010). Magnetic circular dichroism spectroscopy as a probe of the structures of the metal sites in metalloproteins. *Current Opinion in Structural Biology 20*(5), 615–622.

Monod, J., J. Wyman, and J.-P. Changeux (1965). On the nature of allosteric transitions: a plausible model. *J Mol Biol 12*(1), 88–118.

Ohno, H., H. Munekata, T. Penney, S. Von Molnar, and L. Chang (1992). Magnetotransport properties of p-type (in, mn) as diluted magnetic iii-v semiconductors. *Physical Review Letters 68*(17), 2664.

Ohno, H., A. Shen, F. Matsukura, A. Oiwa, A. Endo, S. Katsumoto, and Y. Iye (1996). (Ga, Mn) As: a new diluted magnetic semiconductor based on GaAs. *Applied*

Physics Letters 69(3), 363–365.

Park, S.-Y., T. Yokoyama, N. Shibayama, Y. Shiro, and J. R. Tame (2006). 1.25 å resolution crystal structures of human haemoglobin in the oxy, deoxy and carbonmonoxy forms. *Journal of Molecular Biology 360*(3), 690–701.

Pauling, L. and C. D. Coryell (1936). The magnetic properties and structure of hemoglobin, oxyhemoglobin and carbonmonoxyhemoglobin. *Proceedings of the National Academy of Sciences 22*(4), 210–216.

Perutz, M., M. Rossmann, A. Cullis, H. Muirhead, G. Will, and A. North (1960). Structure of hemoglobin. In *Brookhaven Symp Biol*, Volume 13, pp. 165–183.

Perutz, M. F., A. Wilkinson, M. Paoli, and G. Dodson (1998). The stereochemical mechanism of the cooperative effects in hemoglobin revisited. *Annual Review of Biophysics and Biomolecular Structure 27*(1), 1–34.

Phillips, S. E. (1980). Structure and refinement of oxymyoglobin at 1· 6 å resolution. *Journal of Molecular Biology 142*(4), 531–554.

Poulos, T. L. (2014). Heme enzyme structure and function. *Chemical Reviews 114*(7), 3919–3962.

Reif, D. W. (1992). Ferritin as a source of iron for oxidative damage. *Free Radical Biology and Medicine 12*(5), 417–427.

Scheidt, W. R. and C. A. Reed (1981). Spin-state/stereochemical relationships in iron porphyrins: implications for the hemoproteins. *Chemical Reviews 81*(6), 543–555.

Schuth, N., S. Mebs, D. Huwald, P. Wrzolek, M. Schwalbe, A. Hemschemeier, and M. Haumann (2017). Effective intermediate-spin iron in o2-transporting heme proteins. *Proceedings of the National Academy of Sciences 114*(32), 8556–8561.

Swietach, P., T. Tiffert, J. M. Mauritz, R. Seear, A. Esposito, C. F. Kaminski, V. L. Lew, and R. D. Vaughan-Jones (2010). Hydrogen ion dynamics in human red blood cells. *The Journal of Physiology 588*(24), 4995–5014.

Tomoda, Y., N. Bulut, and S. Maekawa (2009). Inter-impurity and impurity–host magnetic correlations in semiconductors with low-density transition–metal impurities. *Physica B: Condensed Matter 404*(8-11), 1159–1168.

Treu, J. I. and J. Hopfield (1975). Magnetic circular dichroism in hemoglobin. *The Journal of Chemical Physics 63*(2), 613–623.

Vojtěchovskỳ, J., K. Chu, J. Berendzen, R. M. Sweet, and I. Schlichting (1999). Crystal structures of myoglobin-ligand complexes at near-atomic resolution. *Biophysical Journal 77*(4), 2153–2174.

Wang, M. S., K. J. Hoegler, and M. H. Hecht (2019). Unevolved de novo proteins have innate tendencies to bind transition metals. *Life 9*(1), 8.

Weiss, J. J. (1964). Nature of the iron–oxygen bond in oxyhaemoglobin. *Nature 203*(4941), 183.

Yuan, Y., M. F. Tam, V. Simplaceanu, and C. Ho (2015). New look at hemoglobin allostery. *Chemical Reviews 115*(4), 1702–1724.

APPENDIX A

PARAMETERS OF THE ANDERSON HAMILTONIAN

We obtain the one-electron parameters which are ε_m, $\varepsilon_{d\nu}$ and $V_{m\nu}$ for the effective multi-orbital Haldane-Anderson model by using density functional theory (DFT) method (Kohn and Sham (1965)). These calculations are performed for the deoxy-heme and oxy-heme clusters which are reduced form of the human adult hemoglobin (HbA) molecule. the molecular coordinates of these molecules are determined by the X-ray measurements (Park *et al.* (2006)). In DFT calculations, we use the natural atomic orbitals (NAO's) instead of atomic orbitals. The reason is that the atomic orbitals do not form an orthogonal basis. First, we express the Fock matrix in the NAO basis. We take the Fe($3d_\nu$) NAO's as the impurity orbitals and their energy levels as $\varepsilon_{d\nu}$'s in the Anderson Hamiltonian. Diagonalizing the remaining part of the Fock matrix, we obtain the host eigenstates $|u_m\rangle$ and their energy levels ε_m, and, in addition, the hybridization matrix elements $V_{m\nu}$. This procedure is explained in more detail in Ref. (Kandemir *et al.* (2016), Mayda *et al.* (2017), Kandemir (2013)). The DFT calculations are carried out by using the Gaussian program with the BP86 energy functional [BP86] and the 6-31G basis set with $N = 483$ basis functions for the deoxy-heme cluster and $N = 501$ basis functions for the oxy heme cluster. The energy levels of the Fe($3d_\nu$) orbitals ε_ν and of the host states ε_m are shown in Fig. A.1(a) and (b). We use the parameters ε_m, ε_ν and $V_{m\nu}$ as input parameters for the QMC simulations.

The HbA molecule has about 9700 atoms. In our calculations, we retain only 75 atoms for the deoxy-heme cluster and 77 atoms for the oxy-heme cluster as seen in Fig. 1.1(b-c). In the DFT calculation of the energy spectrum of the clusters, it is necessary to be careful with the finite size effect arising from the boundary of the clusters. As shown in Fig.1.1(b), the host states localized on the oxygen and the carbon sites at the boundaries of the cluster has an energy close the Fermi level. On the other hand, if we use the larger clusters containing 87 or 96 atoms, the distal histidine part contains more sites and the oxygen site is not close to the boundary, and we see that the host states arising from the boundary moves away from the Fermi level to the higher energy. Hence, we have removed the boundary host states to control the finite size effects for the 75 atoms.

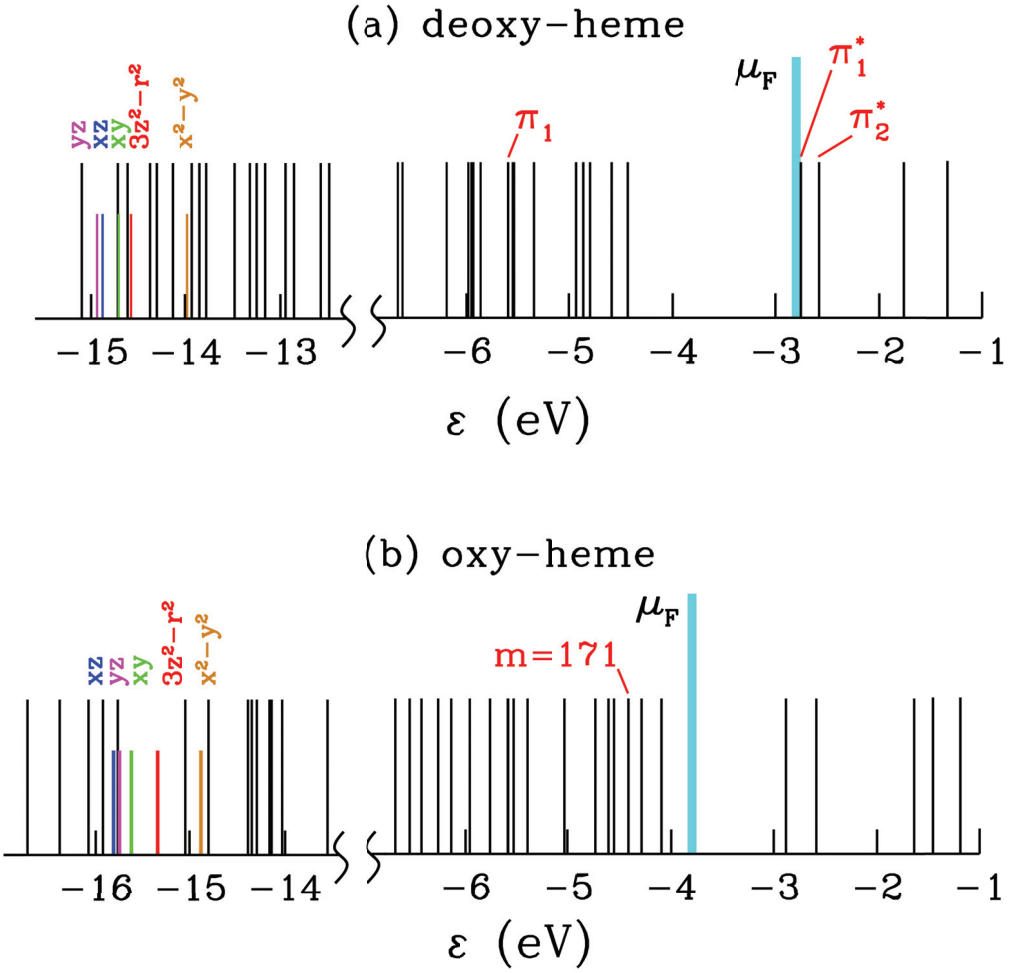

Figure A.1. The energy levels of the host states ε_m and of the Fe(3d) states ϵ_ν are shown of (d) the deoxy and (e) the oxy-heme clusters. These values for ε_m and ε_ν are used in the QMC simulations of the effective Anderson model. In the deoxy case, the bonding state π and the antibonding states π_1^* and π_2^* states are indicated. In the oxy case, the host state which is closest to the Fermi level is composed of the $2p$ orbitals of the O_2 attached to Fe. This state, which we labelled as ϕ_O, is indicated in addition the antibonding π_1^* and π_2^* states. Here, μ_F denotes the location of the Fermi level obtained by the QMC calculations at $T = 300$ K.

A.1. Double-counting term

It is important to note that, in the DFT+QMC approach, the Coulomb interactions U, U' and $U'-J$ are taken into account both by the DFT and the QMC calculations. Therefore, in order to prevent this double counting, an orbital-dependent double-counting term μ_ν^{DC}, which is defined as

$$\mu_\nu^{\mathrm{DC}} = \frac{U n_{d\nu}^{\mathrm{DFT}}}{2} + [U' + (U' - J)] \sum_{\nu' \neq \nu} \frac{n_{d\nu'}^{\mathrm{DFT}}}{2} \tag{A.1}$$

is substracted from the bare Fe($3d_\nu$) levels, $\varepsilon_{d\nu} \rightarrow \tilde{\varepsilon}_{d\nu} = \varepsilon_{d\nu} - \mu_\nu^{\mathrm{DC}}$ (Karolak (2013),Karolak *et al.* (2010),Anisimov *et al.* (1991),Czyżyk and Sawatzky (1994),Kuneš *et al.* (2007)). In the Anderson Hamiltonian, $\tilde{\varepsilon}_{d\nu}$ is used instead of $\varepsilon_{d\nu}$. Here, $\langle n_{d\nu}^{\mathrm{DFT}} \rangle$ is the electron number in the Fe($3d_\nu$) NAO's obtained by the DFT calculations.

A.2. Density of states

In this part, we present the one-electron parameters calculated by DFT for deoxy and oxy molecules. Here, total density of states $D(\epsilon)$ is defined by

$$D(\epsilon) = \sum_{n=1}^{N} \delta(\epsilon - E_n), \tag{A.2}$$

and host density of states is defined by

$$D_h(\epsilon) = \sum_{n=1}^{N-5} \delta(\epsilon - \epsilon_m). \tag{A.3}$$

Figure A.2 (a) shows the total density of states $D(\epsilon)$ of deoxy molecule. In this figure, the highest occupied moleculer orbital (HOMO) is located at -3.52 eV and the lowest occupied moleculer orbital (LUMO) is located at -3.02 eV. The host density of states $D_h(\epsilon)$ as a function of energy ϵ is indicated in Fig A.2 (b). The coloured vertical lines show the shifted energy levels of Fe($3d_\nu$) orbitals $\tilde{\varepsilon}_{d\nu}$. For these parameters, while $\nu =$

$x^2 - y^2$ is located at $\varepsilon_\nu \approx -14$ eV, the other Fe($3d_\nu$) orbitals are located at $\varepsilon_\nu \approx -14.7$ eV. Figure A.3 (a) shows the total density of states $D(\epsilon)$ of oxy molecule. In this figure, the highest occupied molecular orbital (HOMO) is located at -4.11 eV and the lowest occupied molecular orbital (LUMO) is located at -3.84 eV. The host density of states $D_h(\epsilon)$ as a function of energy ϵ is indicated in Fig A.3 (b). The vertical lines show the shifted energy levels of Fe($3d_\nu$) NAO's $\tilde{\varepsilon}_{d\nu}$. For these parameters, Fe($3d_{x^2-y^2}$) NAO's are located at $\varepsilon_\nu \approx -14.88$ eV and the other Fe($3d$) orbitals are located at ≈ -15.7 eV.

A.3. Hybridization matrix elements

The square of the hybridization matrix elements $|V_{m\nu}|^2$ between the m'th host states and Fe($3d_\nu$) orbitals are shown as a function of ε_m in Fig A.4. This figure indicates that $m = 144$'th, 145'th, 146'th, 153'rd and 163'rd host states have the strongest hybridization with $\nu = 3z^2 - r^2$ and $m = 152$'nd host state hybridizes most strongly with Fe($3d_{x^2-y^2}$) orbital. We will see that these host orbitals have the magnetic correlations with Fe($3d$) orbitals.

In addition to these host states, the $|V_{m\nu}|^2$ value of 165, 166 and 167'th host states are shown in Fig. A.4 (a-b). These host states are located at near of the LUMO level and it will be shown that $m = 165$, 166 and 167 also have the magnetic correlations with the Fe($3d$) orbitals. Hence, they are important to obtain the total magnetic moment of deoxy molecule. The square of the hybridization matrix elements $|V_{m\nu}|^2$ between the m'th host states and Fe($3d_\nu$) NAO's are shown as a function of ε_m in Fig A.5. This figure indicates that $m = 153$, 154 and 173'rd host states have the strongest hybridization with $\nu = 3z^2 - r^2$. Figure A.5 (b) shows that $m = 158$ and 159'th host states hybridize most strongly with Fe($3d_{x^2-y^2}$) NAO's.

In addition to these host states, the $|V_{m\nu}|^2$ value of 174, 175 and 176'th host states are shown in Fig. A.5 (a-b). These host states are located at near of the LUMO level and it will be shown that $m = 174$, 175 and 176 also have the magnetic correlations with the Fe($3d$) orbitals. Hence, they are important to obtain the total magnetic moment of oxy molecule.

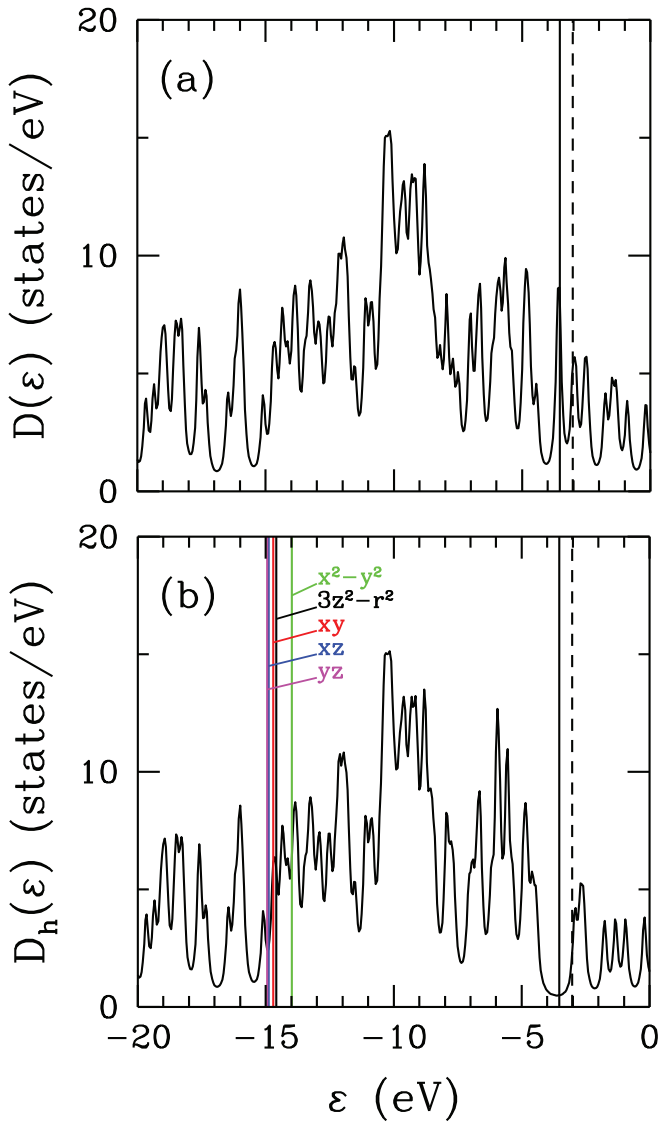

Figure A.2. (a) Total density of states $D(\varepsilon)$ of deoxy obtained by the DFT calculations. (b) Density of states of the host states of the effective Haldane-Anderson model $D_h(\varepsilon)$. Here, energy levels of Fe($3d_\nu$) orbitals are shifted by the double counting term, μ_ν^{DC}, which are obtained for $U = 4$ eV and $J = 0.9$ eV. The shifted Fe($3d_\nu$) energy levels $\tilde{\varepsilon}_{d\nu}$ are indicated by the colored vertical lines. In addition, the vertical black solid and dashed lines denote the HOMO and LUMO levels, respectively.

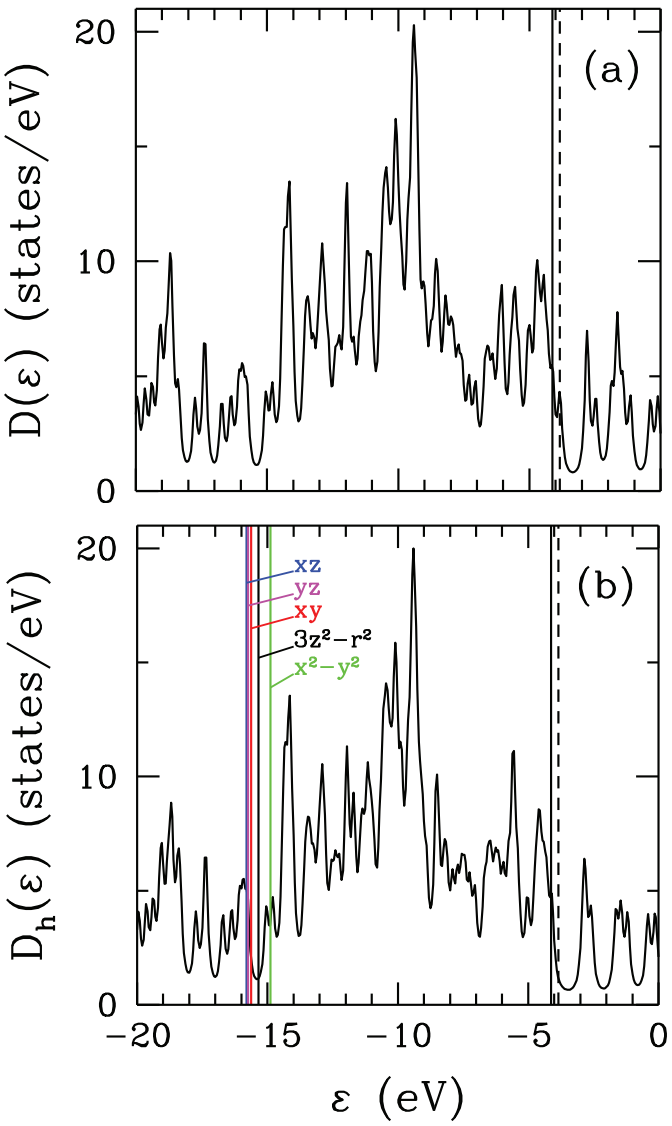

Figure A.3. (a) Total density of states $D(\varepsilon)$ of oxy molecule obtained by the DFT calculations. (b) Density of states of the host states of the effective Haldane-Anderson model $D_h(\varepsilon)$. Here, energy levels of Fe($3d_\nu$) orbitals are shifted by the double counting term, μ_ν^{DC}, which are obtained for $U = 4$ eV and $J = 0.9$ eV. The shifted Fe($3d_\nu$) energy levels $\tilde{\varepsilon}_{d\nu}$ are indicated by the colored vertical lines. In addition, the vertical black solid and dashed lines denote the HOMO and LUMO levels, respectively.

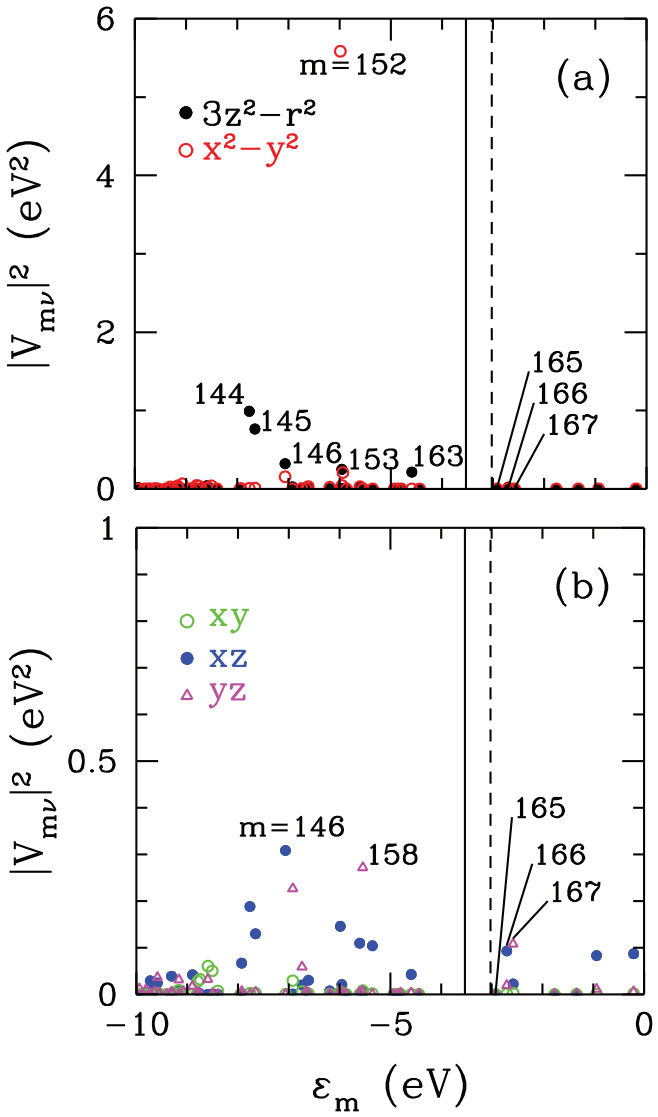

Figure A.4. DFT results for deoxy on the square of the hybridization matrix elements $|V_{m\nu}|^2$ between the Fe($3d_\nu$) natural atomic orbitals and the m'th host states versus the host energy ε_m. In (a) results are shown for the $3d_{3z^2-r^2}$ and $3d_{xy}$ natural atomic orbitals, and in (b) for the $3d_{xz}$, $3d_{x^2-y^2}$ and $3d_{yz}$ natural atomic orbitals. Here, the vertical solid and dashed lines denote the values of the HOMO and LUMO levels, respectively. We observe that $m = 144$, 145, 146, 152, 153 and 163'rd host states have the strongest hybridization matrix elements.

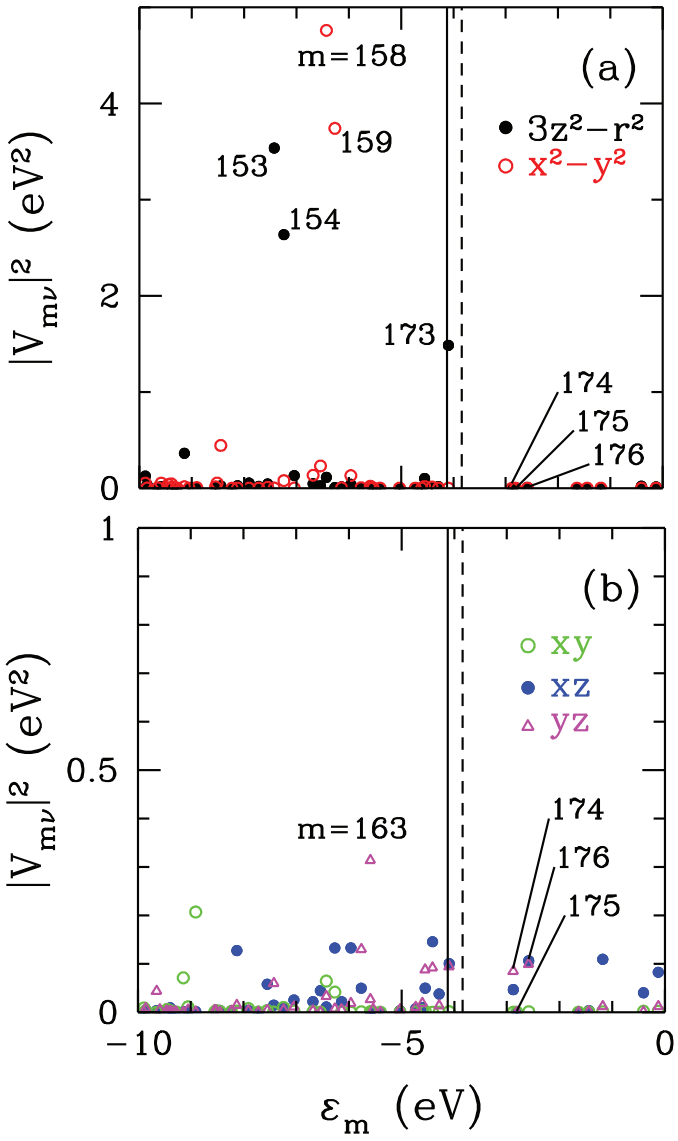

Figure A.5. DFT results for oxy on the square of the hybridization matrix elements $|V_{m\nu}|^2$ between the Fe($3d_\nu$) natural atomic orbitals and the m'th host states versus the host energy ε_m. In (a) results are shown for the $3d_{3z^2-r^2}$ and $3d_{xy}$ natural atomic orbitals, and in (b) for the $3d_{xz}$, $3d_{x^2-y^2}$ and $3d_{yz}$ natural atomic orbitals. Here, the vertical solid and dashed lines denote the values of the HOMO and LUMO levels, respectively. We observe that $m = 153$, 154, 158, 159 and 173'th host states have the strongest hybridization matrix elements.

A.4. Natural atomic orbital weight of the host eigenstates

Figure A.6(a-i) show the NAO composition $|u_{mi}|^2$ of the $m = 144$, 145, 146, 152, 153, 163, 165, 166 and 167'th host states versus the label of host NAO states i for deoxy. Here, NAO weight of the m'th host state is defined as $|u_{mi}|^2 = |\langle\tilde{\phi}_i|u_m\rangle|^2$, where $|\tilde{\phi}_i\rangle$ represents the NAO's for the host states and $|u_m\rangle$ is the m'th host eigenstate. These terms are explained in more detailed in Ref (Kandemir *et al.* (2016), Mayda *et al.* (2017), Kandemir (2013)).

In Fig. A.6(a-b), we observe that $m = 144$ and 145'th states have large weight from the NAO's of the C sites and N sites located around the Fe atom.

Figure A.6(c-d) show that $m = 146$ and 152'nd states have large weight from the NAO's of the N sites and in Fig. A.6(e-f), we observe that $m = 153$ and 163'rd states have large weight from the NAO's of the C sites and N sites

The NAO compositions of the host states $m = 153$, 154, 158, 159, 173, 174 and 175 versus the label of host NAO's i are shown in Fig. A.7 (a-g), respectively. In these figures, we see that $m = 153$, 154, 158 and 159'th host states have large weight from the NAO's of N and C site which attach the Fe atom. On the other hand, Fig. A.7 (e) indicate that $m = 173$'th host states consist of large weight only from the O atoms of the oxy molecule. We see from Fig. A.7 (f) that $m = 174$'th host state consists of C and N sites. $m = 175$'th host state is composed of $2p_x$ and $2p_y$ of C and O as shown in Fig A.7 (g). Similar to $m = 174$'th host state, $m = 176$ also consists of C and N sites as seen in Fig. A.7 (h).

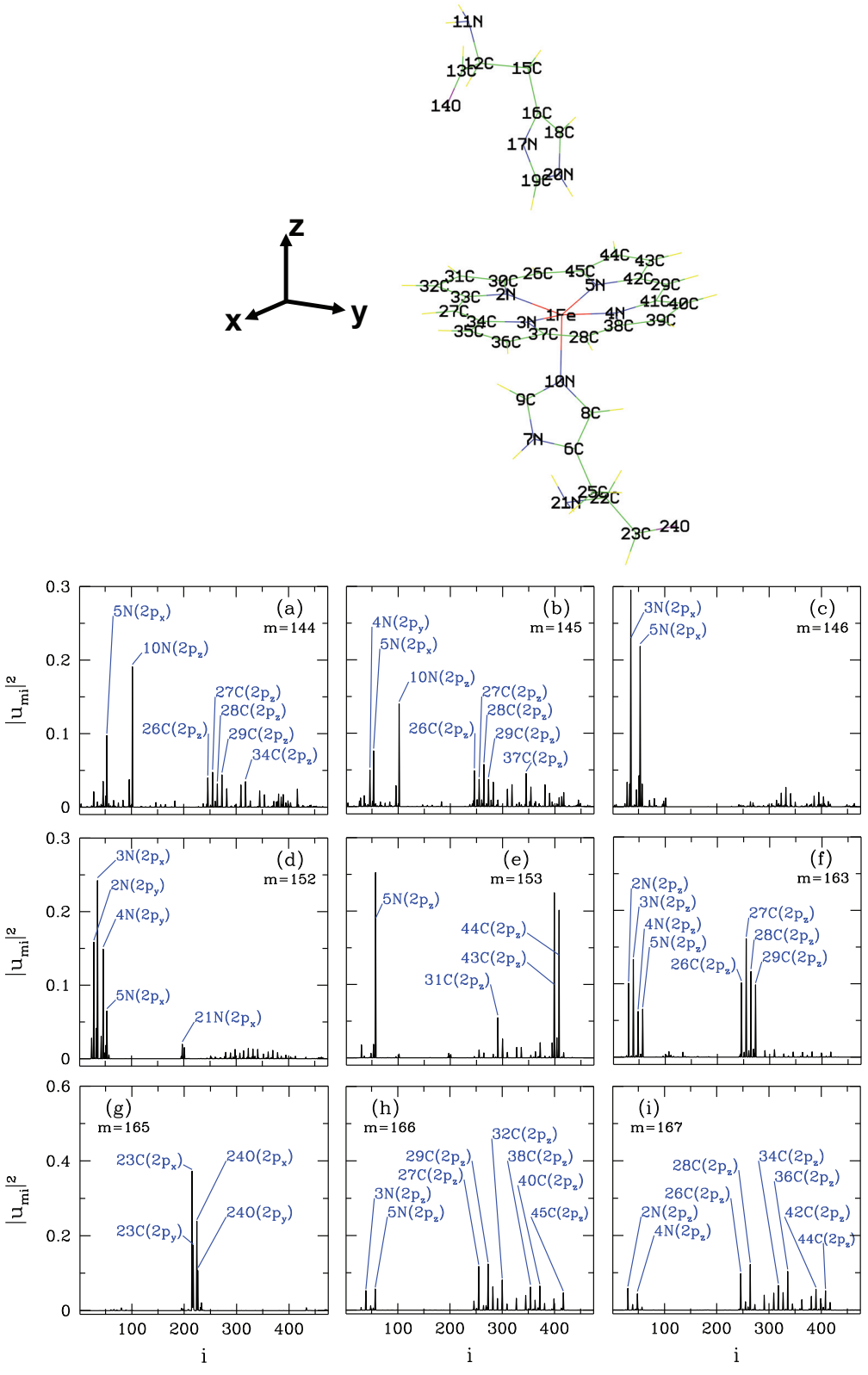

Figure A.6. Natural atomic orbital weight of the m'th host eigenstate $|u_{mi}|^2$ of deoxy versus the label i of the host NAO for (a) $m = 144$, (b) 145, (c) 146, (d) 152, (e) 153. Here, the label of atoms in deoxy molecule is shown at topmost.

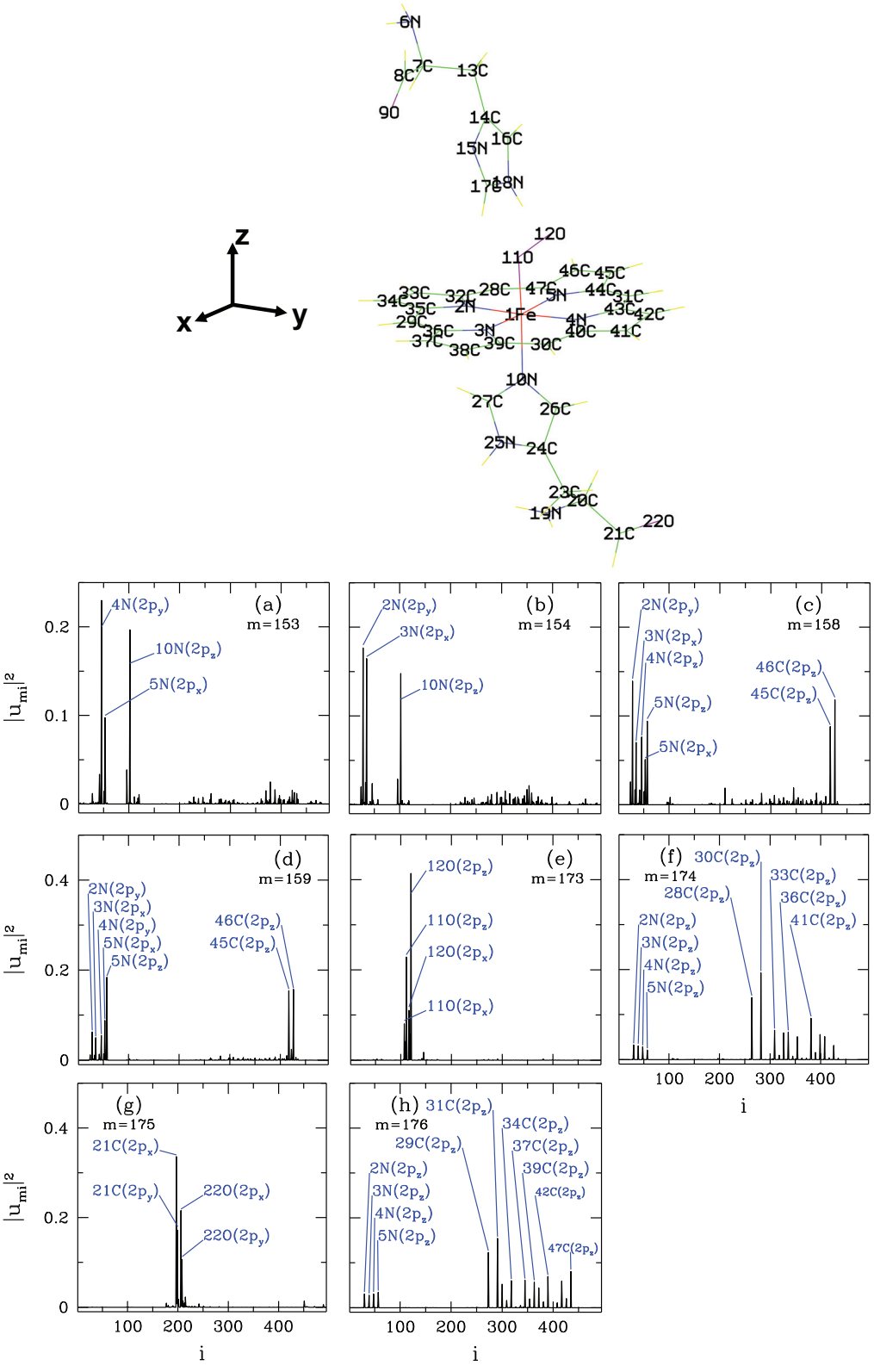

Figure A.7. NAO weight of the m'th host eigenstate $|u_{mi}|^2$ of oxy versus the label i of the host NAO for (a) $m = 153$, (b) 154, (c) 156, (d) 159, (e) 173, (f) 174, (g) 175 and (h) 176. Here, the label of atoms in oxy molecule is shown at topmost.

APPENDIX B

QUANTUM MONTE CARLO ALGORITHM FOR THE MULTI-ORBITAL ANDERSON MODEL WITH THE INTER-ORBITAL COULOMB INTERACTION

In the appendix, the multi-orbital Anderson model is defined by adding inter-orbital Coulomb interaction and the Hirsch-Fye algorithm is explained for this Anderson model. Here, the inter-orbital interaction is included to obtain more accurate results for our molecules and the changes in the algorithm with adding this interaction term are expressed exhaustively.

Firstly, the algorithm is briefly described and its key steps are specified. In section 2, the multi-orbital Anderson Hamiltonian with the inter-orbital Coulomb interaction term is shown and this Hamiltonian is divided into two parts which are the non-interacting (H_0) and the interacting part (H_1).

In section 3, the impurity Green's function $G^0_{\nu\nu'}(i\omega_n)$ with the non-zero hybridization (between the host and impurity orbitals) and zero Hubbard-Stratonovich (HS) field is calculated by using $G^{00}_{\nu\nu'}(i\omega_n)$ and T. $G^{00}_{\nu\nu'}(i\omega_n)$ is the impurity Green's function with the zero hybridization and zero HS field. T is a term which include U, U' and $U'-J$ terms and it is used in H_0. The detailed proof of T is explained in this chapter.

In section 4, the Hubbard-Stratonovich transformations are presented for U, U' and $U'-J$ terms. After these transformations, the exponential form of H_1 is defined by using W^U, $W^{U'}$ and $W^{U'-J}$ which include HS potential terms.

Section 5 shows the initial calculation of $G^\sigma_{\nu\nu'}(l,l')$ by using $G^0_{\nu\nu'}(i\omega_n)$ and W. $G^\sigma_{\nu\nu'}(l,l')$ shows the Green's functions for the non-zero hybridization and HS field and, W contains W^U, $W^{U'}$ and $W^{U'-J}$ terms.

In section 6, R^σ term is described. This term is used for the spin-flip acception and the calculation of the new configuration Green's functions. In this chapter, firstly, the general proof of R^σ is done. After that, R^σ is calculated for U, U' and $U'-J$ terms. $(\,(W_{\nu\sigma}(l))'-(W_{\nu\sigma}(l))\,)$ and A^σ which are used in the calculation of R^σ are explained for the three interaction terms. Here, $(W_{\nu\sigma}(l))'$ is described for the new spin configuration and $(W_{\nu\sigma}(l))$ is described for the old one.

In section 7, the new impurity Green's functions for U, U' and $U'-J$ terms

are explained. In the first two sections, the form of the new Green's functions is shown and (A_σ^{-1}) which are used in the calculation of the new Green's functions are proved for U, U' terms. Then, the last form of the new impurity Green's functions are obtained by replacing (A_σ^{-1}). As for the $U' - J$ term, the form of the new Green's function is explained. $(A_\sigma^{U'-J})_{5L\times 5L}$ matrix is defined and its inverse is obtained. After that, it is shown that $(A_\sigma^{U'-J})^{-1}_{2L\times 2L}$ can be used instead of $(A_\sigma^{U'-J})^{-1}_{5L\times 5L}$. Finally, the last form of the new Green's function are calculated by replacing $(A_\sigma^{U'-J})^{-1}_{2L\times 2L}$ term.

B.1. Schematic derivation

Before embarking on a rigorous derivation of the Hirsch-Fye Quantum Monte Carlo (HF-QMC) algorithm with the inter-orbital Coulomb interaction term, a schematic derivation of this method is given in this section.

The Hirsch-Fye QMC algorithm is numerically exact solver for the Anderson impurity problem. The key steps of these algorithm are the Trotter approximation and the Hubbard-Stratonovich transformation.

The multi-orbital Anderson model Hamiltonian with the inter-orbital interaction term is given by

$$\begin{aligned} H &= \sum_{m\sigma}(\varepsilon_m - \mu)\, c^\dagger_{m\sigma}c_{m\sigma} + \sum_{\nu,\sigma}(\varepsilon_\nu - \mu)n_{\nu\sigma} \\ &+ \sum_m \sum_{\nu,\sigma} V_{m\nu}(c^\dagger_{m\sigma}d_{\nu\sigma} + h.c.) \\ &+ \sum_\nu U n_{\nu\uparrow}n_{\nu\downarrow} \\ &+ \sum_{\nu>\nu'}[U' n_{\nu\sigma}n_{\nu' -\sigma} + (U' - J)n_{\nu\sigma}n_{\nu'\sigma}]. \end{aligned} \tag{B.1}$$

where $c^\dagger_{m\sigma}(c_{m\sigma})$ creates (annihilates) an electron in host state m, with spin σ, $d^\dagger_{\nu\sigma}(d_{\nu\sigma})$ is the creation (annihilation) operator for a localized electron at the ν'th d orbital. Here, ε_m and ε_ν are the energies of the host and d impurity states, respectively, $V_{m\nu}$ is the hybridization matrix elements between host and impurity orbitals, μ is the chemical potential, $n_{\nu\sigma}$ is the occupation number of ν'th d orbital and U is the on-site d electrons Coulomb repulsion. U' and $(U' - J)$ are the Coulomb interaction between two d electrons in different orbitals with opposite spins and parallel spins, respectively. $J_{\nu\nu'}$ is the z component of

Hund's coupling. The relation between U, U' and J is

$$U = U' + 2J. \tag{B.2}$$

The partition function of this system is

$$Z = Tre^{-\beta\hat{H}}. \tag{B.3}$$

The imaginary time interval $[0, \beta]$ is discretized into L time slices for the numerical calculation,

$$\begin{aligned} \tau_l &= l\Delta\tau \ (l = 1, ..., L), \\ \Delta\tau &= \beta/L. \end{aligned} \tag{B.4}$$

With the Trotter approximation, the partition function becomes

$$Z = Tr \prod_{l=1}^{L} e^{-\Delta\tau(\hat{H}_0+\hat{H}_1)} \cong Tr \prod_{l=1}^{L} e^{-\Delta\tau\hat{H}_0} e^{-\Delta\tau\hat{H}_1} + O(\Delta\tau^2). \tag{B.5}$$

This is the only approximation in the determinantal QMC. Typically, one should take $\Delta\tau \leq \sqrt{0.25/U}$ and therefore $L \leq \beta\sqrt{4U}$. In Eq.(B.5), $\hat{H}_0$ and $\hat{H}_1$ represent the non-interacting part and the interacting part of the Anderson Hamiltonian, respectively and they are

$$\begin{aligned} H_0 = &\sum_{m,\sigma} (\varepsilon_m - \mu)\, c^{\dagger}_{m\sigma} c_{m\sigma} + \sum_{m,\nu} \sum_{\sigma} V_{m\nu} \left(c^{\dagger}_{m\sigma} d_{\nu\sigma} + h.c.\right) + \sum_{\nu,\sigma} (\varepsilon_\nu - \mu)\, n_{\nu,\sigma} \\ &+ \sum_{\nu} \frac{U}{2} \left(n_{\nu\uparrow} + n_{\nu\downarrow}\right) + \sum_{\substack{\nu,\nu' \\ \nu>\nu'}} \sum_{\sigma} \left[\frac{U'}{2} \left(n_{\nu,\sigma} + n_{\nu'-\sigma}\right) + \frac{U'-J}{2} \left(n_{\nu,\sigma} + n_{\nu'\sigma}\right) \right] \end{aligned} \tag{B.6}$$

and

$$H_1 = \sum_{\nu} \left[U n_{\nu\uparrow} n_{\nu\downarrow} - \frac{U}{2} \left(n_{\nu\uparrow} + n_{\nu\downarrow} \right) \right] + \sum_{\substack{\nu,\nu' \\ \nu>\nu'}} \sum_{\sigma} \left[U' n_{\nu,\sigma} n_{\nu'-\sigma} - \frac{U'}{2} \left(n_{\nu,\sigma} + n_{\nu'-\sigma} \right) \right] + \sum_{\substack{\nu,\nu' \\ \nu>\nu'}} \sum_{\sigma} \left[\left(U' - J \right) n_{\nu,\sigma} n_{\nu'\sigma} - \frac{U' - J}{2} \left(n_{\nu,\sigma} + n_{\nu'\sigma} \right) \right]. \tag{B.7}$$

The second important step of the algorithm is the Hubbard-Stratonovich transformation. This algorithm uses the Hubbard-Stratonovich (HS) transformation to convert the interacting electron system to a non-interacting one.

The discrete Hubbard-Stratonovich transformation is defined as

$$\begin{aligned} e^{-\Delta\tau H_1} = exp\Big\{ -\Delta\tau \Big(& \sum_{\nu} \left(U n_{\nu\uparrow} n_{\nu\downarrow} - \frac{U}{2} \left(n_{\nu\uparrow} + n_{\nu\downarrow} \right) \right) \\ & + \sum_{\substack{\nu,\nu' \\ \nu\neq\nu'}} \sum_{\sigma} \frac{1}{2} \left(U' n_{\nu,\sigma} n_{\nu'-\sigma} - \frac{U'}{2} \left(n_{\nu,\sigma} + n_{\nu'-\sigma} \right) \right) \\ & + \sum_{\substack{\nu,\nu' \\ \nu>\nu'}} \sum_{\sigma} \left(\left(U' - J \right) n_{\nu,\sigma} n_{\nu'\sigma} - \frac{U' - J}{2} \left(n_{\nu,\sigma} + n_{\nu'\sigma} \right) \right) \Big) \Big\}, \end{aligned} \tag{B.8}$$

and by the Hubbard-Stratonovich transformation, we obtain

$$\begin{aligned} exp\Big\{ -\Delta\tau H_1(l) \Big\} = \frac{1}{2^{45}} \sum_{\{S_{\nu\nu',l,\sigma}=\pm 1\}} exp\Big\{ & \sum_{\nu=1}^{5} \sum_{\sigma} \sigma \, \lambda_1 S^{U}_{\nu,l} \, n_{\nu\sigma} + \\ & + \sum_{\nu=1}^{5} \sum_{\substack{\nu'=1 \\ \nu'\neq\nu}}^{5} \lambda_2 S^{U'}_{\nu\nu',l} (n_{\nu\uparrow} - n_{\nu'\downarrow}) \\ & + \sum_{\nu=1}^{5} \sum_{\substack{\nu'=1 \\ \nu'<\nu}}^{5} \sum_{\sigma} \lambda_3 \, S^{U'-J}_{\nu\nu',l,\sigma} \left(n_{\nu,\sigma} - n_{\nu',\sigma} \right) \Big\}. \end{aligned} \tag{B.9}$$

with

$$cosh(\lambda_1) = e^{\frac{1}{2}\Delta\tau U} \tag{B.10}$$

$$cosh(\lambda_2) = e^{\frac{1}{2}\Delta\tau U'} \tag{B.11}$$

$$cosh(\lambda_3) = e^{\frac{1}{2}\Delta\tau (U'-J)} \tag{B.12}$$

With the HS field, electrons move in a fluctuating field which is defined by random set of spin configurations. These configurations are accepted or rejected by the Monte Carlo (MC) algorithms such as the heat-bath algorithm or the Metropolis algorithm. In this way, the finite temperature Green's functions are calculated.

The multi-orbital Green's function is defined as

$$\begin{aligned} G^{\sigma}_{\nu\nu'}(\tau) &= -\langle\, T_\tau d_{\nu\sigma}(\tau) d^{\dagger}_{\nu'\sigma}(0)\,\rangle \\ &= -\frac{1}{Z}\, Tr\; T_\tau d_{\nu\sigma}(\tau) d^{\dagger}_{\nu'\sigma}(0)\; e^{-\beta\hat{H}}. \end{aligned} \tag{B.13}$$

In the Hirsch-Fye quantum Monte Carlo algorithm, the Green's function is defined by the positive sign and it equals

$$\begin{aligned} G^{\sigma}_{\nu\nu'}(\tau) &= +\langle\, T_\tau d_{\nu\sigma}(\tau) d^{\dagger}_{\nu'\sigma}(0)\,\rangle \\ &= +\frac{1}{Z}\, Tr\; T_\tau d_{\nu\sigma}(\tau) d^{\dagger}_{\nu'\sigma}(0)\; e^{-\beta\hat{H}}. \end{aligned} \tag{B.14}$$

The key steps of HFQMC are:

- Trotter approximation.
- Hubbard-Stratonovich transformation.
- Calculation of the Green's functions.
- Monte Carlo moves for the measurements.

And the flow chart for HFQMC algorithm:

- Calculate the Green's functions $G^{0}_{\nu\nu'}(l_1, l_2)$ for $V_{hyb} \neq 0$ and HS field $= 0$.
- Choose starting HS field configurations by the random number generator.

- Calculate the Green's functions $G_{\nu\nu'}(l_1, l_2)$ for $V_{hyb} \neq 0$ and HS fields $\neq 0$.
- Choose imaginary time slice and one of the impurity orbitals randomly to spin flip and accept or reject the spin flip with respect to the heat-bath MC algorithm.
- Calculate the new Green's functions by using the Dyson's equation.

All details of the algorithm will be explained in the next sections.

B.2. Multi-orbital Anderson Hamiltonian with the inter-orbital Coulomb interaction

The multi-orbital Anderson Hamiltonian with the inter-orbital Coulomb interaction is

$$H = \sum_{m,\sigma}(\varepsilon_m - \mu)\, c^{\dagger}_{m\sigma}c_{m\sigma} + \sum_{m,\nu}\sum_{\sigma} V_{m\nu}\,(c^{\dagger}_{m\sigma}d_{\nu\sigma} + h.c.) + \sum_{\nu,\sigma}(\varepsilon_\nu - \mu)\, n_{\nu,\sigma} + \sum_{\nu} U\, n_{\nu\uparrow}n_{\nu\downarrow} + \sum_{\substack{\nu,\nu'\\ \nu>\nu'}}\sum_{\sigma}\left[\, U' n_{\nu,\sigma}n_{\nu'-\sigma} + (U'-J)n_{\nu,\sigma}n_{\nu'\sigma}\,\right]. \quad \text{(B.15)}$$

U : Coulomb interaction between two electrons in the same d orbital with anti-parallel spins,
U' : Coulomb interaction between two electrons in the different d orbitals with anti-parallel spins,
$(U' - J)$: Coulomb interaction between two electrons in the different d orbitals with paralel spins. The Hamiltonian is divided into two parts which are the non-interacting part (H_0) and the interacting part (H_1),

$$H \equiv H_0 + H_1 \quad \text{(B.16)}$$

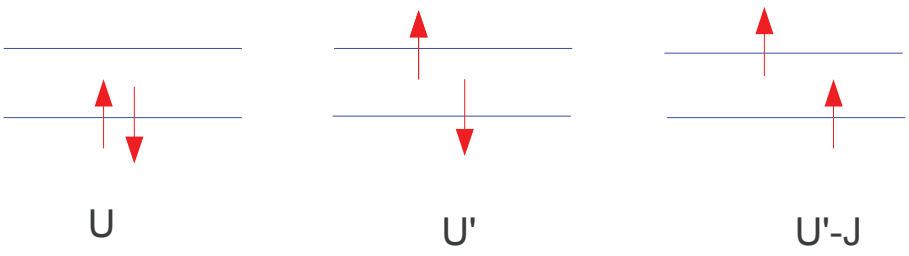

Figure B.1. The left figure indicates intra-orbital Coulomb interaction between d electrons. The mid and the right figures show inter-orbital Coulomb interaction between d electrons.

where

$$H_0 = \sum_{m,\sigma}(\varepsilon_m - \mu)\, c^\dagger_{m\sigma} c_{m\sigma} + \sum_{m,\nu}\sum_{\sigma} V_{m\nu}\,(c^\dagger_{m\sigma} d_{\nu\sigma} + h.c.) + \sum_{\nu,\sigma}(\varepsilon_\nu - \mu)\, n_{\nu,\sigma}$$
$$+ \sum_{\nu} \frac{U}{2}\,(n_{\nu\uparrow} + n_{\nu\downarrow}) + \sum_{\substack{\nu,\nu' \\ \nu>\nu'}}\sum_{\sigma}\left[\frac{U'}{2}\,(n_{\nu,\sigma} + n_{\nu'-\sigma}) + \frac{U'-J}{2}\,(n_{\nu,\sigma} + n_{\nu'\sigma})\right] \tag{B.17}$$

and

$$H_1 = \sum_{\nu}\left[U n_{\nu\uparrow} n_{\nu\downarrow} - \frac{U}{2}\,(n_{\nu\uparrow} + n_{\nu\downarrow})\right] + \sum_{\substack{\nu,\nu' \\ \nu>\nu'}}\sum_{\sigma}\left[U' n_{\nu,\sigma} n_{\nu'-\sigma} - \frac{U'}{2}\,(n_{\nu,\sigma} + n_{\nu'-\sigma})\right]$$
$$+ \sum_{\substack{\nu,\nu' \\ \nu>\nu'}}\sum_{\sigma}\left[(U'-J)\, n_{\nu,\sigma} n_{\nu'\sigma} - \frac{U'-J}{2}\,(n_{\nu,\sigma} + n_{\nu'\sigma})\right]. \tag{B.18}$$

The interaction part H_1 of the Hamiltonian is treated by using the Hubbard-Stratonovich transformation in Section B.4.

B.3. Derivation of G^0

In this chapter, $G^0_{\nu\nu'}$ impurity Green's function will be calculated. For this Green's function, the hybridization terms between the impurity and host orbitals (V_{hyb}) are not zero and the Hubbard-Stratonovich fields ($S_{\nu\nu',l}$) are zero.

The outline of this chapter is the following :

- Firstly, $G^0_{\nu\nu'}$ is derived by using $G^{00}_{\nu\nu'}$ Green's function. $G^{00}_{\nu\nu'}$ is $V_{hyb} = 0$ and $S_{\nu\nu',l} = 0$ Green's function.
- After that, $G^{00}_{\nu\nu'}$ Green's function will be derived from H_{00} and T. H_{00} Hamiltonian does not include the hybridization term and the interaction terms. T includes U, U' and $U' - J$ terms.
- Then, the derivation of T will be explained. T includes T^U, $T^{U'}$ and $T^{U'-J}$ terms which are shown in the following sections.

B.3.1. Derivation of G^0 from G^{00}

$G^0_{\nu\nu'}(i\omega_n)$ Green's function is calculated from H_0 which is

$$H_0 = \sum_{m,\sigma}(\varepsilon_m - \mu)\, c^\dagger_{m\sigma}c_{m\sigma} + \sum_{m,\nu}\sum_{\sigma} V_{m\nu}\,(c^\dagger_{m\sigma}d_{\nu\sigma} + h.c.) + \sum_{\nu,\sigma}(\,(\varepsilon_\nu - \mu) + T\,)\, n_{\nu,\sigma}$$

where

$$T = \frac{U}{2} + 2U' + 2(U' - J). \tag{B.19}$$

Now, let's derive $G^0_{\nu\nu'}(i\omega_n)$ Green's function by using the Feynman diagrams as shown at top of the page. From this diagram, we obtain that

$$G^0_{\nu\nu'}(i\omega_n) = G^{00}_{\nu\nu'}(i\omega_n) + \sum_{\nu''}\sum_{\nu'''} G^{00}_{\nu\nu''}(i\omega_n) \sum_{m}\sum_{m'} V_{\nu'' m}\, G^{00}_{mm'}(i\omega_n)\, V_{m'\,\nu'''}\, G^0_{\nu'''\,\nu'}(i\omega_n) \tag{B.20}$$

$$(-G^0_{\nu\nu'}(i\omega_n)) \;=\; (-G^{00}_{\nu\nu'}(i\omega_n)) \;+(-G^{00}_{\nu\nu''}(i\omega_n))\,(-V_{\nu''\,m})\,(-G^{00}_{mm'}(i\omega_n))\;(-V_{m'\,\nu'''})\,(-G^0_{\nu'''\,\nu'}(i\omega_n))$$

In the Feynman diagram, the double lines represent $G^0_{\nu\nu'}(i\omega_n)$, the single lines indicate $G^{00}_{\nu\,\nu'}(i\omega_n)$ and $G^{00}_{mm'}(i\omega_n)$ and the crosses represent the hybridization term between the host and impurity orbitals. Here, $G^{00}_{\nu\nu'}(i\omega_n)$ and $G^{00}_{mm'}(i\omega_n)$ Green's functions show $V_{hyb} = 0$ and $S_{\nu\nu',l} = 0$ impurity and host Green's functions, respectively. They are calculated from H_{00} which is

$$H_{00} = \sum_{m,\sigma} (\varepsilon_m - \mu)\, c^\dagger_{m\sigma}\, c_{m\sigma} + \sum_{\nu,\,\sigma} (\varepsilon_\nu - \mu)\, n_{\nu,\sigma} + \sum_{\nu,\sigma} T\, n_{\nu,\sigma} \tag{B.21}$$

where

$$T = \frac{U}{2} + 2U' + 2(U' - J). \tag{B.22}$$

The $G^{00}_{\nu\nu'}(i\omega_n)$ and $G^{00}_{mm'}(i\omega_n)$ Green's functions are

$$G^{00}_{\nu\nu'}(i\omega_n) = \frac{\delta_{\nu\nu'}}{i\omega_n - (\varepsilon_\nu - \mu + T)} \tag{B.23}$$

and

$$G^{00}_{mm'}(i\omega_n) = \frac{\delta_{mm'}}{i\omega_n - (\varepsilon_m - \mu)}. \tag{B.24}$$

If these Green's functions are placed in Eq.(B.20), we can obtain

$$\begin{aligned} G^0_{\nu\nu'}(i\omega_n) \;&=\; G^{00}_{\nu\nu'}(i\omega_n) \\ &+\; \sum_{\nu''}\sum_{\nu'''} \frac{\delta_{\nu\nu''}}{i\omega_n - (\varepsilon_\nu - \mu + T)} \sum_m \sum_{m'} V_{\nu''\,m}\, \frac{\delta_{mm'}}{i\omega_n - (\varepsilon_m - \mu)}\, V_{m'\,\nu'''}\, G^0_{\nu'''\,\nu'}(i\omega_n). \end{aligned} \tag{B.25}$$

Then,

$$\begin{aligned} G^0_{\nu\nu'}(i\omega_n) &= G^{00}_{\nu\nu'}(i\omega_n) \\ &+ \sum_{\nu'''} \frac{1}{i\omega_n - (\varepsilon_\nu - \mu + T)} \sum_m V_{\nu\, m} \frac{1}{i\omega_n - (\varepsilon_m - \mu)} V_{m\,\nu'''} G^0_{\nu'''\,\nu'}(i\omega_n). \end{aligned} \tag{B.26}$$

Here, the self energy is defined by

$$F_{\nu\nu'''}(i\omega_n) \equiv \sum_m V_{\nu\, m} \frac{1}{i\omega_n - (\varepsilon_m - \mu)} V_{m\,\nu'''} \tag{B.27}$$

so

$$G^0_{\nu\nu'}(i\omega_n) = G^{00}_{\nu\nu'}(i\omega_n) + \frac{1}{i\omega_n - (\varepsilon_\nu - \mu + T)} \sum_{\nu'''} F_{\nu\nu'''}(i\omega_n)\, G^0_{\nu'''\,\nu'}(i\omega_n). \tag{B.28}$$

When the second term at the right side goes to left side, we can obtain

$$G^0_{\nu\nu'}(i\omega_n) - \frac{1}{i\omega_n - (\varepsilon_\nu - \mu + T)} \sum_{\nu'''} F_{\nu\nu'''}(i\omega_n)\, G^0_{\nu'''\,\nu'}(i\omega_n) = G^{00}_{\nu\nu'}(i\omega_n) \tag{B.29}$$

and

$$\sum_{\nu'''} \left(\delta_{\nu\nu'''} - \frac{1}{i\omega_n - (\varepsilon_\nu - \mu + T)} F_{\nu\nu'''}(i\omega_n) \right) G^0_{\nu'''\,\nu'}(i\omega_n) = G^{00}_{\nu\nu'}(i\omega_n). \tag{B.30}$$

Here, let's define

$$T_{\nu\nu'''}(i\omega_n) \equiv \delta_{\nu\nu'''} - \frac{1}{i\omega_n - (\varepsilon_\nu - \mu + T)} F_{\nu\nu'''}(i\omega_n). \tag{B.31}$$

Then,

$$\sum_{\nu'''} (\, \tilde{T}(i\omega_n)\,)_{\nu\nu'''} (\, \tilde{G}^0(i\omega_n)\,)_{\nu'''\nu'} = (\, \tilde{G}^{00}(i\omega_n)\,)_{\nu\nu'}. \tag{B.32}$$

The Green's function $G^0_{\nu\nu'}(i\omega_n)$ is calculated from

$$(\,\tilde{G}^0(i\omega_n)\,)_{\nu\nu'} = \sum_{\nu'''} (\,\tilde{T}^{-1}(i\omega_n)\,)_{\nu\nu'''}\,(\,\tilde{G}^{00}(i\omega_n)\,)_{\nu'''\nu'}. \tag{B.33}$$

If $G^{00}_{\nu'''\nu'}(i\omega_n)$ is put in above equation, we can obtain

$$(\,\tilde{G}^0(i\omega_n)\,)_{\nu\nu'} = \sum_{\nu'''} (\,\tilde{T}^{-1}(i\omega_n)\,)_{\nu\nu'''}\,\frac{\delta_{\nu'''\nu'}}{i\omega_n - (\varepsilon_{\nu'''} - \mu + T)}. \tag{B.34}$$

$$\Rightarrow\ (\,\tilde{G}^0(i\omega_n)\,)_{\nu\nu'} = \frac{(\,\tilde{T}^{-1}(i\omega_n)\,)_{\nu\nu'}}{i\omega_n - (\varepsilon_{\nu'} - \mu + T)} \tag{B.35}$$

B.3.2. Derivation of $G^{00}_{\nu\nu'}(i\omega_n)$ from H_{00} and T

H_{00} does not include V_{hyb} term and it is

$$H_{00} = \sum_{m,\sigma} (\varepsilon_m - \mu)\, c^\dagger_{m\sigma}\, c_{m\sigma} + \sum_{\nu,\,\sigma} (\varepsilon_\nu - \mu)\, n_{\nu,\sigma} + \sum_{\nu,\sigma} T\, n_{\nu,\sigma} \tag{B.36}$$

where

$$T = \frac{U}{2} + 2U' + 2(U' - J). \tag{B.37}$$

From this Hamiltonian, $G^{00}_{\nu\nu'}(i\omega_n)$ Green's function is written as

$$G^{00}_{\nu\nu'}(i\omega_n) = \frac{\delta_{\nu\nu'}}{i\omega_n - (\varepsilon_\nu - \mu + T)}. \tag{B.38}$$

This is the impurity Green's function for $V_{hyb} = 0$ and $S_{\nu\nu',l} = 0$. The host Green's function for $V_{hyb} = 0$ and $S_{l\nu\nu'} = 0$ is

$$G^{00}_{mm'}(i\omega_n) = \frac{\delta_{mm'}}{i\omega_n - (\varepsilon_m - \mu)}. \tag{B.39}$$

B.3.3. Derivation of T

We know that H_0 is

$$H_0 = \sum_{m,\sigma}(\varepsilon_m - \mu)\, c^\dagger_{m\sigma}c_{m\sigma} + \sum_{m,\nu}\sum_{\sigma} V_{m\nu}\,(c^\dagger_{m\sigma}d_{\nu\sigma} + h.c.) + \sum_{\nu,\sigma}(\varepsilon_\nu - \mu)\, n_{\nu,\sigma}$$
$$+ \sum_{\nu}\frac{U}{2}\,(n_{\nu\uparrow} + n_{\nu\downarrow}) + \sum_{\substack{\nu,\nu'\\ \nu>\nu'}}\sum_{\sigma}\left[\frac{U'}{2}\,(n_{\nu,\sigma} + n_{\nu'-\sigma}) + \frac{U'-J}{2}\,(n_{\nu,\sigma} + n_{\nu'\sigma})\right]. \tag{B.40}$$

I want to write a term which is $\sum_{\nu,\sigma} T\, n_{\nu,\sigma}$ and T includes U, U' and $U' - J$ terms as

$$\sum_{\nu,\sigma} T\, n_{\nu,\sigma} = \sum_{\nu,\sigma}(\, T^U + T^{U'} + T^{U'-J}\,)\, n_{\nu,\sigma}. \tag{B.41}$$

Now, let's calculate T^U,$T^{U'}$ and $T^{U'-J}$.

B.3.3.1. Calculation of T^U

We have

$$\sum_{\nu,\sigma} = \frac{U}{2}\, n_{\nu,\sigma} \tag{B.42}$$

in H_0 so

$$T^U = \frac{U}{2}. \tag{B.43}$$

B.3.3.2. Calculation of $T^{U'}$

As we write in the Eq.(B.15),the multi-orbital Anderson Hamiltonian is

$$H = \sum_{m,\sigma}(\varepsilon_m - \mu)\, c^\dagger_{m\sigma} c_{m\sigma} + \sum_{m,\nu}\sum_{\sigma} V_{m\nu}\,(c^\dagger_{m\sigma} d_{\nu\sigma} + h.c.) + \sum_{\nu,\sigma}(\varepsilon_\nu - \mu)\, n_{\nu,\sigma} + \sum_{\nu} U\, n_{\nu\uparrow} n_{\nu\downarrow} + \sum_{\substack{\nu,\nu' \\ \nu>\nu'}}\sum_{\sigma}\left[\, U' n_{\nu,\sigma} n_{\nu'-\sigma} + (U'-J) n_{\nu,\sigma} n_{\nu'\sigma}\,\right]. \tag{B.44}$$

If we write the condition $\nu \neq \nu'$ instead of $\nu > \nu'$ in the Hamiltonian, we will have such terms which are shown in Fig 3.1 . Due to $[n_{\nu,\sigma},\, n_{\nu',-\sigma}] = 0$, $n_{1\uparrow}\, n_{3\downarrow} = n_{3\downarrow}\, n_{1\uparrow}$, we can

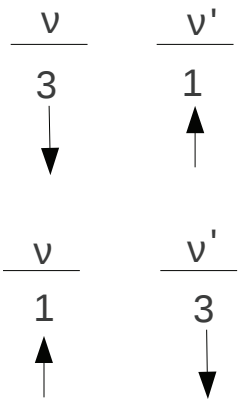

write

$$U' \sum_{\sigma}\sum_{\substack{\nu,\nu' \\ \nu>\nu'}} n_{\nu,\sigma}\, n_{\nu',-\sigma} \longrightarrow \frac{U'}{2}\sum_{\sigma}\sum_{\substack{\nu,\nu' \\ \nu\neq\nu'}} n_{\nu,\sigma}\, n_{\nu',-\sigma}. \tag{B.45}$$

This term can be written as

$$\frac{U'}{2}\sum_{\sigma}\sum_{\substack{\nu,\nu'\\ \nu\neq\nu'}} n_{\nu,\sigma}\, n_{\nu',-\sigma} = \frac{U'}{2}\Big(\sum_{\sigma}\sum_{\substack{\nu,\nu'\\ \nu\neq\nu'}}[n_{\nu,\sigma}\, n_{\nu',-\sigma} - \frac{1}{2}\,(\, n_{\nu,\sigma} + n_{\nu',-\sigma}\,)] + \sum_{\sigma}\sum_{\substack{\nu,\nu'\\ \nu\neq\nu'}}\frac{1}{2}\,(\, n_{\nu,\sigma} + n_{\nu',-\sigma}\,)\Big). \quad \text{(B.46)}$$

The first part at the right side goes in the interaction Hamiltonian H_1 and the second part at the right side goes in the H_0. If I rewrite H_0, it can be as the following

$$\begin{aligned} H_0 \longrightarrow \tilde{H}_0 = \sum_{m,\sigma}(\varepsilon_m - \mu)\, c^{\dagger}_{m\sigma}c_{m\sigma} \;&+\; \sum_{m,\nu}\sum_{\sigma} V_{m\nu}\,(c^{\dagger}_{m\sigma}d_{\nu\sigma} + h.c.) + \sum_{\nu,\sigma}(\varepsilon_\nu - \mu)\, n_{\nu,\sigma} \\ &+\; \sum_{\nu}\frac{U}{2}\,(n_{\nu\uparrow} + n_{\nu\downarrow}) + \frac{1}{2}\sum_{\substack{\nu,\nu'\\ \nu\neq\nu'}}\sum_{\sigma}\frac{U'}{2}\,(n_{\nu,\sigma} + n_{\nu'-\sigma}) \\ &+\; \sum_{\substack{\nu,\nu'\\ \nu>\nu'}}\frac{U'-J}{2}\,(n_{\nu,\sigma} + n_{\nu'\sigma})\,. \end{aligned} \quad \text{(B.47)}$$

Here,

$$\begin{aligned} \frac{U'}{4}\sum_{\substack{\nu,\nu'\\ \nu\neq\nu'}}\sum_{\sigma}(n_{\nu,\sigma} + n_{\nu'-\sigma}) &= \frac{U'}{4}\sum_{\nu=1}^{5}\sum_{\substack{\nu'=1\\ \nu'\neq\nu}}^{5}\Big[\Big(\sum_{\sigma} n_{\nu,\sigma}\Big) + \Big(\sum_{\sigma} n_{\nu',-\sigma}\Big)\Big] \\ &= \frac{U'}{4}\sum_{\nu=1}^{5}\underbrace{\sum_{\substack{\nu'=1\\ \nu'\neq\nu}}^{5}}_{\substack{\text{generates}\\ \text{4 terms}}}\Big(\sum_{\sigma} n_{\nu,\sigma}\Big) + \frac{U'}{4}\sum_{\nu=1}^{5}\sum_{\substack{\nu'=1\\ \nu'\neq\nu}}^{5}\Big(\sum_{\sigma} n_{\nu',-\sigma}\Big). \end{aligned} \quad \text{(B.48)}$$

The second term can be written as

$$\frac{U'}{4}\sum_{\nu=1}^{5}\sum_{\substack{\nu'=1\\ \nu'\neq\nu}}^{5}\Big(\sum_{\sigma} n_{\nu',-\sigma}\Big) = \frac{U'}{4}\sum_{\nu'=1}^{5}\underbrace{\sum_{\substack{\nu=1\\ \nu\neq\nu'}}^{5}}_{\substack{\text{generates}\\ \text{4 terms}}}\Big(\sum_{\sigma} n_{\nu',-\sigma}\Big). \quad \text{(B.49)}$$

Then,

$$\frac{U'}{4}\sum_{\nu=1}^{5} 4\Big(\sum_{\sigma} n_{\nu,\sigma}\Big) + \frac{U'}{4}\sum_{\nu'=1}^{5} 4\Big(\sum_{\sigma} n_{\nu',-\sigma}\Big) = 2\,U'\sum_{\nu=1}^{5}\sum_{\sigma} n_{\nu,\sigma}. \tag{B.50}$$

From this equation, we can write

$$\sum_{\sigma}\sum_{\nu=1}^{5} T^{U'}\, n_{\nu,\sigma} = \sum_{\sigma}\sum_{\nu=1}^{5} 2\,U'\, n_{\nu,\sigma}. \tag{B.51}$$

$$\Rightarrow\; T^{U'} = 2\,U'. \tag{B.52}$$

B.3.3.3. Calculation of $T^{U'-J}$

As we know from Eq.(B.15), we have $U' - J$ term in multi-orbital Anderson Hamiltonian as

$$\sum_{\substack{\nu,\nu'\\ \nu>\nu'}}\sum_{\sigma} (U' - J)\, n_{\nu,\sigma} n_{\nu',\sigma}. \tag{B.53}$$

If we write the condition $\nu \neq \nu'$ instead of $\nu > \nu'$, we will have such terms which are shown in Fig 3.2 . Due to $[n_{\nu,\sigma},\, n_{\nu',\sigma}] = 0$, $n_{1\uparrow}\, n_{3,\uparrow} = n_{3,\uparrow}\, n_{1\uparrow}$, we can write

$$(U' - J)\sum_{\sigma}\sum_{\substack{\nu,\nu'\\ \nu>\nu'}} n_{\nu,\sigma}\, n_{\nu',\sigma} \;\longrightarrow\; \frac{U' - J}{2}\sum_{\sigma}\sum_{\substack{\nu,\nu'\\ \nu\neq\nu'}} n_{\nu,\sigma}\, n_{\nu',\sigma}. \tag{B.54}$$

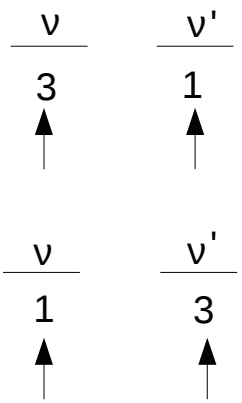

This term can be written as

$$\frac{U'-J}{2}\sum_{\sigma}\sum_{\substack{\nu,\nu'\\ \nu\neq\nu'}} n_{\nu,\sigma}\, n_{\nu',\sigma} \;\; = \;\;$$
$$\frac{U'-J}{2}\Big(\sum_{\sigma}\sum_{\substack{\nu,\nu'\\ \nu\neq\nu'}}[n_{\nu,\sigma}\, n_{\nu',\sigma} - \frac{1}{2}\,(\,n_{\nu,\sigma}+n_{\nu',\sigma}\,)] \;\; + \;\; \sum_{\sigma}\sum_{\substack{\nu,\nu'\\ \nu\neq\nu'}}\frac{1}{2}\,(\,n_{\nu,\sigma}+n_{\nu',\sigma}\,)\Big). \tag{B.55}$$

The first part at the right side goes in the interaction Hamiltonian H_1 and the second part at the right side goes in the H_0.

$$\frac{U'-J}{2}\sum_{\substack{\nu,\nu'\\ \nu\neq\nu'}}\sum_{\sigma}\frac{1}{2}\,(n_{\nu,\sigma}+n_{\nu'\sigma}) = \frac{U'-J}{4}\sum_{\nu=1}^{5}\sum_{\substack{\nu'=1\\ \nu'\neq\nu}}^{5}\Big[\Big(\sum_{\sigma} n_{\nu,\sigma}\Big)+\Big(\sum_{\sigma} n_{\nu',\sigma}\Big)\Big] \tag{B.56}$$

Then,

$$\frac{U'-J}{2}\sum_{\substack{\nu,\nu'\\ \nu\neq\nu'}}\sum_{\sigma}\frac{1}{2}\,(n_{\nu,\sigma}+n_{\nu'\sigma}) \;\; = \;\;$$
$$\underbrace{\frac{U'-J}{4}\sum_{\nu=1}^{5}\sum_{\substack{\nu'=1\\ \nu'\neq\nu}}^{5}\Big(\sum_{\sigma} n_{\nu,\sigma}\Big)}_{\substack{\text{generates}\\ \text{4 terms}}} \;\; + \;\; \frac{U'-J}{4}\sum_{\nu=1}^{5}\sum_{\substack{\nu'=1\\ \nu'\neq\nu}}^{5}\Big(\sum_{\sigma} n_{\nu',\sigma}\Big). \tag{B.57}$$

The second term can be written as

$$\frac{U'-J}{4}\sum_{\nu=1}^{5}\sum_{\substack{\nu'=1\\ \nu'\neq\nu}}^{5}\Big(\sum_{\sigma} n_{\nu',\sigma}\Big)=\frac{U'-J}{4}\sum_{\nu'=1}^{5}\underbrace{\sum_{\substack{\nu=1\\ \nu\neq\nu'}}^{5}}_{\substack{\text{generates}\\ \text{4 terms}}}\Big(\sum_{\sigma} n_{\nu',\sigma}\Big). \tag{B.58}$$

Then,

$$\frac{U'-J}{4}\sum_{\nu=1}^{5}4\Big(\sum_{\sigma} n_{\nu,\sigma}\Big)+\frac{U'-J}{4}\sum_{\nu'=1}^{5}4\Big(\sum_{\sigma} n_{\nu',\sigma}\Big)=2\,(U'-J)\sum_{\nu=1}^{5}\sum_{\sigma} n_{\nu,\sigma}. \tag{B.59}$$

From this equation, we can write

$$\sum_{\sigma}\sum_{\nu=1}^{5} T^{U'-J}\,n_{\nu,\sigma}=\sum_{\sigma}\sum_{\nu=1}^{5}2\,(U'-J)\,n_{\nu,\sigma}. \tag{B.60}$$

$$\Rightarrow\; T^{U'-J}=2\,(U'-J). \tag{B.61}$$

Now, let's write H_0 with T term:

$$H_0=\sum_{m,\sigma}(\varepsilon_m-\mu)\,c^{\dagger}_{m\sigma}c_{m\sigma}+\sum_{m,\nu}\sum_{\sigma}V_{m\nu}\,(c^{\dagger}_{m\sigma}d_{\nu\sigma}+h.c.)+\sum_{\nu,\sigma}(\,(\varepsilon_\nu-\mu)+T\,)\,n_{\nu,\sigma}. \tag{B.62}$$

where

$$\begin{aligned}T&=T^{U}+T^{U'}+T^{U'-J}\\&=\frac{U}{2}+2U'+2(U'-J).\end{aligned} \tag{B.63}$$

B.4. Hubbard-Stratonovich transformation

In this section, the Hubbard-Stratonovich transformation will be introduced. When U,U' and $U'-J$ terms are taken into account in H, this problem is very difficult. In order to treat it, we use the Trotter decomposition and the Hubbard-Stratonovich transformation. They introduce the freedom on the imaginary time (Trotter break-up) and convert the interaction part of H into a form where electrons become decoupled from the each other (Hubbard-Stratonovich transformation).

The outline of this section is the following :

- Firstly, the Hubbard-Stratonovich transformation for U,U' and $U'-J$ terms will be introduced.
- After that, the Hubbard-Stratonovich terms will be rewritten by using W^{U},$W^{U'}$ and $W^{U'-J}$ terms.
- The calculation of W^{U},$W^{U'}$ and $W^{U'-J}$ terms will be done.

The multi-orbital Anderson Hamiltonian was written in Eq B.15 as

$$H = \sum_{m,\sigma}(\varepsilon_m - \mu)\, c^{\dagger}_{m\sigma}c_{m\sigma} + \sum_{m,\nu}\sum_{\sigma} V_{m\nu}\,(c^{\dagger}_{m\sigma}d_{\nu\sigma} + h.c.) + \sum_{\nu,\sigma}(\varepsilon_\nu - \mu)\, n_{\nu,\sigma} + \sum_{\nu} U\, n_{\nu\uparrow}n_{\nu\downarrow} + \sum_{\substack{\nu,\nu' \\ \nu>\nu'}}\sum_{\sigma}\left[\, U' n_{\nu,\sigma}n_{\nu'-\sigma} + (U'-J)n_{\nu,\sigma}n_{\nu'\sigma}\,\right]. \quad \text{(B.64)}$$

After the condition $\nu > \nu'$ was changed to $\nu \neq \nu'$ for U' term in H, H_0 and H_1 parts were written as

$$H_0 = \sum_{m,\sigma}(\varepsilon_m - \mu)\, c^{\dagger}_{m\sigma}c_{m\sigma} + \sum_{m,\nu}\sum_{\sigma} V_{m\nu}\,(c^{\dagger}_{m\sigma}d_{\nu\sigma} + h.c.) + \sum_{\nu,\sigma}(\,(\varepsilon_\nu - \mu) + T\,)\, n_{\nu,\sigma} \quad \text{(B.65)}$$

where

$$T = \frac{U}{2} + 2U' + 2(U' - J) \tag{B.66}$$

and

$$H_1 = \sum_{\nu} \left[U n_{\nu\uparrow} n_{\nu\downarrow} - \frac{U}{2} \left(n_{\nu\uparrow} + n_{\nu\downarrow} \right) \right] + \frac{1}{2} \sum_{\substack{\nu,\nu' \\ \nu \neq \nu'}} \sum_{\sigma} \left[U' \, n_{\nu,\sigma} n_{\nu'-\sigma} - \frac{U'}{2} \left(n_{\nu,\sigma} + n_{\nu'-\sigma} \right) \right] + \sum_{\substack{\nu,\nu' \\ \nu > \nu'}} \sum_{\sigma} \left[\left(U' - J \right) n_{\nu,\sigma} n_{\nu'\sigma} - \frac{U' - J}{2} \left(n_{\nu,\sigma} + n_{\nu'\sigma} \right) \right]. \tag{B.67}$$

The partition function Z is

$$Z = Tr \, e^{-\beta \hat{H}} = Tr \prod_{l=1}^{L} e^{-\Delta\tau \, (H_0 + H_1)} \cong Tr \prod_{l=1}^{L} (\, e^{-\Delta\tau H_0} \, e^{-\Delta\tau H_1}), \tag{B.68}$$

Trotter break-up

with $\beta = L \, \Delta\tau$. Now, let's look at $e^{-\Delta\tau H_1}$ term:

$$\begin{aligned} e^{-\Delta\tau H_1} = exp \quad \Big\{ \quad & -\Delta\tau \Big(\sum_{\nu} (\, U n_{\nu\uparrow} n_{\nu\downarrow} - \frac{U}{2} \left(n_{\nu\uparrow} + n_{\nu\downarrow} \right)) \\ + \quad & \frac{1}{2} \sum_{\substack{\nu,\nu' \\ \nu \neq \nu'}} \sum_{\sigma} (\, U' \, n_{\nu,\sigma} n_{\nu'-\sigma} - \frac{U'}{2} \left(n_{\nu,\sigma} + n_{\nu'-\sigma} \right)) \\ + \quad & \sum_{\substack{\nu,\nu' \\ \nu > \nu'}} \sum_{\sigma} (\, \left(U' - J \right) n_{\nu,\sigma} n_{\nu'\sigma} - \frac{U' - J}{2} \left(n_{\nu,\sigma} + n_{\nu'\sigma} \right)) \Big) \quad \Big\}. \end{aligned} \tag{B.69}$$

Because of $[n_{\nu,\sigma},\, n_{\nu',-\sigma}] = 0$, we can write $e^{-\Delta\tau H_1}$ as

$$e^{-\Delta\tau H_1} = exp\Big\{ -\Delta\tau \sum_{\nu} \big(U n_{\nu\uparrow} n_{\nu\downarrow} - \frac{U}{2} \left(n_{\nu\uparrow} + n_{\nu\downarrow} \right) \big) \Big\}$$
$$\times exp\Big\{ -\Delta\tau \sum_{\substack{\nu,\nu' \\ \nu\neq\nu'}} \sum_{\sigma} \frac{1}{2} \big(U' \, n_{\nu,\sigma} n_{\nu'-\sigma} - \frac{U'}{2} \left(n_{\nu,\sigma} + n_{\nu'-\sigma} \right) \big) \Big\}$$
$$\times exp\Big\{ -\Delta\tau \sum_{\substack{\nu,\nu' \\ \nu>\nu'}} \sum_{\sigma} \big(\left(U' - J \right) n_{\nu,\sigma} n_{\nu'\sigma} - \frac{U' - J}{2} \left(n_{\nu,\sigma} + n_{\nu'\sigma} \right) \big) \Big\}. \tag{B.70}$$

Now, let's write $H_1^U(l)$, $H_1^{U'}(l)$ and $H_1^{U'-J}(l)$ for fixed l:

$$H_1^U(l) = \sum_{\nu} \big(U n_{\nu\uparrow} n_{\nu\downarrow} - \frac{U}{2} \left(n_{\nu\uparrow} + n_{\nu\downarrow} \right) \big), \tag{B.71}$$

$$\boxed{H_1^{U'}(l) = \frac{1}{2} \sum_{\substack{\nu,\nu' \\ \nu\neq\nu'}} \sum_{\sigma} \big(U' \, n_{\nu,\sigma} n_{\nu'-\sigma} - \frac{U'}{2} \left(n_{\nu,\sigma} + n_{\nu'-\sigma} \right) \big),} \tag{B.72}$$

$$H_1^{U'-J}(l) = \sum_{\substack{\nu,\nu' \\ \nu>\nu'}} \sum_{\sigma} \big(\left(U' - J \right) n_{\nu,\sigma} n_{\nu',\sigma} - \frac{U' - J}{2} \left(n_{\nu,\sigma} + n_{\nu',\sigma} \right) \big). \tag{B.73}$$

Then

$$e^{-\Delta\tau H_1(l)} = e^{-\Delta\tau H_1^U(l)} \, e^{-\Delta\tau H_1^{U'}(l)} \, e^{-\Delta\tau H_1^{U'-J}(l)}. \tag{B.74}$$

Let's do the Hubbard-Stratonovich transformations of the above exponential terms.

B.4.1. Hubbard-Stratonovich transformation for U term

We know that

$$exp\Big\{ -\Delta\tau H_1^U(l)\Big\} = exp\Big\{ -\Delta\tau \sum_{\nu=1}^{5} (\, U n_{\nu\uparrow} n_{\nu\downarrow} - \frac{U}{2}\,(n_{\nu\uparrow} + n_{\nu\downarrow})\,)\Big\}. \qquad \text{(B.75)}$$

When the ν summation is written explicitly, we can obtain

$$\begin{aligned} exp\Big\{ -\Delta\tau H_1^U(l)\Big\} = exp\Big\{ -\Delta\tau\Big[(\, U n_{1\uparrow} n_{1\downarrow} - \frac{U}{2}\,(n_{1\uparrow} + n_{1\downarrow})\,) + (\, U n_{2\uparrow} n_{2\downarrow} - \frac{U}{2}\,(n_{2\uparrow} + n_{2\downarrow})\,) + \\ (\, U n_{3\uparrow} n_{3\downarrow} - \frac{U}{2}\,(n_{3\uparrow} + n_{3\downarrow})\,) + (\, U n_{4\uparrow} n_{4\downarrow} - \frac{U}{2}\,(n_{4\uparrow} + n_{4\downarrow})\,) + \\ (\, U n_{5\uparrow} n_{5\downarrow} - \frac{U}{2}\,(n_{5\uparrow} + n_{5\downarrow})\,)\Big]\Big\}. \end{aligned}$$

Because of $[n_{\nu,\sigma},\, n_{\nu,\sigma'}] = 0$ which is proved in Appendix, we can write this term as

$$\begin{aligned} exp\Big\{ -\Delta\tau H_1^U(l)\Big\} = exp\Big\{ -\Delta\tau(\, U n_{1\uparrow} n_{1\downarrow} - \frac{U}{2}\,(n_{1\uparrow} + n_{1\downarrow})\,)\Big\} \\ \times exp\Big\{ -\Delta\tau(\, U n_{2\uparrow} n_{2\downarrow} - \frac{U}{2}\,(n_{2\uparrow} + n_{2\downarrow})\,)\Big\} \times exp\Big\{ -\Delta\tau(\, U n_{3\uparrow} n_{3\downarrow} - \frac{U}{2}\,(n_{3\uparrow} + n_{3\downarrow})\,)\Big\} \\ \times exp\Big\{ -\Delta\tau(\, U n_{4\uparrow} n_{4\downarrow} - \frac{U}{2}\,(n_{4\uparrow} + n_{4\downarrow})\,)\Big\} \times exp\Big\{ -\Delta\tau(\, U n_{5\uparrow} n_{5\downarrow} - \frac{U}{2}\,(n_{5\uparrow} + n_{5\downarrow})\,)\Big\}. \end{aligned} \qquad \text{(B.76)}$$

If the Eq (B.76) is written by ν product, the new form of this equation is

$$\Rightarrow exp\Big\{ -\Delta\tau H_1^U(l)\Big\} = \prod_{\nu=1}^{5} exp\Big\{ -\Delta\tau(\, U n_{\nu\uparrow} n_{\nu\downarrow} - \frac{U}{2}\,(n_{\nu\uparrow} + n_{\nu\downarrow})\,)\Big\}. \qquad \text{(B.77)}$$

With the Hubbard-Stratonovich transformation :

$$exp\Big\{ -\Delta\tau H_1^U(l)\Big\} = \prod_{\substack{\nu=1 \\ \text{generates} \\ \text{5 terms}}}^{5} \Big\{ \frac{1}{2} \sum_{\{S_{\nu l}^U = \pm 1\}} exp\Big[\lambda_1 S_{\nu l}^U (n_{\nu\uparrow} - n_{\nu\downarrow})\Big]\Big\}. \qquad \text{(B.78)}$$

$$\Rightarrow exp\Big\{ -\Delta\tau H_1^U(l)\Big\} = \frac{1}{2^5}\prod_{\nu=1}^{5}\Big\{ \sum_{\{S_{\nu l}^U=\pm 1\}} exp\Big[\lambda_1 S_{\nu l}^U(n_{\nu\uparrow}-n_{\nu\downarrow})\Big]\Big\}. \qquad \text{(B.79)}$$

For one ν term, we have two $S_{\nu l}^U$ values which are 1 and -1 so we have

$$S_{1l}^U=1 \quad S_{1l}^U=-1 \qquad S_{2l}^U=1 \quad S_{2l}^U=-1 \qquad\qquad S_{5l}^U=1 \quad S_{5l}^U=-1$$

$$exp\Big\{ -\Delta\tau H_1^U(l)\Big\} = \frac{1}{2^5}\Big[\{exp(\ )+exp(\ )\}\{exp(\ )+exp(\ )\}.....\{exp(\ )+exp(\ )\}\Big].$$

$$\nu=1 \qquad\qquad \nu=2 \qquad\qquad \nu=5$$

Here, we have 2^5 terms.

Because of $[n_{\nu,\sigma},\, n_{\nu,\sigma'}] = 0$, we can write this equation as

$$exp\Big\{ -\Delta\tau H_1^U(l)\Big\} = \frac{1}{2^5}\Big[\sum_{\{S_{\nu,l}^U=\pm 1\}} exp\Big\{ \sum_{\nu=1}^{5} \lambda_1 S_{\nu l}^U(n_{\nu\uparrow}-n_{\nu\downarrow})\Big\}\Big]. \qquad \text{(B.80)}$$

B.4.2. Hubbard-Stratonovich transformation for U' term

In Section B.3.3.2, we showed the new form of U' term as

$$U'\sum_{\sigma}\sum_{\substack{\nu,\nu'\\ \nu>\nu'}} n_{\nu,\sigma}\, n_{\nu',-\sigma} \longrightarrow \frac{U'}{2}\sum_{\sigma}\sum_{\substack{\nu,\nu'\\ \nu\neq\nu'}} n_{\nu,\sigma}\, n_{\nu',-\sigma}. \qquad \text{(B.81)}$$

Now, we try to write it as

$$U'\sum_{\substack{\nu,\nu'\\ \nu\neq\nu'}} n_{\nu\uparrow}\, n_{\nu'\downarrow}. \qquad \text{(B.82)}$$

Note that, we do not have σ summation. We should do this, because we want to obtain the Hubbard-Stratonovich transformation of U' term like the Hubbard-Stratonovich transformation for U term.

$$U' \sum_{\sigma} \sum_{\substack{\nu,\nu' \\ \nu>\nu'}} n_{\nu,\sigma}\, n_{\nu',-\sigma} = \sum_{\nu=1}^{5} \sum_{\substack{\nu'=1 \\ \nu'<\nu}}^{5} U'\, n_{\nu\uparrow} n_{\nu'\downarrow} + \sum_{\nu=1}^{5} \sum_{\substack{\nu'=1 \\ \nu'<\nu}}^{5} U'\, n_{\nu\downarrow} n_{\nu'\uparrow}. \tag{B.83}$$

Because of $[n_{\nu,\sigma},\, n_{\nu',\sigma'}] = 0$ which is proved in Appendix, we can write the above equation as

$$U' \sum_{\sigma} \sum_{\substack{\nu,\nu' \\ \nu>\nu'}} n_{\nu,\sigma}\, n_{\nu',-\sigma} = \sum_{\nu=1}^{5} \sum_{\substack{\nu'=1 \\ \nu'<\nu}}^{5} U'\, n_{\nu\uparrow} n_{\nu'\downarrow} + \sum_{\nu=1}^{5} \sum_{\substack{\nu'=1 \\ \nu'<\nu}}^{5} U'\, n_{\nu'\uparrow} n_{\nu\downarrow} \tag{B.84}$$

$$\Downarrow \text{ by switching } \nu \text{ and } \nu'$$

$$= \sum_{\nu=1}^{5} \sum_{\substack{\nu'=1 \\ \nu'<\nu}}^{5} U'\, n_{\nu\uparrow} n_{\nu'\downarrow} + \sum_{\nu=1}^{5} \sum_{\substack{\nu'=1 \\ \nu'>\nu}}^{5} U'\, n_{\nu\uparrow} n_{\nu'\downarrow}. \tag{B.85}$$

Then,

$$\sum_{\sigma} \sum_{\substack{\nu,\nu' \\ \nu>\nu'}} U'\, n_{\nu,\sigma}\, n_{\nu',-\sigma} = \sum_{\nu=1}^{5} \sum_{\substack{\nu'=1 \\ \nu'\neq\nu}}^{5} U'\, n_{\nu\uparrow}\, n_{\nu'\downarrow}. \tag{B.86}$$

This term can be written as

$$\sum_{\nu=1}^{5} \sum_{\substack{\nu'=1 \\ \nu'\neq\nu}}^{5} U'\, n_{\nu\uparrow}\, n_{\nu'\downarrow} = \Big(\sum_{\nu=1}^{5} \sum_{\substack{\nu'=1 \\ \nu'\neq\nu}}^{5} [U'\, n_{\nu\uparrow}\, n_{\nu'\downarrow} - \frac{U'}{2}\,(\, n_{\nu\uparrow} + n_{\nu'\downarrow}\,)] + \sum_{\nu=1}^{5} \sum_{\substack{\nu'=1 \\ \nu'\neq\nu}}^{5} \frac{U'}{2}\,(\, n_{\nu\uparrow} + n_{\nu'\downarrow}\,) \Big).$$

The first term at the right side goes to Hubbard-Stratonovich transformation and the sec-

ond term at the right side goes in H_0. Now, we have

$$exp\Big\{ -\Delta\tau H_1^{U'}(l)\Big\} = exp\Big\{ -\Delta\tau \sum_{\nu=1}^{5}\sum_{\substack{\nu'=1\\ \nu'\neq\nu}}^{5} (\, U' n_{\nu\uparrow} n_{\nu'\downarrow} - \frac{U'}{2}\,(n_{\nu\uparrow}+n_{\nu'\downarrow})\,)\Big\}. \quad \text{(B.87)}$$

Because of $[n_{\nu,\sigma},\, n_{\nu',\sigma'}] = 0$, we can write this term as

$$exp\Big\{ -\Delta\tau H_1^{U'}(l)\Big\} = \prod_{\substack{\nu,\nu'=1\\ \nu'\neq\nu}}^{5} exp\Big\{ -\Delta\tau[\, U' n_{\nu\uparrow} n_{\nu'\downarrow} - \frac{U'}{2}\,(n_{\nu\uparrow}+n_{\nu'\downarrow})\,]\Big\}, \quad \text{(B.88)}$$

and with the Hubbard-Stratonovich transformation, we can obtain

$$exp\Big\{ -\Delta\tau H_1^{U'}(l)\Big\} = \prod_{\substack{\nu,\nu'=1\\ \nu'\neq\nu\\ \text{generates}\\ \text{20 terms}}}^{5} \Big\{ \frac{1}{2} \sum_{\{S^{U'}_{\nu\nu',l}=\pm 1} exp[\lambda_2 S^{U'}_{\nu\nu',l}(n_{\nu\uparrow}-n_{\nu'\downarrow})]\Big\}. \quad \text{(B.89)}$$

$$\Rightarrow exp\Big\{ -\Delta\tau H_1^{U'}(l)\Big\} = \frac{1}{2^{20}} \prod_{\substack{\nu,\nu'=1\\ \nu'\neq\nu}}^{5} \Big\{ \sum_{\{S^{U'}_{\nu\nu',l}=\pm 1\}} exp[\lambda_2 S^{U'}_{\nu\nu',l}(n_{\nu\uparrow}-n_{\nu'\downarrow})]\Big\}. \quad \text{(B.90)}$$

Here, we have 2^{20} terms.

Because of $[n_{\nu,\sigma},\, n_{\nu',\sigma'}] = 0$, we can change the product form to the summation form in the exponential and so we have

$$exp\Big\{ -\Delta\tau H_1^{U'}(l)\Big\} = \frac{1}{2^{20}}\Big[\sum_{\{S^{U'}_{\nu\nu',l}=\pm 1\}} exp\Big\{ \sum_{\nu=1}^{5}\sum_{\substack{\nu'=1\\ \nu'\neq\nu}}^{5} \lambda_2 S^{U'}_{\nu\nu',l}(n_{\nu\uparrow}-n_{\nu'\downarrow})\Big\}\Big]. \quad \text{(B.91)}$$

B.4.3. Hubbard-Stratonovich transformation for $U' - J$ term

We have

$$exp\Big\{ -\Delta\tau H_1^{U'-J}(l)\Big\} = exp\Big\{ -\Delta\tau \sum_{\substack{\nu,\nu' \\ \nu>\nu'}} \sum_{\sigma} \big((U'-J)\, n_{\nu,\sigma} n_{\nu',\sigma} - \frac{U'-J}{2}\,(n_{\nu,\sigma} + n_{\nu',\sigma})\,\big)\Big\}. \tag{B.92}$$

Because of $[n_{\nu,\sigma},\, n_{\nu',\sigma}] = 0$ which is proved in Appendix, we can write Eq.(B.92) in product from as

$$exp\Big\{ -\Delta\tau H_1^{U'-J}(l)\Big\} = \prod_{\substack{\nu,\nu'=1 \\ \nu>\nu'}}^{5} \prod_{\sigma} exp\Big\{ -\Delta\tau[\,(U'-J)\, n_{\nu,\sigma} n_{\nu'\sigma} - \frac{U'-J}{2}\,(n_{\nu,\sigma} + n_{\nu'\sigma})\,]\Big\}. \tag{B.93}$$

With the Hubbard-Stratonovich transformation, we obtain

$$exp\Big\{ -\Delta\tau H_1^{U'-J}(l)\Big\} = \prod_{\substack{\nu,\nu'=1 \\ \nu>\nu'}}^{5} \prod_{\sigma} \Big\{ \frac{1}{2} \sum_{\{S^{U'-J}_{\nu\nu',l,\sigma}=\pm 1\}} exp[\lambda_3\, S^{U'-J}_{\nu\nu',l,\sigma}\,(n_{\nu,\sigma} - n_{\nu',\sigma})]\Big\}. \tag{B.94}$$

This equation can be rewritten by multipling $\uparrow$ and $\downarrow$ spins as

$$\begin{aligned} exp\Big\{ -\Delta\tau H_1^{U'-J}(l)\Big\} = \prod_{\substack{\nu,\nu'=1 \\ \nu>\nu'}}^{5} & \Big\{ \frac{1}{2} \sum_{\{S^{U'-J}_{\nu\nu',l,\uparrow}=\pm 1\}} exp[\lambda_3\, S^{U'-J}_{\nu\nu',l,\uparrow}\,(n_{\nu\uparrow} - n_{\nu'\uparrow})]\Big\} \\ & \times \Big\{ \frac{1}{2} \sum_{\{S^{U'-J}_{\nu\nu',l,\downarrow}=\pm 1\}} exp[\lambda_3\, S^{U'-J}_{\nu\nu',l,\downarrow}\,(n_{\nu\downarrow} - n_{\nu'\downarrow})]\Big\}. \end{aligned} \tag{B.95}$$

Because of $[n_{\nu,\sigma},\, n_{\nu',\sigma}] = 0$, we can write

$$exp\Big\{ -\Delta\tau H_1^{U'-J}(l)\Big\} = \prod_{\substack{\nu,\nu'=1\\ \nu>\nu'}}^{5} \frac{1}{2^2}\Big\{ \sum_{\substack{\{S^{U'-J}_{\nu\nu',l,\uparrow}=\pm 1\\ S^{U'-J}_{\nu\nu',l,\downarrow}=\pm 1\}}} exp[\lambda_3\, S^{U'-J}_{\nu\nu',l,\uparrow}\,(n_{\nu\uparrow} - n_{\nu'\uparrow}) + \lambda_3\, S^{U'-J}_{\nu\nu',l,\downarrow}\,(n_{\nu\downarrow} - n_{\nu'\downarrow})]\Big\}. \quad \text{(B.96)}$$

$$exp\Big\{ -\Delta\tau H_1^{U'-J}(l)\Big\} = \prod_{\substack{\nu,\nu'=1\\ \nu>\nu'}}^{5} \frac{1}{2^2}\Big\{ \sum_{\{S^{U'-J}_{\nu\nu',l,\sigma}=\pm 1\}} exp\Big[\lambda_3 \sum_{\sigma} S^{U'-J}_{\nu\nu',l,\sigma}\,(n_{\nu,\sigma} - n_{\nu',\sigma})\Big]\Big\}. \quad \text{(B.97)}$$

We have 2^{10} terms, due to $\prod_{\substack{\nu,\nu'=1\\ \nu>\nu'}}^{5}$. Because of $[n_{\nu,\sigma},\, n_{\nu',\sigma}] = 0$, we can write

$$exp\Big\{ -\Delta\tau H_1^{U'-J}(l)\Big\} = \frac{1}{2^{20}}\Big\{ \sum_{\{S^{U'-J}_{\nu\nu',l,\sigma}=\pm 1\}} exp\Big[\sum_{\substack{\nu,\nu'\\ \nu>\nu'}} \sum_{\sigma} \lambda_3\, S^{U'-J}_{\nu\nu',l,\sigma}\,(n_{\nu,\sigma} - n_{\nu',\sigma})\Big]\Big\}. \quad \text{(B.98)}$$

B.5. Writing the Hubbard-Stratonovich transformation terms by using W terms

We wrote $e^{-\Delta\tau H_1(l)}$ term as

$$e^{-\Delta\tau H_1(l)} = e^{-\Delta\tau H_1^{U}(l)}\, e^{-\Delta\tau H_1^{U'}(l)}\, e^{-\Delta\tau H_1^{U'-J}(l)}. \quad \text{(B.99)}$$

With the Hubbard-Stratonovich transformation of $e^{-\Delta\tau H_1^U(l)}$, $e^{-\Delta\tau H_1^{U'}(l)}$ and $e^{-\Delta\tau H_1^{U'-J}(l)}$ and $[n_{\nu,\sigma},\, n_{\nu',\sigma'}] = 0$, we can write this term as

$$exp\Big\{ -\Delta\tau H_1(l)\Big\} = \frac{1}{2^{45}} \sum_{\{S_{\nu\nu',l,\sigma}=\pm 1\}} exp\Big\{ \sum_{\nu=1}^{5} \sum_{\sigma} \sigma\, \lambda_1 S_{\nu,l}^{U}\, n_{\nu,\sigma} + \sum_{\nu=1}^{5} \sum_{\substack{\nu'=1 \\ \nu'\neq\nu}}^{5} \lambda_2 S_{\nu\nu',l}^{U'}(n_{\nu\uparrow} - n_{\nu'\downarrow}) + \sum_{\nu=1}^{5} \sum_{\substack{\nu'=1 \\ \nu'<\nu}}^{5} \sum_{\sigma} \lambda_3\, S_{\nu\nu',l,\sigma}^{U'-J}\, (n_{\nu,\sigma} - n_{\nu',\sigma}) \Big\}.$$

Here,

$$S_{\nu\nu',l,\sigma} = S_{\nu,l}^{U} \quad \text{for } U \text{ term} \tag{B.100}$$

$$S_{\nu\nu',l,\sigma} = S_{\nu\nu',l}^{U'} \quad \text{for } U' \text{ term} \tag{B.101}$$

$$S_{\nu\nu',l,\sigma} = S_{\nu\nu',l,\sigma}^{U'-J} \quad \text{for } U'-J \text{ term} \tag{B.102}$$

Now, we want to write $e^{-\Delta\tau H_1(l)}$ as

$$exp\Big\{ -\Delta\tau H_1(l)\Big\} = \frac{1}{2^{45}} \sum_{\{S_{\nu\nu',l,\sigma}=\pm 1\}} \exp\Big\{ \sum_{\nu,\sigma} W_{\nu\sigma}^{U}(l)\, n_{\nu,\sigma} + \sum_{\nu=1}^{5} \Big[W_{\nu\uparrow}^{U'}(l)\, n_{\nu\uparrow} + W_{\nu\downarrow}^{U'}(l)\, n_{\nu\downarrow} \Big] + \sum_{\nu,\sigma} W_{\nu\sigma}^{U'-J}(l)\, n_{\nu,\sigma} \Big\}.$$

B.5.1. Calculation of $W_{\nu\sigma}^{U}(l)$

We know from Section B.4.1 that

$$exp\Big\{ -\Delta\tau H_1^{U}(l)\Big\} = \frac{1}{2^5}\Big(\sum_{\{S_{\nu,l}^{U}=\pm 1\}} exp\Big\{ \sum_{\nu,\sigma} \sigma\, \lambda_1 S_{\nu,l}^{U}\, n_{\nu,\sigma} \Big\} \Big). \tag{B.103}$$

We try to obtain the following equation:

$$exp\Big\{ -\Delta\tau H_1^U(l)\Big\} = \frac{1}{2^5}\Big(\sum_{\{S^U_{\nu,l}=\pm 1\}} exp\Big\{ \sum_{\nu,\sigma} W^U_{\nu\sigma}(l)\, n_{\nu,\sigma}\Big\}\Big). \tag{B.104}$$

$$\Rightarrow\ W^U_{\nu\sigma}(l) = \sigma\,\lambda_1 S^U_{\nu,l}. \tag{B.105}$$

Now, let's visualize $S^U_{\nu,l}$:

$$\begin{bmatrix} S^U_{1,l,\sigma} & & & & 0 \\ & S^U_{2,l,\sigma} & & & \\ & & S^U_{3,l,\sigma} & & \\ 0 & & & S^U_{4,l,\sigma} & \\ & & & & S^U_{5,l,\sigma} \end{bmatrix}$$

B.5.2. Calculation of $W^{U'}_{\nu\sigma}(l)$

After the Hubbard-Stratonovich transformation in Section B.4.2, we obtained that

$$exp\Big\{ -\Delta\tau H_1^{U'}(l)\Big\} = \frac{1}{2^{20}}\Big[\sum_{\{S^{U'}_{\nu\nu',l}=\pm 1\}} exp\Big\{ \sum_{\nu=1}^{5}\sum_{\substack{\nu'=1\\ \nu'\neq\nu}}^{5} \lambda_2 S^{U'}_{\nu\nu',l}(n_{\nu\uparrow} - n_{\nu'\downarrow})\Big\}\Big]. \tag{B.106}$$

We try to obtain the following equation:

$$exp\Big\{ -\Delta\tau H_1^{U'}(l)\Big\} = \frac{1}{2^{20}} \sum_{\{S^{U'}_{\nu\nu',l}=\pm 1\}} exp\Big\{ \sum_{\nu=1}^{5} \Big[W^{U'}_{\nu\uparrow}(l)\, n_{\nu\uparrow} + W^{U'}_{\nu\downarrow}(l)\, n_{\nu\downarrow} \Big] \Big\}. \tag{B.107}$$

To obtain Eq.(B.107), firstly, let's write

$$\sum_{\nu=1}^{5} \sum_{\substack{\nu'=1 \\ \nu'\neq\nu}}^{5} \lambda_2 S^{U'}_{\nu\nu',l}(n_{\nu\uparrow} - n_{\nu'\downarrow}) \tag{B.108}$$

as

$$\sum_{\nu=1}^{5} \sum_{\substack{\nu'=1 \\ \nu'\neq\nu}}^{5} \lambda_2 S^{U'}_{\nu\nu',l}(n_{\nu\uparrow} - n_{\nu'\downarrow}) = \lambda_2 \sum_{\nu=1}^{5} \sum_{\substack{\nu'=1 \\ \nu'\neq\nu}}^{5} S^{U'}_{\nu\nu',l}\, n_{\nu\uparrow} - \lambda_2 \sum_{\nu=1}^{5} \sum_{\substack{\nu'=1 \\ \nu'\neq\nu}}^{5} S^{U'}_{\nu\nu',l}\, n_{\nu'\downarrow}$$

watch for the switch of ν and ν'

$$\Downarrow$$

$$= \lambda_2 \sum_{\nu=1}^{5} \sum_{\substack{\nu'=1 \\ \nu'\neq\nu}}^{5} S^{U'}_{\nu\nu',l}\, n_{\nu\uparrow} - \lambda_2 \sum_{\nu'=1}^{5} \sum_{\substack{\nu=1 \\ \nu\neq\nu'}}^{5} S^{U'}_{\nu'\nu,l}\, n_{\nu\downarrow}. \tag{B.109}$$

we change the place of summation of ν and ν' in the second term

$$\rightleftharpoons$$

Then

$$\sum_{\nu=1}^{5} \sum_{\substack{\nu'=1 \\ \nu'\neq\nu}}^{5} \lambda_2 S^{U'}_{\nu\nu',l}(n_{\nu\uparrow} - n_{\nu'\downarrow}) = \lambda_2 \sum_{\nu=1}^{5} \sum_{\substack{\nu'=1 \\ \nu'\neq\nu}}^{5} S^{U'}_{\nu\nu',l}\, n_{\nu\uparrow} - \lambda_2 \sum_{\nu=1}^{5} \sum_{\substack{\nu'=1 \\ \nu'\neq\nu}}^{5} S^{U'}_{\nu'\nu,l}\, n_{\nu\downarrow}$$

$$= \sum_{\nu=1}^{5} \Big(\lambda_2 \sum_{\substack{\nu'=1 \\ \nu' \neq \nu}}^{5} S^{U'}_{\nu\nu',l}\, n_{\nu\uparrow} - \lambda_2 \sum_{\substack{\nu'=1 \\ \nu' \neq \nu}}^{5} S^{U'}_{\nu'\nu,l}\, n_{\nu\downarrow} \Big)$$

$$= \sum_{\nu=1}^{5} \Big(W^{U'}_{\nu\uparrow}(l)\, n_{\nu\uparrow} + W^{U'}_{\nu\downarrow}(l)\, n_{\nu\downarrow} \Big), \tag{B.110}$$

where

$$W^{U'}_{\nu\uparrow}(l) = \lambda_2 \sum_{\substack{\nu'=1 \\ \nu' \neq \nu}}^{5} S^{U'}_{\nu\nu',l} \tag{B.111}$$

and

$$W^{U'}_{\nu\downarrow}(l) = -\lambda_2 \sum_{\substack{\nu'=1 \\ \nu' \neq \nu}}^{5} S^{U'}_{\nu'\nu,l}. \tag{B.112}$$

Now, let's visualize $S^{U'}_{\nu\nu',l}$ and $S^{U'}_{\nu'\nu,l}$ terms : Let's say $\nu = 3$, then

$$\text{used for } \sigma = \uparrow \quad \overset{\text{for } \sigma = \downarrow}{\begin{bmatrix} \bullet & S^{U'}_{12,l} & S^{U'}_{13,l} & S^{U'}_{14,l} & S^{U'}_{15,l} \\ S^{U'}_{21,l} & \bullet & S^{U'}_{23,l} & S^{U'}_{24,l} & S^{U'}_{25,l} \\ S^{U'}_{31,l} & S^{U'}_{32,l} & \bullet & S^{U'}_{34,l} & S^{U'}_{35,l} \\ S^{U'}_{41,l} & S^{U'}_{42,l} & S^{U'}_{43,l} & \bullet & S^{U'}_{45,l} \\ S^{U'}_{51,l} & S^{U'}_{52,l} & S^{U'}_{53,l} & S^{U'}_{54,l} & \bullet \end{bmatrix}}$$

$$W^{U'}_{3,\uparrow} = \lambda_2 \,(S^{U'}_{31,l} + S^{U'}_{32,l} + S^{U'}_{34,l} + S^{U'}_{35,l}). \tag{B.113}$$

$$W^{U'}_{3,\downarrow} = -\lambda_2 \,(S^{U'}_{13,l} + S^{U'}_{23,l} + S^{U'}_{43,l} + S^{U'}_{53,l}). \tag{B.114}$$

B.5.3. Calculation of $W_{\nu\sigma}^{U'-J}(l)$

After the Hubbard-Stratonovich transformation in Section B.4.3, we obtained that

$$exp\Big\{ -\Delta\tau H_1^{U'-J}(l)\Big\} = \frac{1}{2^{20}}\Big\{ \sum_{\{S_{\nu\nu',l,\sigma}^{U'-J}=\pm 1\}} exp\Big[\sum_{\substack{\nu,\nu' \\ \nu>\nu'}} \sum_{\sigma} \lambda_3\, S_{\nu\nu',l,\sigma}^{U'-J}\,(n_{\nu,\sigma} - n_{\nu',\sigma})\Big]\Big\}. \tag{B.115}$$

We try to write this equation as the following:

$$exp\Big\{ -\Delta\tau H_1^{U'-J}(l)\Big\} = \frac{1}{2^{20}} \sum_{\{S_{\nu\nu',l,\sigma}^{U'-J}=\pm 1\}} exp\Big\{ \sum_{\nu=1}^{5} \sum_{\sigma} W_{\nu\sigma}^{U'-J}(l)\, n_{\nu,\sigma}\Big\}. \tag{B.116}$$

The term

$$\sum_{\substack{\nu,\nu' \\ \nu>\nu'}} \sum_{\sigma} \lambda_3\, S_{\nu\nu',l,\sigma}^{U'-J}\,(n_{\nu,\sigma} - n_{\nu',\sigma}) \tag{B.117}$$

can be written as (here, note that $(\nu\nu') = (11)$ is not included)

$$\sum_{\nu=2}^{5}\sum_{\nu'=1}^{\nu-1}\sum_{\sigma} \lambda_3\, S_{\nu\nu',l,\sigma}^{U'-J}\,(n_{\nu,\sigma} - n_{\nu',\sigma}) = \sum_{\nu=2}^{5}\sum_{\nu'=1}^{\nu-1}\sum_{\sigma} \lambda_3\, S_{\nu\nu',l,\sigma}^{U'-J}\, n_{\nu,\sigma} - \sum_{\nu=2}^{5}\sum_{\nu'=1}^{\nu-1}\sum_{\sigma} \lambda_3\, S_{\nu\nu',l,\sigma}^{U'-J}\, n_{\nu',\sigma}$$

$$\Downarrow \text{ watch for the switch of } \nu \text{ and } \nu'$$

$$= \sum_{\nu=2}^{5}\sum_{\nu'=1}^{\nu-1}\sum_{\sigma} \lambda_3\, S_{\nu\nu',l,\sigma}^{U'-J}\, n_{\nu,\sigma} - \sum_{\nu'=2}^{5}\sum_{\nu=1}^{\nu'-1}\sum_{\sigma} \lambda_3\, S_{\nu'\nu,l,\sigma}^{U'-J}\, n_{\nu,\sigma}.$$

The first term in Eq.(B.118) can be rewritten as

$$\sum_{\nu=2}^{5}\sum_{\nu'=1}^{\nu-1}\sum_{\sigma}\lambda_3\, S^{U'-J}_{\nu\nu',l,\sigma}\, n_{\nu,\sigma} \;\rightarrow \sum_{\nu=1}^{5}\sum_{\nu'=1}^{\nu-1}\sum_{\sigma}\lambda_3\, S^{U'-J}_{\nu\nu',l,\sigma}\, n_{\nu,\sigma}. \tag{B.118}$$

The second term in Eq.(B.118) can be written as

$$-\sum_{\nu'=2}^{5}\sum_{\nu=1}^{\nu'-1}\sum_{\sigma}\lambda_3\, S^{U'-J}_{\nu'\nu,l,\sigma}\, n_{\nu,\sigma} = -\sum_{\nu=1}^{4}\sum_{\nu'=\nu+1}^{5}\sum_{\sigma}\lambda_3\, S^{U'-J}_{\nu'\nu,l,\sigma}\, n_{\nu,\sigma} \tag{B.119}$$

and

$$\sum_{\nu=1}^{4}\sum_{\nu'=\nu+1}^{5} \;\rightarrow \sum_{\nu=1}^{5}\sum_{\nu'=\nu+1}^{5}. \tag{B.120}$$

$$\Rightarrow\; -\sum_{\nu'=2}^{5}\sum_{\nu=1}^{\nu'-1}\sum_{\sigma}\lambda_3\, S^{U'-J}_{\nu'\nu,l,\sigma}\, n_{\nu,\sigma} = -\sum_{\nu=1}^{5}\sum_{\nu'=\nu+1}^{5}\sum_{\sigma}\lambda_3\, S^{U'-J}_{\nu'\nu,l,\sigma}\, n_{\nu,\sigma}. \tag{B.121}$$

By using the first term and the second term, we obtain

$$\begin{aligned}\sum_{\nu=2}^{5}\sum_{\nu'=1}^{\nu-1}\sum_{\sigma}\Big(\lambda_3\, S^{U'-J}_{\nu\nu',l,\sigma}\,(n_{\nu,\sigma}-n_{\nu',\sigma})\Big) &= \sum_{\nu=1}^{5}\sum_{\sigma}\Big\{\lambda_3\sum_{\nu'=1}^{\nu-1}S^{U'-J}_{\nu\nu',l,\sigma} - \lambda_3\sum_{\nu'=\nu+1}^{5}S^{U'-J}_{\nu'\nu,l,\sigma}\Big\}n_{\nu,\sigma} \\ &= \sum_{\nu=1}^{5}\sum_{\sigma}W^{U'-J}_{\nu\sigma}(l)n_{\nu,\sigma} \end{aligned}\tag{B.122}$$

where

$$W^{U'-J}_{\nu\sigma}(l) = \lambda_3\sum_{\nu'=1}^{\nu-1}S^{U'-J}_{\nu\nu',l,\sigma} - \lambda_3\sum_{\nu'=\nu+1}^{5}S^{U'-J}_{\nu'\nu,l,\sigma}. \tag{B.123}$$

Now, let's visualize $S^{U'-J}_{\nu\nu',l,\sigma}$ terms :

$$\begin{bmatrix} \bullet & & & 0 \\ S^{U'-J}_{21,l,\sigma} & \bullet & & \\ S^{U'-J}_{31,l,\sigma} & S^{U'-J}_{32,l,\sigma} & \bullet & \\ S^{U'-J}_{41,l,\sigma} & S^{U'-J}_{42,l,\sigma} & S^{U'-J}_{43,l,\sigma} & \bullet \\ S^{U'-J}_{51,l,\sigma} & S^{U'-J}_{52,l,\sigma} & S^{U'-J}_{53,l,\sigma} & S^{U'-J}_{54,l,\sigma} \quad \bullet \end{bmatrix}_{\text{I}}$$

What have we done in this section?

- Before the Hubbard-Stratonovich transformation, we wrote $exp\{-\Delta\tau H_1\}$ as

$$\begin{aligned} e^{-\Delta\tau H_1} = exp\Big\{ -\Delta\tau\Big(\sum_{\nu} \big(U n_{\nu\uparrow} n_{\nu\downarrow} - \frac{U}{2}\left(n_{\nu\uparrow} + n_{\nu\downarrow}\right)\big) \\ + \sum_{\substack{\nu,\nu' \\ \nu\neq\nu'}} \frac{1}{2}\big(U'\, n_{\nu\uparrow} n_{\nu'\downarrow} - \frac{U'}{2}\left(n_{\nu\uparrow} + n_{\nu'\downarrow}\right)\big) \\ + \sum_{\substack{\nu,\nu' \\ \nu>\nu'}} \sum_{\sigma} \big(\left(U' - J\right) n_{\nu,\sigma} n_{\nu'\sigma} - \frac{U'-J}{2}\left(n_{\nu,\sigma} + n_{\nu'\sigma}\right)\big)\Big)\Big\}. \end{aligned} \tag{B.124}$$

- By the Hubbard-Stratonovich transformation, we wrote this equation as

$$\begin{aligned} exp\Big\{ -\Delta\tau H_1(l)\Big\} = \frac{1}{2^{45}} \sum_{\{S_{\nu\nu',l,\sigma}=\pm 1\}} exp\Big\{ \sum_{\nu=1}^{5}\sum_{\sigma} \sigma\, \lambda_1 S^{U}_{\nu,l}\, n_{\nu\sigma} + \sum_{\nu=1}^{5}\sum_{\substack{\nu'=1 \\ \nu'\neq\nu}}^{5} \lambda_2 S^{U'}_{\nu\nu',l}(n_{\nu\uparrow} - n_{\nu'\downarrow}) \\ + \sum_{\nu=1}^{5}\sum_{\substack{\nu'=1 \\ \nu'<\nu}}^{5}\sum_{\sigma} \lambda_3\, S^{U'-J}_{\nu\nu',l,\sigma}\left(n_{\nu,\sigma} - n_{\nu',\sigma}\right)\Big\}. \end{aligned} \tag{B.125}$$

- Finally, we wrote $exp\Big\{ -\Delta\tau H_1(l)\Big\}$ by using Ws for the three interaction terms

and it is

$$exp\Big\{ -\Delta\tau H_1(l)\Big\} = \frac{1}{2^{45}} \sum_{\{S_{\nu\nu',l,\sigma}=\pm 1\}} \exp\Big\{ \sum_{\nu,\sigma} W^{U}_{\nu\sigma}(l)\, n_{\nu,\sigma} + \sum_{\nu=1}^{5} \Big[W^{U'}_{\nu\uparrow}(l)\, n_{\nu,\uparrow} + W^{U'}_{\nu\downarrow}(l)\, n_{\nu,\downarrow} \Big] + \sum_{\nu,\sigma} W^{U'-J}_{\nu\sigma}(l)\, n_{\nu,\sigma} \Big\}. \tag{B.126}$$

where

$$W^{U}_{\nu\sigma}(l) = \sigma\, \lambda_1 S^{U}_{\nu,l}, \tag{B.127}$$

$$\begin{aligned} W^{U'}_{\nu\uparrow}(l) &= \lambda_2 \sum_{\substack{\nu'=1 \\ \nu'\neq\nu}}^{5} S^{U'}_{\nu\nu',l} \\ W^{U'}_{\nu\downarrow}(l) &= -\lambda_2 \sum_{\substack{\nu'=1 \\ \nu'\neq\nu}}^{5} S^{U'}_{\nu'\nu,l}, \end{aligned} \tag{B.128}$$

$$W^{U'-J}_{\nu\sigma}(l) = \lambda_3 \sum_{\nu'=1}^{\nu-1} S^{U'-J}_{\nu\nu',l,\sigma} - \lambda_3 \sum_{\nu'=\nu+1}^{5} S^{U'-J}_{\nu'\nu,l,\sigma}, \tag{B.129}$$

. and

$$W_{\nu\sigma}(l) = W^{U}_{\nu\sigma}(l) + W^{U'}_{\nu\sigma}(l) + W^{U'-J}_{\nu\sigma}(l). \tag{B.130}$$

B.6. Initial calculation of G^{σ} Green's function from G^{0} and W

In this chapter, $G^{\sigma}_{\nu\nu'}$ Green's function is calculated. This Green's function is the non-zero hybridization and non-zero HS field function. $G^{0}_{\nu\nu'}$ and W are used for calculation of $G^{\sigma}_{\nu\nu'}$. Now, let's describe the initial form of $G^{\sigma}_{\nu\nu'}$.

Hirsch and Fye (HIRSCH, 1986) used the following relation between the initial Green's function G and the new Green's function G' (σ omitted):

$$\tilde{G'} = \tilde{G} + (\tilde{G} - \tilde{I})\,(e^{V'-V} - \tilde{I})\,\tilde{G'}. \tag{B.131}$$

V is a diagonal matrix for the Hirsch-Fye quantum Monte Carlo algorithm which includes only the intra-orbital Coulomb interaction. Its exponential is used in the algorithm and because V is diagonal matrix, e^{V} is calculated easily. When the inter-orbital Coulomb interaction is added, V is not diagonal matrix and the calculation of the exponential of V is very diffucult. Therefore, we define W (instead of V) term which includes W^{U}, $W^{U'}$ and $W^{U'-J}$ and it is a diagonal matrix like V. The calculation of $G^{\sigma}_{\nu\nu'}$ does not change too much by way of defining W.

Let's write Eq.(B.131) as

$$\tilde{G'} = \tilde{G} + (\tilde{G} - \tilde{I})\,(e^{W'-W} - \tilde{I})\,\tilde{G'}. \tag{B.132}$$

When the second term at the right side goes to left side, we obtain

$$\tilde{G'} - (\tilde{G} - \tilde{I})\,(e^{W'-W} - I)\,\tilde{G'} = \tilde{G}. \tag{B.133}$$

$$\Rightarrow\ \tilde{G'} = [\tilde{I} - (\tilde{G} - \tilde{I})\,(e^{W'-W} - \tilde{I})]^{-1}\,\tilde{G} \tag{B.134}$$

Because the potential acts only at the d sites, this equation can be rewritten as

$$\tilde{G'}_{\nu\nu'} = [\tilde{I} - (\tilde{G}_{\nu\nu'} - \tilde{I})\,(e^{\sum_\nu W'_\nu - \sum_\nu W_\nu} - \tilde{I})]^{-1}\,\tilde{G}_{\nu\nu'}. \tag{B.135}$$

When we calculate the initial Green's functions $\tilde{G}_{\nu\nu'}$, the terms in Eq.(B.135) change as

$$\begin{aligned} \tilde{G'}_{\nu\nu'} &\rightarrow \tilde{G}_{\nu\nu'}, \\ \tilde{G}_{\nu\nu'} &\rightarrow \tilde{G}^0_{\nu\nu'}, \\ e^{W'-W} &\rightarrow e^{W}, \end{aligned} \tag{B.136}$$

and so the equation of the initial Green's function becomes

$$\tilde{G}_{\nu\nu'} = [\tilde{I} - (\tilde{G}^0_{\nu\nu'} - \tilde{I})\,(e^{\sum_\nu W_\nu} - \tilde{I})]^{-1}\,\tilde{G}^0_{\nu\nu'}. \tag{B.137}$$

In the Hirsch and Fye's paper (HIRSCH, 1986), the sign of $G^0_{\nu\nu'}$ was changed and $G^0_{\nu\nu'}$ was defined by $+$ sign. Therefore, the Green's function is defined as

$$G^\sigma_{\nu\nu'}(l,l') = + \left\langle T\, d_{\nu\sigma}(l)\, d^\dagger_{\nu\sigma}(l') \right\rangle. \tag{B.138}$$

with $+$ sign in our program.

B.7. Calculation of the ratio of the determinants R_σ for the single spin flip

The new Green's functions are recalculated for the spin configurations differing from the previous one by a single-spin flip which is illustrated as $S_{\nu\nu',l} \rightarrow S'_{\nu\nu',l} = -S_{\nu\nu',l}$. These spin configurations are generated with a probability proportional to $\frac{det\theta'_\sigma}{det\theta_\sigma}$ where $\theta = G^{-1}$. The probability of acceptance for the new configuration is calculated by the heat-bath Monte Carlo algorithm and it is defined by the following relation

$$P(s \rightarrow s') = \frac{\prod_\sigma det\theta'_\sigma(\{S'_{\nu\nu',l}\})}{\prod_\sigma det\theta'_\sigma(\{S'_{\nu\nu',l}\}) + \prod_\sigma det\theta_\sigma(\{S_{\nu\nu',l}\})}. \tag{B.139}$$

In this chapter, we proof the ratio of the determinants for the single-spin flip equal to $detA_\sigma$. The outline of this section is the following

- Firstly, the general proof of $R_\sigma = \frac{det\theta'_\sigma}{det\theta_\sigma} = detA_\sigma$ will be shown.
- After that, R_σ will be calculated for U, U' and $U' - J$ terms.
- We need $(W_{\nu\sigma}(l))' - (W_{\nu\sigma}(l))$ term for U, U' and $U' - J$ to calculate the ratio of the determinants. Therefore, these terms will be calculated. Here, $(W_{\nu\sigma}(l))'$ is defined for the new spin configuration and $(W_{\nu\sigma}(l))$ is defined for the old spin configuration.
- Finally, the calculations of A_σ will be done for U, U' and $U' - J$ terms.

B.7.1. Proof of R_σ

For a change of the Hubbard-Stratonovich (HS) field $S_{\nu\nu',l}$,

$$S_{\nu\nu',l} \rightarrow S'_{\nu\nu',l} = -S_{\nu\nu',l}. \tag{B.140}$$

The ratio of the determinants for the new and old configuration is

$$R_\sigma = \frac{det\theta'_\sigma(\{S'_{\nu\nu',l}\})}{det\theta_\sigma(\{S_{\nu\nu',l}\})} = detA_\sigma, \tag{B.141}$$

where

$$\tilde{A}_\sigma = \tilde{I} + (\tilde{I} - \tilde{G}^\sigma)(e^{W'_\sigma - W_\sigma} - \tilde{I}). \tag{B.142}$$

Now, let's prove this equation and start from the following equation (by omitting σ)

$$\begin{aligned} \tilde{G}' = \tilde{G} - \tilde{G}\,(e^{-W'} - e^{-W})\,\tilde{G}' \\ \text{where} \quad \tilde{G} = e^W\,G. \end{aligned} \tag{B.143}$$

- Multiply both sides with $(\tilde{G}')^{-1}$ on the write,

$$\tilde{I} = \tilde{G}\,(\tilde{G}')^{-1} - \tilde{G}\,(e^{-W'} - e^{-W}). \tag{B.144}$$

$$\Rightarrow \tilde{G}\,(\tilde{G}')^{-1} = \tilde{I} + \tilde{G}\,(e^{-W'} - e^{-W}). \tag{B.145}$$

- Since $\tilde{G} = e^W\,G = e^W\,\theta^{-1}$, where $\theta = G^{-1}$, we have

$$(e^W\,\theta^{-1})[e^{W'}\,(\theta')^{-1}]^{-1} = I + e^W\,G\,(e^{-W'} - e^{-W}). \tag{B.146}$$

- Here, we multiply on the left with e^{-W} and on the right with $e^{W'}$, which yields

$$\theta^{-1}\,\theta' = e^{-W}\,e^{W'} + G\,(e^{-W'} - e^{-W})\,e^{W'} \quad \text{(B.147)}$$

$$= e^{W'-W} + G\,(I - e^{W'-W}) \quad \text{(B.148)}$$

$$= e^{W'-W} + (G - I)\,(I - e^{W'-W}) + I(I - e^{W'-W}). \quad \text{(B.149)}$$

$$\Rightarrow \theta^{-1}\,\theta' = I + (I - G)\,(e^{W'-W} - I). \quad \text{(B.150)}$$

- Taking the determinant of the both side, we obtain

$$\frac{det\theta'}{det\theta} = det\Big\{ \underbrace{I + (I - G)\,(e^{W'-W} - I)}_{A} \Big\}. \quad \text{(B.151)}$$

Then

$$R_\sigma = \frac{det\theta'_\sigma}{det\theta_\sigma} = detA_\sigma. \quad \text{(B.152)}$$

B.7.1.1. R_σ for U term

We can write from the previous part that

$$R^U_\sigma = detA^U_\sigma, \quad \text{(B.153)}$$

where

$$\tilde{A}^U_\sigma = \tilde{I} + (\tilde{I} - \tilde{G}^\sigma)\,(e^{W^{U'}_\sigma - W^U_\sigma} - \tilde{I}). \tag{B.154}$$

For U term, when the single-spin flip occurs, $S^U_{\nu,l} \rightarrow S^{U'}_{\nu,l} = -S^U_{\nu,l}$, we have

$$(W^U_{\nu\sigma}(l))' - (W^U_{\nu\sigma}(l)) = -2\lambda_1 \sigma S^U_{\nu,l}. \tag{B.155}$$

Now, let's look at the form of $\tilde{A}^U_\sigma$ and calculate $detA^U_\sigma$.

We know from Section B.7.3.1, A^U_σ has the following form and here, the black point indicates $(A_\sigma)^U_{\nu l,\nu l}$ and the spin is changed at (ν, l). The means of the red solid line is that this column has the non-zero elements. $detA^U_{\nu\sigma}$ can be found by using the

$$A^U_\sigma = \left[\begin{array}{cc|ccccc} 1 & 0 & 0 & \dots & 0 & 0 \\ 0 & 1 & 0 & \dots & 0 & 0 \\ 0 & 0 & 0 & \dots & 0 & 0 \\ 0 & 0 & 1 & 0 & \dots & 0 \\ \vdots & \vdots & 0 & \ddots & \vdots & \vdots \\ \vdots & \vdots & \vdots & \dots & 1 & 0 \\ 0 & 0 & 0 & \dots & 0 & 1 \end{array}\right]_{5L\times 5L}$$

expansion of the minors.

$$|A^U_\sigma| = \sum_{i=1}^{k} (-1)^{i+k}\, a_{ij}\, (A^U_\sigma)_{ij}. \tag{B.156}$$

Here, only the first minor at the right side is not zero and the other expanded minors give

$$detA^U_\sigma = \begin{vmatrix} 1 & & & & & \\ & 1 & & 0 & & \\ & & \bullet & & & \\ 0 & & 1 & & & \\ & & & \ddots & & \\ & & & & 1 & \\ & & & & & 1 \end{vmatrix} = 1\times \begin{vmatrix} 1 & & & & \\ & \bullet & & 0 & \\ 0 & & 1 & & \\ & & & \ddots & \\ & & & & 1 \\ & & & & 1 \end{vmatrix} - 0\times \begin{vmatrix} 0 & & & & \\ & \bullet & & 0 & \\ 0 & & 1 & & \\ & & & \ddots & \\ & & & & 1 \\ & & & & 1 \end{vmatrix} + 0 - 0 \ldots + 0.$$

zero. If the first determinant is expanded up to spin flip point, we have

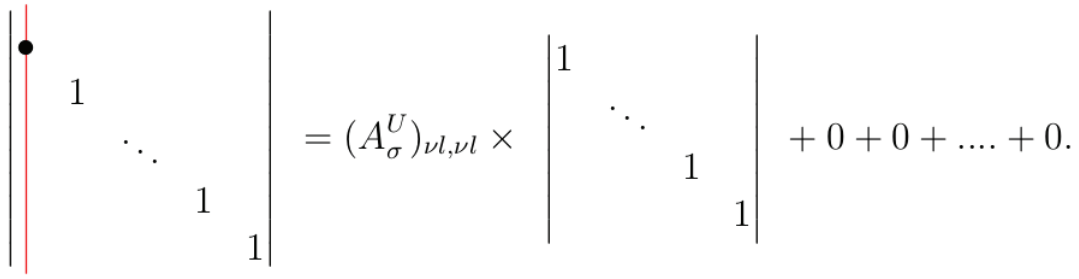

$$\Rightarrow \; detA^U_\sigma = (A^U_\sigma)_{\nu l,\nu l}. \tag{B.157}$$

and we know from Section B.7.3.1 that

$$(A^U_\sigma)_{\nu l,\nu l} \equiv 1 + (1 - G^\sigma_{\nu\nu}(l,l))\,(e^{W^{U}_{\nu,l,\sigma}{}' - W^U_{\nu,l,\sigma}} - 1), \tag{B.158}$$

and

$$R^U_\sigma = \frac{det\theta'_\sigma}{det\theta_\sigma} = detA^U_\sigma. \tag{B.159}$$

Then

$$R^U_\sigma = 1 + (1 - G^\sigma_{\nu\nu}(l,l))\,(e^{W^{U}_{\nu,l,\sigma}{}' - W^U_{\nu,l,\sigma}} - 1). \tag{B.160}$$

B.7.1.2. R_σ for U' term

We can write the following relation from Section B.7.1 that

$$R^{U'}_\sigma = detA^{U'}_\sigma. \tag{B.161}$$

where

$$\tilde{A}^{U'}_{\uparrow} \equiv \tilde{I} + (\tilde{I} - \tilde{G}^{\uparrow})\,(e^{W^{U'}_{\uparrow}{}' - W^{U'}_{\uparrow}} - \tilde{I}), \tag{B.162}$$

$$\tilde{A}^{U'}_{\downarrow} \equiv \tilde{I} + (\tilde{I} - \tilde{G}^{\downarrow})\,(e^{W^{U'}_{\downarrow}{}' - W^{U'}_{\downarrow}} - \tilde{I}). \tag{B.163}$$

For U' term, when the single-spin flip occurs, $S^{U'}_{\nu\nu',l} \rightarrow S^{U'}_{\nu\nu',l}{}' = -S^{U'}_{\nu\nu',l}$, we have the relations

$$(W^{U'}_{\nu\uparrow}(l))' - (W^{U'}_{\nu\uparrow}(l)) = -2\,\lambda_2\,S^{U'}_{\nu\nu',l}, \tag{B.164}$$

$$(W^{U'}_{\nu'\downarrow}(l))' - (W^{U'}_{\nu'\downarrow}(l)) = +2\,\lambda_2\,S^{U'}_{\nu\nu',l}. \tag{B.165}$$

Now, let's look at the form of $\tilde{A}^{U'}_{\sigma}$ and calculate $detA^{U'}_{\sigma}$.

$\uparrow$ spin is flipped at (ν, l) and $\downarrow$ spin is flipped at (ν', l) for . The form of $\tilde{A}^{U'}$ and the $detA^{U'}$ are the same both $\uparrow$ and $\downarrow$ spin. Therefore, the matrix form of $\tilde{A}^{U'}$ and the $detA^{U'}$ will be indicated only for the up spin. While writing their equations, instead of (ν, l), (ν', l) will be used for the down spin.

We know from Section B.7.3.2, $A^{U'}_{\uparrow}$ has the following form and here, the black point indicates $(A^{U'}_{\uparrow})_{\nu l,\nu l}$ and the spin flip occurs at (ν, l). The means of the red solid line is that this column has the non-zero elements. $detA^{U'}_{\nu\uparrow}$ can be found by using the

$$A^{U'}_{\uparrow} = \left[\begin{array}{cc|ccccc} 1 & 0 & 0 & \dots & 0 & 0 \\ 0 & 1 & 0 & \dots & 0 & 0 \\ 0 & 0 & 0 & \dots & 0 & 0 \\ 0 & 0 & 1 & 0 & \dots & 0 \\ \vdots & \vdots & 0 & \ddots & \vdots & \vdots \\ \vdots & \vdots & \vdots & \dots & 1 & 0 \\ 0 & 0 & 0 & \dots & 0 & 1 \end{array}\right]_{5L\times 5L}$$

expansion of the minors.

$$|A^{U'}_{\uparrow}| = \sum_{i=1}^{k} (-1)^{i+k}\,a_{ij}\,(A^{U'}_{\uparrow})_{ij}. \tag{B.166}$$

Here, only the first minor at the right side is not zero and the other expanded minors give

$$detA^{U'}_{\uparrow} = \begin{vmatrix} 1 & & & & \\ & 1 & & 0 & \\ & & \bullet & & \\ & 0 & & 1 & \\ & & & & \ddots \\ & & & & & 1 \\ & & & & & & 1 \end{vmatrix} = 1\times \begin{vmatrix} 1 & & & 0 & \\ & \bullet & & & \\ & & 1 & & \\ & & & \ddots & \\ & & & & 1 \\ 0 & & & & & 1 \end{vmatrix} - 0\times \begin{vmatrix} 0 & & & 0 & \\ & \bullet & & & \\ & & 1 & & \\ & & & \ddots & \\ & & & & 1 \\ 0 & & & & & 1 \end{vmatrix} + 0 - 0 ... + 0.$$

zero. If the first determinant is expanded up to spin flip point, we have Then,

$$\begin{vmatrix} \bullet & & & \\ & 1 & & \\ & & \ddots & \\ & & & 1 \\ & & & & 1 \end{vmatrix} = (A^{U'}_{\uparrow})_{\nu l,\nu l} \times \begin{vmatrix} 1 & & \\ & \ddots & \\ & & 1 \\ & & & 1 \end{vmatrix} + 0 + 0 + ... + 0$$

$$\Rightarrow \begin{aligned} detA^{U'}_{\uparrow} &= (A^{U'}_{\uparrow})_{\nu l,\nu l}, \\ detA^{U'}_{\downarrow} &= (A^{U'}_{\downarrow})_{\nu' l,\nu' l}. \end{aligned} \tag{B.167}$$

and we know from Section B.7.3.2 that

$$\begin{aligned} (A^{U'}_{\uparrow})_{\nu l,\nu l} &\equiv 1 + (1 - G^{\uparrow}_{\nu\nu}(l,l))\,(e^{W^{U'}_{\nu,l,\uparrow}{}' - W^{U'}_{\nu,l,\uparrow}} - 1), \\ (A^{U'}_{\downarrow})_{\nu' l,\nu' l} &\equiv 1 + (1 - G^{\downarrow}_{\nu'\nu'}(l,l))\,(e^{W^{U'}_{\nu',l,\downarrow}{}' - W^{U'}_{\nu',l,\downarrow}} - 1), \end{aligned} \tag{B.168}$$

and

$$\begin{aligned} R^{U'}_{\uparrow} &= \frac{det\theta'_{\uparrow}}{det\theta_{\uparrow}} = detA^{U'}_{\uparrow}, \\ R^{U'}_{\downarrow} &= \frac{det\theta'_{\downarrow}}{det\theta_{\downarrow}} = detA^{U'}_{\downarrow}. \end{aligned} \tag{B.169}$$

Then

$$
\begin{aligned}
R_{\uparrow}^{U'} &= 1 + (1 - G_{\nu\nu}^{\uparrow}(l,l))\,(e^{W_{\nu,l,\uparrow}^{U'}{}' - W_{\nu,l,\uparrow}^{U'}} - 1), \\
R_{\downarrow}^{U} &= 1 + (1 - G_{\nu'\nu'}^{\downarrow}(l,l))\,(e^{W_{\nu',l,\downarrow}^{U'}{}' - W_{\nu,l,\downarrow}^{U'}} - 1).
\end{aligned}
\tag{B.170}
$$

B.7.1.3. R_σ for $U' - J$ term

We can write the following relation from Section B.7.1

$$
R_{\sigma}^{U'-J} = detA_{\sigma}^{U'-J}, \tag{B.171}
$$

where

$$
\tilde{A}_{\sigma}^{U'-J} \equiv \tilde{I} + (\tilde{I} - \tilde{G}^{\sigma})\,(e^{W_{\sigma}^{U'-J}{}' - W_{\sigma}^{U'-J}} - \tilde{I}). \tag{B.172}
$$

For $U' - J$ term, when the single-spin flip occurs, $S_{\nu\nu',l,\sigma}^{U'-J} \rightarrow (S_{\nu\nu',l,\sigma}^{U'-J})' = -S_{\nu\nu',l,\sigma}^{U'-J}$, we have

$$
\begin{aligned}
(W_{\nu\sigma}^{U'-J}(l))' - (W_{\nu\sigma}^{U'-J}(l)) &= \quad -2\lambda_3 S_{\nu\nu',l,\sigma}^{U'-J}, \\
(W_{\nu'\sigma}^{U'-J}(l))' - (W_{\nu'\sigma}^{U'-J}(l)) &= \quad 2\lambda_3 S_{\nu\nu',l,\sigma}^{U'-J}.
\end{aligned}
\tag{B.173}
$$

Now, let's look at the form of $\tilde{A}_{\sigma}^{U'-J}$ and calculate the $detA_{\sigma}^{U'-J}$. Here, we know that the spin flip occurs at both (ν', l) and (ν, l) for spin σ and, the black points indicate $(A_{\sigma}^{U'-J})_{\nu' l,\nu' l}$ and $(A_{\sigma}^{U'-J})_{\nu l,\nu l}$, respectively. The means of the red solid lines is that this column has non-zero elements. $detA_{\sigma}^{U'-J}$ can be found by using the expansion of the minors. In the below matrices, the lowermost black point on the left solid line represents $(A_{\sigma}^{U'-J})_{\nu l,\nu' l}$ and the upmost black point on the right solid line represents $(A_{\sigma}^{U'-J})_{\nu' l,\nu l}$. Here, only the first minor at the right side is not zero and the other expanded minors give zero. If the first determinant is expanded up to spin flip point, we have The last

$$A_\sigma^{U'-J} = \left[\begin{array}{cc|ccc|c} 1 & 0 & 0 & \dots & 0 \\ 0 & 1 & 0 & \dots & 0 \\ 0 & 0 & 0 & \dots & 0 \\ 0 & 0 & 1 & 0 & 0 \\ \vdots & \vdots & 0 & \ddots & \vdots \\ \vdots & \vdots & \vdots & \dots & 0 \\ 0 & 0 & 0 & \dots & 1 \end{array}\right]_{5L\times 5L}$$

$$detA_\sigma^{U'-J} = \begin{vmatrix} 1 & & & & \\ & 1 & & 0 & \\ & & 1 & & \\ & 0 & & \ddots & \\ & & & & 1 \end{vmatrix} = 1\times \begin{vmatrix} 1 & & & \\ & 1 & 0 & \\ 0 & & \ddots & \\ & & & 1 \end{vmatrix} - 0\times \begin{vmatrix} 0 & & & \\ & 1 & 0 & \\ 0 & & \ddots & \\ & & & 1 \end{vmatrix} + 0 - 0 \ldots + 0.$$

determinant equals below determinant:

$$detA_\sigma^{U'-J} = \begin{vmatrix} \bullet & \bullet \\ \bullet & \bullet \end{vmatrix} = \begin{vmatrix} A_{11} & A_{12} \\ A_{21} & A_{22} \end{vmatrix}$$

where

$$\begin{aligned} A_{11}^\sigma &= (A_\sigma^{U'-J})_{\nu' l, \nu' l}, \\ A_{12}^\sigma &= (A_\sigma^{U'-J})_{\nu' l, \nu l}, \\ A_{21}^\sigma &= (A_\sigma^{U'-J})_{\nu l, \nu' l}, \\ A_{22}^\sigma &= (A_\sigma^{U'-J})_{\nu l, \nu l}. \end{aligned} \tag{B.174}$$

$$\Rightarrow R_\sigma^{U'-J} = detA_\sigma^{U'-J} = A_{11}^\sigma A_{22}^\sigma - A_{12}^\sigma A_{21}^\sigma. \tag{B.175}$$

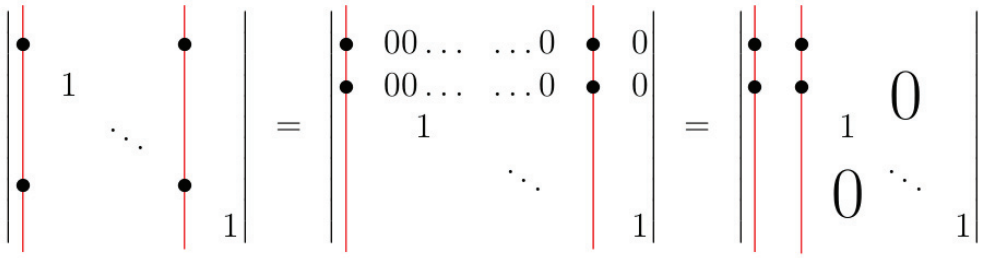

by changing rows

Here, these terms are

$$A^{\sigma}_{11} = (A^{U'-J}_{\sigma})_{\nu' l,\nu' l} = 1 + (1 - G^{\sigma}_{\nu'\nu'}(l,l))\,(e^{+2\lambda_3 S^{U'-J}_{\nu\nu',l,\sigma}} - 1), \tag{B.176}$$

$$A^{\sigma}_{22} = (A^{U'-J}_{\sigma})_{\nu l,\nu l} = 1 + (1 - G^{\sigma}_{\nu\nu}(l,l))\,(e^{-2\lambda_3 S^{U'-J}_{\nu\nu',l,\sigma}} - 1), \tag{B.177}$$

$$A^{\sigma}_{12} = (A^{U'-J}_{\sigma})_{\nu' l,\nu l} = -\,G^{\sigma}_{\nu'\nu}(l,l)\,(e^{-2\lambda_3 S^{U'-J}_{\nu\nu',l,\sigma}} - 1), \tag{B.178}$$

$$A^{\sigma}_{21} = (A^{U'-J}_{\sigma})_{\nu l,\nu' l} = -\,G^{\sigma}_{\nu\nu'}(l,l)\,(e^{+2\lambda_3 S^{U'-J}_{\nu\nu',l,\sigma}} - 1). \tag{B.179}$$

B.7.2. Calculation of $(W_{\nu\sigma}(l))' - (W_{\nu\sigma}(l))$ terms

In this section, the proof of $(W_{\nu\sigma}(l))' - (W_{\nu\sigma}(l))$ will be presented for U, U' and $U' - J$ terms.

B.7.2.1. Calculation of $(W^U_{\nu\sigma}(l))' - (W^U_{\nu\sigma}(l))$

For U term, when the single-spin flip occurs, $S^U_{\nu,l} \rightarrow S^{U\,'}_{\nu,l} = -S^U_{\nu,l}$. Moreover, we know from Section B.5.1 that

$$(W^U_{\nu\sigma}(l)) = \sigma\,\lambda_1 S^U_{\nu,l}, \tag{B.180}$$

$$(W^U_{\nu\sigma}(l))' = -\sigma\,\lambda_1 S^U_{\nu,l}. \tag{B.181}$$

$$\begin{aligned} \Rightarrow (W^U_{\nu\sigma}(l))' - (W^U_{\nu\sigma}(l)) &= -\sigma\,\lambda_1 S^U_{\nu,l} - \sigma\,\lambda_1 S^U_{\nu,l} && \text{(B.182)} \\ &= -2\,\sigma\,\lambda_1 S^U_{\nu,l}. && \text{(B.183)} \end{aligned}$$

For $\sigma = \uparrow$:

$$(W^U_{\nu\uparrow}(l))' - (W^U_{\nu\uparrow}(l)) = -\,2\,\lambda_1 S^U_{\nu,l}. \tag{B.184}$$

For $\sigma = \downarrow$:

$$(W^U_{\nu\downarrow}(l))' - (W^U_{\nu\downarrow}(l)) = +\,2\,\lambda_1 S^U_{\nu,l}. \tag{B.185}$$

B.7.2.2. Calculation of $(W^{U'}_{\nu\sigma}(l))' - (W^{U'}_{\nu\sigma}(l))$

We know from Section B.5.2 that

$$W^{U'}_{\nu\uparrow}(l) = \lambda_2 \sum_{\substack{\nu'=1 \\ \nu'\neq\nu}}^{5} S^{U'}_{\nu\nu',l}, \tag{B.186}$$

and

$$W^{U'}_{\nu\downarrow}(l) = -\lambda_2 \sum_{\substack{\nu'=1 \\ \nu'\neq\nu}}^{5} S^{U'}_{\nu'\nu,l}. \tag{B.187}$$

For $\sigma =\uparrow$

For the single-spin flip, $S^{U'}_{\nu\nu',l} \rightarrow (S^{U'}_{\nu\nu',l})' = -S^{U'}_{\nu\nu',l}$ and

$$(W^{U'}_{\nu\uparrow}(l))' = \lambda_2 \sum_{\substack{\nu'=1 \\ \nu'\neq\nu}}^{5} (S^{U'}_{\nu\nu',l})', \tag{B.188}$$

so

$$\begin{aligned} (W^{U'}_{\nu\uparrow}(l))' - (W^{U'}_{\nu\uparrow}(l)) &= -\lambda_2\, S^{U'}_{\nu\nu',l} - \lambda_2\, S^{U'}_{\nu\nu',l} && \text{(B.189)} \\ &= -2\,\lambda_2\, S^{U'}_{\nu\nu',l}. && \text{(B.190)} \end{aligned}$$

$$\Rightarrow (W^{U'}_{\nu\uparrow}(l))' - (W^{U'}_{\nu\uparrow}(l)) = -2\,\lambda_2\, S^{U'}_{\nu\nu',l}. \tag{B.191}$$

Here, the important point is that the single-spin flip is seen at (ν, l) for $\uparrow$ spin.

For $\sigma =\downarrow$

We know that

$$W^{U'}_{\nu\downarrow}(l) = -\lambda_2 \sum_{\substack{\nu'=1 \\ \nu'\neq\nu}}^{5} S^{U'}_{\nu'\nu,l}. \tag{B.192}$$

Now, let's write $W^{U'}_{\nu\downarrow}(l)$ by using $S^{U'}_{\nu\nu',l}$.

$$W^{U'}_{\nu\downarrow}(l) = -\lambda_2 \sum_{\substack{\nu'=1 \\ \nu'\neq\nu}}^{5} S^{U'}_{\nu'\nu,l}, \tag{B.193}$$

$$\text{watch for the switch of } \nu \text{ and } \nu'$$
$$\Downarrow$$

$$W^{U'}_{\nu'\downarrow}(l) = -\lambda_2 \sum_{\substack{\nu=1 \\ \nu\neq\nu'}}^{5} S^{U'}_{\nu\nu',l}. \tag{B.194}$$

Then

$$\begin{aligned} (W^{U'}_{\nu'\downarrow}(l))' - (W^{U'}_{\nu'\downarrow}(l)) &= -(-\lambda_2\, S^{U'}_{\nu\nu',l}) - (-\lambda_2\, S^{U'}_{\nu\nu',l}) && \text{(B.195)} \\ &= 2\,\lambda_2\, S^{U'}_{\nu\nu',l}. && \text{(B.196)} \end{aligned}$$

$$\Rightarrow (W^{U'}_{\nu'\downarrow}(l))' - (W^{U'}_{\nu'\downarrow}(l)) = 2\,\lambda_2\, S^{U'}_{\nu\nu',l}. \tag{B.197}$$

Here, the important point is that the single-spin flip is seen at (ν', l) for $\downarrow$ spin.

B.7.2.3. Calculation of $(W^{U'-J}_{\nu\sigma}(l))' - (W^{U'-J}_{\nu\sigma}(l))$

We know from Section B.5.3 that

$$W^{U'-J}_{\nu\sigma}(l) = \lambda_3 \sum_{\nu'=1}^{\nu-1} S^{U'-J}_{\nu\nu',l,\sigma} - \lambda_3 \sum_{\nu'=\nu+1}^{5} S^{U'-J}_{\nu'\nu,l,\sigma}. \tag{B.198}$$

and here $\nu > \nu'$.

Single HS spin flip: $S^{U'-J}_{\nu\nu',l,\sigma} \rightarrow (S^{U'-J}_{\nu\nu',l,\sigma})' = -S^{U'-J}_{\nu\nu',l,\sigma}$.

When the spin flips, $S^{U'-J}_{\nu\nu',l,\sigma}$ changes in both $W^{U'-J}_{\nu\sigma}(l)$ and $W^{U'-J}_{\nu'\sigma}(l)$. To see this, let's look at an example:

• Let's say single-spin flip at $(\nu = 4, l)$ and $(\nu' = 3, l)$ and we have $S^{U'-J}_{43,l,\sigma}$ which is in both $W^{U'-J}_{4\sigma}(l)$ and $W^{U'-J}_{3\sigma}(l)$:

$$W^{U'-J}_{4\sigma}(l) = \lambda_3 \, (\, S^{U'-J}_{41,l,\sigma} + S^{U'-J}_{42,l,\sigma} + \boxed{S^{U'-J}_{43,l,\sigma}} \,) - \lambda_3 \, S^{U'-J}_{54,l,\sigma}, \tag{B.199}$$

$$W^{U'-J}_{3\sigma}(l) = \lambda_3 \, (\, S^{U'-J}_{31,l,\sigma} + S^{U'-J}_{32,l,\sigma} \,) - \lambda_3 \, (\, \boxed{S^{U'-J}_{43,l,\sigma}} + S^{U'-J}_{53,l,\sigma} \,). \tag{B.200}$$

Therefore, both $W^{U'-J}_{\nu\sigma}(l)$ and $W^{U'-J}_{\nu'\sigma}(l)$ should be used. If these terms are written, they can be

$$\begin{aligned} W^{U'-J}_{\nu\sigma}(l) &= \lambda_3 \sum_{\nu'=1}^{\nu-1} S^{U'-J}_{\nu\nu',l,\sigma} - \lambda_3 \sum_{\nu'=\nu+1}^{5} S^{U'-J}_{\nu'\nu,l,\sigma}, \\ W^{U'-J}_{\nu'\sigma}(l) &= \lambda_3 \sum_{\nu=1}^{\nu'-1} S^{U'-J}_{\nu'\nu,l,\sigma} - \lambda_3 \sum_{\nu=\nu'+1}^{5} S^{U'-J}_{\nu\nu',l,\sigma}, \end{aligned} \tag{B.201}$$

and $\nu > \nu'$. We should be careful about that

- $S^{U'-J}_{\nu\nu',l,\sigma}$ term has $+$ sign in $W^{U'-J}_{\nu\sigma}(l)$,
- $S^{U'-J}_{\nu\nu',l,\sigma}$ term has $-$ sign in $W^{U'-J}_{\nu'\sigma}(l)$.

Then

$$\begin{aligned} (W^{U'-J}_{\nu\sigma}(l))' - (W^{U'-J}_{\nu\sigma}(l)) &= -\lambda_3 \, S^{U'-J}_{\nu\nu',l,\sigma} - \lambda_3 \, S^{U'-J}_{\nu\nu',l,\sigma} = -2 \, \lambda_3 \, S^{U'-J}_{\nu\nu',l,\sigma}, \\ (W^{U'-J}_{\nu'\sigma}(l))' - (W^{U'-J}_{\nu'\sigma}(l)) &= -(-\lambda_3 \, S^{U'-J}_{\nu\nu',l,\sigma}) - (-\lambda_3 \, S^{U'-J}_{\nu\nu',l,\sigma}) = +2 \, \lambda_3 \, S^{U'-J}_{\nu\nu',l,\sigma}. \end{aligned} \tag{B.202}$$

So for $\nu > \nu'$, we obtain

$$\begin{aligned} (W^{U'-J}_{\nu\sigma}(l))' - (W^{U'-J}_{\nu\sigma}(l)) &= -2 \, \lambda_3 \, S^{U'-J}_{\nu\nu',l,\sigma}, \\ (W^{U'-J}_{\nu'\sigma}(l))' - (W^{U'-J}_{\nu'\sigma}(l)) &= +2 \, \lambda_3 \, S^{U'-J}_{\nu\nu',l,\sigma}. \end{aligned} \tag{B.203}$$

B.7.3. Calculation of A_σ terms

In this section, A_σ will be presented for U, U' and $U' - J$ terms.

B.7.3.1. Calculation of A^U_σ

After the $S^U_{\nu,l}$ is flipped, the new impurity Green's function is obtained from the following relation (by omittin σ)

$$\tilde{G'} = \tilde{G} + (\tilde{G} - \tilde{I})\,(e^{W^{U'} - W^U} - \tilde{I})\,\tilde{G'}, \tag{B.204}$$

by substituting

$$\tilde{G'} = [\tilde{I} - (\tilde{G} - \tilde{I})\,(e^{W^{U'} - W^U} - \tilde{I})]^{-1}\,\tilde{G}, \tag{B.205}$$

$$\Rightarrow \tilde{G'} = \tilde{G} + (\tilde{G} - \tilde{I})\,(e^{W^{U'} - W^U} - \tilde{I})\,[\underbrace{\tilde{I} - (\tilde{G} - \tilde{I})\,(e^{W^{U'} - W^U} - \tilde{I})}_{\tilde{A}^U}]^{-1}\,\tilde{G}. \tag{B.206}$$

Here, we define that

$$\tilde{A}^U \equiv \tilde{I} + (\tilde{I} - \tilde{G})\,(e^{W^{U'} - W^U} - \tilde{I}). \tag{B.207}$$

It is known from Section B.7.2.1 that for $S^U_{\nu,l} \rightarrow S^{U'}_{\nu,l} = -S^U_{\nu,l}$:

$$\begin{aligned} (W^U_{\nu\sigma}(l))' - (W^U_{\nu\sigma}(l)) &= -\sigma\,\lambda_1 S^U_{\nu,l} - \sigma\,\lambda_1 S^U_{\nu,l} \\ &= -2\,\sigma\,\lambda_1 S^U_{\nu,l}. \end{aligned} \tag{B.208}$$

Spin changes only at (ν, l) for U term and so we can define $(W_\sigma^{U'} - W_\sigma^U)_{ii1}$ as the following

$$(W_\sigma^{U'} - W_\sigma^U)_{ii1} = \delta_{\nu,\nu_1}\,\delta_{l,l_1}\,(-2\,\sigma\,\lambda_1 S_{ii}^U), \tag{B.209}$$

where

$$ii1 = (\nu_1, l_1), \tag{B.210}$$
$$ii = ((\nu\nu), l). \tag{B.211}$$

The matrix elements of $(W_\sigma^{U'} - W_\sigma^U)$ is

$$(W_\sigma^{U'} - W_\sigma^U)_{ii1,ii2} = \delta_{\nu,\nu_1}\,\delta_{\nu,\nu_2}\,\delta_{l,l_1}\,\delta_{l,l_2}\,(-2\,\sigma\,\lambda_1 S_{ii}^U), \tag{B.212}$$

where

$$ii2 = (\nu_2, l_2). \tag{B.213}$$

To find the matrix representation of $\tilde{A}^U$, let's write $(e^{W_\sigma^{U'} - W_\sigma^U} - \tilde{I})$ and $(\tilde{I} - \tilde{G})$ matrices. The matrix representation of $(W_\sigma^{U'} - W_\sigma^U)_{ii1,ii2}$ is This is a diagonal matrix and we know

$$(W_\sigma^{U'} - W_\sigma^U) = \begin{bmatrix} 0 & & & & & & \\ & 0 & & & & 0 & \\ & & \ddots & \overset{\nu,\mathrm{l}}{\downarrow} & & & \\ & & & \bullet & & & \\ & & & & 0 & & \\ & 0 & & & & 0 & \\ & & & & & & \ddots \\ & & & & & & & 0 \end{bmatrix}_{5L\times 5L}$$

that if a matrix is diagonal, its exponential can be performed simply by exponentiating each of the diagonal elements. Then, $(e^{W_\sigma^{U'} - W_\sigma^U} - 1)_{ii1,ii2}$ is

$$(e^{W_\sigma^{U'}-W_\sigma^U}-1)=$$

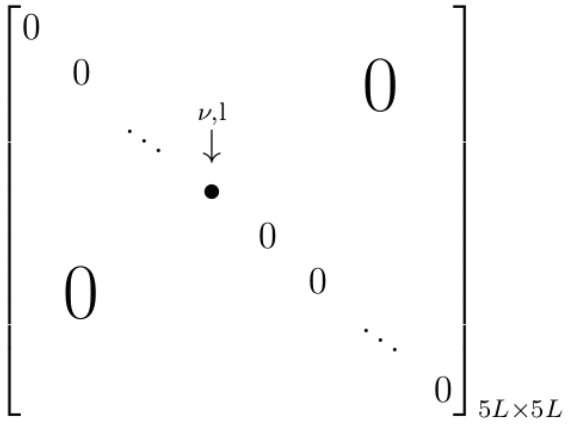

$$\Rightarrow (e^{W_\sigma^{U'}-W_\sigma^U}-1)_{ii1,ii2}=\delta_{\nu,\nu_1}\,\delta_{\nu,\nu_2}\,\delta_{l,l_1}\,\delta_{l,l_2}\,(e^{-2\,\sigma\,\lambda_1 S_{ii}^U}-1). \tag{B.214}$$

Now, let's look at matrix representation of $(I-G)$.

$$(I-G)=$$

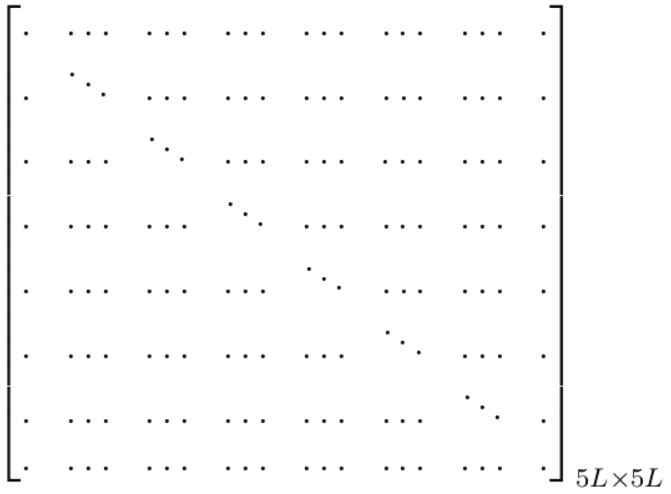

$$\tilde{A}^U=\tilde{I}+(\tilde{I}-\tilde{G})\,(e^{W^{U'}-W^U}-\tilde{I}). \tag{B.215}$$

Here, the black point indicates $(A_\sigma^U)_{\nu l,\nu l}$ and the spin flip occurs at (ν,l). The means of

$$\Rightarrow \tilde{A}^U=\tilde{I}+$$

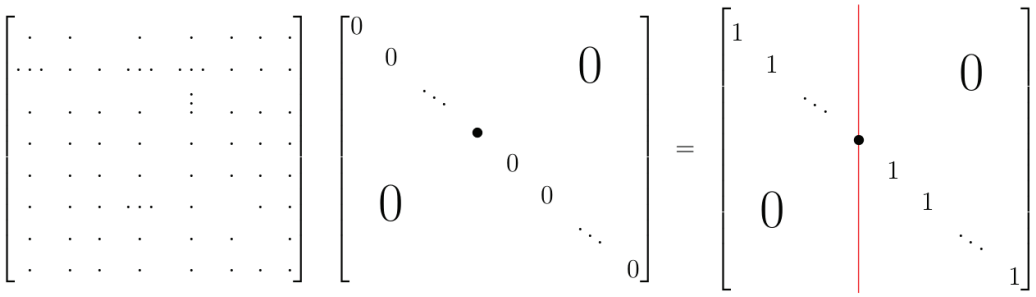

the red solid line is that this column has non-zero elements.

Then, the equation of $(A_\sigma^U)_{\nu_1 l_1,\nu_2 l_2}$ equals

$$(A_\sigma^U)_{\nu_1 l_1,\nu_2 l_2} = \delta_{\nu_1,\nu_2}\,\delta_{l_1,l_2} + \sum_{\nu_3,l_3}(I - G^\sigma)_{\nu_1 l_1,\nu_3 l_3}\,(e^{W_\sigma^{U'} - W_\sigma^U} - 1)_{\nu_3 l_3,\nu_2 l_2}. \quad \text{(B.216)}$$

If the Eq.(B.214) is put in the above equation, we can obtain

$$(A_\sigma^U)_{\nu_1 l_1,\nu_2 l_2} = \delta_{\nu_1,\nu_2}\,\delta_{l_1,l_2} + \sum_{\nu_3,l_3}(I - G^\sigma)_{\nu_1 l_1,\nu_3 l_3}\,(\,\delta_{\nu,\nu_3}\,\delta_{\nu,\nu_2}\,\delta_{l,l_3}\,\delta_{l,l_2}\,(e^{-2\,\sigma\,\lambda_1 S_{ii}^U} - 1)\,). \quad \text{(B.217)}$$

$$\Rightarrow\ (A_\sigma^U)_{\nu_1 l_1,\nu_2 l_2} = \delta_{\nu_1,\nu_2}\,\delta_{l_1,l_2} + \delta_{\nu,\nu_2}\,\delta_{l,l_2}\,(I - G^\sigma)_{\nu_1 l_1,\nu\,l}\,(e^{-2\,\sigma\,\lambda_1 S_{ii}^U} - 1). \quad \text{(B.218)}$$

We know from Section B.7.1.1 that $(A_\sigma^U)_{\nu l,\nu l}$ is used to calculate R_σ^U and it equals

$$(A_\sigma^U)_{\nu l,\nu l} = 1 + (1 - G^\sigma_{\nu l,\nu l})\,(e^{-2\,\sigma\,\lambda_1 S_{ii}^U} - 1). \quad \text{(B.219)}$$

B.7.3.2. Calculation of $A_\sigma^{U'}$

After $S^{U'}_{\nu\,\nu',l}$ is flipped, the new impurity Green's function is obtained from the following relation (by omittin σ)

$$\tilde{G}' = \tilde{G} + (\tilde{G} - \tilde{I})\,(e^{W^{U'^{'}} - W^{U'}} - \tilde{I})\,\tilde{G}', \quad \text{(B.220)}$$

by substituting

$$\tilde{G}' = [\tilde{I} - (\tilde{G} - \tilde{I})\,(e^{W^{U'^{'}} - W^{U'}} - \tilde{I})]^{-1}\,\tilde{G}, \quad \text{(B.221)}$$

$$\Rightarrow \tilde{G}' = \tilde{G} + (\tilde{G} - \tilde{I})\,(e^{W^{U'^{'}} - W^{U'}} - \tilde{I})\,[\underbrace{\tilde{I} - (\tilde{G} - \tilde{I})\,(e^{W^{U'^{'}} - W^{U'}} - \tilde{I})}_{\tilde{A}^{U'}}]^{-1}\,\tilde{G}. \quad \text{(B.222)}$$

Here, we define that

$$\tilde{A}^{U'} \equiv \tilde{I} + (\tilde{I} - \tilde{G})\,(e^{W^{U'^{'}} - W^{U'}} - \tilde{I}). \quad \text{(B.223)}$$

It is known from Section B.7.2.2 that for $S^{U'}_{\nu\,\nu',l} \rightarrow S^{U'}_{\nu\,\nu',l}{}^{'} = -S^{U'}_{\nu\,\nu',l}$:

$$\begin{aligned} (W^{U'}_{\nu\uparrow}(l))' - (W^{U'}_{\nu\uparrow}(l)) &= -2\,\lambda_2\,S^{U'}_{\nu\nu',l}, \\ (W^{U'}_{\nu'\downarrow}(l))' - (W^{U'}_{\nu'\downarrow}(l)) &= +2\,\lambda_2\,S^{U'}_{\nu\nu',l}. \end{aligned} \quad \text{(B.224)}$$

$\uparrow$ spin changes only at (ν, l) and $\downarrow$ spin changes only at (ν', l) for U' term so we can define $(W^{U'^{'}}_{\sigma} - W^{U'}_{\sigma})_{ii1}$ as the following

$$(W^{U'^{'}}_{\uparrow} - W^{U'}_{\uparrow})_{ii1} = \delta_{\nu,\nu_1}\,\delta_{l,l_1}\,(-2\,\lambda_2 S^{U'}_{ii}), \quad \text{(B.225)}$$

$$(W^{U'^{'}}_{\downarrow} - W^{U'}_{\downarrow})_{ii1} = \delta_{\nu',\nu_1}\,\delta_{l,l_1}\,(+2\,\lambda_2 S^{U'}_{ii}), \quad \text{(B.226)}$$

where

$$ii1 = (\nu_1, l_1), \quad \text{(B.227)}$$

$$ii = ((\nu\nu'), l). \quad \text{(B.228)}$$

The matrix elements of $(W^{U'^{'}}_{\uparrow} - W^{U'}_{\uparrow})$ is

$$(W^{U'^{'}}_{\uparrow} - W^{U'}_{\uparrow})_{ii1,ii2} = \delta_{\nu,\nu_1}\,\delta_{\nu,\nu_2}\,\delta_{l,l_1}\,\delta_{l,l_2}\,(-2\,\lambda_2 S^{U'}_{ii}), \quad \text{(B.229)}$$

and the matrix elements of $(W^{U'^{'}}_{\downarrow} - W^{U'}_{\downarrow})$ is

$$(W^{U'^{'}}_{\downarrow} - W^{U'}_{\downarrow})_{ii1,ii2} = \delta_{\nu',\nu_1}\,\delta_{\nu',\nu_2}\,\delta_{l,l_1}\,\delta_{l,l_2}\,(+2\,\lambda_2 S^{U'}_{ii}). \quad \text{(B.230)}$$

where

$$ii2 = (\nu_2, l_2). \tag{B.231}$$

To find the matrix representation of $\tilde{A}^{U'}$, let's write $(e^{W^{U'^{'}} - W^{U'}} - \tilde{I})$ and $(\tilde{I} - \tilde{G})$ matrices.

• Spin changes at (ν, l) for $\uparrow$ spin and at (ν', l) for $\downarrow$ spin.

• The form of $\tilde{A}^{U'}$,$(e^{W^{U'^{'}} - W^{U'}} - \tilde{I})$ and $(\tilde{I} - \tilde{G})$ are the same for both $\uparrow$ and $\downarrow$ spin.

Therefore, the matrix form of $\tilde{A}^{U'}$, the $(e^{W^{U'^{'}} - W^{U'}} - \tilde{I})$ and $(\tilde{I} - \tilde{G})$ will be indicated only for the up spin. While writing their equations, instead of (ν, l), (ν', l) will be used for the down spin.

The matrix representation of $(W_{\uparrow}^{U'^{'}} - W_{\uparrow}^{U'})_{ii1,ii2}$ is This is a diagonal matrix and

$$(W_{\uparrow}^{U'^{'}} - W_{\uparrow}^{U'}) = \begin{bmatrix} 0 & & & & & & \\ & 0 & & & & 0 & \\ & & \ddots & \overset{\nu,l}{\downarrow} & & & \\ & & & \bullet & & & \\ & & & & 0 & & \\ & 0 & & & & 0 & \\ & & & & & & \ddots \\ & & & & & & 0 \end{bmatrix}_{5L \times 5L}$$

we know that if a matrix is a diagonal, its exponential can be performed simply by exponentiating each of the diagonal elements. Then, $(e^{W_{\uparrow}^{U'^{'}} - W_{\uparrow}^{U'}} - 1)_{ii1,ii2}$ is

$$(e^{W_{\uparrow}^{U'^{'}} - W_{\uparrow}^{U'}} - 1) = \begin{bmatrix} 0 & & & & & & \\ & 0 & & & & 0 & \\ & & \ddots & \overset{\nu,l}{\downarrow} & & & \\ & & & \bullet & & & \\ & & & & 0 & & \\ & 0 & & & & 0 & \\ & & & & & & \ddots \\ & & & & & & 0 \end{bmatrix}_{5L \times 5L}$$

$$
\begin{aligned}
& (e^{W_{\uparrow}^{U'^{'}} - W_{\uparrow}^{U'}} - 1)_{ii1,ii2} = \delta_{\nu,\nu_1}\,\delta_{\nu,\nu_2}\,\delta_{l,l_1}\,\delta_{l,l_2}\,(e^{-2\,\lambda_2 S_{ii}^{U'}} - 1), \\
\Rightarrow\ & (e^{W_{\downarrow}^{U'^{'}} - W_{\downarrow}^{U'}} - 1)_{ii1,ii2} = \delta_{\nu',\nu_1}\,\delta_{\nu',\nu_2}\,\delta_{l,l_1}\,\delta_{l,l_2}\,(e^{+2\,\lambda_2 S_{ii}^{U'}} - 1).
\end{aligned}
\tag{B.232}
$$

Now, let's look at matrix representation of $(I - G)$.

$$
(I - G) = \begin{bmatrix}
\cdot & \cdots & \cdots & \cdots & \cdots & \cdots & \cdots & \cdot \\
\cdot & \ddots & \cdots & \cdots & \cdots & \cdots & \cdots & \cdot \\
\cdot & \cdots & \ddots & \cdots & \cdots & \cdots & \cdots & \cdot \\
\cdot & \cdots & \cdots & \ddots & \cdots & \cdots & \cdots & \cdot \\
\cdot & \cdots & \cdots & \cdots & \ddots & \cdots & \cdots & \cdot \\
\cdot & \cdots & \cdots & \cdots & \cdots & \ddots & \cdots & \cdot \\
\cdot & \cdots & \cdots & \cdots & \cdots & \cdots & \ddots & \cdot \\
\cdot & \cdots & \cdots & \cdots & \cdots & \cdots & \cdots & \cdot
\end{bmatrix}_{5L\times 5L}
$$

$$
\begin{aligned}
\tilde{A}_{\uparrow}^{U'} &= \tilde{I} + (\tilde{I} - \tilde{G^{\uparrow}})\,(e^{W_{\uparrow}^{U'^{'}} - W_{\uparrow}^{U'}} - \tilde{I}), \\
\tilde{A}_{\downarrow}^{U'} &= \tilde{I} + (\tilde{I} - \tilde{G^{\downarrow}})\,(e^{W_{\downarrow}^{U'^{'}} - W_{\downarrow}^{U'}} - \tilde{I}).
\end{aligned}
\tag{B.233}
$$

Here, black point indicates $(A_{\uparrow}^{U'})_{\nu l,\nu l}$ and the spin flip occurs at (ν, l). The means of the

$$
\Rightarrow \tilde{A}_{\uparrow}^{U'} = \tilde{I} + \begin{bmatrix}
\cdot & \cdot & \cdot & \cdot & \cdot & \cdot & \cdot \\
\cdots & \cdot & \cdot & \cdots & \cdots & \cdot & \cdot \\
\cdot & \cdot & \cdot & \cdot & \vdots & \cdot & \cdot \\
\cdot & \cdot & \cdot & \cdot & \cdot & \cdot & \cdot \\
\cdot & \cdot & \cdot & \cdot & \cdot & \cdot & \cdot \\
\cdot & \cdot & \cdot & \cdots & \cdot & \cdot & \cdot \\
\cdot & \cdot & \cdot & \cdot & \cdot & \cdot & \cdot \\
\cdot & \cdot & \cdot & \cdot & \cdot & \cdot & \cdot
\end{bmatrix}
\begin{bmatrix}
0 & & & & & & \\
& 0 & & & & & \\
& & \ddots & & & & \\
& & & \bullet & & & 0 \\
& & & & 0 & & \\
& & & & & 0 & \\
0 & & & & & & \ddots \\
& & & & & & & 0
\end{bmatrix}
=
\left[\begin{array}{ccc|ccc}
1 & & & & & \\
& 1 & & & & 0 \\
& & \ddots & & & \\
& & & \bullet & & \\
0 & & & & 1 & \\
& & & & & 1 \\
& & & & & & \ddots \\
& & & & & & & 1
\end{array}\right]
$$

red solid line is that this column has non-zero elements.

Then, the equations of $(A_{\uparrow}^{U'})_{\nu_1 l_1,\nu_2 l_2}$ and $(A_{\downarrow}^{U'})_{\nu_1 l_1,\nu_2 l_2}$ are

$$
(A_{\uparrow}^{U'})_{\nu_1 l_1,\nu_2 l_2} = \delta_{\nu_1,\nu_2}\,\delta_{l_1,l_2} + \sum_{\nu_3,l_3} (I - G^{\uparrow})_{\nu_1 l_1,\nu_3 l_3}\,(e^{W_{\uparrow}^{U'^{'}} - W_{\uparrow}^{U'}} - 1)_{\nu_3 l_3,\nu_2 l_2}, \tag{B.234}
$$

$$(A_{\downarrow}^{U'})_{\nu_1 l_1,\nu_2 l_2} = \delta_{\nu_1,\nu_2}\,\delta_{l_1,l_2} + \sum_{\nu_3,l_3}(I - G^{\downarrow})_{\nu_1 l_1,\nu_3 l_3}\,(e^{W_{\downarrow}^{U'^{'}} - W_{\downarrow}^{U'}} - 1)_{\nu_3 l_3,\nu_2 l_2}. \quad \text{(B.235)}$$

If Eq.(B.232) is put in the above equations, we can obtain

$$(A_{\uparrow}^{U'})_{\nu_1 l_1,\nu_2 l_2} = \delta_{\nu_1,\nu_2}\,\delta_{l_1,l_2} + \sum_{\nu_3,l_3}(I - G^{\uparrow})_{\nu_1 l_1,\nu_3 l_3}\,(\delta_{\nu,\nu_3}\,\delta_{\nu,\nu_2}\,\delta_{l,l_3}\,\delta_{l,l_2}\,(e^{-2\,\lambda_2 S_{ii}^{U'}} - 1)). \quad \text{(B.236)}$$

$$\Rightarrow\ (A_{\uparrow}^{U'})_{\nu_1 l_1,\nu_2 l_2} = \delta_{\nu_1,\nu_2}\,\delta_{l_1,l_2} + \delta_{\nu,\nu_2}\,\delta_{l,l_2}\,(I - G^{\uparrow})_{\nu_1 l_1,\nu\, l}\,(e^{-2\,\lambda_2 S_{ii}^{U'}} - 1), \quad \text{(B.237)}$$

and

$$(A_{\downarrow}^{U'})_{\nu_1 l_1,\nu_2 l_2} = \delta_{\nu_1,\nu_2}\,\delta_{l_1,l_2} + \sum_{\nu_3,l_3}(I - G^{\downarrow})_{\nu_1 l_1,\nu_3 l_3}\,(\delta_{\nu',\nu_3}\,\delta_{\nu',\nu_2}\,\delta_{l,l_3}\,\delta_{l,l_2}\,(e^{+2\,\lambda_2 S_{ii}^{U'}} - 1)). \quad \text{(B.238)}$$

$$\Rightarrow\ (A_{\downarrow}^{U'})_{\nu_1 l_1,\nu_2 l_2} = \delta_{\nu_1,\nu_2}\,\delta_{l_1,l_2} + \delta_{\nu',\nu_2}\,\delta_{l,l_2}\,(I - G^{\downarrow})_{\nu_1 l_1,\nu'\, l}\,(e^{+2\,\lambda_2 S_{ii}^{U'}} - 1). \quad \text{(B.239)}$$

We know from Section B.7.1.3 that $(A_{\uparrow}^{U'})_{\nu l,\nu l}$ is used to calculate $R_{\uparrow}^{U'}$ and $(A_{\downarrow}^{U'})_{\nu' l,\nu' l}$ is used to calculate $R_{\downarrow}^{U'}$ so they equal

$$(A_{\uparrow}^{U'})_{\nu l,\nu l} = 1 + (1 - G_{\nu l,\nu l}^{\uparrow})\,(e^{-2\,\lambda_2 S_{ii}^{U'}} - 1), \quad \text{(B.240)}$$

and

$$(A_{\downarrow}^{U'})_{\nu' l,\nu' l} = 1 + (1 - G_{\nu' l,\nu' l}^{\downarrow})\,(e^{+2\,\lambda_2 S_{ii}^{U'}} - 1). \quad \text{(B.241)}$$

B.7.3.3. Calculation of $A_{\sigma}^{U'-J}$

After $S_{\nu\nu',l,\sigma}^{U'-J}$ is flipped, the new impurity Green's function is obtained from the following relation (by omitting σ)

$$\tilde{G}' = \tilde{G} + (\tilde{G} - \tilde{I})\,(e^{W^{U'-J'} - W^{U'-J}} - \tilde{I})\,\tilde{G}', \tag{B.242}$$

by substituting

$$\tilde{G}' = [\tilde{I} - (\tilde{G} - \tilde{I})\,(e^{W^{U'-J'} - W^{U'-J}} - \tilde{I})]^{-1}\,\tilde{G}, \tag{B.243}$$

$$\tilde{G}' = \tilde{G} + (\tilde{G} - \tilde{I})\,(e^{W^{U'-J'} - W^{U'-J}} - \tilde{I})\,[\underbrace{\tilde{I} - (\tilde{G} - \tilde{I})\,(e^{W^{U'-J'} - W^{U'-J}} - \tilde{I})}_{\tilde{A}^{U'-J}}]^{-1}\,\tilde{G}. \tag{B.244}$$

Here, we define that

$$\tilde{A}^{U'-J} \equiv \tilde{I} + (\tilde{I} - \tilde{G})\,(e^{W^{U'-J'} - W^{U'-J}} - \tilde{I}). \tag{B.245}$$

Let's look at $(W^{U'-J'} - W^{U'-J})_{ii1}$ to write $\tilde{A}^{U'-J}$.

• For $U' - J$ term, spin changes at both (ν, l) and (ν', l).

Therefore, $S_{\nu\nu',l,\sigma}^{U'-J}$ changes in both $W_{\nu\sigma}^{U'-J}$ and $W_{\nu'\sigma}^{U'-J}$. We know from Section B.7.2.3 that

$$\begin{aligned} W_{\nu\sigma}^{U'-J}(l) &= \lambda_3 \sum_{\nu'=1}^{\nu-1} \boxed{S_{\nu\nu',l,\sigma}^{U'-J}} - \lambda_3 \sum_{\nu'=\nu+1}^{5} S_{\nu'\nu,l,\sigma}^{U'-J}, \\ W_{\nu'\sigma}^{U'-J}(l) &= \lambda_3 \sum_{\nu=1}^{\nu'-1} S_{\nu'\nu,l,\sigma}^{U'-J} - \lambda_3 \sum_{\nu=\nu'+1}^{5} \boxed{S_{\nu\nu',l,\sigma}^{U'-J}}, \end{aligned} \tag{B.246}$$

so we have

$$(W_\sigma^{U'-J'} - W_\sigma^{U'-J})_{ii1} = (-\delta_{\nu',\nu_1}\,\delta_{l,l_1}\,\lambda_3(S_{ii}^{U'-J'} - S_{ii}^{U'-J}) + \delta_{\nu,\nu_1}\,\delta_{l,l_1}\,\lambda_3(S_{ii}^{U'-J'} - S_{ii}^{U'-J})), \tag{B.247}$$

where

$$ii1 = (\nu_1, l_1), \tag{B.248}$$

$$ii = ((\nu\nu'), l, \sigma). \tag{B.249}$$

$$S_{ii}^{U'-J} \;\rightarrow\; S_{ii}^{U'-J'} = -S_{ii}^{U'-J}, \tag{B.250}$$

$$(W_\sigma^{U'-J'} - W_\sigma^{U'-J})_{ii1} = \delta_{\nu',\nu_1}\,\delta_{l,l_1}\,(+2\,\lambda_3\,S_{ii}^{U'-J}) + \delta_{\nu,\nu_1}\,\delta_{l,l_1}\,(-2\,\lambda_3\,S_{ii}^{U'-J}). \tag{B.251}$$

From this equation, we can write

$$(W_\sigma^{U'-J'} - W_\sigma^{U'-J})_{ii1,ii2} = \delta_{\nu',\nu_1}\,\delta_{\nu',\nu_2}\,\delta_{l,l_1}\,\delta_{l,l_2}\,(+2\,\lambda_3\,S_{ii}^{U'-J}) + \delta_{\nu,\nu_1}\,\delta_{\nu,\nu_2}\;\delta_{l,l_1}\,\delta_{l,l_2}\,(-2\,\lambda_3\,S_{ii}^{U'-J}). \tag{B.252}$$

To find the matrix representation of $\tilde{A}^{U'-J}$, let's write $(e^{W_\sigma^{U'-J'} - W_\sigma^{U'-J}} - \tilde{I})$ and $(\tilde{I} - \tilde{G})$ matrices.

The matrix representation of $(W_\sigma^{U'-J'} - W_\sigma^{U'-J})_{ii1,ii2}$ is

$$(W_\sigma^{U'-J'} - W_\sigma^{U'-J}) = \begin{bmatrix} 0 & & & & & & & & \\ & 0 & & & & & & 0 & \\ & & \ddots & \overset{\nu',\mathrm{l}}{\downarrow} & & & & & \\ & & & \bullet & & & & & \\ & & & & 0 & \overset{\nu,\mathrm{l}}{\downarrow} & & & \\ & & & & & \bullet & & & \\ & 0 & & & & & 0 & & \\ & & & & & & & \ddots & \\ & & & & & & & & 0 \end{bmatrix}_{5L\times 5L}$$

This is a diagonal matrix and we know that if a matrix is a diagonal, its exponential can be performed simply by exponentiating each of the diagonal elements. Then, $(e^{W_\sigma^{U'-J'} - W_\sigma^{U'-J}} - 1)_{ii1,ii2}$ is

$$(e^{W_\sigma^{U'-J'} - W_\sigma^{U'-J}} - 1) = \begin{bmatrix} 0 & & & & & & & & \\ & 0 & & & & & & 0 & \\ & & \ddots & \overset{\nu',\mathrm{l}}{\downarrow} & & & & & \\ & & & \bullet & & & & & \\ & & & & 0 & \overset{\nu,\mathrm{l}}{\downarrow} & & & \\ & & & & & \bullet & & & \\ & 0 & & & & & 0 & & \\ & & & & & & & \ddots & \\ & & & & & & & & 0 \end{bmatrix}_{5L\times 5L}$$

$$\begin{aligned} \Rightarrow (e^{W_\sigma^{U'-J'} - W_\sigma^{U'-J}} - 1)_{ii1,ii2} = & \quad \delta_{\nu',\nu_1}\,\delta_{\nu',\nu_2}\,\delta_{l,l_1}\,\delta_{l,l_2}\,(e^{+2\,\lambda_3\,S_{ii}^{U'-J}} - 1) \\ & + \quad \delta_{\nu,\nu_1}\,\delta_{\nu,\nu_2}\;\,\delta_{l,l_1}\,\delta_{l,l_2}\,(e^{-2\,\lambda_3\,S_{ii}^{U'-J}} - 1). \end{aligned} \tag{B.253}$$

The matrix form of $(I - G)$ is

$$(I-G)=$$

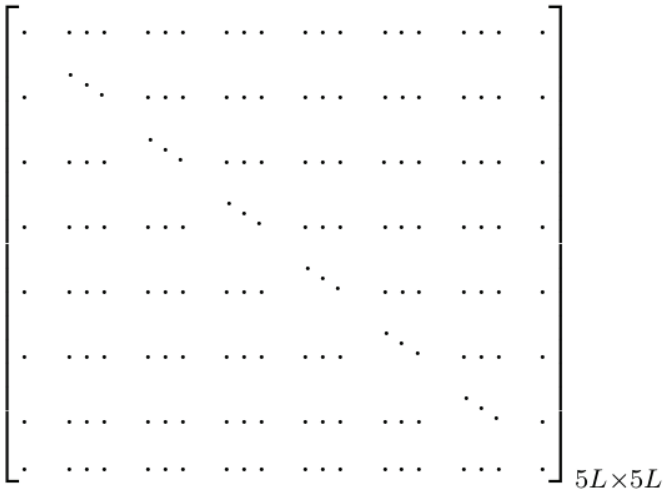

$$\tilde{A}^{U'-J}=\tilde{I}+(\tilde{I}-\tilde{G})\,(e^{W^{U'-J}{}'-W^{U'-J}}-\tilde{I}) \tag{B.254}$$

$$\Rightarrow \tilde{A}^{U'-J}=\tilde{I}+$$

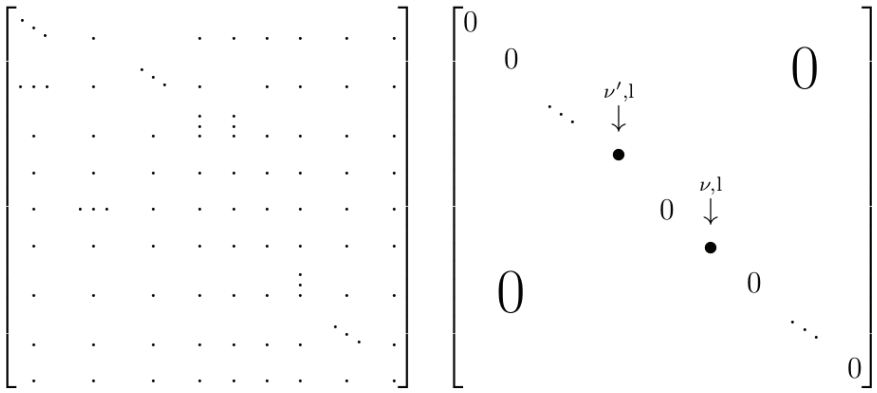

$$\Rightarrow \tilde{A}^{U'-J}=$$

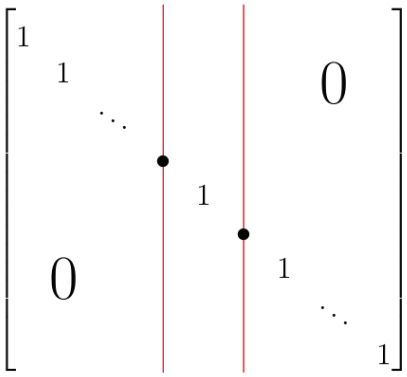

Here, the black points indicate $(A_\sigma^{U'-J})_{\nu' l,\nu' l}$ and $(A_\sigma^{U'-J})_{\nu l,\nu l}$, respectively. The meaning of the red solid lines is that this column has non-zero elements.

Then, the equation of $(A_\sigma^{U'-J})_{\nu_1 l,\nu_2 l}$ equals

$$(A_\sigma^{U'-J})_{\nu_1 l,\nu_2 l} = \delta_{\nu_1,\nu_2}\,\delta_{l_1,l_2} + \sum_{\nu_3,l_3}(I-G^\sigma)_{\nu_1 l_1,\nu_3 l_3}\,(e^{W_\sigma^{U'-J'}-W_\sigma^{U'-J}}-1)_{\nu_3 l_3,\nu_2 l_2}. \tag{B.255}$$

If Eq.(B.253) is placed in the above equation, we obtain

$$\begin{aligned}(A_\sigma^{U'-J})_{\nu_1 l,\nu_2 l} = \delta_{\nu_1,\nu_2}\,\delta_{l_1,l_2} + \sum_{\nu_3,l_3}(I-G^\sigma)_{\nu_1 l_1,\nu_3 l_3}\Big(\,&\delta_{\nu',\nu_3}\,\delta_{\nu',\nu_2}\,\delta_{l,l_3}\,\delta_{l,l_2}\,(e^{+2\,\lambda_3\,S_{ii}^{U'-J}}-1)\\ &+\delta_{\nu,\nu_3}\,\delta_{\nu,\nu_2}\,\delta_{l,l_3}\,\delta_{l,l_2}\,(e^{-2\,\lambda_3\,S_{ii}^{U'-J}}-1)\Big).\end{aligned} \tag{B.256}$$

$$\begin{aligned}\Rightarrow\ (A_\sigma^{U'-J})_{\nu_1 l,\nu_2 l} = \delta_{\nu_1,\nu_2}\,\delta_{l_1,l_2} + \Big\{&(I-G^\sigma)_{\nu_1 l_1,\nu' l}\,\delta_{\nu',\nu_2}\,\delta_{l,l_2}\,(e^{+2\,\lambda_3\,S_{ii}^{U'-J}}-1)\\ &+\ (I-G^\sigma)_{\nu_1 l_1,\nu l}\,\delta_{\nu,\nu_2}\,\delta_{l,l_2}\,(e^{-2\,\lambda_3\,S_{ii}^{U'-J}}-1)\Big\}.\end{aligned} \tag{B.257}$$

As we will show in Section B.8.3, we need only the terms which are $(A_\sigma^{U'-J})_{\nu' l,\nu' l}$, $(A_\sigma^{U'-J})_{\nu l,\nu l}$, $(A_\sigma^{U'-J})_{\nu' l,\nu l}$ and $(A_\sigma^{U'-J})_{\nu l,\nu' l}$. Therefore, we can use $(A_\sigma^{U'-J})_{2L\times 2L}$ matrix which is

$$(A_\sigma^{U'-J}) = \begin{bmatrix}(A_\sigma^{U'-J})_{\nu' l,\nu' l} & (A_\sigma^{U'-J})_{\nu' l,\nu l}\\ (A_\sigma^{U'-J})_{\nu l,\nu' l} & (A_\sigma^{U'-J})_{\nu l,\nu l}\end{bmatrix} = \begin{bmatrix}A_{11}^\sigma & A_{12}^\sigma\\ A_{21}^\sigma & A_{22}^\sigma\end{bmatrix}$$

We know that $ii = ((\nu\nu'), l, \sigma)$ and the matrix elements can be written by using Eq.(B.257):

$$A_{11}^\sigma = (A_\sigma^{U'-J})_{\nu' l,\nu' l} = 1 + (1-G_{\nu'\nu'}^\sigma(l,l))\,(e^{+2\lambda_3 S_{ii}^{U'-J}}-1), \tag{B.258}$$

$$A_{22}^{\sigma} = (A_{\sigma}^{U'-J})_{\nu l,\nu l} = 1 + (1 - G_{\nu\nu}^{\sigma}(l,l))\,(e^{-2\lambda_3 S_{ii}^{U'-J}} - 1), \tag{B.259}$$

$$A_{12}^{\sigma} = (A_{\sigma}^{U'-J})_{\nu' l,\nu l} = -\,G_{\nu'\nu}^{\sigma}(l,l)\,(e^{-2\lambda_3 S_{ii}^{U'-J}} - 1), \tag{B.260}$$

$$A_{21}^{\sigma} = (A_{\sigma}^{U'-J})_{\nu l,\nu' l} = -\,G_{\nu\nu'}^{\sigma}(l,l)\,(e^{+2\lambda_3 S_{ii}^{U'-J}} - 1). \tag{B.261}$$

B.8. Updated Green's functions

As we know that the new spin configuration is accepted or rejected with the probability in Hirsch-Fye quantum Monte Carlo algorithm. If the spin flip is accepted, the new Green's function will be calculated by using the old spin configuration Green's function.

In this chapter, the new spin configuration Green's function for U, U' and $U' - J$ terms are calculated. The outline of this section is the following:

- Firstly, the new impurity Green's function for U term will be calculated. We will use the $(A_{\sigma}^{U})^{-1}$ for this Green's function so $(A_{\sigma}^{U})^{-1}$ will be obtained. After that, the last form of the updated Green's function for U term will be written by using $(A_{\sigma}^{U})^{-1}$.

- Same steps will be used for U' term. The new impurity Green's function for U' term will be calculated. We will use the $(A_{\sigma}^{U'})^{-1}$ for this Green's function so $(A_{\sigma}^{U'})^{-1}$ will be obtained. After that, the last form of updated Green's function for U' term will be written by using $(A_{\sigma}^{U'})^{-1}$.

- Finally, the form of the new Green's function is explained for $U'-J$ term. $(A_{\sigma}^{U'-J})_{5L\times 5L}$ matrix is defined and its inverse is obtained. After that, it is shown that $[(A_{\sigma}^{U'-J})^{-1}]_{2L\times 2L}$ can be used instead of $[(A_{\sigma}^{U'-J})^{-1}]_{5L\times 5L}$ for the calculation of the new Green's functions. Then, the last form of the new Green's function are calculated by replacing elements of $[(A_{\sigma}^{U'-J})^{-1}]_{2L\times 2L}$.

B.8.1. New impurity Green's function for U term

After S_{ii}^{U} is flipped, the new impurity Green's function is obtained from

$$\tilde{G'} = \tilde{G} + (\tilde{G} - \tilde{I})\,(e^{W^{U'} - W^{U}} - \tilde{I})\,\tilde{G'}, \tag{B.262}$$

by substituting

$$\tilde{G'} = [\tilde{I} - (\tilde{G} - \tilde{I})\,(e^{W^{U'} - W^{U}} - \tilde{I})]^{-1}\,\tilde{G}, \tag{B.263}$$

$$\Rightarrow \tilde{G'} = \tilde{G} + (\tilde{G} - \tilde{I})\,(e^{W^{U'} - W^{U}} - \tilde{I})\,[\underbrace{\tilde{I} - (\tilde{G} - \tilde{I})\,(e^{W^{U'} - W^{U}} - \tilde{I})}_{\tilde{A}^{U}}]^{-1}\,\tilde{G}. \tag{B.264}$$

Here, we define that

$$\tilde{A}^{U} \equiv \tilde{I} + (\tilde{I} - \tilde{G})\,(e^{W^{U'} - W^{U}} - \tilde{I}). \tag{B.265}$$

$$\Rightarrow \tilde{G'} = \tilde{G} + (\tilde{G} - \tilde{I})\,(e^{W^{U'} - W^{U}} - \tilde{I})\,(\tilde{A}^{U})^{-1}\,\tilde{G}. \tag{B.266}$$

Now, let's write G':

$$\begin{aligned}(G^{\sigma}_{\nu_1,\nu_2}(l_1,l_2))' &= G^{\sigma}_{\nu_1,\nu_2}(l_1,l_2) \\ + \sum_{l_3,l_4}\sum_{\nu_3,\nu_4} &(G^{\sigma} - I)_{\nu_1\,l_1,\nu_3\,l_3}\,(e^{W^{U'}_{\sigma} - W^{U}_{\sigma}} - I)_{\nu_3\,l_3,\nu_3\,l_3}\,(A^{-1}_{\sigma})^{U}_{\nu_3\,l_3,\nu_4\,l_4}\,G^{\sigma}_{\nu_4,\nu_2}(l_4,l_2).\end{aligned} \tag{B.267}$$

We know from Section B.7.2.1 that

$$(W^U_{\nu\sigma}(l))' - (W^U_{\nu\sigma}(l)) = -\,2\,\sigma\lambda_1 S^U_{ii}\,, \tag{B.268}$$

and the spin flip ocuurs at $(ii) = (\nu, l)$. In Section B.7.3.1, we proved that

$$\Rightarrow\ (e^{W^{U'}_{\sigma} - W^U_{\sigma}} - 1)_{ii1,ii2} = \delta_{\nu,\nu_1}\,\delta_{\nu,\nu_2}\,\delta_{l,l_1}\,\delta_{l,l_2}\,(e^{-2\,\sigma\,\lambda_1 S^U_{ii}} - 1). \tag{B.269}$$

If we place Eq.(B.269) into Eq.(B.267), we can obtain

$$\begin{aligned}(G^{\sigma}_{\nu_1,\nu_2}(l_1,l_2))' &= G^{\sigma}_{\nu_1,\nu_2}(l_1,l_2) \\ &+ \sum_{l_3,l_4}\sum_{\nu_3,\nu_4}(G^{\sigma} - I)_{\nu_1\,l_1,\nu_3\,l_3}\,[\delta_{\nu,\nu_3}\,\delta_{l,l_3}\,(e^{-2\,\sigma\,\lambda_1 S^U_{ii}} - 1)]\,[(A^U_{\sigma})^{-1}]_{\nu_3\,l_3,\nu_4\,l_4}\,G^{\sigma}_{\nu_4,\nu_2}(l_4,l_2),\end{aligned} \tag{B.270}$$

so

$$\begin{aligned}(G^{\sigma}_{\nu_1,\nu_2}(l_1,l_2))' &= G^{\sigma}_{\nu_1,\nu_2}(l_1,l_2) \\ &+ \sum_{\nu_4,l_4}(G^{\sigma} - I)_{\nu_1\,l_1,\nu\,l}\,(e^{-2\,\sigma\,\lambda_1 S^U_{ii}} - 1)\,[(A^U_{\sigma})^{-1}]_{\nu\,l,\nu_4\,l_4}\,G^{\sigma}_{\nu_4,\nu_2}(l_4,l_2)\end{aligned} \tag{B.271}$$

Now, let's calculate $(A^U_{\sigma})^{-1}$.

B.8.1.1. Calculation of $(A^U_{\sigma})^{-1}$

The matrix form of the $(A^U_{\sigma})^{-1}$ can be illustrated as

$$\Rightarrow \boxed{[(A^U_{\sigma})^{-1}]_{\nu\,l,\nu\,l} = \frac{1}{(A^U_{\sigma})_{\nu\,l,\nu\,l}}.} \tag{B.272}$$

We need only $(A^U_{\sigma})_{\nu\,l,\nu\,l}$ term for the calculation of the updated impurity Green's

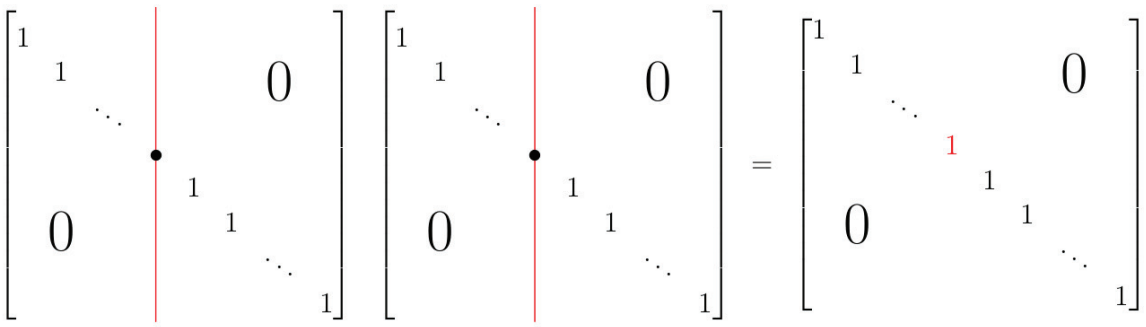

A^U_σ $(A^U_\sigma)^{-1}$ I

function. This term was calculated in Section B.7.3.1 and it equals

$$(A^U_\sigma)_{\nu l,\nu l} = 1 + (1 - G^\sigma_{\nu l,\nu l})\,(e^{-2\,\sigma\,\lambda_1 S^U_{ii}} - 1). \tag{B.273}$$

$$\Rightarrow\ [(A^U_\sigma)^{-1}]_{\nu\,l,\nu_4\,l_4} = \delta_{\nu,\nu_4}\,\delta_{l,l_4}\,\frac{1}{1 + (1 - G^\sigma_{\nu l,\nu l})\,(e^{-2\,\sigma\,\lambda_1 S^U_{ii}} - 1)} \tag{B.274}$$

B.8.1.2. Last form of the new impurity Green's function for U term

In Eq.(B.271), we calculated

$$\begin{aligned}(G^\sigma_{\nu_1,\nu_2}(l_1,l_2))' &= G^\sigma_{\nu_1,\nu_2}(l_1,l_2) \\ &+ \sum_{\nu_4,l_4}(G^\sigma - I)_{\nu_1\,l_1,\nu\,l}\,(e^{-2\,\sigma\,\lambda_1 S^U_{ii}} - 1)\,[(A^U_\sigma)^{-1}]_{\nu\,l,\nu_4\,l_4}\,G^\sigma_{\nu_4,\nu_2}(l_4,l_2),\end{aligned} \tag{B.275}$$

and in Eq.(B.274), we defined

$$(A^U_\sigma)^{-1}_{\nu\,l,\nu_4 l_4} = \delta_{\nu,\nu_4}\,\delta_{l,l_4}\,\frac{1}{1 + (1 - G^\sigma_{\nu l,\nu l})\,(e^{-2\,\sigma\,\lambda_1 S^U_{ii}} - 1)}. \tag{B.276}$$

The new impurity Green's function with these terms are

$$\begin{aligned}(G^{\sigma}_{\nu_1,\nu_2}(l_1,l_2))' &= G^{\sigma}_{\nu_1,\nu_2}(l_1,l_2) + \sum_{\nu_4,l_4}(G^{\sigma}-I)_{\nu_1\,l_1,\nu\,l}\,(e^{-2\,\sigma\,\lambda_1 S^U_{ii}}-1) \\ &\times \left(\delta_{\nu,\nu_4}\,\delta_{l,l_4}\,\frac{1}{1+(1-G^{\sigma}_{\nu l,\nu l})\,(e^{-2\,\sigma\,\lambda_1 S^U_{ii}}-1)}\right) G^{\sigma}_{\nu_4,\nu_2}(l_4,l_2).\end{aligned} \tag{B.277}$$

The new impurity Green's function for U term equals

$$\begin{aligned}&(G^{\sigma}_{\nu_1,\nu_2}(l_1,l_2))' = G^{\sigma}_{\nu_1,\nu_2}(l_1,l_2) \\ \Rightarrow\ &+(G^{\sigma}-I)_{\nu_1\,l_1,\nu\,l}\,(e^{-2\,\sigma\,\lambda_1 S^U_{ii}}-1)\,\frac{1}{1+(1-G^{\sigma}_{\nu l,\nu l})\,(e^{-2\,\sigma\,\lambda_1 S^U_{ii}}-1)}\,G^{\sigma}_{\nu,\nu_2}(l,l_2).\end{aligned} \tag{B.278}$$

In this result, $G^{\sigma}_{\nu,\nu'}(l,l')$ is defined as

$$G^{\sigma}_{\nu,\nu'}(l,l') = +\left\langle\, d_{\nu\,\sigma}(l)\, d^{\dagger}_{\nu'\,\sigma}(l')\,\right\rangle \tag{B.279}$$

without $-$ sign so we have to be careful.

B.8.2. New impurity Green's function for U' term

After $S^{U'}_{ii}$ is flipped, the new impurity Green's function is obtained from

$$\tilde{G}' = \tilde{G} + (\tilde{G}-\tilde{I})\,(e^{W^{U'}{}'-W^{U'}}-\tilde{I})\,\tilde{G}', \tag{B.280}$$

by substituting

$$\tilde{G}' = [\tilde{I} - (\tilde{G}-\tilde{I})\,(e^{W^{U'}{}'-W^{U'}}-\tilde{I})]^{-1}\,\tilde{G}. \tag{B.281}$$

$$\Rightarrow \tilde{G}' = \tilde{G} + (\tilde{G} - \tilde{I})\,(e^{W^{U'^{'}} - W^{U'}} - \tilde{I})\,[\underbrace{\tilde{I} - (\tilde{G} - \tilde{I})\,(e^{W^{U'^{'}} - W^{U'}} - \tilde{I})}_{\tilde{A}^{U'}}]^{-1}\,\tilde{G}. \quad \text{(B.282)}$$

Here, we define that

$$\tilde{A}^{U'} \equiv \tilde{I} + (\tilde{I} - \tilde{G})\,(e^{W^{U'^{'}} - W^{U'}} - \tilde{I}). \quad \text{(B.283)}$$

$$\Rightarrow \tilde{G}' = \tilde{G} + (\tilde{G} - \tilde{I})\,(e^{W^{U'^{'}} - W^{U'}} - \tilde{I})\,(A^{U'})^{-1}\,\tilde{G}. \quad \text{(B.284)}$$

Now, let's write G':

$$\begin{aligned}(G^{\sigma}_{\nu_1,\nu_2}(l_1,l_2))' &= G^{\sigma}_{\nu_1,\nu_2}(l_1,l_2) \\ + \sum_{l_3,l_4}\sum_{\nu_3,\nu_4} &(G^{\sigma} - I)_{\nu_1\,l_1,\nu_3\,l_3}\,(e^{W^{U'^{'}}_{\sigma} - W^{U'}_{\sigma}} - I)_{\nu_3\,l_3,\nu_3\,l_3}\,[(A^{U'}_{\sigma})^{-1}]_{\nu_3\,l_3,\nu_4\,l_4}\,G^{\sigma}_{\nu_4,\nu_2}(l_4,l_2).\end{aligned} \quad \text{(B.285)}$$

We know from Section B.7.2.2 that

$$\begin{aligned}(W^{U'}_{\nu\uparrow}(l))' - (W^{U'}_{\nu\uparrow}(l)) &= -2\,\lambda_2\,S^{U'}_{\nu\nu',l}, \\ (W^{U'}_{\nu'\downarrow}(l))' - (W^{U'}_{\nu'\downarrow}(l)) &= 2\,\lambda_2\,S^{U'}_{\nu\nu',l}.\end{aligned} \quad \text{(B.286)}$$

Here, we should be careful, because $\uparrow$ spin changes at (ν, l) and $\downarrow$ spin changes at (ν', l). In Section B.7.3.2, we calculated that

$$\Rightarrow \begin{aligned}(e^{W^{U'^{'}}_{\uparrow} - W^{U'}_{\uparrow}} - 1)_{ii1,ii2} &= \delta_{\nu,\nu_1}\,\delta_{\nu,\nu_2}\,\delta_{l,l_1}\,\delta_{l,l_2}\,(e^{-2\,\lambda_2 S^{U'}_{ii}} - 1), \\ (e^{W^{U'^{'}}_{\downarrow} - W^{U'}_{\downarrow}} - 1)_{ii1,ii2} &= \delta_{\nu',\nu_1}\,\delta_{\nu',\nu_2}\,\delta_{l,l_1}\,\delta_{l,l_2}\,(e^{+2\,\lambda_2 S^{U'}_{ii}} - 1).\end{aligned} \quad \text{(B.287)}$$

If Eq.(B.287) is placed in Eq.(B.285), the following equations can be obtained for $\uparrow$ and $\downarrow$ spins, respectively.

For $\sigma = \uparrow$:

$$(G^{\uparrow}_{\nu_1,\nu_2}(l_1,l_2))' = G^{\uparrow}_{\nu_1,\nu_2}(l_1,l_2)$$
$$+\sum_{l_3,l_4}\sum_{\nu_3,\nu_4}(G^{\uparrow}-I)_{\nu_1\,l_1,\nu_3\,l_3}\,[\delta_{\nu,\nu_3}\,\delta_{l,l_3}\,(e^{-2\,\lambda_2 S^{U'}_{ii}}-1)]\,[(A^{U'}_{\uparrow})^{-1}]_{\nu_3\,l_3,\nu_4\,l_4}\,G^{\uparrow}_{\nu_4,\nu_2}(l_4,l_2), \tag{B.288}$$

so

$$(G^{\uparrow}_{\nu_1,\nu_2}(l_1,l_2))' = G^{\uparrow}_{\nu_1,\nu_2}(l_1,l_2) + \sum_{\nu_4,l_4}(G^{\uparrow}-I)_{\nu_1\,l_1,\nu\,l}\,(e^{-2\,\lambda_2 S^{U'}_{ii}}-1)\,[(A^{U'}_{\uparrow})^{-1}]_{\nu\,l,\nu_4\,l_4}\,G^{\uparrow}_{\nu_4,\nu_2}(l_4,l_2) \tag{B.289}$$

For $\sigma =\downarrow$:

$$(G^{\downarrow}_{\nu_1,\nu_2}(l_1,l_2))' = G^{\downarrow}_{\nu_1,\nu_2}(l_1,l_2)$$
$$+\sum_{l_3,l_4}\sum_{\nu_3,\nu_4}(G^{\downarrow}-I)_{\nu_1\,l_1,\nu_3\,l_3}\,[\delta_{\nu',\nu_3}\,\delta_{l,l_3}\,(e^{+2\,\lambda_2 S^{U'}_{ii}}-1)]\,[(A^{U'}_{\downarrow})^{-1}]_{\nu_3\,l_3,\nu_4\,l_4}\,G^{\downarrow}_{\nu_4,\nu_2}(l_4,l_2), \tag{B.290}$$

so

$$(G^{\downarrow}_{\nu_1,\nu_2}(l_1,l_2))' = G^{\downarrow}_{\nu_1,\nu_2}(l_1,l_2) + \sum_{\nu_4,l_4}(G^{\downarrow}-I)_{\nu_1\,l_1,\nu'\,l}\,(e^{+2\,\lambda_2 S^{U'}_{ii}}-1)\,[(A^{U'}_{\downarrow})^{-1}]_{\nu'\,l,\nu_4\,l_4}\,G^{\downarrow}_{\nu_4,\nu_2}(l_4,l_2). \tag{B.291}$$

Now, let's calculate $(A^{U'}_{\uparrow})^{-1}$ and $(A^{U'}_{\downarrow})^{-1}$.

B.8.2.1. Calculation of $(A_\sigma^{U'})^{-1}$

The Green's function form and $A^{U'}$ form are the similar for the up and the down spin for U' term. The only difference is that the up spin changes at (ν, l) and the down spin changes at (ν', l).

The matrix form of $(A_\sigma^{U'})^{-1}$ is represented as For $\sigma =\uparrow$, the black point shows

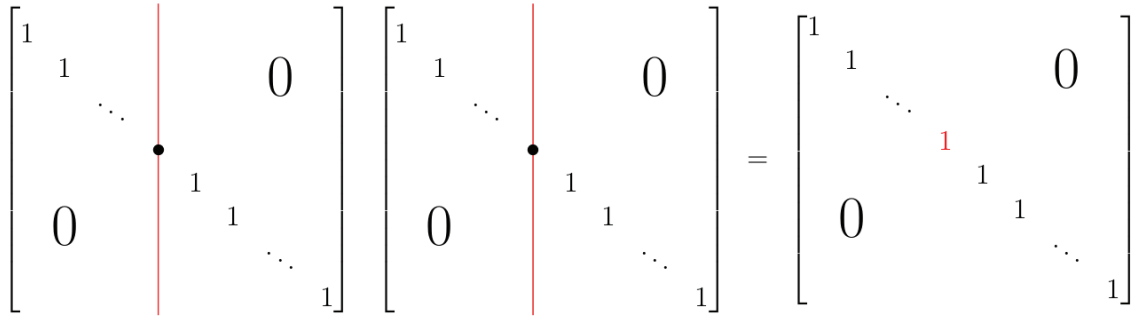

(ν, l) but, for $\sigma =\downarrow$, the black point indicatese (ν', l). We can say from the above matrix representation that

$$\Rightarrow [(A_\uparrow^{U'})^{-1}]_{\nu\, l,\nu\, l} = \frac{1}{(A_\uparrow^{U'})_{\nu\, l,\nu\, l}}, \tag{B.292}$$

$$\Rightarrow [(A_\downarrow^{U'})^{-1}]_{\nu'\, l,\nu'\, l} = \frac{1}{(A_\downarrow^{U'})_{\nu'\, l,\nu'\, l}}. \tag{B.293}$$

We need only $(A_\uparrow^{U'})_{\nu\, l,\nu\, l}$ and $(A_\downarrow^{U'})_{\nu'\, l,\nu'\, l}$ terms for the calculation of the updated impurity Green's function. These terms were calculated in Section B.7.3.2 and they equal

$$(A_\uparrow^{U'})_{\nu l,\nu l} = 1 + (1 - G^\uparrow_{\nu l,\nu l})\,(e^{-2\,\lambda_2 S_{ii}^{U'}} - 1), \tag{B.294}$$

and

$$(A_\downarrow^{U'})_{\nu' l,\nu' l} = 1 + (1 - G^\downarrow_{\nu' l,\nu' l})\,(e^{+2\,\lambda_2 S_{ii}^{U'}} - 1), \tag{B.295}$$

so

$$\Rightarrow [(A_{\uparrow}^{U'})^{-1}]_{\nu\, l,\nu_4,l_4} = \delta_{\nu,\nu_4}\, \delta_{l,l_4}\, \frac{1}{1+(1-G^{\uparrow}_{\nu l,\nu l})\,(e^{-2\,\lambda_2 S_{ii}^{U'}}-1)}, \tag{B.296}$$

and

$$[(A_{\downarrow}^{U'})^{-1}]_{\nu'\, l,\nu_4\, l_4} = \delta_{\nu',\nu_4}\, \delta_{l,l_4}\, \frac{1}{1+(1-G^{\downarrow}_{\nu' l,\nu' l})\,(e^{+2\,\lambda_2 S_{ii}^{U'}}-1)}. \tag{B.297}$$

B.8.2.2. Last form of the new impurity Green's function for U' term

If Eq.(B.296) is placed in Eq.(B.289) and, Eq.(B.297) is placed in Eq.(B.291), the updated Green's functions for $\sigma =\uparrow$ and $\sigma =\downarrow$ can be obtained.

For $\sigma =\uparrow$:

$$\begin{aligned}(G^{\uparrow}_{\nu_1,\nu_2}(l_1,l_2))' &= G^{\uparrow}_{\nu_1,\nu_2}(l_1,l_2) \\ &+ \sum_{\nu_4,l_4}(G^{\uparrow}-I)_{\nu_1\, l_1,\nu\, l}\,(e^{-2\,\lambda_2 S_{ii}^{U'}}-1)\,[(A_{\uparrow}^{U'})^{-1}]_{\nu\, l,\nu_4\, l_4}\, G^{\uparrow}_{\nu_4,\nu_2}(l_4,l_2),\end{aligned} \tag{B.298}$$

and

$$[(A_{\uparrow}^{U'})^{-1}]_{\nu\, l,\nu_4,l_4} = \delta_{\nu,\nu_4}\, \delta_{l,l_4}\, \frac{1}{1+(1-G^{\uparrow}_{\nu l,\nu l})\,(e^{-2\,\lambda_2 S_{ii}^{U'}}-1)}. \tag{B.299}$$

Then, the new impurity Green's function with these terms are

$$\begin{aligned}(G^{\uparrow}_{\nu_1,\nu_2}(l_1,l_2))' &= G^{\uparrow}_{\nu_1,\nu_2}(l_1,l_2) + \sum_{\nu_4,l_4}(G^{\uparrow}-I)_{\nu_1\,l_1,\nu\,l}\,(e^{-2\,\lambda_2 S^{U'}_{ii}}-1) \\ &\times \left(\delta_{\nu,\nu_4}\,\delta_{l,l_4}\,\frac{1}{1+(1-G^{\uparrow}_{\nu l,\nu l})\,(e^{-2\,\lambda_2 S^{U}_{ii}}-1)}\right) G^{\uparrow}_{\nu_4,\nu_2}(l_4,l_2),\end{aligned} \tag{B.300}$$

and the last form of updated Green's function for U' and $\sigma =\uparrow$ equals

$$\begin{aligned}&(G^{\uparrow}_{\nu_1,\nu_2}(l_1,l_2))' = G^{\uparrow}_{\nu_1,\nu_2}(l_1,l_2) \\ \Rightarrow\ &+(G^{\uparrow}-I)_{\nu_1\,l_1,\nu\,l}\,(e^{-2\,\lambda_2 S^{U'}_{ii}}-1)\,\frac{1}{1+(1-G^{\uparrow}_{\nu l,\nu l})\,(e^{-2\,\lambda_2 S^{U'}_{ii}}-1)}\,G^{\uparrow}_{\nu,\nu_2}(l,l_2).\end{aligned} \tag{B.301}$$

In this result, $G^{\uparrow}_{\nu,\nu'}(l,l')$ is defined as

$$G^{\uparrow}_{\nu,\nu'}(l,l') = +\left\langle\, d_{\nu\uparrow}(l)\, d^{\dagger}_{\nu'\uparrow}(l')\,\right\rangle \tag{B.302}$$

without $-$ sign so we have to be careful.

For $\sigma =\downarrow$:

$$\begin{aligned}(G^{\downarrow}_{\nu_1,\nu_2}(l_1,l_2))' &= G^{\downarrow}_{\nu_1,\nu_2}(l_1,l_2) \\ &+ \sum_{\nu_4,l_4}(G^{\downarrow}-I)_{\nu_1\,l_1,\nu'\,l}\,(e^{+2\,\lambda_2 S^{U'}_{ii}}-1)\,[(A^{U'}_{\downarrow})^{-1}]_{\nu'\,l,\nu_4\,l_4}\,G^{\downarrow}_{\nu_4,\nu_2}(l_4,l_2),\end{aligned} \tag{B.303}$$

and

$$[(A^{U'}_{\downarrow})^{-1}]_{\nu'\,l,\nu_4,l_4} = \delta_{\nu',\nu_4}\,\delta_{l,l_4}\,\frac{1}{1+(1-G^{\downarrow}_{\nu' l,\nu' l})\,(e^{+2\,\lambda_2 S^{U'}_{ii}}-1)}. \tag{B.304}$$

Then, the new impurity Green's function with these terms are

$$\begin{aligned}(G^{\downarrow}_{\nu_1,\nu_2}(l_1,l_2))' &= G^{\downarrow}_{\nu_1,\nu_2}(l_1,l_2) + \sum_{\nu_4,l_4}(G^{\downarrow}-I)_{\nu_1\,l_1,\nu'\,l}\,(e^{+2\,\lambda_2 S^{U'}_{ii}}-1) \\ &\times \left(\delta_{\nu',\nu_4}\,\delta_{l,l_4}\,\frac{1}{1+(1-G^{\downarrow}_{\nu'l,\nu'l})\,(e^{+2\,\lambda_2 S^{U}_{ii}}-1)}\right) G^{\downarrow}_{\nu_4,\nu_2}(l_4,l_2),\end{aligned} \tag{B.305}$$

and the last form of updated Green's function for U' and $\sigma =\downarrow$ equals

$$\begin{aligned}(G^{\downarrow}_{\nu_1,\nu_2}(l_1,l_2))' &= G^{\downarrow}_{\nu_1,\nu_2}(l_1,l_2) \\ +(G^{\downarrow}-I)_{\nu_1\,l_1,\nu'\,l}\,(e^{+2\,\lambda_2 S^{U'}_{ii}}-1)\,&\frac{1}{1+(1-G^{\downarrow}_{\nu'l,\nu'l})\,(e^{+2\,\lambda_2 S^{U'}_{ii}}-1)}\,G^{\downarrow}_{\nu',\nu_2}(l,l_2).\end{aligned} \tag{B.306}$$

In this result, $G^{\downarrow}_{\nu,\nu'}(l,l')$ is defined as

$$G^{\downarrow}_{\nu,\nu'}(l,l') = +\left\langle\, d_{\nu\downarrow}(l)\, d^{\dagger}_{\nu'\downarrow}(l')\,\right\rangle \tag{B.307}$$

without $-$ sign so we have to be careful.

B.8.3. New impurity Green's function for $U'-J$ term

After $S^{U'-J}_{ii}$ is flipped, the new impurity Green's function is obtained from

$$\tilde{G}' = \tilde{G} + (\tilde{G}-\tilde{I})\,(e^{W^{U'-J'}-W^{U'-J}}-\tilde{I})\,\tilde{G}', \tag{B.308}$$

by substituting

$$\tilde{G}' = [\tilde{I} - (\tilde{G}-\tilde{I})\,(e^{W^{U'-J'}-W^{U'-J}}-\tilde{I})]^{-1}\,\tilde{G}. \tag{B.309}$$

$$\tilde{G}' = \tilde{G} + (\tilde{G} - \tilde{I})\,(e^{W^{U'-J}{}' - W^{U-J'}} - \tilde{I})\,[\underbrace{\tilde{I} - (\tilde{G} - \tilde{I})\,(e^{W^{U'-J}{}' - W^{U'-J}} - \tilde{I})}_{\tilde{A}^{U'-J}}]^{-1}\,\tilde{G}. \tag{B.310}$$

Here, we define

$$\tilde{A}^{U'-J} \equiv \tilde{I} + (\tilde{I} - \tilde{G})\,(e^{W^{U'-J}{}' - W^{U'-J}} - \tilde{I}). \tag{B.311}$$

$$\Rightarrow \tilde{G}' = \tilde{G} + (\tilde{G} - \tilde{I})\,(e^{W^{U'-J}{}' - W^{U'-J}} - \tilde{I})\,(A^{U'-J})^{-1}\,\tilde{G}. \tag{B.312}$$

Now, let's write G':

$$\begin{aligned}
(G^{\sigma}_{\nu_1,\nu_2}(l_1,l_2))' &= G^{\sigma}_{\nu_1,\nu_2}(l_1,l_2) \\
&+ \sum_{l_3,l_4}\sum_{\nu_3,\nu_4}(G^{\sigma} - I)_{\nu_1\,l_1,\nu_3\,l_3}\,(e^{W^{U'-J}{}'_{\sigma} - W^{U'-J}_{\sigma}} - I)_{\nu_3\,l_3,\nu_3\,l_3} \\
&\times\ [(A^{U'-J}_{\sigma})^{-1}]_{\nu_3\,l_3,\nu_4\,l_4}\,G^{\sigma}_{\nu_4,\nu_2}(l_4,l_2).
\end{aligned} \tag{B.313}$$

We know from Section B.7.2.3:

$$\begin{aligned}
(W^{U'-J}_{\nu\sigma}(l))' - (W^{U'-J}_{\nu\sigma}(l)) &= -2\,\lambda_3\,S^{U'-J}_{\nu\nu',l,\sigma}, \\
(W^{U'-J}_{\nu'\sigma}(l))' - (W^{U'-J}_{\nu'\sigma}(l)) &= +2\,\lambda_3\,S^{U'-J}_{\nu\nu',l,\sigma}.
\end{aligned} \tag{B.314}$$

For $U' - J$ term, we know that the spin flip occurs at both (ν', l) and (ν, l), and we proved in Section B.7.3.3 that

$$\begin{aligned}
(e^{W^{U'-J}{}'_{\sigma} - W^{U'-J}_{\sigma}} - 1)_{ii1,ii2} &= \delta_{\nu',\nu_1}\,\delta_{\nu',\nu_2}\,\delta_{l,l_1}\,\delta_{l,l_2}\,(e^{+2\,\lambda_3\,S^{U'-J}_{ii}} - 1) \\
&+ \delta_{\nu,\nu_1}\,\delta_{\nu,\nu_2}\ \delta_{l,l_1}\,\delta_{l,l_2}\,(e^{-2\,\lambda_3\,S^{U'-J}_{ii}} - 1),
\end{aligned} \tag{B.315}$$

where

$$ii = ((\nu\,\nu'), l, \sigma). \tag{B.316}$$

If the Eq.(B.315) is placed in Eq.(B.313), the following equation can be obtained:

$$\begin{aligned}(G^{\sigma}_{\nu_1,\nu_2}(l_1,l_2))' &= G^{\sigma}_{\nu_1,\nu_2}(l_1,l_2) + \sum_{l_3,l_4}\sum_{\nu_3,\nu_4}(G^{\sigma}-I)_{\nu_1\,l_1,\nu_3\,l_3} \\ &\times \quad [\delta_{\nu',\nu_3}\,\delta_{l,l_3}\,(e^{+2\,\lambda_3\,S_{ii}^{U'-J}}-1)+\delta_{\nu,\nu_3}\,\delta_{l,l_3}\,(e^{-2\,\lambda_3\,S_{ii}^{U'-J}}-1)] \\ &\times \quad [(A_{\sigma}^{U'-J})^{-1}]_{\nu_3\,l_3,\nu_4\,l_4}\,G^{\sigma}_{\nu_4,\nu_2}(l_4,l_2).\end{aligned} \tag{B.317}$$

$$\begin{aligned}(G^{\sigma}_{\nu_1,\nu_2}(l_1,l_2))' = G^{\sigma}_{\nu_1,\nu_2}(l_1,l_2) + \Big\{&(G^{\sigma}-I)_{\nu_1\,l_1,\nu'\,l}\,(e^{+2\,\lambda_3\,S_{ii}^{U'-J}}-1) \\ &\times\sum_{\nu_4,l_4}[(A_{\sigma}^{U'-J})^{-1}]_{\nu'\,l,\nu_4\,l_4}\,G^{\sigma}_{\nu_4,\nu_2}(l_4,l_2) \\ +(G^{\sigma}-I)_{\nu_1\,l_1,\nu\,l}\,(e^{-2\,\lambda_3\,S_{ii}^{U'-J}}-1)&\sum_{\nu_4,l_4}[(A_{\sigma}^{U'-J})^{-1}]_{\nu\,l,\nu_4\,l_4}\,G^{\sigma}_{\nu_4,\nu_2}(l_4,l_2)\Big\}.\end{aligned} \tag{B.318}$$

Note that we need only $[(A_{\sigma}^{U'-J})^{-1}]_{\nu'\,l,\nu_4\,l_4}$ and $[(A_{\sigma}^{U'-J})^{-1}]_{\nu\,l,\nu_4\,l_4}$. All of matrix elements of $(A_{\sigma}^{U'-J})^{-1}$ are not necessary.

Now, let's calculate $(A_{\sigma}^{U'-J})^{-1}$.

B.8.3.1. General $(A_{\sigma}^{U'-J})_{5L\times 5L}$ matrix and its inverse

We can show the matrix form of $(A_{\sigma}^{U'-J})^{-1}$ by using When (ν_3, l_3) row and (ν_3, l_3)

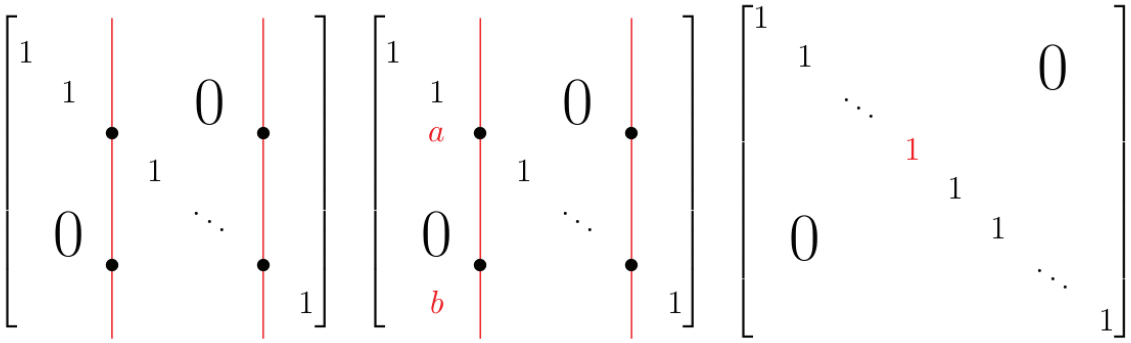

$A_\sigma^{U'-J}$ $(A_\sigma^{U'-J})^{-1}$ I

column is multiplied, the following solution will be obtained:

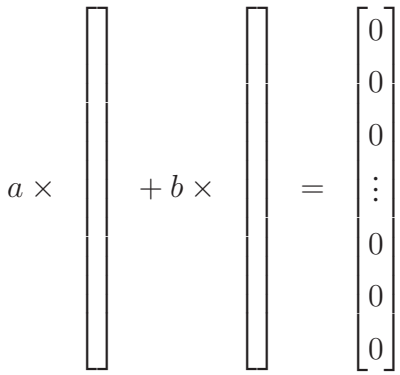

$$\begin{aligned} \Rightarrow a &= 0 \\ b &= 0 \end{aligned} \tag{B.319}$$

Then, $[(A_\sigma^{U'-J})^{-1}]_{5L\times 5L}$ has the form as

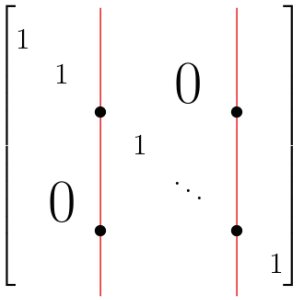

B.8.3.2. Calculation of $[(A_\sigma^{U'-J})^{-1}]_{2L\times 2L}$ matrix

Note that $[(A_\sigma^{U'-J})^{-1}]_{5L\times 5L}$ general matrix has the form The spin is flipped on

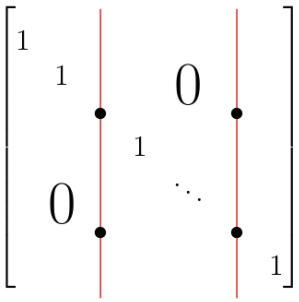

(ν', l) and (ν, l) and so we need only the 4 elements of $[(A_\sigma^{U'-J})^{-1}]_{5L\times 5L}$ which are shown by the black bullets. Therefore, we can use the reduced $[(A_\sigma^{U'-J})^{-1}]_{2L\times 2L}$ which has the form as

$$[(A_\sigma^{U'-J})^{-1}]_{2L\times 2L} = \begin{bmatrix} [(A_\sigma^{U'-J})^{-1}]_{11} & [(A_\sigma^{U'-J})^{-1}]_{12} \\ [(A_\sigma^{U'-J})^{-1}]_{21} & [(A_\sigma^{U'-J})^{-1}]_{22} \end{bmatrix}$$

Here,

$$\begin{aligned} [(A_\sigma^{U'-J})^{-1}]_{11} &= [(A_\sigma^{U'-J})^{-1}]_{\nu' l,\nu' l}, \\ [(A_\sigma^{U'-J})^{-1}]_{22} &= [(A_\sigma^{U'-J})^{-1}]_{\nu l,\nu l}, \\ [(A_\sigma^{U'-J})^{-1}]_{12} &= [(A_\sigma^{U'-J})^{-1}]_{\nu' l,\nu l}, \\ [(A_\sigma^{U'-J})^{-1}]_{21} &= [(A_\sigma^{U'-J})^{-1}]_{\nu l,\nu' l}. \end{aligned} \tag{B.320}$$

We can obtain the elements of $[(A_\sigma^{U'-J})^{-1}]_{2L\times 2L}$ matrix by using the following simple matrix algebra:

$$\begin{bmatrix} (A_\sigma^{U'-J})_{11} & (A_\sigma^{U'-J})_{12} \\ (A_\sigma^{U'-J})_{21} & (A_\sigma^{U'-J})_{22} \end{bmatrix} \begin{bmatrix} [(A_\sigma^{U'-J})^{-1}]_{11} & [(A_\sigma^{U'-J})^{-1}]_{12} \\ [(A_\sigma^{U'-J})^{-1}]_{21} & [(A_\sigma^{U'-J})^{-1}]_{22} \end{bmatrix} = \begin{bmatrix} 1 & 0 \\ 0 & 1 \end{bmatrix}$$

$$
\begin{aligned}
&(A_\sigma^{U'-J})_{11}\,[(A_\sigma^{U'-J})^{-1}]_{11} + (A_\sigma^{U'-J})_{12}\,[(A_\sigma^{U'-J})^{-1}]_{21} = 1 \\
&(A_\sigma^{U'-J})_{11}\,[(A_\sigma^{U'-J})^{-1}]_{12} + (A_\sigma^{U'-J})_{12}\,[(A_\sigma^{U'-J})^{-1}]_{22} = 0 \\
\Rightarrow\ &(A_\sigma^{U'-J})_{21}\,[(A_\sigma^{U'-J})^{-1}]_{11} + (A_\sigma^{U'-J})_{22}\,[(A_\sigma^{U'-J})^{-1}]_{21} = 0 \\
&(A_\sigma^{U'-J})_{21}\,[(A_\sigma^{U'-J})^{-1}]_{12} + (A_\sigma^{U'-J})_{22}\,[(A_\sigma^{U'-J})^{-1}]_{22} = 1
\end{aligned}
\tag{B.321}
$$

Then

$$
[(A_\sigma^{U'-J})^{-1}]_{\nu\,l,\nu\,l} = \frac{(A_\sigma^{U'-J})_{\nu'\,l,\nu'\,l}}{(A_\sigma^{U'-J})_{\nu\,l,\nu\,l}\,(A_\sigma^{U'-J})_{\nu'\,l,\nu'\,l} - (A_\sigma^{U'-J})_{\nu\,l,\nu'\,l}\,(A_\sigma^{U'-J})_{\nu'\,l,\nu\,l}},
\tag{B.322}
$$

$$
[(A_\sigma^{U'-J})^{-1}]_{\nu'\,l,\nu'\,l} = \frac{(A_\sigma^{U'-J})_{\nu\,l,\nu\,l}}{(A_\sigma^{U'-J})_{\nu\,l,\nu\,l}\,(A_\sigma^{U'-J})_{\nu'\,l,\nu'\,l} - (A_\sigma^{U'-J})_{\nu\,l,\nu'\,l}\,(A_\sigma^{U'-J})_{\nu'\,l,\nu\,l}},
\tag{B.323}
$$

$$
[(A_\sigma^{U'-J})^{-1}]_{\nu\,l,\nu'\,l} = \frac{-(A_\sigma^{U'-J})_{\nu\,l,\nu'\,l}}{(A_\sigma^{U'-J})_{\nu\,l,\nu\,l}\,(A_\sigma^{U'-J})_{\nu'\,l,\nu'\,l} - (A_\sigma^{U'-J})_{\nu\,l,\nu'\,l}\,(A_\sigma^{U'-J})_{\nu'\,l,\nu\,l}},
\tag{B.324}
$$

$$
[(A_\sigma^{U'-J})^{-1}]_{\nu'\,l,\nu\,l} = \frac{-(A_\sigma^{U'-J})_{\nu'\,l,\nu\,l}}{(A_\sigma^{U'-J})_{\nu\,l,\nu\,l}\,(A_\sigma^{U'-J})_{\nu'\,l,\nu'\,l} - (A_\sigma^{U'-J})_{\nu\,l,\nu'\,l}\,(A_\sigma^{U'-J})_{\nu'\,l,\nu\,l}},
\tag{B.325}
$$

where

$$
det(A_\sigma^{U'-J}) = (A_\sigma^{U'-J})_{\nu\,l,\nu\,l}\,(A_\sigma^{U'-J})_{\nu'\,l,\nu'\,l} - (A_\sigma^{U'-J})_{\nu\,l,\nu'\,l}\,(A_\sigma^{U'-J})_{\nu'\,l,\nu\,l}.
\tag{B.326}
$$

From these results, we can write a general formula for $[(A_\sigma^{U'-J})^{-1}]_{\nu\,l,\nu_4\,l_4}$ and $[(A_\sigma^{U'-J})^{-1}]_{\nu'\,l,\nu_4\,l_4}$:

$$
\begin{aligned}
[(A_\sigma^{U'-J})^{-1}]_{\nu\,l,\nu_4\,l_4} &= \delta_{l,l_4}\left\{\delta_{\nu_4,\nu}\,\frac{(A_\sigma^{U'-J})_{\nu'\,l,\nu'\,l}}{detA_\sigma^{U'-J}} \;-\; \delta_{\nu_4,\nu'}\,\frac{(A_\sigma^{U'-J})_{\nu\,l,\nu'\,l}}{detA_\sigma^{U'-J}}\right\},\\
[(A_\sigma^{U'-J})^{-1}]_{\nu'\,l,\nu_4\,l_4} &= \delta_{l,l_4}\left\{\delta_{\nu_4,\nu'}\,\frac{(A_\sigma^{U'-J})_{\nu\,l,\nu\,l}}{detA_\sigma^{U'-J}} \;-\; \delta_{\nu_4,\nu}\,\frac{(A_\sigma^{U'-J})_{\nu'\,l,\nu\,l}}{detA_\sigma^{U'-J}}\right\}.
\end{aligned}
\tag{B.327}
$$

Now, let's put these equations in the updated impurity Green's function equation.

B.8.3.3. Last form of the new impurity Green's function for $U' - J$ term

In Section B.8.3, we found that

$$
\begin{aligned}
(G^\sigma_{\nu_1,\nu_2}(l_1,l_2))' = G^\sigma_{\nu_1,\nu_2}(l_1,l_2) + \Big\{&(G^\sigma - I)_{\nu_1\,l_1,\nu'\,l}\,(e^{+2\,\lambda_3\,S_{ii}^{U'-J}} - 1)\\
&\sum_{\nu_4,l_4}[(A_\sigma^{U'-J})^{-1}]_{\nu'\,l,\nu_4\,l_4}\,G^\sigma_{\nu_4,\nu_2}(l_4,l_2)\\
+(G^\sigma - I)_{\nu_1\,l_1,\nu\,l}\,(e^{-2\,\lambda_3\,S_{ii}^{U'-J}} - 1)&\sum_{\nu_4,l_4}[(A_\sigma^{U'-J})^{-1}]_{\nu\,l,\nu_4\,l_4}\,G^\sigma_{\nu_4,\nu_2}(l_4,l_2)\Big\}.
\end{aligned}
\tag{B.328}
$$

If the expressions for $[(A_\sigma^{U'-J})^{-1}]_{\nu'\,l,\nu_4\,l_4}$ and $[(A_\sigma^{U'-J})^{-1}]_{\nu\,l,\nu_4\,l_4}$ are placed in the above equation, the new Green's function can be written as Then, this equation equals

$$
\begin{aligned}
&(G^\sigma_{\nu_1,\nu_2}(l_1,l_2)\,)' = G^\sigma_{\nu_1,\nu_2}(l_1,l_2)\\
&+\Big[(G^\sigma - I)_{\nu_1\,l_1,\nu'\,l}(e^{+2\,\lambda_3\,S_{ii}^{U'-J}} - 1)\sum_{\nu_4,l_4}\delta_{l,l_4}\Big\{\delta_{\nu_4,\nu'}\frac{(A_\sigma^{U'-J})_{\nu\,l,\nu\,l}}{detA_\sigma^{U'-J}} - \delta_{\nu_4,\nu}\frac{(A_\sigma^{U'-J})_{\nu'\,l,\nu\,l}}{detA_\sigma^{U'-J}}\Big\}G^\sigma_{\nu_4,\nu_2}(l_4,l_2)\Big]\\
&+\Big[(G^\sigma - I)_{\nu_1\,l_1,\nu\,l}(e^{-2\,\lambda_3\,S_{ii}^{U'-J}} - 1)\sum_{\nu_4,l_4}\delta_{l,l_4}\Big\{\delta_{\nu_4,\nu}\frac{(A_\sigma^{U'-J})_{\nu'\,l,\nu'\,l}}{detA_\sigma^{U'-J}} - \delta_{\nu_4,\nu'}\frac{(A_\sigma^{U'-J})_{\nu\,l,\nu'\,l}}{detA_\sigma^{U'-J}}\Big\}G^\sigma_{\nu_4,\nu_2}(l_4,l_2)\Big].
\end{aligned}
$$

$$
\begin{aligned}
&(G^{\sigma}_{\nu_1,\nu_2}(l_1,l_2))' = G^{\sigma}_{\nu_1,\nu_2}(l_1,l_2) \\
&+\Big[(G^{\sigma}-I)_{\nu_1\,l_1,\nu'\,l}(e^{+2\,\lambda_3\,S_{ii}^{U'-J}}-1)\Big\{-\frac{(A_{\sigma}^{U'-J})_{\nu'\,l,\nu\,l}}{detA_{\sigma}^{U'-J}}G^{\sigma}_{\nu\,\nu_2}(l,l_2)+\frac{(A_{\sigma}^{U'-J})_{\nu\,l,\nu\,l}}{detA_{\sigma}^{U'-J}}G^{\sigma}_{\nu',\nu_2}(l,l_2)\Big\}\Big] \\
&+\Big[(G^{\sigma}-I)_{\nu_1\,l_1,\nu\,l}(e^{-2\,\lambda_3\,S_{ii}^{U'-J}}-1)\Big\{\frac{(A_{\sigma}^{U'-J})_{\nu'\,l,\nu'\,l}}{detA_{\sigma}^{U'-J}}G^{\sigma}_{\nu\,\nu_2}(l,l_2)-\frac{(A_{\sigma}^{U'-J})_{\nu\,l,\nu'\,l}}{detA_{\sigma}^{U'-J}}G^{\sigma}_{\nu',\nu_2}(l,l_2)\Big\}\Big].
\end{aligned}
$$

We define that

$$
\begin{aligned}
(A_{\sigma}^{U'-J})_{11} &= (A_{\sigma}^{U'-J})_{\nu'\,l,\nu'\,l}, \\
(A_{\sigma}^{U'-J})_{22} &= (A_{\sigma}^{U'-J})_{\nu\,l,\nu\,l}, \\
(A_{\sigma}^{U'-J})_{12} &= (A_{\sigma}^{U'-J})_{\nu'\,l,\nu\,l}, \\
(A_{\sigma}^{U'-J})_{21} &= (A_{\sigma}^{U'-J})_{\nu\,l,\nu'\,l},
\end{aligned}
$$

and

$$
det(A_{\sigma}^{U'-J}) = (A_{\sigma}^{U'-J})_{\nu\,l,\nu\,l}\,(A_{\sigma}^{U'-J})_{\nu'\,l,\nu'\,l} - (A_{\sigma}^{U'-J})_{\nu\,l,\nu'\,l}\,(A_{\sigma}^{U'-J})_{\nu'\,l,\nu\,l}. \quad \text{(B.329)}
$$

Therefore, the last form of the updated Green's function for $U'-J$ terms equals

$$
\begin{aligned}
&(G^{\sigma}_{\nu_1,\nu_2}(l_1,l_2))' = G^{\sigma}_{\nu_1,\nu_2}(l_1,l_2) \\
\Rightarrow\ &+\Big[(G^{\sigma}-I)_{\nu_1\,l_1,\nu'\,l}(e^{+2\,\lambda_3\,S_{ii}^{U'-J}}-1)\Big\{-\frac{(A_{\sigma}^{U'-J})_{12}}{detA_{\sigma}^{U'-J}}G^{\sigma}_{\nu\,\nu_2}(l,l_2)+\frac{(A_{\sigma}^{U'-J})_{22}}{detA_{\sigma}^{U'-J}}G^{\sigma}_{\nu',\nu_2}(l,l_2)\Big\}\Big] \\
&+\Big[(G^{\sigma}-I)_{\nu_1\,l_1,\nu\,l}(e^{-2\,\lambda_3\,S_{ii}^{U'-J}}-1)\Big\{\frac{(A_{\sigma}^{U'-J})_{11}}{detA_{\sigma}^{U'-J}}G^{\sigma}_{\nu\,\nu_2}(l,l_2)-\frac{(A_{\sigma}^{U'-J})_{21}}{detA_{\sigma}^{U'-J}}G^{\sigma}_{\nu',\nu_2}(l,l_2)\Big\}\Big].
\end{aligned}
$$

In this result, $G^{\sigma}_{\nu,\nu'}(l,l')$ is defined as the following and without $-$ sign so we have to be careful.

$$
G^{\sigma}_{\nu,\nu'}(l,l') = +\left\langle\, d_{\nu\,\sigma}(l)\, d^{\dagger}_{\nu'\,\sigma}(l')\,\right\rangle \quad \text{(B.330)}
$$

APPENDIX C

DETERMINATION OF THE FERMI LEVELS FOR THE HEME CLUSTERS

In this section, we present the QMC data on the Fermi levels of deoxy and oxy molecules. QMC results on the chemical potential of molecules are different than the DFT results. The reason is that Coulomb interactions between the Fe(3d) orbitals are taken into account without any approximation in the QMC calculations. These interactions lead to broaden in the energy levels of the 3d states. Hence, the chemical potential for deoxy and oxy molecules are calculated differently by QMC and DFT.

Deoxy molecule contains 334 electrons and Figure A.2 indicates that the HOMO level of deoxy molecule is obtained at -3.53 eV by DFT calculations. Different from the deoxy, oxy molecule have 350 electrons and Fig. A.3 shows that HOMO level is obtained at -4.12 eV by DFT calculations.

In Fig. C.1(a), we present QMC data on the total electron occupation of the Fe($3d_\nu$) orbitals $\langle n_{\rm d}\rangle$ as a function of μ for deoxy. We see that $\langle n_{\rm d}\rangle$ increases continuosly up to $\mu = -4$ eV. At $\mu = -4$ eV, there is a discontinuity in $\langle n_d\rangle$ and this point will be very important to explain the spin state of the deoxy molecule. Total electron number of Fe(3d) orbitals do not change between -4 eV $\lesssim \mu \lesssim -3$ eV. Above the ≈ -3 eV, $\langle n_{\rm d}\rangle$ increases. The total number of the host electrons $\langle n_{\rm h}\rangle$ is shown in Fig. C.1(b). Here, $\langle n_{\rm h}\rangle$ increases up to ≈ -4 eV. $\langle n_d\rangle$ does not change between the -4 eV $\lesssim \mu \lesssim -3$ eV. This is because that any host states are not located in this energy interval. $\langle n_{\rm h}\rangle$ increases above the $\mu \approx -3$ eV by the filling of the host states. Figure C.1(c) shows the total electron number for deoxy $\langle n_{\rm T}\rangle = \langle n_{\rm d}\rangle + \langle n_{\rm h}\rangle$ versus μ. Here, we clearly see that at $\mu = -2.8$ eV the total electron number $\langle n_{\rm T}\rangle = 334$ corresponding to the neutral deoxy molecule. This means that $\mu = -2.8$ eV is the Fermi level of deoxy obtained by the QMC calculations. At this μ value, total electron number of Fe(3d) orbitals is $\langle n_{\rm d}\rangle \approx 5.3$.

We discuss QMC data on the total electron occupation of the Fe($3d_\nu$) orbitals $\langle n_{\rm d}\rangle$ for oxy as a function of μ in Fig. C.2 (a). We see that $\langle n_{\rm d}\rangle$ increases continuously. The total number of the host electrons $\langle n_{\rm h}\rangle$ is shown in Fig. C.2(b). Similar to $\langle n_{\rm d}\rangle$, $\langle n_{\rm h}\rangle$ also increases with changing μ. Figure C.2(c) shows the total electron number for oxy $\langle n_{\rm T}\rangle = \langle n_{\rm d}\rangle + \langle n_{\rm h}\rangle$ versus μ. Here, we clearly see that at $\mu = -3.8$ eV the total electron

number $\langle n_{\mathrm{T}} \rangle = 350$ corresponding to the neutral oxy molecule. These results imply that $\mu = -3.8$ eV is the Fermi level for oxy molecule. At this μ value, total electron number of Fe(3d) orbitals is $\langle n_{\mathrm{d}} \rangle \approx 5.84$.

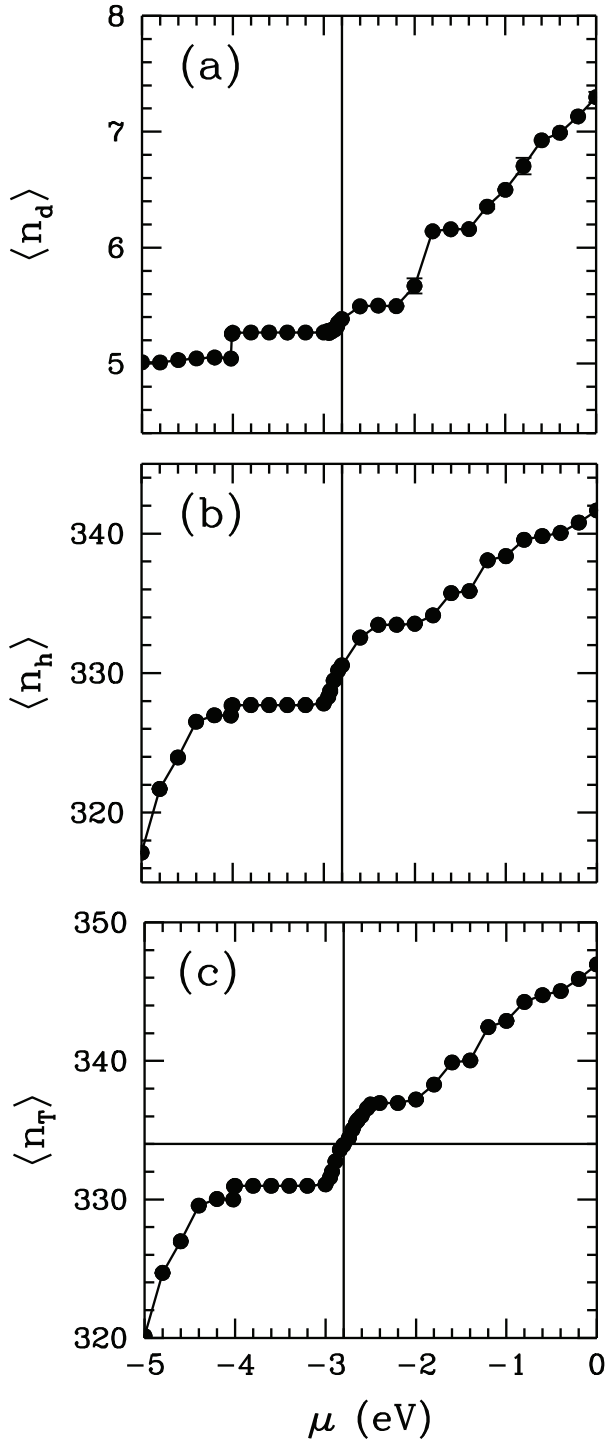

Figure C.1. QMC results for deoxy on the occupation numbers. (a) Total electron occupation number $\langle n_{\rm d} \rangle$ of the Fe($3d$) natural atomic orbitals versus the chemical potential μ. (b) Total number of the host electrons $\langle n_{\rm h} \rangle$ versus μ. (c) Total number of electrons $\langle n_{\rm T} \rangle = \langle n_{\rm d} \rangle + \langle n_{\rm h} \rangle$ for deoxy versus μ. Here, the vertical solid black line denotes the Fermi level obtained by QMC. Deoxy molecule contains 334 electrons. These results are for $U = 4$ eV, $J = 0.9$ eV and $T = 300$ K.

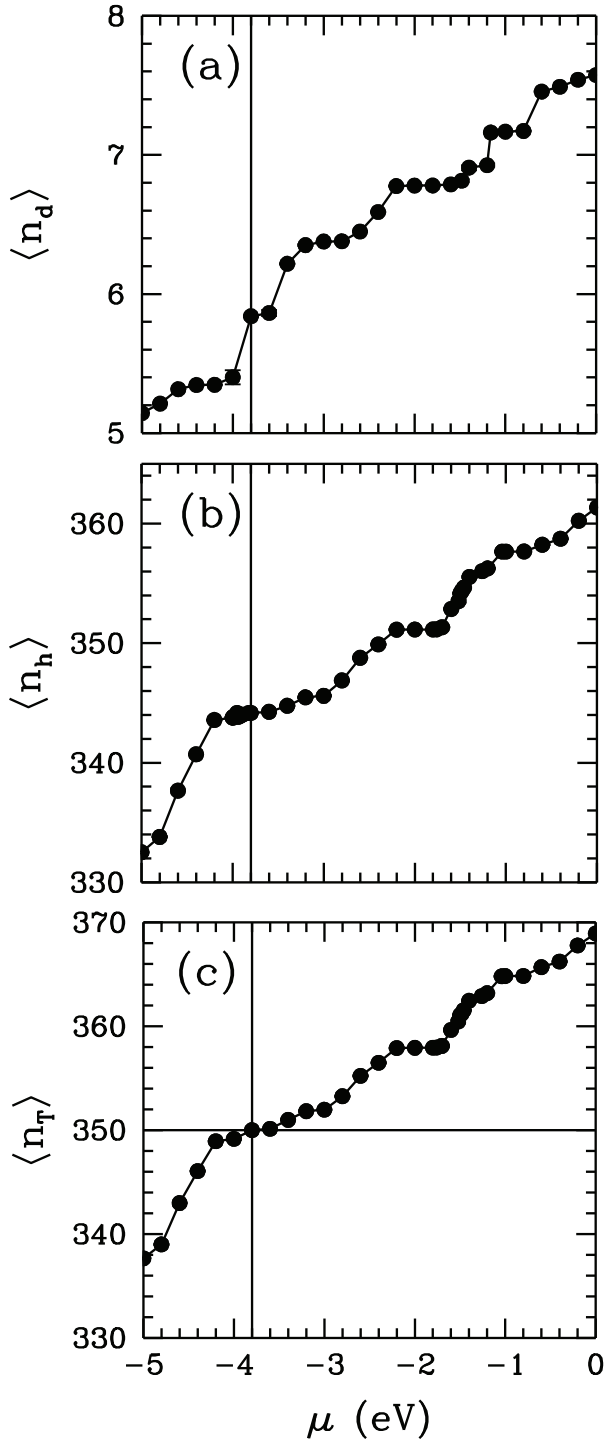

Figure C.2. QMC results for oxy on the occupation numbers. (a) Total electron occupation number $\langle n_{\rm d} \rangle$ of the Fe($3d$) natural atomic orbitals versus the chemical potential μ, (b) Total number of the host electrons $\langle n_{\rm h} \rangle$ versus μ and (c) Total number of electrons $\langle n_{\rm T} \rangle = \langle n_{\rm d} \rangle + \langle n_{\rm h} \rangle$ versus μ. Here, the vertical solid line indicates the Fermi level obtained by QMC for oxy. Oxy molecule contains 350 electrons. These results are for $U = 4$ eV, $J = 0.9$ eV and $T = 300$ K.

APPENDIX D

COMPETITION OF THE HUND'S COUPLING WITH THE FE(3D)-HOST ANTIFERROMAGNETIC CORRELATIONS

In this section, we explain the competition of the Hund's coupling with the Fe(3d)-host antiferromagnetic (AF) correlations.

In deoxy molecule, Fe($3d$) orbitals have strong ferromagnetic correlations due to Hund's coupling. IBS are located below the chemical potential and are occupied in deoxy. In addition, we observe weak ferromagnetic correlations between the Fe($3d$) and the surrounding host states. Hence, deoxy molecule has the high-spin state. On the other hand, IBS are located above the chemical potential and are not occupied in oxy molecule. We observe that weak ferromagnetic correlations occur between the Fe($3d$) orbitals. In addition, Fe(3d)-host correlations are strongly antiferromagnetic. This causes to obtain low-spin state for oxy with respect to deoxy. These AF correlations suppress the ferromagnetic correlations in Fe($3d$) orbitals and Hund's coupling compete with the Fe(3d)-host AF correlations.

Competition between the Hund's coupling and Fe(3d)-host AF correlations will be explained as follow. Fe(3d) orbitals have the strong ferromagnetic correlations due to Hund's coupling. In addition, one of these Fe(3d) orbitals has the strong hybridization with a host orbitals as shown in Fig. A.4 for deoxy and Fig. A.5 for oxy. We know that Fe(3d)-host system is described by the Anderson Hamiltonian in Eq. 1.4. This system has two situation; in one of which, anti-ferromagnetic correlations occur between the Fe(3d) and host states, and in the other, ferromagnetic correlations are seen between the Fe(3d) and host states. The energy of the first situation is less than the second one, and the energy differences between them equals $|V_{m\nu}|^2/U$. When an electron in host state jumps to the Fe(3d) orbitals which have the strongest hybridization with the host, the Hund's coupling at Fe(3d) site disappers. If the acquired energy, $|V_{m\nu}|^2/(U+J)$, is larger than the J in this situation, the ferromagnetic correlations at Fe(3d) orbitals are suppressed by Fe(3d)-host AF correlations. Hence, system goes to low-spin state.

Figure D.1 shows the competition of the Hund's coupling and AF correlations between the 3d orbitals and host orbitals. In these calculations for oxy, the hybridization between the 158'th host state and the Fe(3d) orbitals ,$V_{158,\nu}$, are zero except V_{158,x^2-y^2},

and the other hybridization elements are the same with the DFT results. We change the $(V_{158,x^2-y^2})^2$ from 0 to 5 to observe the competition between the Hund's coupling and antiferromagnetic correlations between the Fe(3d)-host states.

Figure D.1(a) shows that the host magnetic moment increases with increasing the hybridization. We see in Fig. D.1 (b) that the AF correlations between the $3d_{x^2-y^2}$ and $m = 158$'th host states increases with changing hybridization. On the other hand, the magnetic correlations between the 3d orbitals decreases with increasing hybridization as seen in Fig. D.1(c). These results show that the hybridization between the host and 3d orbitals lead to decrease Hund's coupling between the 3d orbital and to increase the AF correlations between the host and 3d orbitals. Ferromagnetic correlations occur between the 3d orbitals due to Hund's coupling. When the hybridization increases, Hund's coupling is suppressed by the 3d-host AF correlations.

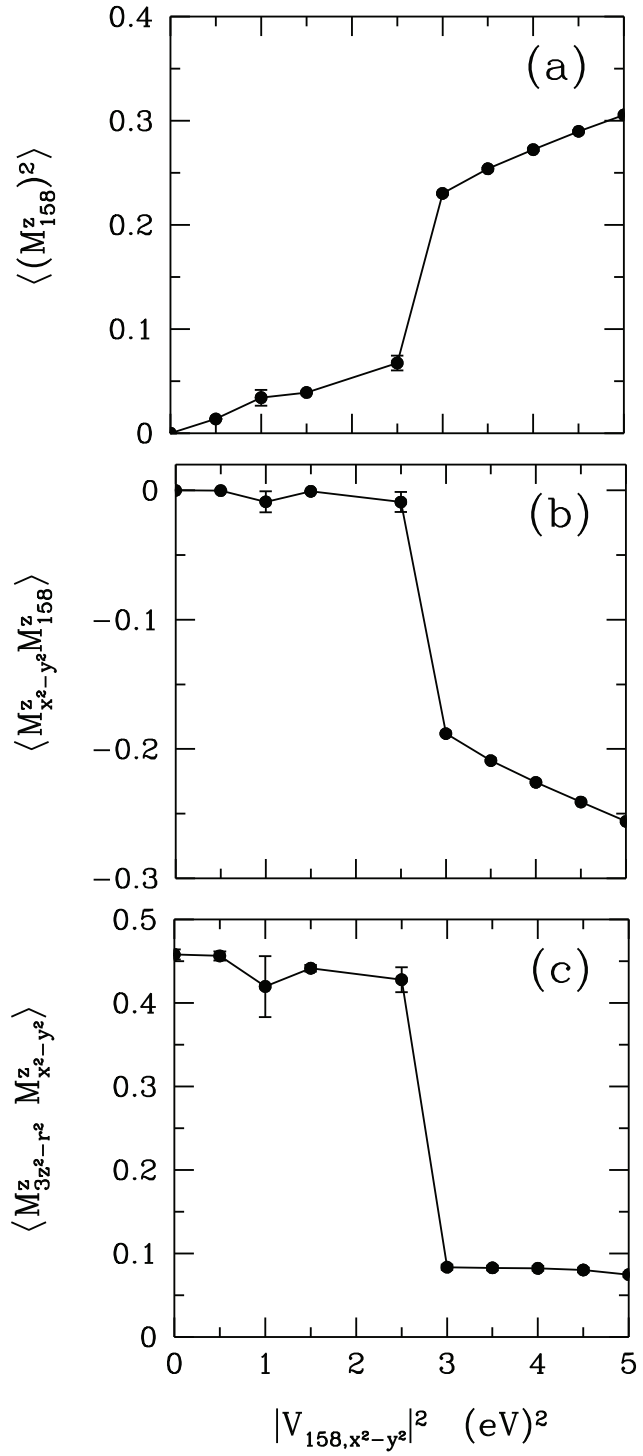

Figure D.1. For oxy-heme cluster, the hybridization between the 158'th host state and the Fe(3d) orbitals ,$V_{158,\nu}$, are zero except V_{158,x^2-y^2}, and the other hybridization elements are the same with the DFT results. (a) the square of the total magnetic moment of 158'th host state $\langle (M^z_{158})^2 \rangle$ versus $|V_{158,x^2-y^2}|^2$, in (b) the magnetic correlation function between the x^2-y^2 and 158'th host state $\langle M^z_{x^2-y^2} M^z_{158} \rangle$ versus $|V_{158,x^2-y^2}|^2$, and in (c) the magnetic correlation function between the $3z^2-r^2$ and x^2-y^2 orbital $\langle M^z_{3z^2-r^2} M^z_{x^2-y^2} \rangle$ versus the square of the hybridization between the x^2-y^2 and 158'th host state $|V_{158,x^2-y^2}|^2$. Here, $U = 4$ eV, $J = 0.9$ eV and $T = 700$ K.

APPENDIX E

EFFECT OF THE U' AND J TERMS ON THE IMPURITY BOUND STATES

In this section, we show the effect of the U' and $U' - J$ terms on the impurity bound states both in the deoxy molecule and oxy molecule.

Figure E.1 shows the magnetic correlation function between the Fe(3d) orbitals and the host orbital. Here, Figure E.1 (a) show the magnetic correlations between the Fe(3d) orbitals and $m = 152$ for deoxy molecule. Figure E.1 (b) shows the magnetic correlations between the Fe(3d) orbitals and $m = 158$ for oxy molecule. In these results, we take the $U = 4$ eV and $U' = U' - J = 0$ eV to observe the effect of the inter-orbital correlations on the impurity bound states.

In Figure E.1 (a-b), we see that impurity bound states exist for deoxy and oxy molecules even inter-orbital correlations are 0. On the other hand, the situation is different for deoxy molecule with respect to results in which U' and $U' - J$ do not equal 0. We know from Fig.2.6 (b) that IBS are located below the Fermi level of deoxy, and hence molecule has the high-spin state. However, Figure E.1 (a) shows that IBS are located above the Fermi level for deoxy and so molecule has the low-spin state.

These results show that inter-orbital correlations are very important to observe the high-spin to low-spin transition in hemoglobin molecule. If U' and $U' - J$ term were not taken into account, we could observe the IBS both in the oxy and deoxy molecules, but deoxy molecule had the low-spin state.

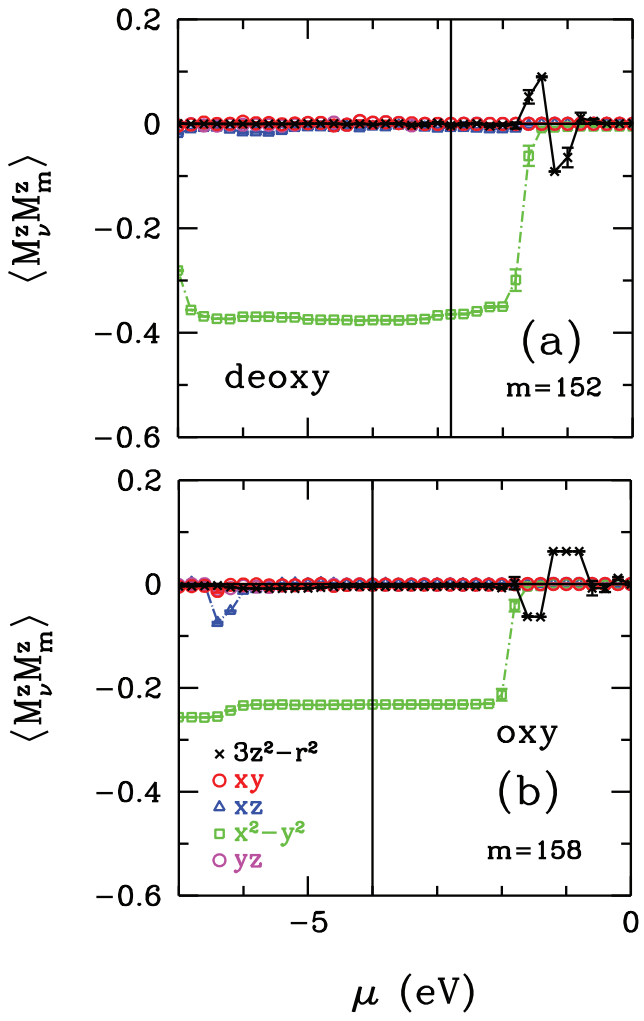

Figure E.1. (a) Fe(3d)-host magnetic correlation function $\langle M_\nu^z M_{m=152}^2 \rangle$ versus chemical potential μ for deoxy molecule. The black line shows the Fermi level of deoxy-heme. (b) Fe(3d)-host magnetic correlation function $\langle M_\nu^z M_{m=158}^2 \rangle$ versus μ for oxy molecule. The black solid line represents the Fermi level of oxy-heme. Here, $U = 4$ eV, $U' = U' - J = 0$ eV and $T = 700$ K.

APPENDIX F

POTENTIAL SOURCES FOR THE COMPUTATIONAL ERRORS IN DFT+QMC APPROACH

In this chapter, we will show some potential sources for the computational errors in DFT+QMC. These are the double-counting term, $\Delta\tau$ error and the neglect of the pair hopping and spin-flip terms.

F.1. Double-counting term

As mentioned in Appendix A, we substract the double-counting term from the energy levels of Fe(3d) orbitals. The orbital dependent μ_{ν}^{DC} and the orbital independent double-counting μ^{DC} terms are

$$\mu_{\nu}^{\mathrm{DC}} = \frac{U n_{d\nu}^{\mathrm{DFT}}}{2} + [U' + U''] \sum_{\nu' \neq \nu} \frac{n_{d\nu'}^{\mathrm{DFT}}}{2} \tag{F.1}$$

and

$$\mu^{\mathrm{DC}} = (U + 4U' + 4U'') \frac{n_{d}^{\mathrm{DFT}}}{10} \tag{F.2}$$

For the DFT+QMC results, we use $U = 4$ eV and $J = 0.9$ eV. These values are for the free Fe atom. On the other hand, we do not know exactly which U and J values are used in DFT calculations. In addition, which kind of double-counting terms is true for our calculations. These uncertainties in double-counting term may lead some error in DFT+QMC results.

Table F.1 and F.2 show the total Fe(3d) magnetic moment M_{3d}, total magnetic moment of molecule M_t, total Fe(3d) effective spin S_{3d} and the total effective spin of molecule S_t for different U, J and double counting term for deoxy-heme and oxy-heme,

Table F.1. For deoxy-heme, total Fe(3d) magnetic moment M_{3d}, total magnetic moment of molecule M_t, total Fe(3d) effective spin S_{3d} and the total effective spin of molecule S_t for different U, J and double counting term. Here, temperature equals 300 K for $U = 4$ eV and $T = 1500$ K for $U = 3$ eV.

	$M_{3d}(\mu_b)$	$M_t(\mu_b)$	S_{3d}	S_t
$U = 4$ eV, $J = 0.9$ eV, μ_ν^{DC}=11.3 eV	4.55	4.08	1.83	1.60
$U = 4$ eV, $J = 0.9$ eV, μ^{DC}=13.0 eV	3.83	4.03	1.45	1.58
$U = 3$ eV, $J = 0.6$ eV, μ^{DC}=9.35 eV	3.83	4.03	1.45	1.58

Table F.2. For oxy-heme, total Fe(3d) magnetic moment M_{3d}, total magnetic moment of molecule M_t, total Fe(3d) effective spin S_{3d} and the total effective spin of molecule S_t for different U, J and double counting term. Here, temperature equals 300 K for $U = 4$ eV and $T = 1500$ K for $U = 3$ eV.

	$M_{3d}(\mu_b)$	$M_t(\mu_b)$	S_{3d}	S_t
$U = 4$ eV, $J = 0.9$ eV, μ_ν^{DC}=11.3 eV	2.50	2.13	0.85	0.68
$U = 4$ eV, $J = 0.9$ eV, μ^{DC}=13.0 eV	1.55	0.77	0.42	0.13
$U = 3$ eV, $J = 0.6$ eV, μ^{DC}=9.35 eV	1.45	0.67	0.38	0.10

respectively. Here, it is seen that we obtain different magnetic moments and effective spin for different parameters. These results show that DFT+QMC results are very different for the different double-counting terms.

F.2. $\Delta\tau$ error

In this section, we will show the effect of the $\Delta\tau$ error on the results for oxy-heme cluster.

In Hirsch-Fye algorithm, we use Trotter approximation in order to write partition function. In DFT+QMC results, we have $\Delta\tau$ error due to this approximation. The temperature is calculated as $T^{-1} = \Delta\tau\, L$. In the low temperatures, we use big L values, which increases the time cost of QMC simulations. In order to optimize the running time of simulations, we have to make small changes in $\Delta\tau$ for different L values.

In DFT+QMC calculations, for $T = 300$ K, $\Delta\tau = 0.1295$, for $T = 200$ K,

$\Delta\tau = 0.1578$ and for $T = 150$ K, $\Delta\tau = 0.1933$. In order to see the effect of $\Delta\tau$ values in DFT+QMC results, we calculate the total Fe(3d) electron number n_{3d}, the total electron number, total magnetic susceptibility χ_t and total magnetic moment M_t of molecule n_t as a function of $\Delta\tau$ for different temperatures. These results are shown in Fig. F.1(a-d). Here, we extrapolate these results to see the values for $\Delta\tau \rightarrow 0$ because in this limit, QMC results become exact.

Figure F.1(a) and (b) show the total 3d electrons and the total electron number of molecule as a function of $\Delta\tau$ for different temperatures. We see from these results that the electron numbers increase with decreasing of $\Delta\tau$ for all temperatures. For $T = 300$ K, $\langle n_d \rangle$ goes to 5.85. On the other hand, for 200 K and 150 K, $\langle n_d \rangle$ is higher than 6 electrons. The charge neutral oxy cluster has the 350 electrons. As seen in Fig. F.1(b), when $\Delta\tau$ goes to 0, the electron number of oxy case equals approximately 350 for all temperatures.

In Figure F.1(c-d), the χ_t and M_t are shown as a function of $\Delta\tau$, respectively. Here, we observe that χ_t and M_t values decrease with the decreasing in $\Delta\tau$. These graphs show that at $T = 300$ K, the susceptibility and the magnetic moment do not go to 0 with decreasing in $\Delta\tau$. On the contrary, for $T = 200$ K and $T = 150$ K, the susceptibility and the magnetic moments go to 0. As mentioned in the previous chapters, the magnetic gap is formed at low temperatures ($T < 300$ K). The O_2-Fe(3d) charge transfer occurs and the the spin state of the molecule goes to 0. When we look χ_t and M_t at the $\Delta\tau$ values used for $T = 200$ K and $T = 150$ K, χ_t and M_t is small but they are not equal 0. These results show that when $\Delta\tau \rightarrow 0$, the χ_t and M_t goes to 0.

Figure F.1(a-d) show that when $\langle n_d \rangle$ > 6, the susceptibility and the magnetic moment of molecule equal approximation 0. This means that the spin state of molecule is S=0.

The results presented in this section the effect of $\Delta\tau$ values on the DFT+QMC results. In the light of these results, the spin state does not go 0 for $T = 300$ K as $\Delta\tau \rightarrow 0$. On the other hand, χ_t and M_t go to 0 as $\Delta\tau \rightarrow 0$. In addition, we see that the $\Delta\tau$ does not affect our conclusions.

F.3. Spin-flip and the pair-hopping terms

Our results show that oxy-heme has effective spin $S = 0.65$ at $T = 300$ K. When the temperature is decreased, the spin state of the oxy-heme is lowered. The reason is that the magnetic gap is formed at lower temperatures and the charge transfer between the

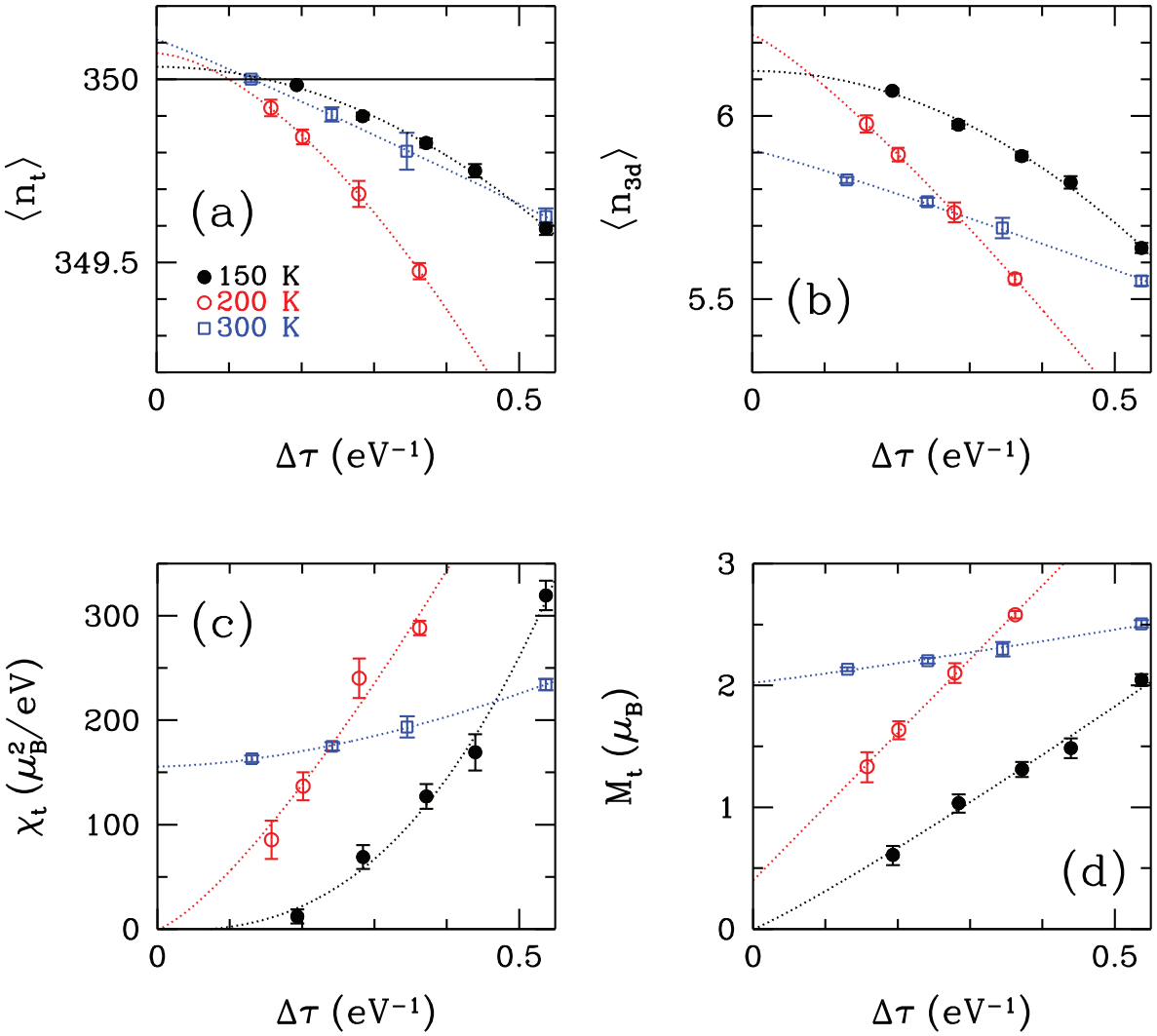

Figure F.1. (a) Total number of the electrons in the cluster $\langle n_{\rm t} \rangle$, (b) the total electron number in the Fe($3d$) orbitals $\langle n_{3d} \rangle$, (c) the total spin susceptibility $\chi_{\rm t}$, and (d) the total magnetic moment $M_{\rm t}$ plotted as a function of $\Delta\tau$ for the various values of T shown in (a). Here, $\Delta\tau$ is the Matsubara-time step used in the QMC simulations. The dotted curves are the least-squares fits to the QMC data.

O_2 to Fe(3d) orbitals occur. This charge transfer decreases the total magnetic moment of molecule.

In DFT+QMC calculations, we ignore the spin-flip and the pair-hopping terms. We do not know the effect of these terms on results for oxy-heme and deoxy-heme clusters. In order to see the possible effect of these terms, we do exact diagonalization calculations for the deoxy and oxy-heme cluster.

The spin-flip and the pair-hopping terms are defined by

$$H_J \equiv J \sum_{\nu>\nu'} (d^\dagger_{\nu\uparrow} d^\dagger_{\nu'\downarrow} d_{\nu\downarrow} d_{\nu'\uparrow} + d^\dagger_{\nu\uparrow} d^\dagger_{\nu\downarrow} d_{\nu'\downarrow} d_{\nu'\uparrow} + h.c.). \tag{F.3}$$

To explaine the effect of spin-flip and pair-hopping terms, we show the expectation values of total electron number of Fe(3d) orbitals and the square of the total magnetic moment of Fe(3d) orbitals as a function of chemical potential μ in Fig. F.2 (a) and (b), respectively. Here, the black line represents that spin-flip and pair-hopping terms (H_J) equal 0 and the red line represents that H_J is not zero. In these calculations, the hybridization between the Fe(3d) orbitals and host orbitals are set to zero. Figure F.2 (a) shows that H_J terms do not affect the total occupation number of Fe(3d) orbitals. On the other hand, the situation is not the same for the total magnetic moment of Fe(3d) orbitals. As seen in Fig. F.2 (b), $\langle (M_{\rm d})^2 \rangle$ decreases at $\mu = -3$ eV and $\mu = -11$ eV with H_J term. Hence, spin-flip and pair-hopping terms will be important to explaine the spin transition in hemoglobin molecule.

Figure F.3 shows the exact diagonalization results for the expectation value of H_J part of the Anderson Hamiltonian. This figure shows that the expectation value of H_J is not zero for $H_J \neq 0$ eV and our QMC results will be change with including the spin-flip and pair-hopping terms.

We calculate the expectation value of H_J by using QMC. In these calculations, we use the Green's functions which were obtained for the Anderson Hamiltonian in Eq. 1.4. This Hamiltonian does not include the spin-flip and pair-hopping terms. Hence, we find the expectation value of H_J term by using the first-order approximation.

Figure F.4 shows the expectation value of $\langle H_J \rangle$ as a function of chemical potential μ for deoxy and oxy molecules. This figure indicates that the $\langle H_J \rangle$ equals 0 for deoxy. On the other hand, the contribution of pair-hopping and spin-flip terms change with respect to μ for oxy.

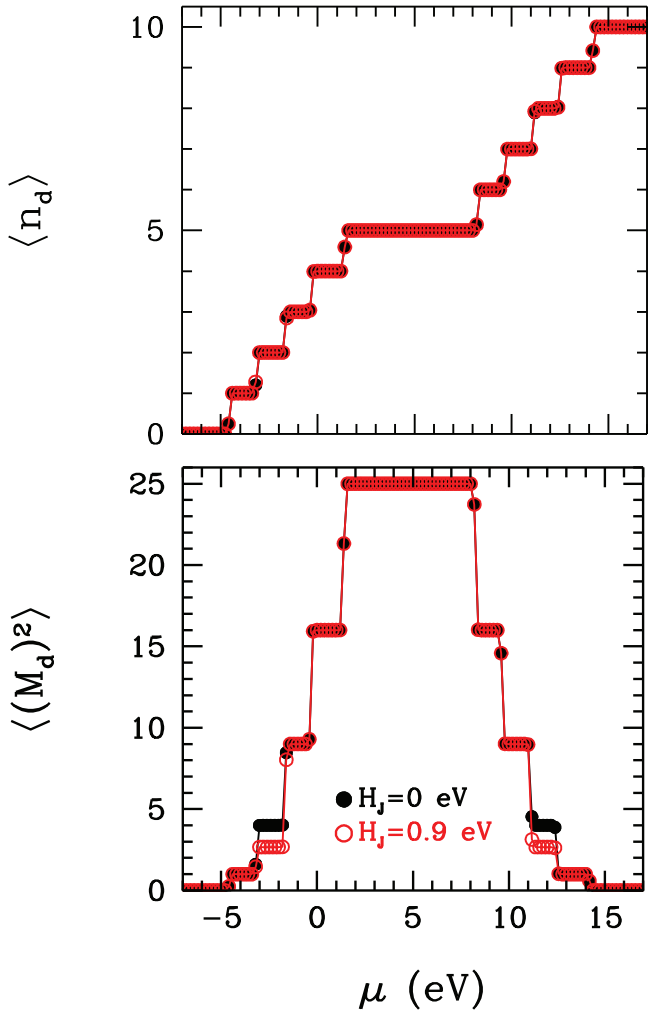

Figure F.2. Exact diagonalization results for (a) total electron number of Fe(3d) orbitals $\langle n_d \rangle$ for oxy molecule versus chemical potential μ and (b) square of the total Fe(3d) magnetic moment $\langle (M_{\rm d})^2 \rangle$ versus μ. The black circular represents results for zero spin-flip and pair hopping terms, $H_J = 0$ eV, and the red circular represents results for $H_J = 0.9$ eV. Here, $U = 4$ eV, $U'' = 1.3$ eV and $T = 300$ K.

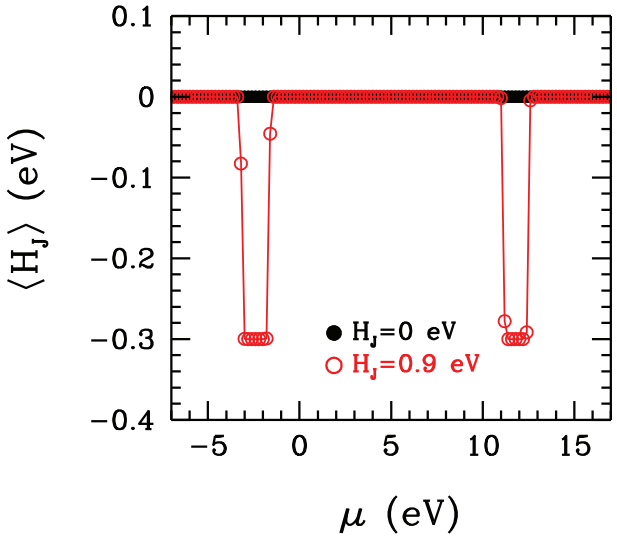

Figure F.3. Exact diagonalization results for expectation value H_J $\langle H_J \rangle$ for oxy molecule versus μ. The black circular represents results for $H_J = 0$ eV and the red circular represents results for $H_J = 0.9$ eV. Here, $U = 4$ eV, $U'' = 1.3$ eV and $T = 300$ K.

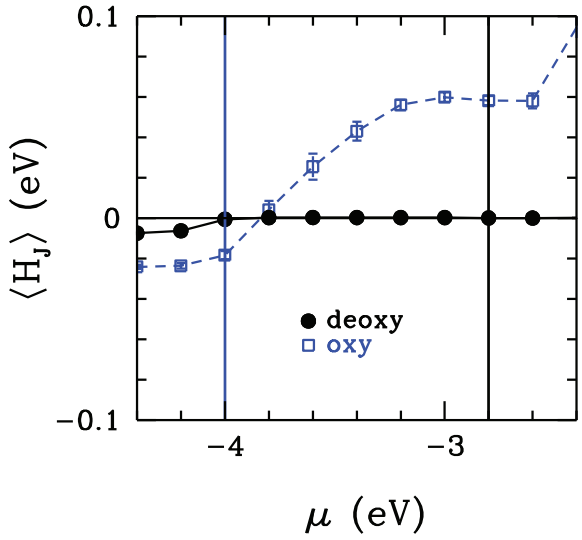

Figure F.4. QMC results for the expectation value of the spin-flip and pair-hopping terms $\langle H_J \rangle$ of Anderson Hamiltonian versus μ for deoxy and oxy molecules. The black circular represents the deoxy and the blue square represents the oxy-heme. Here, vertical solid blue line shows the Fermi level of oxy and the vertical black line shows the Fermi level of deoxy-heme. These chemical potential values are obtained by QMC calculations. These results are for $U = 4$ eV, $J = 0.9$ eV and $T = 300$ K.

APPENDIX G

DEPENDENCE ON THE FE-PORPHYRIN DISTANCE FOR DEOXY-HEME CLUSTER

In this chapter, we show the the effects of the doming of the porphyrin layer on the electronic and magnetic properties for deoxy heme. In particular, we change the Fe-porphyrin distance d by hand from 0.6 Å down to 0.0 Å by hand. For each value of d, we perform the DFT calculation for the Anderson model parameters. Then we perform QMC simulations for each DFT parameter set.

Table G.1. For different Fe-porphyrin ring distance d and square of the hybridization between the Fe(3d) and host states $W = \sum_\nu \sum_m |V_{m\nu}|^2$ in deoxy-heme molecule, DFT+QMC results on the total electron number of the Fe($3d_\nu$) NAO's $\langle n_{\rm d} \rangle$, total effective magnetic moment of the Fe($3d_\nu$) NAO's, $M_{\rm 3d}^{\rm eff}$, total effective magnetic moment of the host states $M_{\rm h}^{\rm eff}$, total Fe(3d)-host magnetic correlation function $\langle M_{\rm 3d}^z M_{\rm h}^z \rangle$, total effective magnetic moment of the molecule $M_{\rm T}^{\rm eff}$, total Fe(3d) effective spin $S_{\rm 3d}^{\rm eff}$, total host spin $S_{\rm h}^{\rm eff}$, total effective spin of the molecule $S_{\rm T}^{\rm eff}$. Here, effective spin is calculated by using $M_{\rm T}^{\rm eff} = 2\sqrt{S_{\rm T}^{\rm eff}(S_{\rm T}^{\rm eff}+1)}$. These results are for $U = 4$ eV, $J = 0.9$ eV and $T = 700$ K.

d(Å)	W (eV)^2	$\langle n_{\rm 3d} \rangle$	$M_{\rm 3d}^{\rm eff}$	$M_{\rm h}^{\rm eff}$	$\langle M_{\rm 3d}^z M_{\rm h}^z \rangle$	$M_{\rm T}^{\rm eff}$	$S_{\rm 3d}^{\rm eff}$	$S_{\rm h}^{\rm eff}$	$S_{\rm T}^{\rm eff}$
0.04	29.76	5.38	4.54	1.06	-1.17	4.40	1.82	0.22	1.76
0.10	29.58	5.37	4.51	1.08	-1.01	4.46	1.81	0.24	1.79
0.20	29.14	5.32	4.61	1.04	-0.19	4.69	1.86	0.22	1.90
0.30	28.65	5.30	4.64	1.01	0.28	4.81	1.87	0.21	1.96
0.40	28.30	5.29	4.64	0.98	0.44	4.84	1.88	0.20	1.97
0.50	28.29	5.29	4.64	0.99	0.62	4.88	1.87	0.20	1.99
0.60	29.14	5.28	4.65	1.00	0.69	4.90	1.88	0.21	2.00

In Table G.1, we see that as d decreases from 0.6 Å to 0.0 Å, the parameter W increases from 29.14 to 29.76 due to the increase in the hybridization, as Fe approaches the porphyrin layer. We note that during this decrease of d, the total spin S_T varies only from 2 to 1.76. Hence, we do not observe a high-spin to low-spin transition by only varying the Fe-porphyrin distance.

The reason is that when the distance between the Fe and porphyrin layer is changed,

the distance between the imidazole and Fe remains is not constant. Hence, we should do our calculations for the situation in which the Fe-imidazole distance is constant and the only variable is the distance between the Fe and the porphyrin layer.

VITA

Date and Place of Birth: 04.07.1988, Isparta-TURKEY

EDUCATION

2013 - 2019 Doctor of Philosophy in Department of Materials Science and Engineering
Graduate School of Engineering and Sciences, İzmir Institute of Technology,
İzmir -Turkey
Thesis Title: Magnetic effect in the biological functioning of hemoglobin: DFT+QMC approach within an effective multi-orbital Anderson impurity model
Supervisor: Prof. Dr. Nejat BULUT
Co-Supervisor: Prof. Dr. Mustafa M. DEMİR

2011 - 2013 Master of Science in Physics
Graduate School of Engineering and Sciences, İzmir Institute of Technology
İzmir -Turkey
Thesis Title: Electronic correlations in metalloproteins: a quantum Monte Carlo study
Supervisor: Prof. Dr. Nejat BULUT

SELECTED PUBLICATIONS

Kandemir, Z., Mayda, S., and Bulut, N.
(2016). ”Electronic structure and correlations of vitamin B_{12} studied within the Haldane-Anderson impurity model”.
The European Physical Journal B, 89(5), 113.

Mayda, S., Kandemir, Z., and Bulut, N.
(2017). ”Electronic structure of cyanocobalamin: DFT+QMC study”.
Journal of Superconductivity and Novel Magnetism, 30(11), 3301–3308.

Mayda, S., Kandemir, Z., and Bulut, N.
(2018). ”Future applications of artificially-synthesized organic molecules containing transition-metal atoms”.
Handbook of Nanomaterials for Industrial Applications, Elsevier, 386–391.